COMPUTATIONAL FLUID DYNAMICS (CFD) SIMULATIONS OF DILUTE

FLUID-PARTICLE FLOWS IN AEROSOL CONCENTRATORS

A Dissertation

by

SRIDHAR HARI

Submitted to the Office of Graduate Studies of
Texas A&M University
in partial fulfillment of the requirements for the degree of

DOCTOR OF PHILOSOPHY

December 2003

Major Subject: Nuclear Engineering

COMPUTATIONAL FLUID DYNAMICS (CFD) SIMULATIONS OF DILUTE

FLUID-PARTICLE FLOWS IN AEROSOL CONCENTRATORS

A Dissertation

by

SRIDHAR HARI

Submitted to Texas A&M University
in partial fulfillment of the requirements
for the degree of

DOCTOR OF PHILOSOPHY

Approved as to style and content by:

_____
Yassin A. Hassan
(Co-Chair of Committee)

_____
Andrew R. McFarland
(Co-Chair of Committee)

_____
William H. Marlow
(Member)

_____
Ian S. Hamilton
(Member)

_____
William E. Burchill
(Head of Department)

December 2003

Major Subject: Nuclear Engineering

ABSTRACT

Computational Fluid Dynamics (CFD) Simulations of Dilute Fluid-Particle Flows in

Aerosol Concentrators.

(December 2003)

Sridhar Hari, B.E., Annamalai University; M.S., Texas A&M University

Co-Chairs of Advisory Committee: Dr. Yassin A. Hassan
                                                            Dr. Andrew R. McFarland

In this study, commercially available Computational Fluid Dynamics (CFD) software, CFX-4.4 has been used for the simulations of aerosol transport through various aerosol-sampling devices. Aerosol transport was modeled as a classical dilute and dispersed two-phase flow problem. Eulerian-Lagrangian framework was adopted wherein the fluid was treated as the continuous phase and aerosol as the dispersed phase, with a one-way coupling between the phases.

Initially, performance of the particle transport algorithm implemented in the code was validated against available experimental and numerical data in the literature. Code predictions were found to be in good agreement against experimental data and previous numerical predictions.

As a next step, the code was used as a tool to optimize the performance of a virtual impactor prototype. Suggestions on critical geometrical details available in the literature, for a virtual impactor, were numerically investigated on the prototype and the optimum set of parameters was determined. Performance curves were generated for the optimized design at various operating conditions.

A computational model of the Linear Slot Virtual Impactor (LSVI) fabricated based on the optimization study, was constructed using the worst-case values of the measured geometrical parameters, with offsets in the horizontal and vertical planes. Simulations were performed on this model for the LSVI operating conditions. Behavior of various sized particles inside the impactor was illustrated with the corresponding particle tracks. Fair agreement was obtained between code predictions and experimental results. Important information on the virtual impactor performance, not known earlier, or, not reported in the literature in the past, obtained from this study, is presented.

In the final part of this study, simulations on aerosol deposition in turbulent pipe flow were performed. Code predictions were found to be completely uncorrelated to experimental data. The discrepancy was traced to the performance of the code's turbulent dispersion model. A detailed literature survey revealed the inherent technical deficiencies in the model, even for particle dispersion. Based on the results of this study, it was determined that while the code can be used for simulating aerosol transport under laminar flow conditions, it is not capable of simulating aerosol transport under turbulent flow conditions.

DEDICATION

I would like to dedicate this work to the members of my family. My parents were instrumental in imparting to me the appropriate education and other necessary skills required to come to the present stage and egged me on to make an attempt for higher education in this country. My sister and her family took care of me in my initial days in this country, and along with my brother, were supportive of me at all times. My wife married me knowing full well that I was a student. She was very understanding and supportive of my effort. My daughter was born during the course of this work and stood as an additional reminder to me of my responsibility!

Finally, I dedicate this work to the Almighty who is the indweller in all of us, the actual doer, and enjoyer of all our good deeds.

ACKNOWLEDGMENTS

TABLE OF CONTENTS

LIST OF FIGURES

LIST OF TABLES

NOMENCLATURE

$\eta_{\min}$ — Collection Efficiency based on the Number of Particles Collected in the Minor Flow, for the Virtual Impactor

η — Collection Efficiency on the Wall, for the Real Impactor

ψ — Gravitational Potential

τ_p — Particle Relaxation Time

ε — Dissipation

∇ — Divergence Operator

ρ — Fluid Density

λ — Mean Free Path of the Fluid

α — Correlation Coefficient in the Case of Time-Correlated Eddy Interaction Model

μ — Dynamic Viscosity of the Fluid

ν — Kinematic Viscosity of the Fluid

ω — Turbulence Frequency

$\theta_1, \theta_2, \theta_3, \theta_4$ — Various Angles in the Acceleration and Receiver Nozzles

ρ_p — Particle Density

ν_T — Turbulent Viscosity

y^+ — Non-Dimensional Distance from the Wall

x_p, y_p, z_p — Spatial Components of the Particle Position Vector

WL — Percentage Wall Loss in the Virtual Impactor Case

W_2, T_2 - Throat Width and Depth of the Receiver Nozzle (in the Case of the Virtual Impactor)

W_1, T_1 - Throat Width and Depth of the Acceleration Nozzle (in the Case of the Virtual Impactor)

W - Throat Width (in the Case of the Real Impactor)

V_0, V_T - Average Velocity at the Throat (scalar) in the Case of Real and Virtual Impactor

u_p, v_p, w_p - Components of the Particle Velocity Vector

u, v, w - Components of the Fluid Velocity Vector

u', v', w' - Components of the Fluctuation Velocity

U - Velocity Vector

T - Throat Length

StK - Stokes Number

$SQRT(StK)$ - Value of Square Root Stokes Number at 50% Cutpoint

$SD1, SD2, SD3$ - Various Stand-off Distances in the Acceleration and Receiver Nozzles

S - Stopping Distance in the Case of Real Impactor, Separation Distance between the Acceleration and Receiver Nozzles in the Case of Virtual Impactor

Re_p - Particle Reynolds Number

Re - Fluid Reynolds Number

$R1, R2$ - Radius of Curvature in the Acceleration and Receiver Nozzle Sections, for the Virtual Impactor

p - Modified Pressure

P — Absolute System Pressure

n_{wall} — Number of Particles Deposited on the Walls, for the Virtual Impactor Case

n_w — Number of Particles Collected on the Wall, for the Real Impactor Case

n_{min} — Number of Particles Collected in the Minor Flow, for the Virtual Impactor Case

n_{maj} — Number of Particles Collected in the Major Flow, for the Virtual Impactor Case

n_{in} — Total Number of Particles Specified at the Inlet Patch, for the Real Impactor Case

m_p — Particle Mass

g — Acceleration due to Gravity

F_{VM} — Virtual Mass Force

F_{PG} — Pressure Gradient Force

F_L — Lift Force

F_D — Drag Force

F_B — Buoyancy Force

C_D — Drag Coefficient

C_c — Cunningham Slip Correction Factor

$C_\mu, C_{\varepsilon 1}, C_{\varepsilon 2}, \sigma_K, \sigma_\varepsilon$ — Model Constants in the $k\text{-}\varepsilon$ Turbulence Model

$C_{\omega 1}, C_{\omega 2}, \sigma_\omega$ — Model Constants in the $k\text{-}\omega$ Turbulence Model

$\delta 1, \delta 2$	- Value of the Offset in the Horizontal and Vertical Planes, for the Asymmetric Virtual Impactor
k	- Turbulent Kinetic Energy
d_p	- Particle Aerodynamic Diameter
d_p^{50}	- 50% Cutpoint Aerodynamic Diameter of the Particle
$u_i u_j$	- Reynolds Stress in the Tensor Form
t_r	- Particle Transit Time
X_p	- Particle Position Vector
l_e	- Length Scale of the Eddy
$\hat{G}$	- Gravitational Vector
t_{int}	- Eddy-Particle Interaction Time
f_u, f_v, f_w	- Damping Factors (in the Three Directions)
$u_i'\left(t_j\right)$	- Time-Correlated Fluctuation Velocities Generated by the Eddy Interaction Model as a Combination of the Fluctuation Velocities of the 'j' th and the 'j-1' th Time Steps
$Y_i'\left(t_j\right)$	- Fluctuation Velocities Generated by the Eddy Interaction Model at the 'j' th Time Step
$Y_i'\left(t_{j-1}\right)$	- Fluctuation Velocities Generated by the Eddy Interaction Model at the 'j-1' th Time Step
V_R	- Scalar Value of the Relative Velocity = $|U-V_p|$
V_p	- Particle Velocity Vector

t_e - Eddy Timescale

ABBREVIATIONS

ACL   Active Command Line Interface

AD   Particle Aerodynamic Diameter

AMG   Algebraic Multigrid Solver

ATL   Aerosol Technology Laboratory

CAD   Computer Aided Design

CDS   Central Differencing Scheme

CFD   Computational Fluid Dynamics

DNS   Direct Numerical Simulation

EIM   Eddy Interaction Model

EXP, EXPT   Experiment

FD   Finite Difference

FE   Finite Element

FV   Finite Volume

GUI   Graphical User Interface

HDS   Hybrid Differencing Scheme

HDS   Hybrid Differencing Scheme

HIST   Homogeneous, Isotropic and Stationary Turbulence

ICCG   Conjugate Gradient Solver

LES   Large Eddy Simulation

LSVI   Linear Slot Virtual Impactor

MB	Multi Block
MOD	Modified
NSE	Navier-Stokes Equations
ORG	Original
RANS	Reynolds Averaged Navier-Stokes
RITW	Ratio of the Inlet to the Throat Width
RNG	Re-Normalized Group
RSM	Reynolds Stress Model
SB	Single Block
SCFH	Standard Cubic Feet Per Hour
STP	Standard Temperature and Pressure
TAMU	Texas A&M University
TD	Turbulent Dispersion
URF	Under-Relaxation Factors
USD	Ultra-Stokesian Drag

CHAPTER I

INTRODUCTION

Computational modeling of the physical phenomena observed in nature is an evolving field. The availability of high-speed supercomputers has given impetus to the development and use of advanced computational methods for solving conservation equations that represent the phenomena. In the last couple of decades, a separate field known as Computational Fluid Dynamics (CFD) has evolved for this purpose[1,2]. This field is popularly known as CFD and a good number of the scientific community is involved in research related to its various aspects as developing fast and accurate numerical algorithms and modeling and analysis of new applications.

The use of CFD was previously limited to the research community in national laboratories and universities. However, with the availability of commercial CFD software as CFX-5.6[3], FLUENT6[4] and STAR-CD[5] and advanced supercomputers, it is gaining increasing use in industry as a reasonable analytical tool. Once validated, such software can be used for the design and performance optimization of industrial equipment. Moreover, these softwares are normally equipped with post-processing capabilities that facilitate visualization of physical phenomena that occur in the system.

The flow of particles and droplets in a continuous fluid medium has numerous applications in industrial processes. The removal of particulate matter from exhaust gases is essential for controlling air pollution in fossil fired power plants. Efficient combustion of droplets or particles in a fuel furnace, spray-drying of many food products

---

This dissertation follows the style and format of *Nuclear Technology*.

and transportation of powders are among many other examples where two-phase flow is prevalent in the chemical, pharmaceutical and food-processing industry.

In the past, the design of systems in which these operations were carried out was based on empiricism. However, increased computational capability has enabled the development of numerical models that can complement experimentation in the design and development of engineering systems. Recently, evolving measurement techniques have resulted in quantifying the fundamental parameters. This has lead to an improved understanding of the physical phenomenon of the involved processes with its multi-scale interactions. It is expected that the coupled knowledge from CFD and the experiments would complement each other in upgrading the operation efficiency of the current processes and support the development of innovative designs.

In this study, a commercially available CFD program CFX-4.4[3] has been used to model two-phase flow phenomenon. From literature, it can be seen that the applications for which this software has been used range from the chemical industry[6] to the medical field[7], in addition to the more conventional areas such as fluid flow and heat transfer machinery[8]. In the present study, this software is used as a tool to analyze and optimize the performance of aerosol sampling instruments as real and virtual impactors[9].

This dissertation includes eight chapters and a general framework has been adopted in the arrangement of the chapters. As different chapters in the present work deal with different sampling instruments, the literature review for the instruments have been presented at the beginning of the related chapter, instead of presenting them in the

introduction. A glimpse of the subject matter covered in each of the chapters is provided in the following paragraphs.

In the first chapter, a basic introduction to the work is provided. In addition, the organization of subsequent chapters and the topic addressed in each of them is briefly mentioned. Transport of aerosols through aerosol sampling devices and biological agent detectors can be treated as a classical two-phase (solid-gas) flow problem. There are two approaches to model the gas-solid flow, namely, Eulerian-Eulerian approach and Eulerian-Lagrangian approach[10]. A brief review of the above modeling approaches, the approach chosen in the present work, and justification for choosing the approach is presented in Chapter II. In addition, the theoretical aspects of the modeling approach are presented in detail with the appropriate equations.

The third chapter provides a brief introduction to the CFD tool used in this study and describes the salient features of the software as relevant to the present work. Basic concepts of using the CFX-4.4 code, with respect to certain specific features as the grid generation, solvers, turbulent models, and Lagrangian particle tracking are explained. This chapter has been done basically with a view to acclimatize a new user with the various options at his disposal, in addition to introducing the capabilities of the software.

Chapter IV presents details on the simulations undertaken with CFX4.4 to validate the code performance for the present study. A brief physical description of the simulated cases is presented. The numerical aspects of the simulations are introduced and the setting up of the simulation is explained in detail. The important features of the simulation as the grid details, solvers used, and the convergence criterion are

summarized. The results of the simulations are presented and discussed and the conclusions of the study are presented.

In the fifth chapter, it is shown how CFD can be used as a tool in equipment design and analysis. The performance of a prototype slit virtual impactor was optimized based on the results of a detailed numerical study. In this study, the effect of various geometrical parameters on the prototype design was investigated. The optimized prototype design was considered as the base design and its performance characteristics were generated. The chapter concludes with a summary of the results of the various simulations carried out on the optimized prototype design.

Chapter VI presents details of simulations performed on a rectangular Linear Slot Virtual Impactor (LSVI) fabricated based on the optimization studies presented in the previous chapter. The predicted performance characteristics of the virtual impactor are compared against the experimental results. It is shown that a reasonable agreement is obtained between the simulation predictions and experimental results.

Chapter VII is devoted to issues related to the modeling of turbulent flows with suspended aerosol particles. The origin and development of the stochastic modeling approach, to account for the turbulence dispersion force on the particles, based on the two-equation turbulence models is explained in detail, as this approach is invariably used in most of the commercial CFD software. Our experience and understanding on the suitability of this approach, for the prediction of the behavior of aerosol particles in turbulent flow is presented.

In Chapter VIII, a brief summary of the results of the different parts of the present work is presented. The chapter also concludes with important observations on modeling the transport of aerosols using the commercial codes and on detailed directions of the future work to be performed in the field.

CHAPTER II

CFD MODELING OF TWO-PHASE FLOWS -THEORETICAL ASPECTS

A variety of two-phase flows exist in nature. The rising of bubbles through liquid and transport of particles through air are simple examples of this phenomenon. In general, two-phase flows may be broadly classified under three category namely gas-liquid flows, gas-solid flows, and liquid-solid flows. Depending on the specific nature of the problem, two-phase flows may further be classified as continuous-continuous or continuous-dispersed flows. The annular flow pattern that occurs in a heated fuel rod is a good example of the former, where both water and steam are continuous phases. The transport of particulates through the atmosphere is an illustration of the latter, where air is the continuous phase and particles are the dispersed phase.

Dispersed two-phase flows can further be classified as dilute and dense flows[10]. In the case of dilute flows, the forces exerted by the fluid control the particle motion and particle-particle interactions are not significant. However, in the case of dense flows, particle-particle interactions become significant. The determination is made based on a comparison of the momentum response time of the particle to the average time between particle-particle collisions.

The transport of aerosols through sampling instruments falls under the former classification and can be treated as dilute, dispersed two-phase flows. Some of the important features that are characteristic of modeling aerosol transport are

(1) The concentration of aerosols in the fluid stream is dilute.

(2) The size of the aerosols is on the order of microns.

(3) The characteristic length of the flow path through which the aerosol is transported may be small (millimeters or less).

There are two approaches to model the dilute dispersed two-phase flow. They are the Eulerian-Eulerian approach and Eulerian-Lagrangian approach[10]. In the Eulerian-Eulerian approach, conservation equations for the fluid and particle phases are independently solved, by assuming average particle phase properties. The interaction between phases is modeled by means of interphase terms that are included in the conservation equations. In the Eulerian-Lagrangian approach, first, the fluid flow field is resolved in the domain under consideration. A number of particles (solid or liquid) are then introduced into the domain at appropriate locations and the path of the individual particles is tracked by solving the particle force balance equations.

Further, in the Eulerian-Lagrangian approach, interaction between the phases may or may not be present. This concept is called coupling and the phases may be coupled to a different extent depending on the physical nature of the problem under consideration, such as the particle concentration. If the flow of one phase affects the other and there is no reverse effect, then the problem is known as a one-way coupled problem. However, if there is a mutual effect between the flowing phases, then the problem is to be treated as two-way coupled. Moreover, as already stated, coupling may take place through an exchange of mass, momentum and energy between the phases.

Simulations of one-way coupling cases and the analyses of the results are simple and straightforward, than two-way coupling between the phases. However, in the case of two-way coupling, it is difficult; even to set up the simulation, as uncertainty is involved

in making a proper estimation of the interaction forces. Experience and intuition are required to determine the degree of detail required in the simulation setup to obtain meaningful results from the simulation.

In the present study, the Eulerian-Lagrangian approach with a one-way coupling has been used to model aerosol transport. The fluid phase (air) is treated as the continuous phase and the solid phase (aerosol) is treated as the dispersed phase. The principle of Eulerian modeling is applied to the fluid phase and Lagrangian modeling to the solid phase. The justification for using the one-way coupled Eulerian-Lagrangian approach is presented below:

(a) Aerosol particle concentration under consideration is low and on the order of 20 particles per liter of air.

(b) The particle Aerodynamic Diameter is assumed as 20 μm AD[9].

(c) The bulk density of the particle phase, defined as the ratio of mass of the dispersed phase per unit volume of the mixture, is of the order of 8.3775E-08 kilograms per cubic meter of air.

(d) Air at room temperature (25°C, density=1.225 kilograms per cubic meter) is the fluid in which these aerosol particles are suspended.

(e) Under the above assumptions, the average spacing between air molecules is 3.0E-09 m, the mean free path is 6.0E-08 m and the mean time between successive collisions of a molecule is 1.0E-09 seconds

(f) The mass loading, defined as the ratio of the particle mass flux to the air mass flux, would reduce to the ratio of the density of the particle to the density of

air, assuming velocity equilibrium between the phases. Calculating the mass loading for the above values, the value is on the order of 6.84E-08.

(g) The assumption of an Eulerian-Lagrangian modeling approach with a one-way coupling, adopted in this study, is valid for such small values of particle size, bulk density and particle loading.

The mathematical model and the governing equations of this approach are presented in detail in reference 10. A brief review of the governing equations is presented below.

II. A. Governing Equations

II. A. 1. Conservation Equations for the Fluid Phase

The basic transport equations for fluid flow are the equations for the mass conservation (Continuity equation) and the momentum conservation (Navier-Stokes equations (NSE)). For incompressible, constant property, viscous flows[11], the continuity equation is

$$\nabla.U = 0 \qquad (1)$$

and the momentum equation is

$$\frac{DU}{Dt} = -\frac{1}{\rho}\nabla p + \nu \ \nabla^2 U \qquad (2)$$

where the material derivative, or substantial derivative, is defined by

$$\frac{D}{Dt} = \frac{\partial}{\partial t} + U.\nabla \qquad (3)$$

and the symbol ∇ is the divergence operator.

In the above equations, the quantity U is the velocity vector (u, v, w) and $v \equiv \mu/\rho$ is the kinematic viscosity, and, μ and ρ are the molecular viscosity and the density of the fluid, respectively. The quantity p is modified pressure defined as

$$p = P + \rho\psi \tag{4}$$

where ψ is the gravitational potential (i.e., the potential energy per unit mass associated with gravity), which can be, for a constant gravitational field, expressed as $\psi = gz$, g being the gravitational acceleration and z being the vertical coordinate. The quantity P is the actual absolute system pressure.

In turbulent flow, the instantaneous velocity field (U) would have to be decomposed in terms of an averaged velocity field ($\langle U \rangle$) and a fluctuating velocity field (u')[11]. This process is referred to as Reynolds decomposition.

$$U = \langle U \rangle + u' \tag{5}$$

Both these fields would satisfy the continuity equation:

$$\nabla . \langle U \rangle = 0 \tag{6}$$

$$\nabla . u' = 0 \tag{7}$$

Substituting this decomposition into the NSE, taking the mean and rearranging the terms, the Reynolds Averaged Navier-Stokes (RANS) equations can be cast as:

$$\frac{\bar{D}\langle U_j \rangle}{\bar{D}t} = -\frac{1}{\rho}\frac{\partial\langle p \rangle}{\partial x_j} + v \nabla^2 \langle U_j \rangle - \frac{\partial\langle u_i u_j \rangle}{\partial x_i} \tag{8}$$

where, the mean substantial derivative is defined as

$$\frac{\bar{D}}{\bar{D}t} = \frac{\partial}{\partial t} + \langle U \rangle . \nabla \tag{9}$$

and the braces, $\langle \ \rangle$, indicate the time-averaged quantity.

Comparing Equations (8) and (2), it can easily be seen that they are the same except for the last quantity in Equation (8). This tensor quantity, $\langle u_i u_j \rangle$, is known as the Reynolds stress, though, it is actually not a stress. However, for purposes of terminology, it is called so, to be in line with the viscous and the pressure stresses. This is the quantity that accounts for the effect of the turbulence produced by the fluctuating velocity components and their interaction with the mean flow.

II. A. 2. Overview of Turbulence Modeling

The presence of the Reynolds stress tensor in the RANS equations, Equation 8, gives rise to the dilemma that is well known in the turbulence modeling community as the "closure problem". Further details on the above problem and the various approaches adopted to estimate the turbulence details are available elsewhere[11,12,13,14]. It would suffice here to briefly review some of the practical modeling approaches adopted in computational modeling of turbulent flows.

The general approach adopted in the CFD community is to obtain the mean flow field from the solution of the RANS equations. The turbulence effects are modeled in terms of a generation parameter as the turbulent kinetic energy, k, and, a dissipation parameter, such as ε, the rate of dissipation of turbulence energy, or, ω, the turbulence frequency. Conservation equations for these parameters are solved for over the domain, in addition to the RANS equations. This is called the two-equation turbulence modeling

approach. This is the minimum modeling approach that can be considered complete, as flow-dependent specifications are absent. This modeling approach is implemented in the most commercial CFD codes.

Detailed information on the origin, development, and application of the two-equation models is the literature. The conservation equations for the above approach are presented here.

The conservation equations for k and ε are given by:

$$\frac{\bar{D}k}{\bar{D}t} = \nabla.\left(\frac{v_T}{\sigma_k}\nabla k\right) + P - \varepsilon \qquad (10)$$

$$\frac{\bar{D}\varepsilon}{\bar{D}t} = \nabla.\left(\frac{v_T}{\sigma_\varepsilon}\nabla \varepsilon\right) + C_{\varepsilon1}\frac{P\varepsilon}{k} - C_{\varepsilon2}\frac{\varepsilon^2}{k} \qquad (11)$$

In the above equations, v_T is called as the turbulent viscosity and is defined as

$$v_T = \frac{C_\mu k^2}{\varepsilon} \qquad (12)$$

The quantities C_μ, $C_{\varepsilon1}$, $C_{\varepsilon2}$, σ_K and σ_ε are model constants that have values 0.09, 1.44, 1.92, 1.0 and 1.3, respectively.

In the case of the $k\text{-}\omega$ model, the conservation equation for k remains the same, except for the fact that the dissipation would be expressed in terms of ω, rather than ε, as shown below:

$$\frac{\bar{D}k}{\bar{D}t} = \nabla.\left(\frac{v_T}{\sigma_k}\nabla k\right) + P - \omega k \qquad (13)$$

The conservation equation for ω is

$$\frac{\bar{D}\omega}{\bar{D}t} = \nabla \cdot \left(\frac{v_T}{\sigma_\omega} \nabla \omega \right) + C_{\omega 1} \frac{P\omega}{K} - C_{\omega 2}\omega^2 \tag{14}$$

In the above equation, v_T is still the turbulent viscosity but is defined as

$$v_T = \frac{C_\mu k}{\omega} \tag{15}$$

The quantities C_μ, $C_{\omega 1}$, $C_{\omega 2}$, σ_K, and σ_ω are model constants that have values 0.09, 0.5555, 0.075, 2, and 2.3, respectively.

It is to be remembered here that unless stated otherwise, when using the standard k-ε model, the near-wall region in handled through the use of wall functions. The conservation equations are solved only to the buffer region and the profiles are matched at the interface. However, when using the k-ω model, the conservation equations are solved all the way to the wall. Hence, a very fine mesh is required near the wall to resolve the boundary layer accurately.

There are different combinations and improvements on these models that have been proposed, as cited in the references quoted previously. These turbulence models are the Menter-modified k-ω model, low Reynolds number k-ε model, and re-normalized group (RNG) k-ε model. The first two of the above models are low Reynolds number models and require a fine grid near the wall, whereas, the RNG k-ε model is for high Reynolds number flows, where the near wall effects are modeled using the wall function approach.

As a general rule, it is to be remembered that the turbulence models are basically grouped into two categories as the low Reynolds number and the high Reynolds number models. The former class of models requires a fine-grid near the wall, as they resolve the boundary layer, hence, are computationally expensive. However, the latter class of models uses the wall function approach for capturing the near-wall phenomenon; hence the grids may be comparatively coarse, reducing the computational cost.

Other higher-order closures, such as the Reynolds Stress (both algebraic and differential) and the differential Reynolds flux models, solve transport equations for the components of the stress tensor directly. In addition, they also solve for the dissipation, ε. Computationally, these models are more expensive than the two-equation models described previously. However, they incorporate more physics in them, and, hence are supposed to perform better for complex flows, where multiple effects, such as mean streamline curvature, strong swirl with mean rotation, secondary flow and rapidly varying mean flow, are present.

Large Eddy Simulation (LES) is the next higher level of flow description where the three-dimensional, unsteady, turbulent motions that contribute to turbulence, are directly resolved, whereas, the effects of smaller scales that are universal, are modeled. As the larger flow scales are represented directly, LES can be expected to be more accurate and reliable than the Reynolds Stress models. This makes LES computationally more expensive than the Reynolds stress models.

Direct Numerical Simulation (DNS) solves the Navier-Stokes equations, resolving all the scales of motion that are prevalent in the flow. Hence, it provides a

complete description of the flow being resolved. However, it is to be noted that nearly all of the computational effort in DNS is expended in the resolution of the smallest, dissipative scales, whereas the energy and anisotropy of turbulence are contained in the larger scales. As a result, the computational costs are extremely high and increase as the cube of the Reynolds number, limiting DNS to small Reynolds numbers.

The last couple of models, LES and DNS, are still tools in research stage. The possibility of DNS being used as a tool for solving practical problems in turbulence does not seem to be feasible in the near future, even with the increasing computational capabilities. However, the capabilities of LES as a practical problem-solving tool, is being slowly demonstrated and more studies in which LES is used have appeared in the literature recently.

II. A. 3. Overview of Computational Methods for Fluid Dynamics

The numerical solution to the above equations can be taken up once the basic understanding of the common form that underlies the governing transport equations is recognized[15]. Once this is achieved, a generalized solution procedure can be constructed.

The governing equations express a certain conservation principle for the dependent variable, which is usually a specific property (i.e., quantity per unit mass). The different terms in the governing equations represent an influence on the transport of the dependent variable on a unit-volume basis. This can be inferred once the governing equation is written in the conservative form, for a transported dependent variable, ϕ, in tensor notation, as given below:

$$\frac{\partial}{\partial t}\left(\rho\phi\right)+\nabla.\left(\rho u\phi\right)=\nabla.\left(\Gamma\nabla\phi\right)+S \tag{16}$$

In the above equations, Γ is a diffusion coefficient (as the absolute velocity) and S is the source term (as the absolute pressure). The four terms in the above governing equation are the unsteady term, the convection term, the diffusion term and the source term. The dependent variable can be a velocity component, temperature, turbulent kinetic energy or like quantities. The diffusion coefficient and the source term would have to be defined in accordance with the dependent variable. Any other quantity appearing in the conservation equation that cannot be fit into the first three categories can be included in the source term. It can be shown that the governing equations can easily be expressed in this standard form.

The Navier-Stokes equations (NSE) are a system of non-linear second order equations in four independent variables. In combination with the continuity equation, we get a coupled system of four equations in four independent parameters, namely the three velocity components and the pressure. These equations are supposed to accurately describe the flow of the newtonian fluid.

It is well known that an accurate analytical solution for the NSE is not possible for a vast majority of cases, except some simple ones. Even with some assumed simplifications, numerical methods have to be adopted to solve the system of equations. As we step into the domain of practical problems, we are left with no option but to follow the numerical path to solve the NSE.

Once the problem is completely defined along with the initial/boundary conditions, the following steps are involved in the numerical solution of the problem.

a. A suitable discretization method is employed that approximates the differential equations by a system of algebraic equations.

b. A proper coordinate system that fits the physical conditions of the problem is chosen.

c. An appropriate numerical grid is constructed over the geometrical domain and the domain is discretized into a number of control volumes/elements or grid points.

d. The system of algebraic equations is solved at each control volume, by employing appropriate solvers, on a computer.

e. The numerical solution is obtained at those discrete locations and can be visualized using proper aids, to interpret the results.

It is worth remembering that the accuracy of the solution is dependent on the quality of the discretization used. In the following paragraphs, each of the above steps is briefly explained.

Discretization involves approximating the governing differential equations by the system of algebraic equations for the variables at some discrete locations in space and time. Out of the many different methods that are available, the most important methods are the Finite Difference (FD), Finite Volume (FV) and the Finite Element (FE) methods. There are some other methods such as the Spectral method and Boundary Element method but these methods are applicable to a specific category of problems[16]. The same solution should be obtained, irrespective of the method chosen, as long as the

grid is made fine enough. However, a particular method may be more suited for a specific problem than the others.

The common coordinate systems are Cartesian, Cylindrical, and Spherical; most of the physical problems can be adequately described in these systems. However, depending on the complexity of the problem, we may have to choose other options such as a orthogonal or non-orthogonal curvilinear system that may be fixed or moving. The governing conservation equations of the problem may be transformed into any coordinate system, once the base vectors of the system are fixed. The coordinate system chosen for the problem may influence the discretization method and the grid type.

The numerical grid is the discretized representation of the problem to be solved. The solution domain is divided into a number of sub-domains consisting of control volumes or elements on which the variables will be calculated. Various gridding options are available as the regular, structured grid, which is rectangular and orthogonal, structured non-orthogonal grid, block-structured grid that matches at the interface and that does not match at the interface, block-structured grids with overlapping blocks known as composite or chimera grid, and the unstructured grid. The options mentioned are presented in the increasing order of flexibility as well as complexity from the viewpoint of grid generation.

Following the construction of the grid, the method of discretization to be adopted is chosen. In the FD method, the derivatives in the governing equations in the presented form are approximated in terms of differences between the grid points. The resulting algebraic equations are solved to obtain the values of the quantity at the nodes. In the

FV method, however, the governing equation is written in a conservative form from the presented form, wherein the derivatives contain the quantity being transported. The equation in the conservative form is then integrated over the control volume that is constructed using the grid points. The integrated equation is then expressed as a difference across the control volume faces. The algebraic equations obtained from the above are solved, to obtain the value of the transported quantity for the control volume. Hence, in the FV method, approximations are introduced in the level of surface and volume integrals. In the case of the FE method, the variation of the function across the domain is to be assumed to be of some form. The governing equations are then multiplied by a weighting function and integrated over the entire domain. The assumed form of the solutions is then substituted into the weighted integral of the governing equations. The algebraic equations to be solved are derived by requiring the derivative of the integral be zero with respect to each nodal value. The solution of the above non-linear system of algebraic equations gives the coefficients of the assumed functional variation over the domain.

The choice of the chosen method and the level of approximation that is resorted to in the discretization process of the governing equations within the chosen method dictate some of the important aspects involved in the development and performance of a code, such as

(a) the effort involved in the development of a code

(b) the memory requirements and the computational efficiency of the code, and

(c) The accuracy of obtained solution.

The coupled, non-linear system of algebraic equations obtained from the discretization process has to be solved using suitable tools. The equations can be written in the matrix form and the solution matrix would give the value of the quantity solved for, at the discrete nodes (FD) or control volumes/elements (FV/FE) in the domain. This requires inversion of the coefficient matrix. It is well known that direct inversion of the coefficient matrix would be computationally expensive. These being a non-linear system, iterative methods are utilized to solve the system of equations. The choice of the solver depends on the grid type and the number of nodes involved in each algebraic equation. There are a variety of solvers available starting from the elementary line solvers, full-field Stone solvers, to the more sophisticated conjugate gradient solvers and the multi-grid solvers that can be employed.

II. A. 4. Conservation Equations for the Solid Phase

Particle motion in the flow field under consideration is governed by Newton's Second Law[10] which expresses the force balance on the particles:

$$m_p \frac{dV_p}{dt} = F_D + F_B + F_{PG} + F_{VM} + F_L \tag{17}$$

$$\frac{dX_p}{dt} = V_p \tag{18}$$

where, m_p is the mass of the particle, V_p is the particle velocity vector (u_p, v_p, w_p), X_p is the particle position (x_p, y_p, z_p), and the quantity on the RHS of Equation (17) is the sum of all the forces that act on the particle.

The forces that act on the particle are, F_D, the drag force, F_B, the buoyancy force, F_{PG}, the pressure gradient force, F_{VM}, the virtual mass force and F_L, the lift forces. The forces that need to be included in a particular simulation are dependent on the physical conditions that are characteristic of the simulated problem. For most of the gas-particle simulations, as the ratio of the dispersed to the continuous phase is of the order of 1000, the only force that needs to be included is the drag force, as the other forces are insignificant[10]. Hence, the particle motion equations get simplified to:

$$m_p \frac{dV_p}{dt} = F_D \tag{19}$$

The drag force exerted on the particle by the continuous phase is calculated as follows[10]:

$$F_D = \frac{1}{8} \pi d_p^2 C_D |V_R| V_R \tag{20}$$

where, V_R is the relative velocity between the phases, d_p is the particle diameter, and, the drag coefficient, C_D, is calculated by

$$C_D = \frac{24}{\mathrm{Re}_p} (1 + 0.15\,\mathrm{Re}_p^{0.687}) \tag{21}$$

The particle Reynolds number, Re_p, in the above equation, is calculated by

$$\mathrm{Re}_p = \frac{\rho V_R d_p}{\mu} \tag{22}$$

where ρ and μ are the density and viscosity of the fluid.

In case the fluid flow is turbulent, the effect of fluid turbulence on the particle has to be accounted for. The force that accounts for the effect of fluid turbulence on particle behavior is termed 'turbulence dispersion force' and is introduced in a variety of ways, which have been excellently summarized[17]. The simplest and most common approach that has found widespread use in the CFD community is the stochastic modeling approach proposed by Gosman and Ioannides[18]. This scheme with the improvement proposed by Shuen et al.,[19] is used extensively in CFD codes equipped with Lagrangian particle tracking, to account for the turbulence dispersion phenomenon. This model was developed to be used in concert with the two-equation k-ε turbulence model and is known as the Eddy Interaction Model (EIM). The popularity of this model is due to its simplicity and robustness.

To simulate the effect of the fluid turbulence on the particles, the instantaneous (mean + fluctuating components) fluid velocity at the particle location, is needed, at each time step. While the components of the mean velocity are obtained from the solution of the RANS equations, there is no way available to directly obtain the fluctuating components. The way in which this is achieved in the EIM will be explained in the subsequent paragraph. It is also to be noted that the turbulence dispersion force is introduced not as a separate, direct force in the equation of particle motion but a stochastic approach is taken. This is due to the reason that turbulence is random and chaotic and a stochastic approach is more appropriate than a deterministic approach.

In this model, the turbulent flow field is regarded as a collection of randomly directed eddies with discrete velocity and time scales. The fluctuating velocity

components are reconstructed from the nodal values of the turbulent kinetic energy, k, corresponding to the particle location, at each time step. Turbulence is assumed to be isotropic and the fluctuation associated with a turbulent eddy is selected randomly from a Gaussian distribution with a mean equal to zero and variance equal to $2k/3$. The particle is assumed to be in the eddy for the duration of the interaction time, which is the minimum of

   (a) the eddy lifetime computed from the k and ε values, and

   (b) the eddy transit time, calculated based on a simplified and linearized equation of motion, for a particle in uniform flow.

Equation 26 (see below) has no solution when $l_e > \tau_p V_r$, that is, when the linear stopping distance of the particle is smaller than the eddy size. In such a case, the eddy traps the particle and the interaction time will be the eddy lifetime. At the end of this time, a new eddy with lifetime and length scale corresponding to the local turbulence field is established, and, a new fluctuation velocity is selected with a random number generator. By repeating this procedure over as many time steps as required, and, over a statistically significant number of particles, the ensemble-averaged behavior should represent the dispersion effect induced by the prevailing turbulent flow field on the particles.

The procedure is summarized below:

   (a) Estimate the length scale of the turbulent eddy

$$l_e = C_\mu^{3/4} \frac{k^{3/2}}{\varepsilon} \tag{23}$$

(b) Estimate the lifetime of the eddy

$$t_e = \frac{l_e}{\sqrt{2k/3}} \tag{24}$$

(c) Estimate the particle relaxation time

$$\tau_p = \left(\frac{4}{3}\right)\left(\frac{\rho_p}{\rho}\right)\left(\frac{d_p}{C_D V_r}\right) \tag{25}$$

(d) Calculate the transit time

$$t_r = -\tau_p \ln\left(1.0 - \frac{l_e}{\tau_p V_r}\right) \tag{26}$$

(e) Calculate the interaction time

$$t_{int} = \min(t_e, t_r) \tag{27}$$

II. A. 5. Generation of Particle Trajectories

Once governing equations for the fluid phase are solved and the flow field in the domain is obtained, the equations of particle motion are solved for, as a post process, to obtain the particle trajectory, for each individual particle. Normally, a forward time marching scheme, as the predictor-corrector method, or, the more accurate Runge-Kutta fourth order method is employed for the integration of the equations. The main disadvantage of the one-way lagrangian tracking is the large computational time required, if a large number of particles need to be tracked.

Normally, particle tracking under laminar flow conditions would not be computationally demanding. However, for particle tracking under turbulent flow

conditions, as a stochastic approach is used, a large number of particles need to be tracked to obtain proper statistical properties. Also, unlike laminar flows, there is a possibility of particles getting trapped in eddies or recirculation zones. Hence, a combination of the above factors may result in the expenditure of substantial amounts of computational time. This problem may be accentuated in the case of flow in complex geometries.

CHAPTER III

CFX-4.4 - A DESCRIPTION

The CFX[3] series of CFD software is a general-purpose multi-phase CFD program used for fluid flow and heat transfer analysis of real industrial processes. It has a variety of additional models to simulate the accompanying effect of turbulence, chemical kinetics, combustion, radiation and non-reacting particles. In this chapter, a brief description of the salient features of CFX-4.4, used in the present study, is presented.

Any CFD software essentially has the following components:

(a) Pre-processing (or) grid generation utility, which breaks down the geometrical domain into discrete control volumes.

(b) Front-end that contains the input specification of the problem.

(c) Solution module which solves the discretized representation of the problem, and

(d) Post-processing (or) the graphics tool using which the solution to the problem is visualized.

III. A. CFX-4.4 Description

III. A. 1. Pre-Processing Module

The pre-processing module contains tools using which the topological data pertaining to the simulated problem is input to the code. It is equipped with CAD based grid generation software in which the geometrical domain is constructed and the boundaries of the domain are declared. Once this is done, a finite-difference grid is generated on the domain. This completes the pre-processing stage of the problem specification.

CFX-4.4 is equipped with four different pre-processor modules namely

(a) CFX-MESHBUILD

(b) CFX-BUILD

(c) CFX-MESHIMPORT

(d) CFX-SETUP

The pre-processing modules are equipped with MSC-PATRAN based geometry and grid generator working on an ICEM-HEXA interface. Each of the above pre-processors is useful for a different application and details are available in the solver manual. One of the above, viz. CFX-BUILD provides direct access to major CAD packages so that geometry files constructed in different packages can be imported into the pre-processing module for meshing. Otherwise, geometry files can be built from scratch using either CFX-BUILD or CFX-MESHBUILD.

CFX-4.4 works on multi-block body-structured grids created from the pre-processors. However, unstructured Finite Element hexahedral meshes from other pre-processors can be imported into CFX-MESHIMPORT and converted to a suitable form to be used with the solver. It has sliding mesh facility and can work on moving grids.

III. A. 2. Front-End Module

Front-end module takes the input specification of the problem and converts it to the machine executable form, while performing detailed error checking. As the geometry and the boundary details are already available, the appropriate values of the initial and boundary conditions of the problem are declared here. In addition, other ingredients of

the problem solving as the information on the fluid, details pertaining to the turbulence model to be used, solvers, and under-relaxation factors employed are declared here.

This module is equipped with a database that contains physical property data for common fluids that can be used with the simulation. Moreover, this module also contains user-defined subroutines wherein special requirements pertaining to the simulated problem can be input to the code, before commencing the simulation.

III. A. 3. Solution Module

The solution module contains tools such as the various solvers and the parallel-processing algorithms that solve the problem. Once the discretized representation of the problem is available from the previous modules, the solution module solves the problem and writes out the results both in the alphanumeric and the graphical formats. The alphanumeric (output) file contains a summary of the progress of the solution and the final results written out, whereas, the graphical (dump) file contains all the results in the binary form so that they can be visualized in a suitable post-processor.

III. A. 4. Post-Processing or the Graphics Module

This module is used to produce the main graphics form of the output; results of the run can be visualized using this module. In addition, this module contains advanced features using which operations/manipulations can be performed on the dump file to obtain the results of the run in different formats as graphs (charts) or movies. The advantage of visualizing the results is that an incisive insight into the physical phenomenon happening in the device internals can be obtained. Hence, this module serves as an excellent trouble-shooting tool.

III. B. CFX-4.4 Features

CFX-4.4 uses the control-volume based finite-difference method to solve the Continuity, Navier-Stokes and the Energy equations. The grid on the geometrical domain is constructed using the multi-block grid methodology. This involves the use of a structured set of blocks that are glued together, on each of which there is a structured grid. Topological features within the domain are described using patches, as the inlet patch, outlet patch etc.

Simulations of steady state and transient flows can be performed on the Cartesian and Cylindrical coordinate systems. Options to use rotating coordinate systems and unmatched and sliding grids are also available.

In addition to regular fluids, different models are available to simulate the performance of

(a) Non-Newtonian fluids and fluid mixtures

(b) Compressible flow

(c) Combustion and Radiation

(d) Single-phase chemical reactions

(e) Porous media and Multi-phase flows

(f) Lagrangian particle transport

Different turbulence models are available in the code for the user to choose, as the standard k - ε model, RNG k - ε model, low Reynolds number k - ε and k - ω model, Menter modified k - ω model, and, algebraic and differential Reynolds Stress model (RSM) and Reynolds Flux model. All these models are available for use with both

incompressible and compressible flows. The code also provides option to the user to modify constants in the turbulence models to suit the modeled problem.

Various discretization methods are available in the software ranging from robust but relative inaccurate hybrid and upwind schemes to the more accurate but less robust higher-order schemes. A list of the schemes is available in the solver manual. Different Pressure-Velocity coupling algorithms as SIMPLE, SIMPLEC, PISO and NON-ITERATIVE PISO are available. A variety of solvers, starting from the basic line solver to a sophisticated Algebraic Multigrid (AMG) solver, are available.

There is a lagrangian particle transport model available in the code. This model can be used to track individual drops (or) particles that are suspended in the flow. The flow may be laminar or turbulent and the fluid may be non-newtonian. The coupling between the phases can either be a one-way coupling or two-way coupling, and, may involve exchange of momentum, heat, and mass. An option to track mass less particles is also available.

Normally for particles suspended in a flowing gas, the drag force is the most important force that influences the particle motion. However, there are a variety of forces as the gravitational force, added (virtual) mass force, pressure-gradient force, rotating coordinates force and the lift force, which may be of importance under specific flow conditions and at specific geometrical locations.

While the added mass force and the rotating coordinates force is included by default in the particle trajectory calculation, the inclusion of other forces is optional. There is no provision to include the lift force as it is not available in the code options.

The effect of the fluid turbulence on the particle is introduced using the stochastic turbulence dispersion force introduced in the previous chapter.

In the process of obtaining the particle tracks, differential equations that govern the particle force balance are integrated. Option to specify the time until which integration needs to be performed is available. This may be necessary to limit the time spent on an individual particle. Options are available to avoid computational problems associated with tracking mass less particles.

A parameter known as 'coefficient of restitution' is available to account for the effect of particle bounce from surfaces. Also, options are available to limit the time that a particle may spend in a control volume, and, to ensure that the particle is collected on the wall. This is used to avoid occasional bouncing of the particles from the wall to prevent wastage of CPU time.

By default, particles are treated to be spherical. However, factors are available to model the effects of non-spherical shapes. Particles can be introduced not only at boundaries but also at any point of interest in the geometrical domain. If the particles are released at the boundary, they may be released uniformly at the boundary or from the center of each cell.

The total number of particles used in the tracking process need to be specified. The release velocity of the particle and the total particle mass flow rate need to be specified. Basic properties of the particle as its size, density etc., need to be specified. The diameter of the particle may be specified using typical distribution functions, if the particles are poly-disperse.

In case the particles need to be released at specific locations, either the block information or the exact physical location in the domain may be specified. The total mass flow rate of the particle phase can be calculated knowing the concentration of the particle phase, size, density, number of particles and the fluid flow rate.

Detailed information on an individual particle is available in the output file. Using the USRPBC subroutine, the number of particles that leave the domain at different locations and the number that stick to the wall may be counted. The track for each particle, with its fate, will be printed to the output file along with the summary information for the particle diagnostics, at the end of the file. Various options are available to control the output printing information. In addition to the above features, a particle track file is written at the end of the tracking run. This file contains the necessary information required for the visualization of the particle tracks.

The post-processing unit for visualizing the results of the run is known as CFX-ANALYSE. This is a very powerful tool using which a lot of operations can be performed on the dump file, in addition to the traditional operations as the creation of visual plots of contour, vectors etc. It is equipped with advanced tools as the macro manager, a calculator, and, an active command line (ACL) interface using which further processing of the results can be performed, and, charts and movies can be produced.

III. C. Problem Setup, Execution and Visualization of the Results

The first part of the problem setup is the construction of the geometry on which the simulation is planned. This is done on the CAD based pre-processor CFX-BUILD. The reference coordinate frame needs to be decided; once this is done, the geometry can

be constructed using the basic geometrical entities as points, lines, curves etc. Being a CAD based tool, the pre-processor is equipped with advanced tools for the construction of complex geometries. For simple geometries, a rectangular coordinate system with a single block would suffice; however, for complex geometries, the geometry needs to be broken down to a number of simple blocks, which are glued together at intersections. This is known as block decomposition of the domain. This approach is known as the 'block-structured' approach and is done to maintain orthogonality during the meshing operation.

If need be, a cylindrical coordinate system can be adopted as the reference frame. Moreover, depending upon the nature of the geometry, simulations can be restricted on a part of the geometry, if there are symmetric planes or periodic repetitions. This would result in decreased computational time, expense, and effort, without loss of important information.

Once the geometry is constructed, proper assignment of its boundaries, in concordance to the actual physical state, needs to be done. This process is called as the assignment of the proper boundary condition. The various options available are the input, output, pressure, mass flow, symmetry, periodic and wall boundaries. Each of the above is known as a 'patch' in code parlance. Any undeclared patch would be conceived by the code as a 'wall' by default. Additional information on handling more complicated boundary conditions is available in the solver manual.

Once the assignment of patches is completed, the geometry needs to be discretized into small control volumes. This process is known as 'meshing'. Meshing

usually starts from the surface and propagates into the domain interiors. Depending upon the geometry being a single block or multi-block geometry, and, depending upon flow details, different mesh densities may be required to capture finer details of flow, at regions of interest in the domain. A variety of options on choosing the mesh density on a specific line as uniform, one-way bias and two-way bias are available in the pre-processor. By utilizing this option, a good degree of freedom on the mesh structure and density can be achieved. However, the disadvantage of this approach is the propagation of the mesh on common vertices. In such a condition, the geometry can be broken into a number of blocks to achieve the desired mesh parameters.

Once the surface mesh is completed, the volume mesh can be constructed. If a scale model of the actual geometry had been constructed, the actual scale factors should be supplied at this point. Also, the details on whether the simulation is two-dimensional or three-dimensional need to be declared here. On completion of this step, the meshing operation is completed and a geometry file (.geo) that contains the discretization details as the mesh quality, information on the blocks, control-volume vertices etc., would be created. The code would indicate in this step if there were inconsistencies in the declaration of the boundary conditions or other details. If need be, the meshed geometry could be visualized at this point. This step concludes the pre-processing operation.

Creation of a proper mesh on the geometry is a very important step in the simulation process. The accuracy of the final solution is very much dependent on the quality of the mesh. Also, as can be seen from the above discussion, mesh generation is a trial-and-error job that requires lot of perseverance and a good insight into the physical

phenomenon expected to occur inside the domain. It is also the most time consuming part of the simulation process.

The next step in the process is the creation of the control file. In this step, all other physical details of the problem (except the geometric details defined in the previous step) are declared. The details include the following:

(a) the flow as laminar/turbulent, newtonian/non-newtonian, buoyant/non-buoyant etc.,

(b) additional models to be used as turbulence models, chemical reaction, particle transport

(c) flow boundaries as the velocity, flow rates, pressure; wall boundary as slip/no-slip; heat transfer as temperature/heat flux and the respective values

(d) turbulence model used; choice of parameters for the chosen model

(e) discretization scheme for the equations; solvers employed and the under-relaxation factors chosen

(f) the convergence criterion adopted, and, the maximum number of iterations

(g) other additional details that are required to define the problem completely.

At the conclusion of the above step, a control file (.fc) in alphanumeric format, containing all the above information, is created. These two files are required to run a problem. At this point, any user-defined FORTRAN subroutines required to be executed along with the problem should be annexed. A window displaying the residuals of the relevant parameters (mass, velocity components, turbulence parameters etc.) as a function of the number of iteration would be opened as the problem is submitted to run.

Assuming that all the previous steps have been carried out successfully, the run would continue till the required mass convergence is reached (or) till the maximum number of iterations is completed. At the conclusion of the run, two output files would be produced; an alphanumeric output file (.fo) that summarizes the problem specification and the results of the run, and, a binary dump file (.dmp) that retains all the information that is required in the post-processing step. Otherwise, error messages would be printed out, with an indication of the nature of the error. Sometimes, the run may terminate immediately and the problem would be written to the output file. Also, if this run is a restart run, the corresponding dump file that supplies the initial values should be annexed.

The dump file produced from a run can be opened in CFX-ANALYSE graphical-user interface (GUI). An outline of the simulated geometry would appear in the screen. Visualization of velocity vectors, streamlines, contours of various quantities and other results can be accomplished using this tool. In case of lagrangian particle transport simulations, particle tracks can be visualized. A command line window is accessible from the pull-down menu using which calculations can be performed on a scalar field variable. In addition, it is also equipped with an Active Command Line (ACL) interface tool called as the macro manager which can perform manipulations on the data from the dump file and produce graphical objects from the results. It also allows automation of post-processing steps to be performed.

III. D. General Comments

(a) The geometry constructed in the pre-processor is in the physical space.

(b) An internal transformation is carried out in the code whereby the non-uniform grid information in the physical space is transformed to a uniform, rectangular grid in the computational space

(c) Grid in the physical space must be smoothly varying and large jumps in the grid spacing or large non-orthogonality in the angles of the control volumes should be avoided.

(d) Grid distortion and non-uniformity will make the solution of the governing equations difficult and the obtained solution may be inaccurate.

(e) If a single block construction is used for non-rectangular geometries, the above problems would be encountered. This is the reason why block-structured methodology is adopted for non-orthogonal geometry.

(f) Before solving the governing equations, the code automatically restructures the blocks internally, to facilitate the efficient utilization of the solvers.

(g) The governing equations for the fluid flow are solved for in the computational space.

(h) The particle transport calculations are performed in the computational space.

(i) Normally, a hermitian interpolation scheme is employed to estimate the particle velocity at a location inside a control volume, from the values at the edges of the control volume

(j) This scheme works well across block boundaries, however, for complicated block structures; hermitian interpolation may not be possible. Under such circumstances, a simple interpolation option is available in the code.

CHAPTER IV

VALIDATION OF THE CFX-4.4 CODE

As is customary in any simulation work, an assessment of the capabilities of the simulation tool for the study has to be undertaken, before commencing any simulation. This step is commonly referred to as 'code validation' and is a very important step in the modeling process. In the past, Zhang et al., [7] reported using CFX-4.3[3] computer code for studying the transportation and deposition of micron size particles in the lung airways. They reported good agreement between the experimental results and the computational predictions of CFX-4.3.

In the present work, the CFD code CFX-4.4[3] was used to model aerosol transport. Studies were performed to assess the capability of the code for the chosen application. Two different validation studies were performed. In the first study, the performance of a slit (rectangular) nozzle real impactor, was numerically simulated using the CFD code CFX-4.4. The results of the simulation were compared against experimental results[20]. In the second study, simulations of Rader and Marple[21] and Marple and Liu[22] were repeated with the CFX-4.4 code and the results were compared.

IV. A. Introduction

Impactors[9,23] are the most primitive of the devices that have been extensively used for the collection and measurement of aerosol particles. They have also been used for classifying particles based on the size (aerodynamic diameter). They work on the principle of inertial impaction. They have been and are being used in a wide variety of disciplines from occupational health to environmental assessment. As of this date it

would not be improper if it were mentioned that inertial impaction was more thoroughly studied than any other aerosol separation process.

Inertial impactors can be classified into two types, namely, the real and the virtual impactor. The real impactor removes particles by impaction on a coated solid surface, whereas, the virtual impactor redirects the particles into two different streams based on their size. Based on the geometry of the nozzle section, the real impactor can further be classified as a slit (rectangular nozzle) impactor and axy-symmetric (round nozzle) impactor.

A lot of work has been devoted in the past to studying the performance of inertial impactors, both theoretically and experimentally. Marple and Liu[22] were the first to undertake the theoretical study on the design and development of inertial impactors. They numerically obtained the characteristic impactor efficiency curves for both rectangular-and-round-jet real virtual impactors with different characteristic geometrical configurations. Subsequently, Rader and Marple[21] refined the previous study by using a finer grid and including appropriate models for ultra-stokesian drag (USD) and interception, for the particulate phase. The results of the above study are treated as a standard in handbooks on aerosol measurement[24].

More numerical studies on the performance of round-nozzle real impactors are available in literature. Jurcik and Wang[25] used the FIDAP[4] code to study the performance of a flat-plate orifice round nozzle impactor and compared their results against experimental data and the numerical results of Rader and Marple[21] for an angled nozzle configuration. More recently, Collazo et al.,[26] reported the design, calibration and

experimental validation of round-nozzle single-and-multi-stage impactors for the size measurement of man-made organic fibers. They reported using the Computational Fluid Dynamics (CFD) code FLUENT[4] in their design stage. Huang et al.,[27] performed a numerical study in which the influence of impaction plate diameter and particle density on the collection efficiency of a round- nozzle inertial impactor was investigated.

IV. B. Comparison against Experimental Data

In this study, the performance of a slit (rectangular) nozzle real impactor was numerically simulated using the CFD code CFX-4.4. The rectangular slit real impactor whose performance is investigated in this study was designed, fabricated and its performance was experimentally evaluated at the Aerosol Technology Laboratory (ATL), Texas A&M University (TAMU). More details on the design and performance evaluation of this impactor are available elsewhere[20].

The sensitivity of the obtained results was analyzed with respect to the total number of particles used in the simulation. The effect of including the buoyancy force (gravity) in the simulations was explored. Moreover, the use of ultra-stokesian drag (USD) formulation to determine the drag coefficient, in place of the usual drag coefficient calculation was investigated. The predicted impactor curve for each of the above cases is compared against experimental data and the obtained results are discussed.

IV. B. 1. Problem Description

Figure 1 presents a two-dimensional view of one-half of a section of a typical rectangular slit impactor. It is to be noted that the flow is symmetric about mid-plane and

the length of the impactor (dimension across the page) is substantially greater than the width. The impactor geometry has a converging section, a throat section and a coated plate at the bottom. The plate is coated with the appropriate material to catch the particles and to prevent re-suspension and bounce.
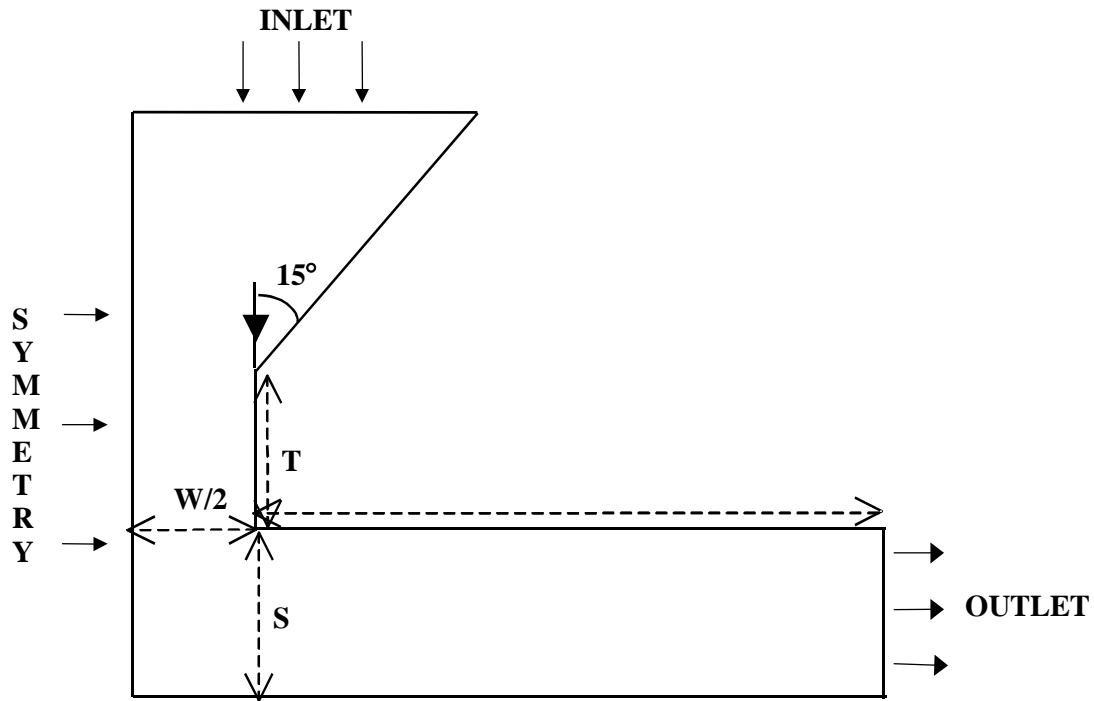
Fig. 1. Two-dimensional schematic of one-half section of the slit impactor with appropriate boundary conditions.

Fluid (usually air) with aerosol particles (either liquid or solid phase) of different sizes entering the inlet plane is accelerated through the converging inlet section. The gas-particle mixture then passes through a throat section that is in the form of a rectangular nozzle and impinges on the wall below and flows out through the sides. Particles above a particular size that acquire enough inertia during the acceleration phase impinge on the wall and stick to it, whereas those below that size are usually carried

along with the fluid stream and flow out of the domain. Hence, there is a selective classification of the particles based on the size and the characteristic throat velocity.

IV. B. 2. Characterization of Impactor Performance

The non-dimensional groups that characterize the performance of the inertial impactor are the Reynolds and the Stokes numbers. It is well known that the Reynolds number characterizes the flow field information and the Stokes number characterizes the particle motion information in the flow field under consideration[9, 23]. The geometric parameters that characterize the performance of the slit impactor are the ratio of the stopping distance to the width of the throat (S/W) and the ratio of the throat length to the width of the throat (T/W). The classification efficiency curve for the impactor under consideration is expressed against the square root of the Stokes number (which can be considered as a non-dimensional diameter), for a particular value of S/W and T/W. For different Reynolds numbers, we will have different impactor efficiency curves. The Reynolds and Stokes numbers are calculated as shown below:

$$\mathrm{Re} = \frac{\rho V_0 2W}{\mu} \qquad (28)$$

$$StK = \frac{\rho_p V_0 d_p^2 C_c}{9\mu W} \qquad (29)$$

In the above expressions, ρ and μ are the fluid density and viscosity, ρ_p and d_p are the particle density and particle aerodynamic diameter, V_0 and *W* are the average

velocity in the throat section of the acceleration nozzle and the width of the throat section.

The factor C_c is the Cunningham slip correction factor, and is calculated as

$$C_c = 1 + \frac{2.52\lambda}{d_p} \tag{30}$$

where λ is the mean free path of the fluid in which the particle motion takes place.

In the case of a real impactor, it is customary in the literature to express the particle classification efficiency in terms of the ratio of the number of particles collected on the wall to the total number of particles that enter the inlet patch. In our simulation, for each particle size, the collection efficiency was calculated as follows:

$$\eta = 100 * \frac{n_w}{n_{in}} \tag{31}$$

where the η is the classification efficiency based on the number of particles collected on the wall, n_{in} is the total number of particles specified at the inlet patch and n_w is the number of particles deposited on the wall.

IV. B. 3. CFX-4.4 Simulations

The exact physical geometry was constructed in the CFX-4.4 pre-processor and a block-structured, body-fitted grid system, consisting of four blocks, was generated over the domain. The code's mesh generation algorithm generated an optimized mesh over the domain, consisting of 22734 computational cells. Figure 1 also is a schematic of the computational model used for our simulations and the boundary and initial conditions

are explained with reference to Figure 1. As the flow field is two-dimensional, unit width was prescribed in the third dimension. Uniform, normal velocity condition was prescribed at the inlet plane and a symmetric (mirror) boundary condition was specified at the left boundary and on both faces of the third dimension. Free boundary conditions were prescribed at the outlet. The rest of the surfaces were automatically treated as wall boundaries with zero slip velocity conditions. Figure 2 presents the computational mesh of the geometry generated by the CFX-4.4 code.
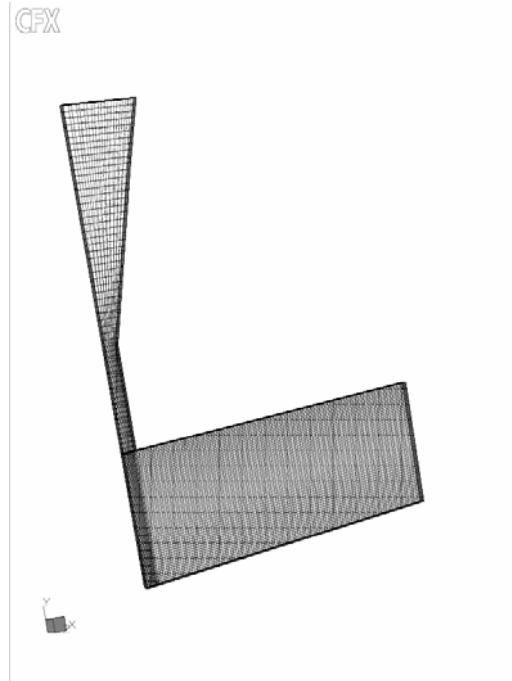
Fig. 2. Computational grid of the slit impactor used for the simulation.

A hybrid-differencing scheme (HDS) was adopted for the discretization of the momentum equations and a central differencing scheme (CDS), for the pressure equation. Pressure-velocity coupling was implemented using the SIMPLEC algorithm.

The discretized momentum and pressure equations were solved using a-full-field Stone Solver (STONE3D) and a preconditioned Conjugate Solver (ICCG), respectively. The under-relaxation factors were 0.65 for the momentum equations and 1 for the pressure correction equation. The important geometrical and numerical parameters are summarized in Table 1.

TABLE I

Geometrical and Numerical Parameters of Interest

GEOMETRICAL DETAILS			
SLIT WIDTH (W) = 2.54E-04 m SLIT LENGTH = 0.127 m NOZZLE AREA = 3.2258E-05 m^2 FLOW RATE = 3.75 m^3/hr THROAT VELOCITY = 32.292 m/s		S/W =5 T/W =3.9 FLUID:AIR AT STP $Re = 2WV_0 / \nu = 1093.6$	
NUMERICAL DETAILS			
TOTAL # OF COMPUTATIONAL CELLS =22734 MASS SOURCE RESIDUALS = 4800 (CORRESPONDING TO 0.1% INLET MASS FLOW RATE)			
EQN	DIFFERENCING SCHEME	SOLUTION ALGORITHM	UNDER RELAXATION FACTOR
U,V,W	HYBRID DS	STONE3D	0.65
P	CENTRAL DS	ICCG	1.00

Convergence was declared when the normalized residual (based on the inlet mass flow rate) was 0.1%. Once convergence was achieved, a fixed number of particles, say 100, of a particular aerodynamic diameter were randomly introduced at different locations at the inlet boundary. The velocity of the particles was set to be equal the fluid inlet velocity. Individual particle motion was tracked until the particle exited the computational domain or impacted the wall. Simulations were repeated with different

particle sizes that ranged from a maximum to a minimum size value. Impactor efficiency curve was generated by plotting the collection efficiency on the wall as a function of the Stokes number (or the particle size).

IV. B. 4. Results and Discussions

The velocity contours resolved by the code are presented in Figure 3. It can be seen that the vectors, after impaction on the plate, are aligned as a sharp jet, parallel to the plate and slowly diverge as they go toward the exit. The rest of the region is void with a strong recirculation zone.
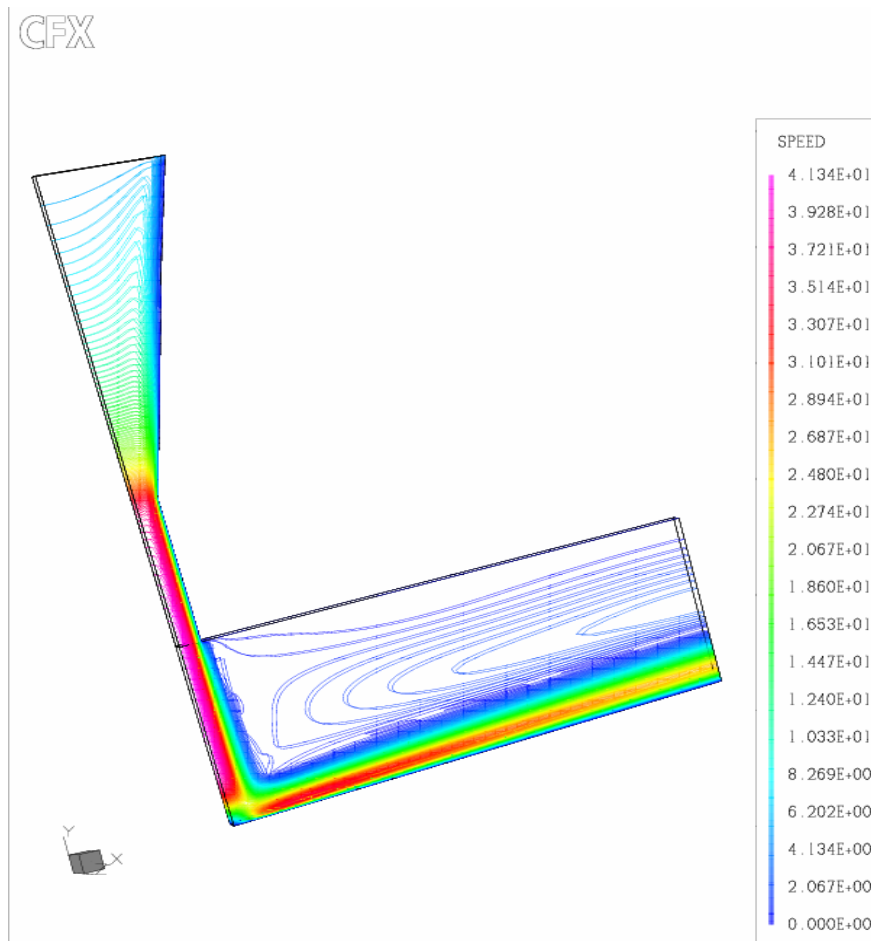
Fig. 3. Velocity contours in the slit impactor.

Figures 4 and 5 present the particle tracks for the maximum and the minimum sizes for which simulations were carried out. In the case of the maximum size (2.5 μm AD), all the particles that enter the domain are deposited at the impaction plate. However, for the minimum size (0.25 μm AD), the particles are carried along the flow a thin stripe along the impaction plate to the exit plate.
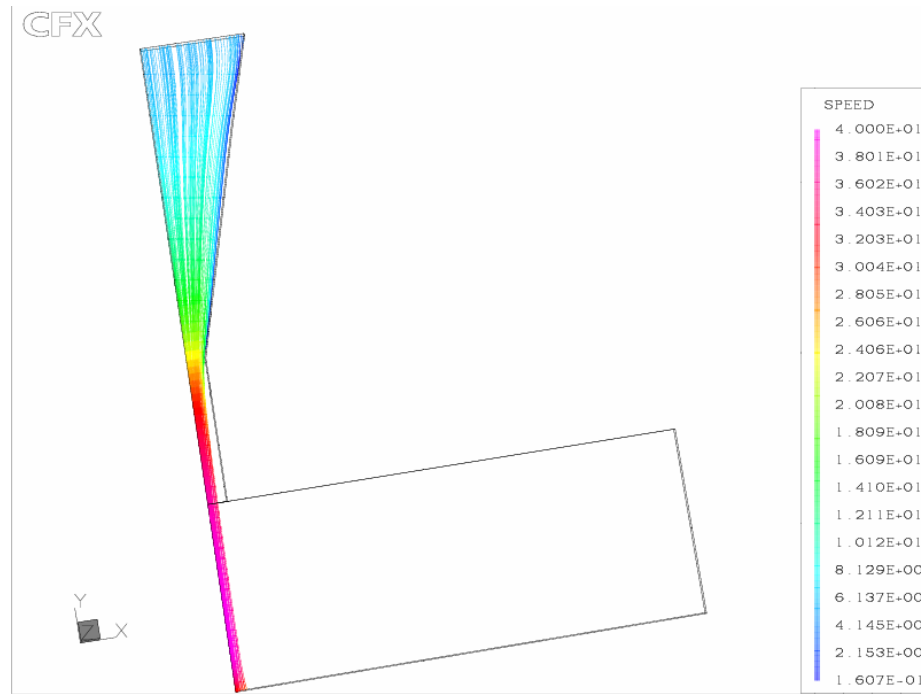
Fig. 4. Particle tracks for 2.5 μm AD particle.

Figure 6 presents the impactor efficiency curve generated from the simulations. The simulation results are compared against the experimental data obtained in the laboratory. It can be seen that the predicted efficiency curve by the CFX-4.4 agrees well with experimental data. The impactor was designed for a 50% cutpoint value (d_p^{50}) of 0.84 microns and both the experimental and numerical results reproduce this value pretty

well. In the subsequent sections, the results of the sensitivity studies that were described

previously will be presented and discussed.
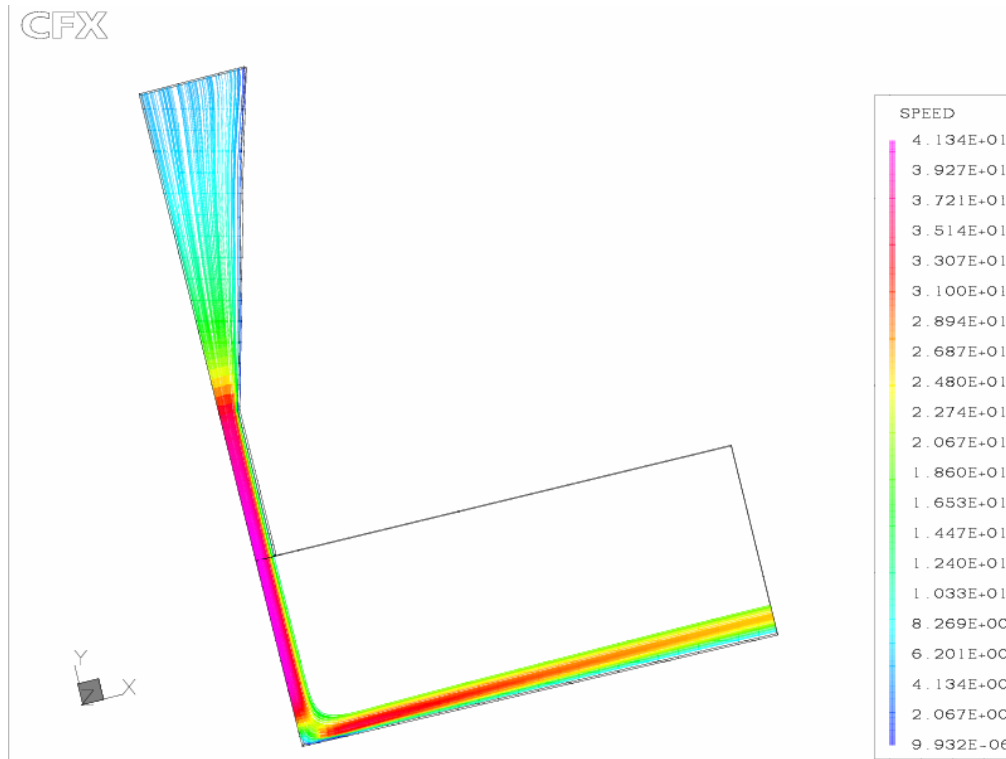
Fig. 5. Particle tracks for 0.25 µm AD particle.

(a) Effect of Total Number of Particles Used for the Simulation

In the previous simulation, 100 particles were randomly distributed at various

positions on the inlet patch. However, in any numerical study, it is to be ensured that the

predicted results are independent of changes in the initial conditions. In this part of the

study, the effect of using 500 particles at the inlet plane on the predicted impactor

efficiency curve was investigated. Figure 7 presents the results of this study. The

experimental results (labeled EXP) are also presented for comparison. It can be seen that

the simulation results for the efficiency curves obtained with 100 (labeled CFX-100) and

500 (labeled CFX-500) particles are not different at all; in fact, the numerical results are sharper with 500 particles and are more focused toward the experimental results.
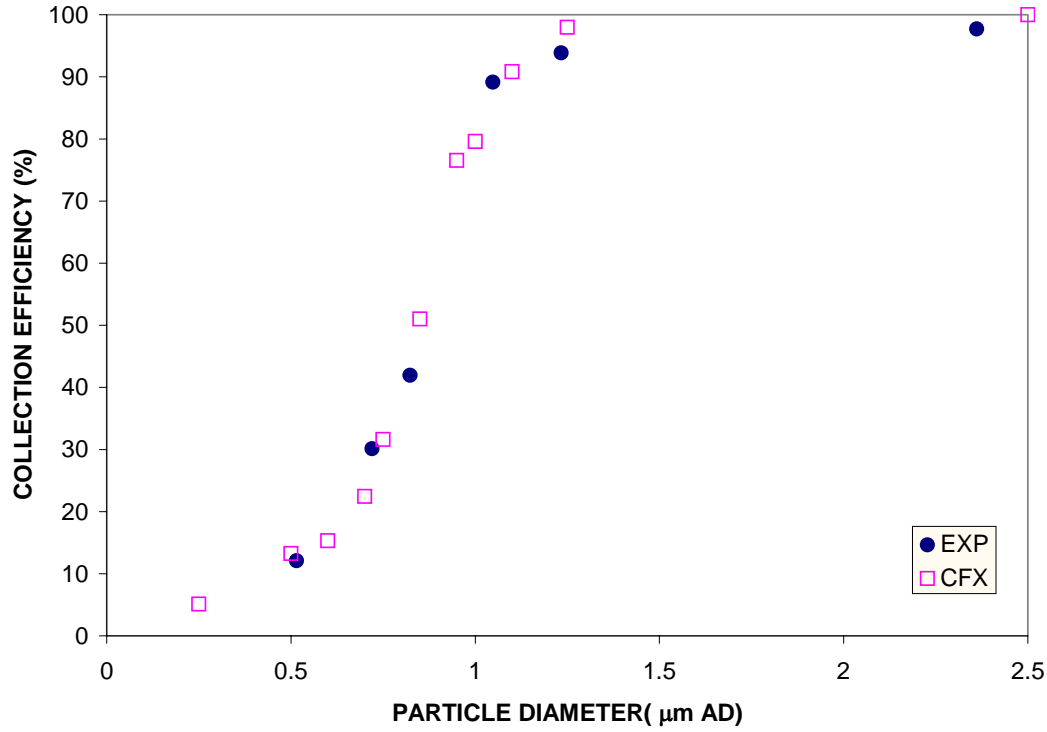
Fig. 6. Particle collection efficiency plot as a function of particle aerodynamic diameter: comparison of the experimental and numerical results.

(b) Effect of Including the Buoyancy Force (Gravity) in the Particle Force Balance Equations

Collazo et al.,[26] reported that the effect of gravity needed to be included to obtain proper agreement with experimental results. Hence, the effect of including the buoyancy force on the impactor efficiency curve predictions was investigated.

The buoyancy force is calculated in the code as

$$F_B = -\frac{1}{6}\pi d_p^3 (\rho_p - \rho)g \qquad (32)$$
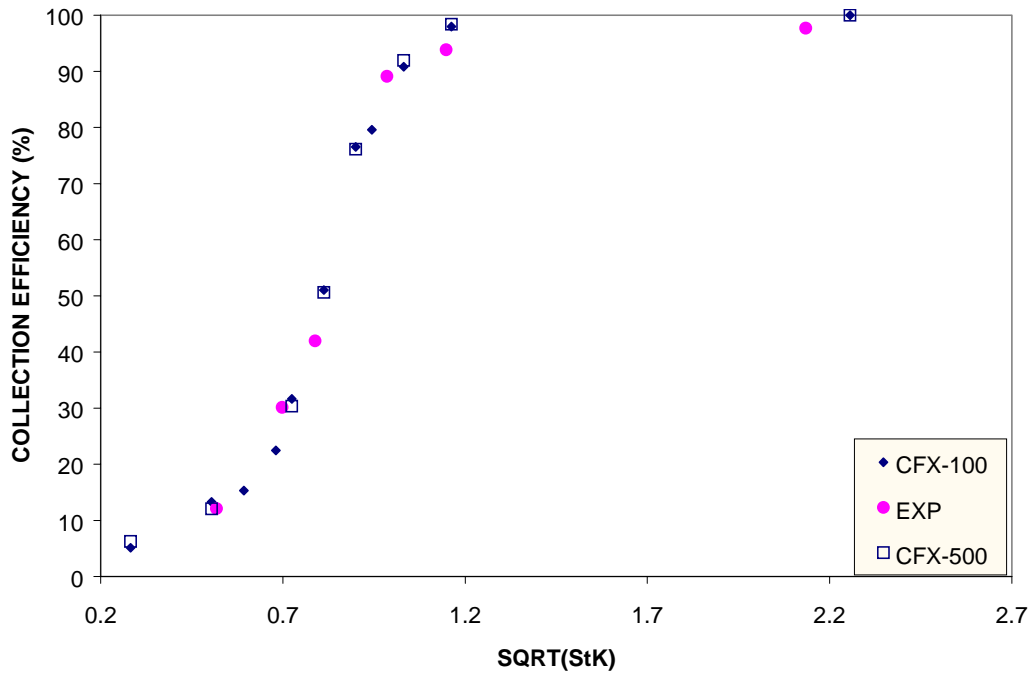
Fig. 7. Impactor efficiency curve: comparison of the experimental and numerical results with 100 and 500 particles.

Figure 8 presents the simulation results with (labeled CFX-G) and without (labeled CFX-NG) gravity force along with the experimental (EXP) results, for comparison. It can be seen from the figure that there is no difference between the results with and without gravity. The above result suggests that gravity is not important in the present case. In this respect, it may seem that the present observations are not in agreement with the previous observations[26] regarding the inclusion of the gravitational force. However, on further investigation, it was found that the definition of gravity vector that is adopted in their study is not the actual value of the acceleration, due to gravity. It is a normalized parameter based on the nozzle diameter, gravity, and the square of the throat velocity as shown below:

$$\hat{G} = \frac{gW}{V_0^2} \tag{33}$$

where g is the acceleration due to gravity, W is the nozzle diameter and V_o is the throat velocity.
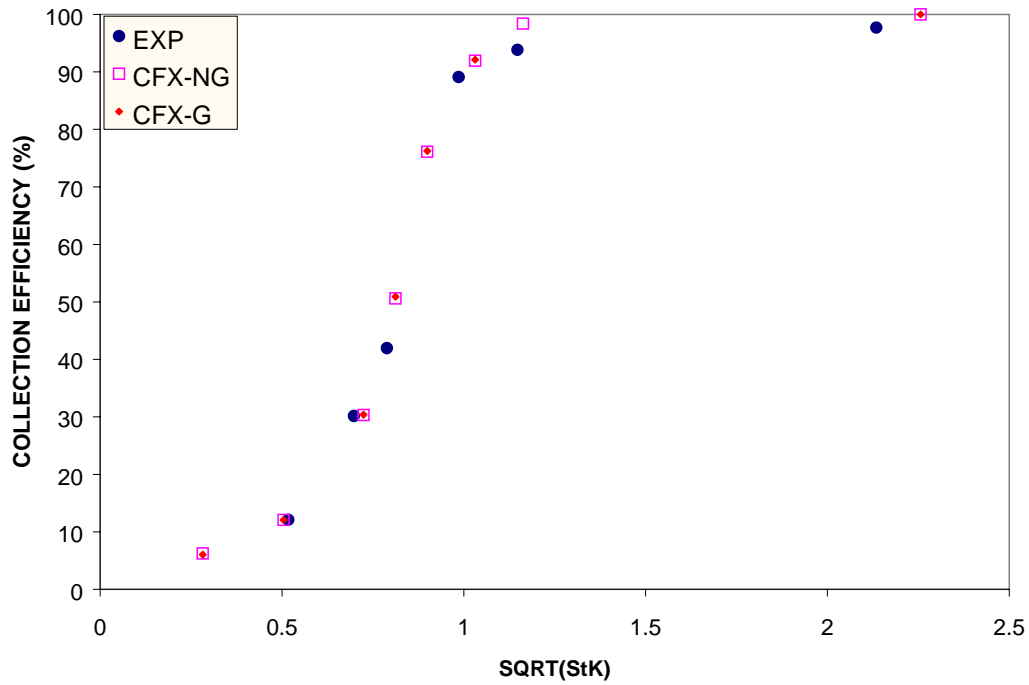
Fig. 8. Impaction efficiency curve: comparison of the experimental results to numerical results with and without gravity force.

It can be seen that this non-dimensional quantity is the inverse of the Froude number. Based on the present geometry and flow conditions, if the normalized gravity parameter is calculated, the obtained value is very small (2.4E-06). However, the above parameter calculated for the geometry and flow conditions of Collazo et al.,[26] turns out to be orders of magnitude higher than the present case (1.5E-02) (The calculation details are presented in Appendix). This is the reason why, in the present case, the effect of

gravity is negligible, whereas, in their case, it was important. In general, for micron-size particles, as the inertial force increases and the nozzle dimension decreases, the effect of gravity should start diminishing.

(c) Effect of Using Ultra-Stokesian Drag in Place of the Standard Drag Formulation

The work of Rader and Marple[4] discussed the need to include proper equations to calculate the drag coefficient based on the concept of ultra-stokesian fluid resistance. The drag coefficient calculation assuming ultra-stokesian conditions is different from the way that is presently being done in the code. It is a function of the particle Reynolds number and is presented below:

For $\text{Re}_p < 5$,

$$C_D = \frac{24}{\text{Re}_p}(1 + 0.916\,\text{Re}_p) \tag{34}$$

and, for $5 < \text{Re}_p < 1000$,

$$C_D = \frac{24}{\text{Re}_p}(1 + 0.158\,\text{Re}_p^{2/3}) \tag{35}$$

These drag formulations were introduced into the appropriate subroutine and the simulations were repeated. Figure 9 presents the results of this simulation. The code predictions with the original drag formulation are labeled at CFX-ORD and that with ultra-stokesian drag is labeled as CFX-USD. These results were then compared with the experimental results. It can be seen that the predictions of the original and ultra-stokesian drag match well in the low-efficiency (<20%) range. However, in the mid-

range (20% to 90%), the ultra-stokesian formulation predictions are a few percent higher than the predictions of the ordinary drag formulation. In the high-efficiency range, it seems that the match is again good.
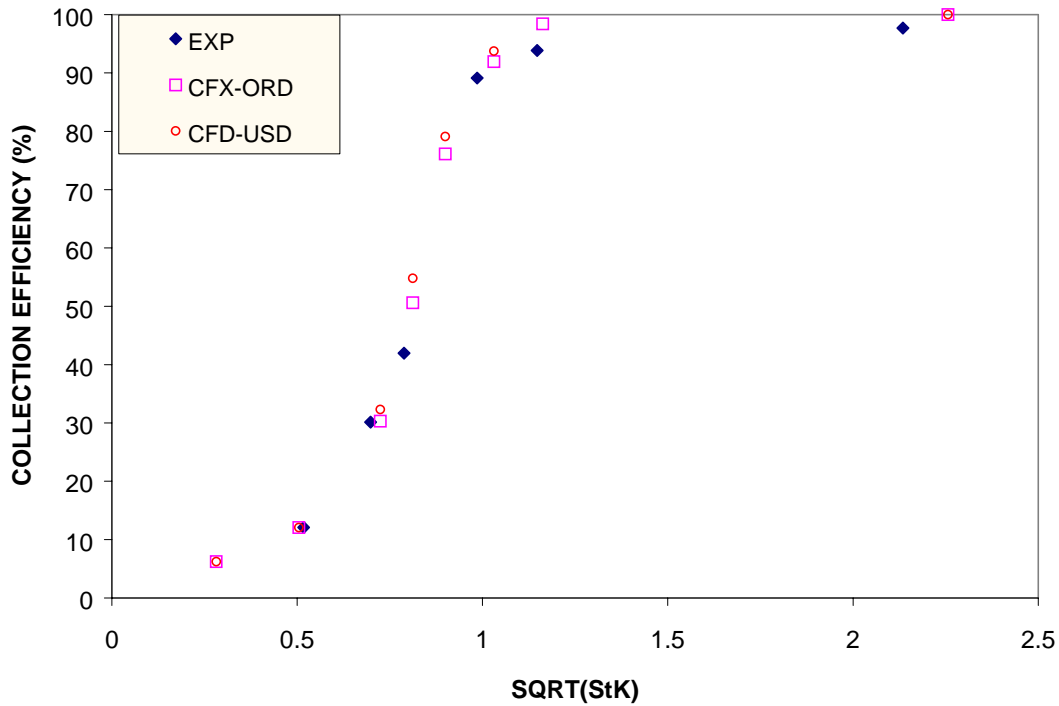
Fig. 9. Impaction efficiency curve: comparison of the experimental results to numerical results with ultra-stokesian drag (USD) and with normal drag.

Rader and Marple[21] report that the use of ultra-stokesian drag (USD) formulation shifts the impactor efficiency curve by 5% toward the right (or) higher SQRT (StK) values, compared to the efficiency curve obtained using the original drag formulation. The reported result was for a rectangular impactor with S/W =1.5, T/W=1.0, and Re=3000. However, we found that the overall shape of the curves, with and without the inclusion of ultra-stokesian drag, is the same for our case (S/W = 5, T/W=3.9, and

Re=1093.6). It is worthwhile to recall here their observation that the shift will be less for lower Reynolds numbers.

IV. B. 5. Conclusions

The performance of a rectangular slit real impactor designed and evaluated at the Aerosol Technology Laboratory (ATL), Texas A&M University has been numerically simulated using the CFD program CFX-4.4. Good agreement was obtained between the impactor efficiency curve obtained from the simulation and experimental results. The CFX-4.4 code was able to reproduce the exact shape and value of the 50% cutpoint aerodynamic diameter (d_p^{50}).

The effect of the total number of particles used for the simulation on the predicted efficiency curve was explored. A study was conducted in which 500 particles were used for the simulation. It was found that the shape of the efficiency curve remained nearly the same as that obtained with 100 particles.

The effect of including the gravity force in the particle force balance equations on the prediction of the efficiency curve was studied. It was found that the efficiency curve obtained with and without the inclusion of gravity coincided, suggesting that gravity force was not important for the simulated case.

Finally, the effect of using the ultra-stokesian drag formulation for estimating the drag coefficient, on the efficiency curve prediction was investigated. No perceptible difference was observed between the predicted efficiency curves obtained using the ultra-stokesian drag formulation and that using the normal drag coefficient formulation.

IV. C. Comparison against Theoretical Data

In this study, simulations were performed on the rectangular jet impactor geometry that Rader and Marple[21] and Marple and Liu[22] studied. The above case was chosen because results are readily available in the literature and a comparison with the predictions of CFX-4.4 can be made.

The predicted results from the CFX-4.4 code were compared against their results, wherever possible. For selected cases, the effect of using the ultra-stokesian drag (USD) formulation to determine the drag coefficient on the predicted efficiency curve was investigated and the results presented.

IV. C. 1. Problem Description

The schematic of the geometry remains the same as in Figure 1, except for the angle of approach in the convergence section. In the present case, it was 31 degrees, whereas in their case, it was 30 degrees. Keeping the ratio of the throat length (T) to the impactor width (W), T/W, constant (=1), the ratio of the stopping distance (S) to the impactor width (W), S/W, was varied from a value of 0.25 to 5. For each particular value of S/W and T/W, the performance curve was obtained for three different Reynolds numbers namely, 10, 100 and 3000.

IV. C. 2. CFX-4.4 Simulations

The exact physical geometry was constructed in the CFX-4.4 pre-processor and a block-structured, body-fitted grid system was generated over the domain. The code's mesh generation algorithm generated an optimized mesh over the domain and the number of computational cells that gave a grid independent solution for each case is

presented in Table II. The boundary and initial condition specification remained the same as in the previous case and can be seen presented in Figure 1. A value of 2.5mm was used for the width of the rectangular nozzle as this was the actual width of the impactor used by Marple and Liu[22] in their experimental study. The value of the normal velocity assigned at the inlet boundary was computed based on the above width and the Reynolds number for which the simulation was performed. Also, as stated earlier, the angle of convergence at the inlet section was 31° compared to the value used in the previous study (30°).

Information on the differencing schemes adopted for the discretization of the momentum and the pressure equations, solvers utilized for the solution, under-relaxation factors employed for each case, along with other important geometrical and numerical parameters are summarized in Table II. Pressure-velocity coupling was implemented using the SIMPLEC algorithm.

Convergence was declared when the normalized residual (based on the inlet mass flow rate) was 0.1%. Once convergence was achieved, a fixed number of particles, say 100, of a particular aerodynamic diameter were randomly introduced at different locations at the inlet boundary. The velocity of the particles was set to be equal the fluid inlet velocity. Individual particle motion was tracked until the particle exited the computational domain or impacted the wall. Simulations were repeated with different particle sizes that range from a maximum to a minimum size value. Impactor efficiency curve was generated by plotting the collection efficiency on the wall as a function of the Stokes number (or the particle size).

TABLE II

Details of the Numerical Simulation for the Various Configurations (T/W = 1)

CONFIGURATION AND REYNOLDS NUMBER		DIFFERENCING SCHEME		UNDER RELAXATION FACTOR		SOLUTION ALGORITHM		# OF CELLS
		U	P	U	P	U	P	
RE=10	S/W=0.25	HDS	CDS	0.65	1.0	STONE3D	ICCG	12960
	S/W=0.5	HDS	CDS	0.65	1.0	STONE3D	ICCG	21600
	S/W=1.0	HDS	CDS	0.65	1.0	STONE3D	ICCG	19200
	S/W=1.5	HDS	CDS	0.65	1.0	STONE3D	ICCG	24240
	S/W=2.0	HDS	CDS	0.65	1.0	STONE3D	ICCG	33600
	S/W=5.0	HDS	CDS	0.65	1.0	STONE3D	ICCG	45120
RE=100	S/W=0.25	HDS	CDS	0.65	1.0	STONE3D	ICCG	12960
	S/W=0.5	HDS	CDS	0.65	1.0	STONE3D	ICCG	21600
	S/W=1.0	HDS	CDS	0.65	1.0	STONE3D	ICCG	19200
	S/W=1.5	HDS	CDS	0.65	1.0	STONE3D	ICCG	24240
	S/W=2.0	HDS	CDS	0.65	1.0	STONE3D	ICCG	33600
	S/W=5.0	HDS	CDS	0.65	1.0	STONE3D	ICCG	45120
RE=3000	S/W=0.25	HDS	CDS	0.3	1.0	BLOCK STONE	ICCG	12960
	S/W=0.5	HDS	CDS	0.2	1.0	BLOCK STONE	ICCG	21600
	S/W=1.0	HDS	CDS	0.1	1.0	STONE3D	STONE3D	19200
	S/W=1.5	HDS	CDS	0.2	1.0	BLOCK STONE	ICCG	24240
	S/W=2.0	HDS	CDS	0.2	1.0	BLOCK STONE	ICCG	33600
	S/W=5.0	HDS	CDS	0.05	1.0	BLOCK STONE	ICCG	45120

IV. C. 3. Results and Discussion

The simulations were conducted for three different values of Reynolds numbers namely 10, 100 and 3000. The value of T/W was maintained constant at 1.0 and the value of S/W was varied from 0.25 to 5. For a particular value of S/W, the impactor efficiency curve for the three Reynolds numbers are presented for each case.

For each case, the computational grid was gradually refined until the time the impactor efficiency curve was found to be invariant to further grid refinement. From previous experience, it had already been determined that the impactor efficiency curve was invariant, as the total number of particles used for the simulation approached a value of 500. So, 500 particles were used in each of these simulations.

(a) <u>Case 1: S/W = 0.25</u>
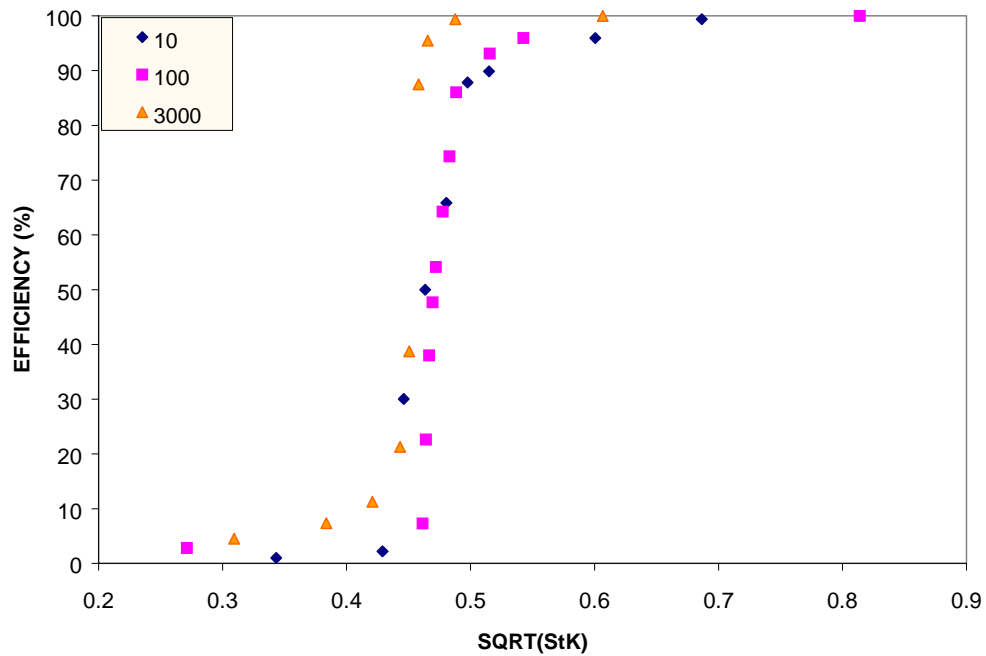
Fig.10. Impactor efficiency curve for various Reynolds numbers (S/W=0.25).

Figure 10 presents the impactor efficiency curves for the three Reynolds numbers. It can be seen from the figure that the curves for Re=10 and Re=100 coincide in this case. However, the curve for Re=3000 stands slightly to the left of the coinciding curves. As the Reynolds number increases, the curve gets sharper and steeper. The SQRT $(StK)_{50}$ values for the Re=100 and Re=10 cases are close; however, the value for Re=3000 is lower than the Re=100 case.
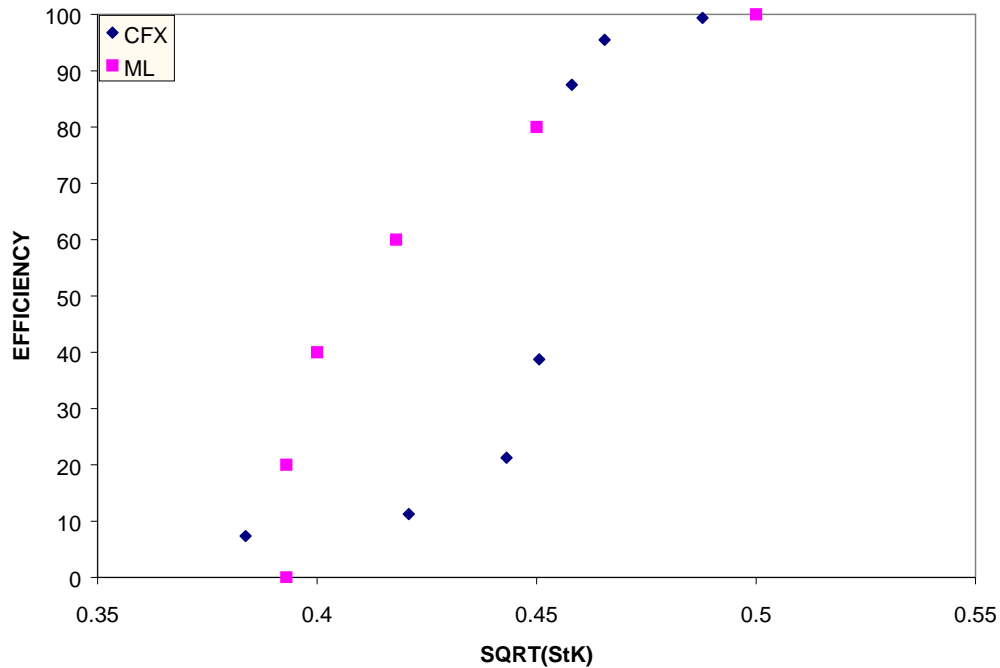
Fig.11. Comparison of the CFX-4.4 predictions of the impactor efficiency curve against the results of Marple and Liu[22] (S/W=0.25, Re=3000).

Figure 11 presents the impactor efficiency curve predicted by the CFX-4.4 code for the Re=3000 case. The results (labeled CFX) are compared against the results of Marple and Liu[22] (labeled ML). It can be seen that though the range (over which the maximum and minimum value for the curve varies) is the same, the shapes of the curves are different. Hence the predicted values of SQRT $(StK)_{50}$ are also different.

(b) <u>Case 2: S/W = 0.5</u>

Figure 12 presents the impactor efficiency curves for the three Reynolds numbers. It can be seen from the figure that the curves start getting apart in this case. However, with the increase in the Reynolds number, the curve gets sharper and steeper. It is interesting to note that the tail portion of the efficiency curve at the high-efficiency end decreases and that at the low efficiency end increases as the Reynolds number increases. The SQRT $(StK)_{50}$ values decrease slightly as the Reynolds number increases.
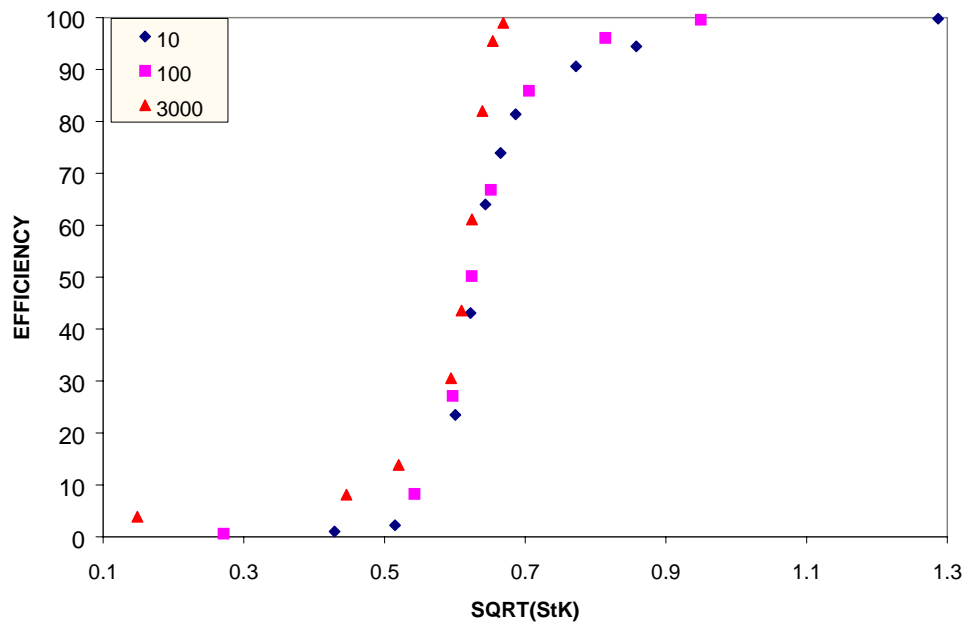
Fig. 12. Impactor efficiency curve for the various Reynolds numbers (S/W=0.5).

Figure 13 compares the impactor efficiency curve predicted by the CFX-4.4 code for Re=3000 case against the results of Marple and Liu[22]. In this case, the discrepancy between the results is found to be substantial.

Fig. 13. Comparison of the CFX-4.4 predictions of the impactor efficiency curve against the results of Marple and Liu[22] (S/W=0.5, Re=3000).

(3) Case 3: S/W = 1.0

Figure 14 presents the impactor efficiency curves for the different Reynolds numbers for this case. The curves start getting significantly separated now with the Re=10 curve being to the extreme right. The curve for Re=3000 is in the middle, and, to the left of the curve for Re=10. The curve for Re=100 is to the left of the Re=3000 curve till it overlaps the curve for Re=100. The crossover occurs at about a value of 80% collection efficiency; then, the Re=100 curve shifts to the right of the curve for Re=3000. The efficiency curve becomes steeper as the Reynolds number increases. Unlike the previous case, the SQRT $(StK)_{50}$ values don't show any direct trend with the variation in the Reynolds number. The SQRT $(StK)_{50}$ value for the Re=3000 case is found to be less than that for the Re=100 case.
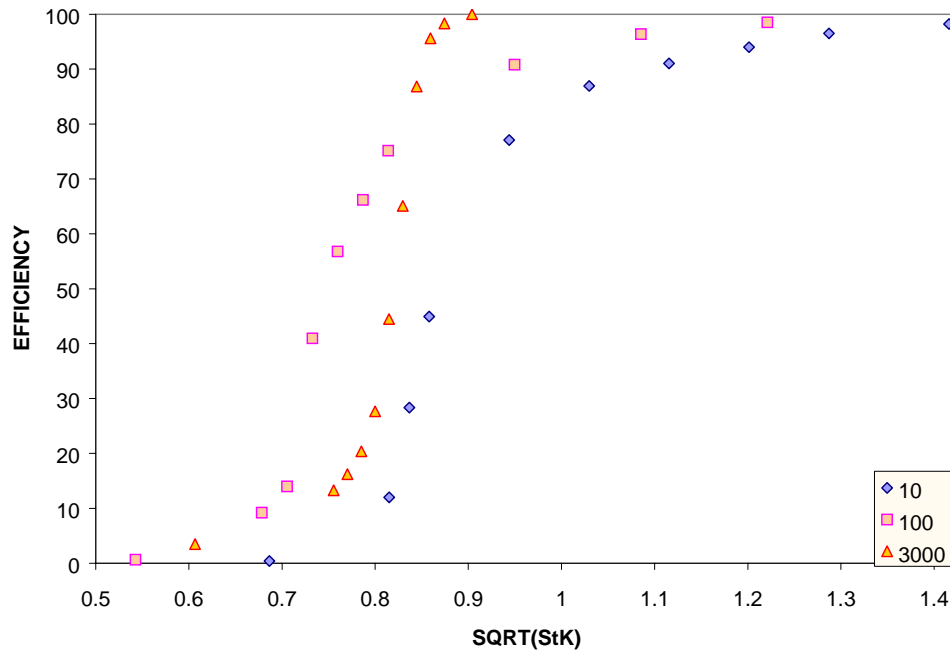
Fig. 14. Impactor efficiency curve for the various Reynolds numbers (S/W=1.0, Re=3000).

Figures 15, 16, and 17 present a comparison of the CFX-4.4 prediction of the efficiency curve against the results of Marple and Liu[22] for the three different Reynolds numbers. A general observation that can be made from the results is that their data is sharp and steep whereas the present data is more spread out. They do not have a small tail at the low efficiency end that is seen in the present simulations.

For the Re=10 and Re=100 cases, a close agreement is obtained between the present predictions and their results. However, there is reasonable difference in the results for Re=3000. Both the shape of the efficiency curve and the SQRT $(StK)_{50}$ value for the Re=3000 case are found to be different for this case. The deviation between the results of the present simulation and the previous results has increased substantially compared to the earlier cases.
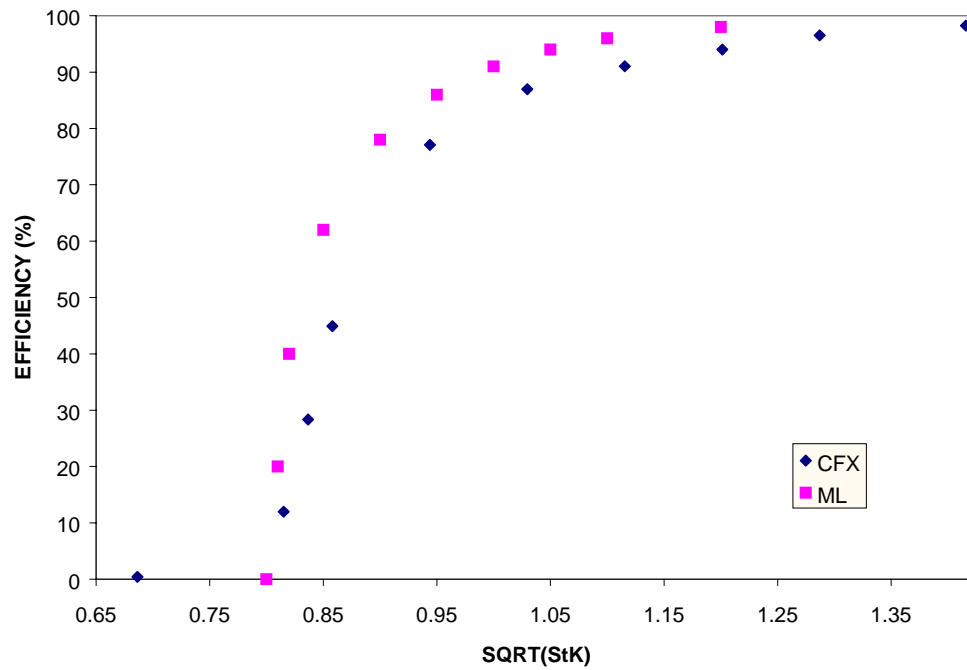
Fig. 15. Comparison of the predicted impactor efficiency curve from the CFX-4.4 Code against the results of Marple and Liu[22] (S/W=1.0, Re=10).
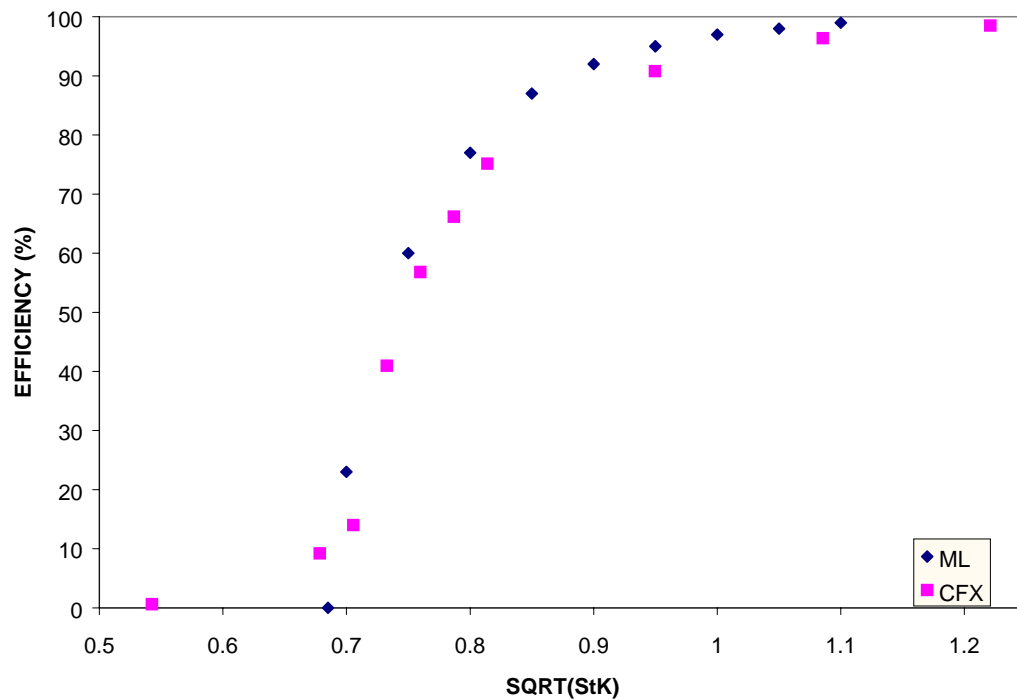
Fig. 16. Comparison of the predicted impactor efficiency curve from the CFX-4.4 Code against the results of Marple and Liu[22] (S/W=1.0, Re=100).
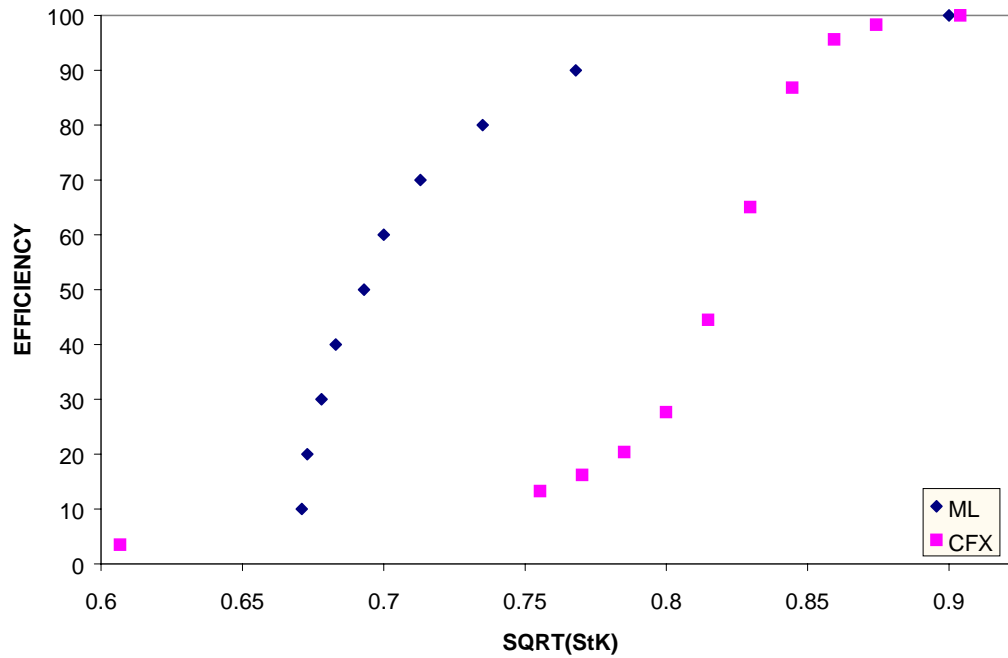
Fig. 17. Comparison of the predicted impactor efficiency curve from the CFX-4.4 Code against the results of Marple and Liu[22] (S/W=1.0, Re=3000).

Rader and Marple[21] have described the need to use ultra-stokesian formulation to estimate the drag coefficient. This formulation was coded into the drag calculation subroutine of the CFX-4.4 program and simulations were carried out for the Re=3000 case. Figure 18 compares the results of the ultra-stokesian drag (USD) formulation against the results of the standard drag formulation. The results of Marple and Liu[22] have also been presented for comparison purposes. It can be seen that the use of USD formulation shifts the curve to the left of the standard curve. This is contrary to the observations of Rader and Marple[21] as the USD curve gets shifted to the right of the standard curve in their case. In spite of the curve shifting to the left with the use of USD formulation, there is a substantial difference between the present curve and their curve.
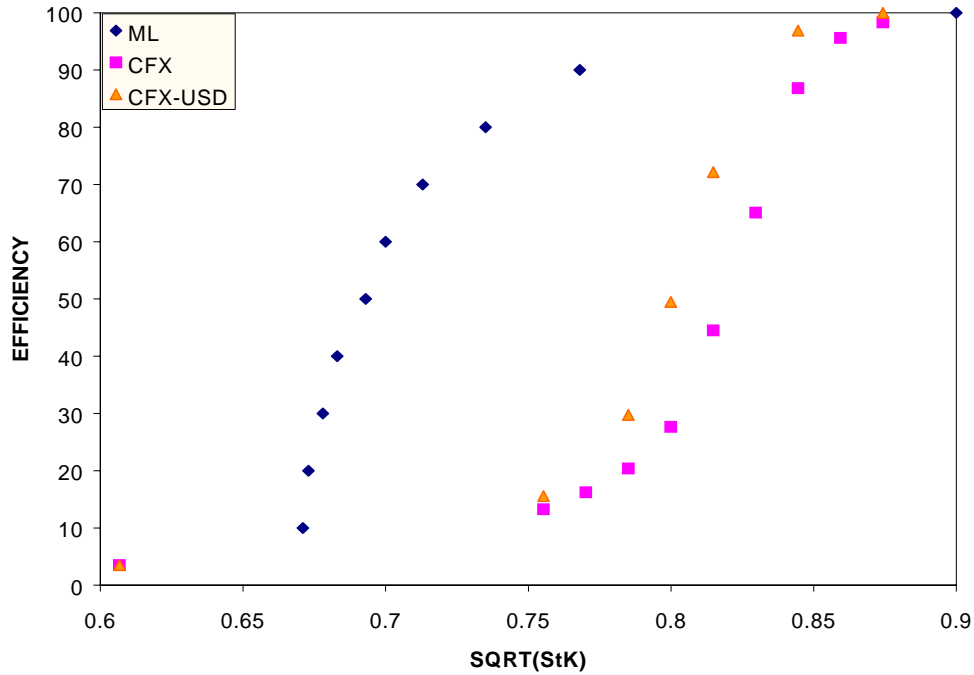
Fig. 18. Comparison of the predicted impactor efficiency curve from the CFX-4.4 Code with and without USD against the results of Marple and Liu[22] (S/W=1.0, Re=3000).

(d) <u>Case 4: S/W = 1.5</u>

Figure 19 presents the results for this case. It can be seen that the general trend of results is the same as in the previous case. However, the efficiency curve for Re=10 starts getting away from the curves for Re=100 and Re=3000. The curves for Re=100 and Re=3000 crossover, as in the previous case and the crossover occurs at around a value of 80% collection efficiency.

Figures 20, 21, and 22 compare the obtained results against the results of Rader and Marple[22] (labeled RM). The general observations that were made about the results of the previous case are found to be valid for this case too. While there is good agreement for the results for Re=100, reasonable discrepancy is observed for the Re=3000 case.
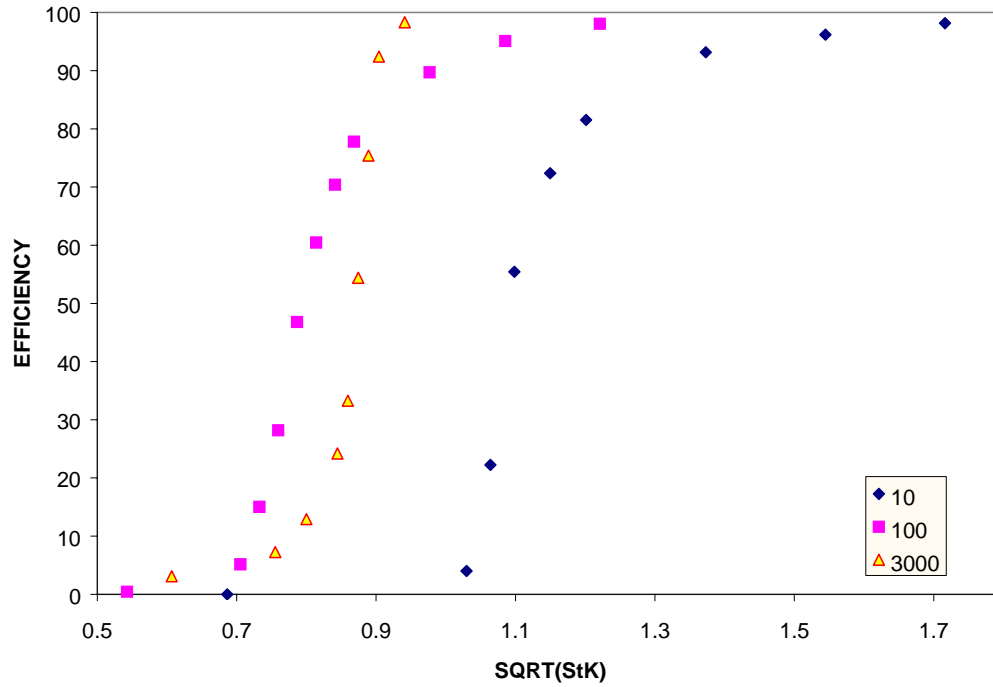
Fig. 19. Predicted impactor efficiency curve for the various Reynolds numbers (S/W=1.5).
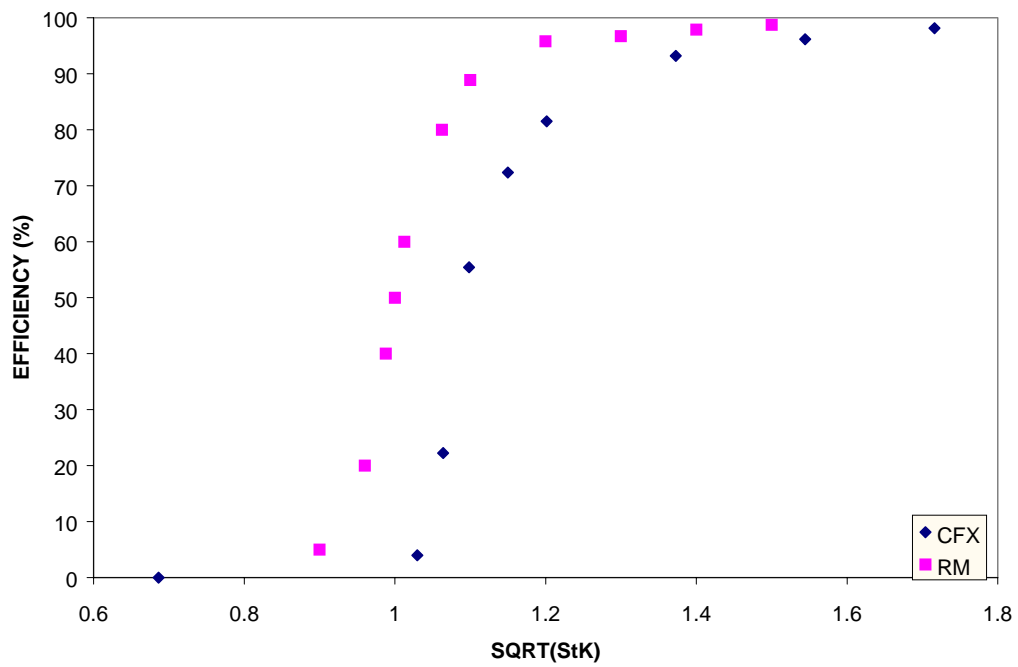
Fig. 20. Comparison of the predicted impactor efficiency curve from the CFX-4.4 Code against the results of Rader and Marple[21] (S/W=1.5, Re=10).
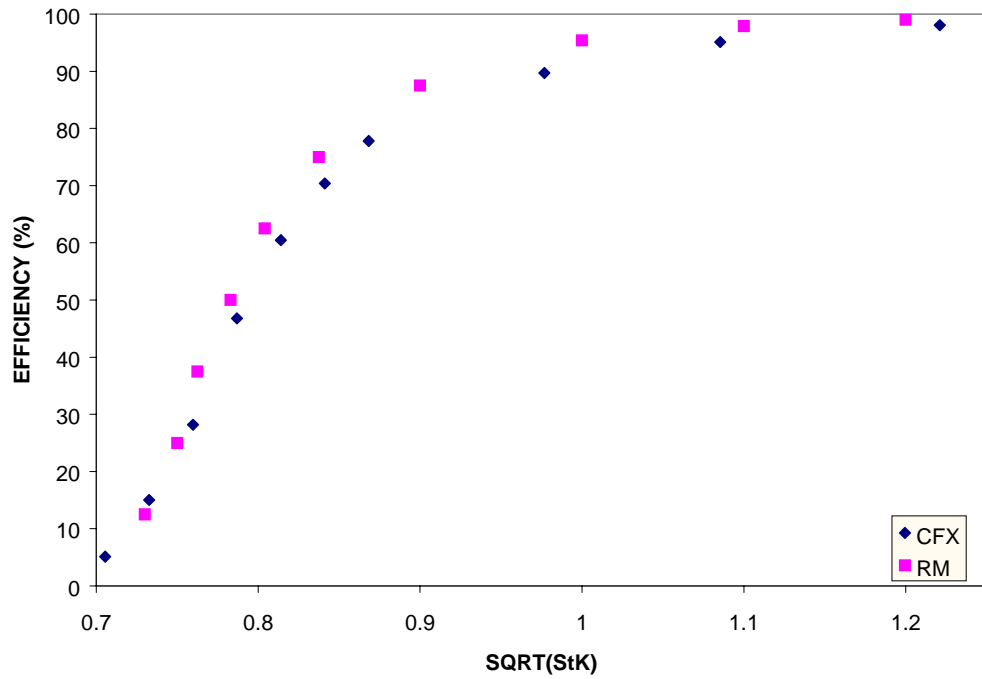
Fig. 21. Comparison of the predicted impactor efficiency curve from the CFX-4.4 Code against the results of Rader and Marple[21] (S/W=1.5, Re=100).
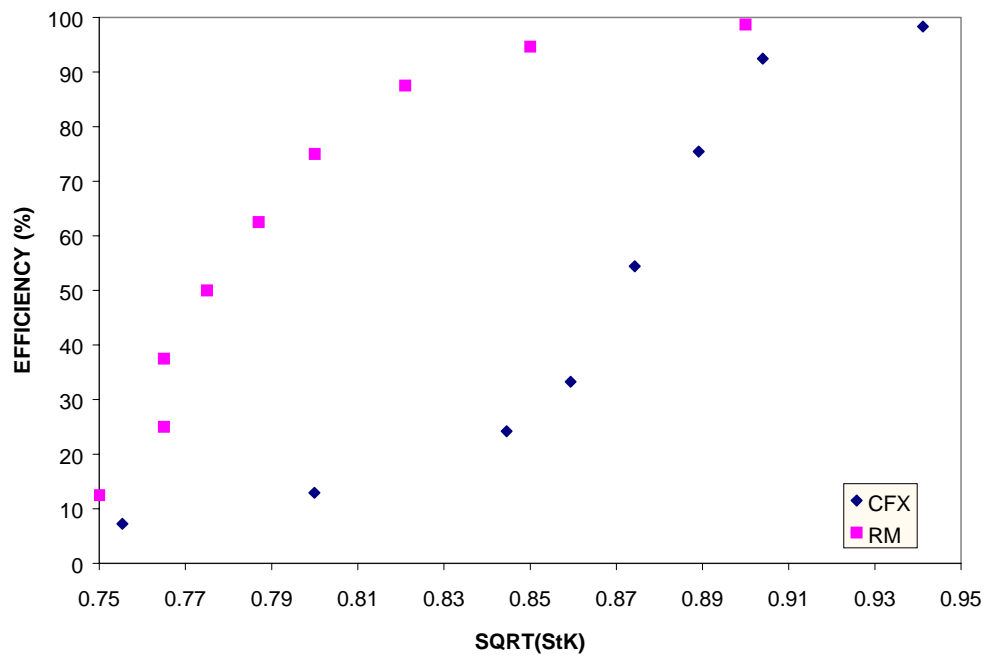
Fig. 22. Comparison of the predicted impactor efficiency curve from the CFX-4.4 Code against the results of Rader and Marple[21] (S/W=1.5, Re=3000).

Figure 23 presents the impactor efficiency curve predictions obtained using USD formulation for the Re=3000 case. The predictions obtained using the standard drag formulation and those of Rader and Marple[21] are presented for comparison. It is to be noted here that the predictions of Rader and Marple[21] were obtained using the USD formulation. There seems to be substantial discrepancy between the present results and the results of Rader and Marple[21].
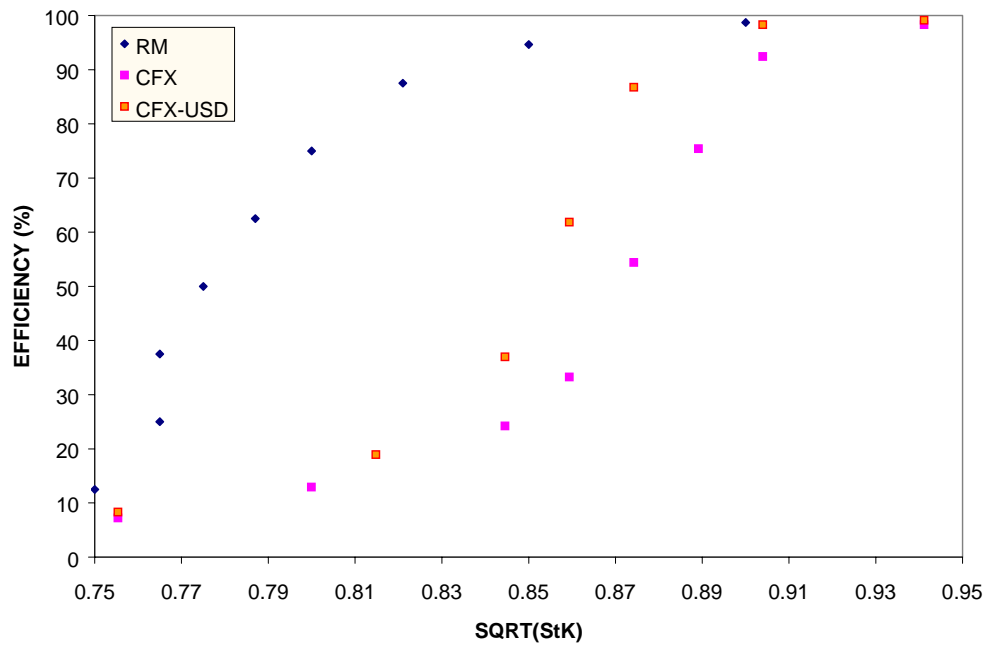
Fig. 23. Comparison of the predicted impactor efficiency curve from the CFX-4.4 Code with and without USD against the results of Rader and Marple[21] (S/W=1.5, Re=3000).

(e) Case 5: S/W = 2.0

Figure 24 presents the impactor efficiency curve for the different Reynolds numbers. For this case, it can be seen that the efficiency curves for Re=100 and Re=3000 are closer than in the previous cases and the Re=10 curve is located far to the right of these curves. As observed in the previous cases, the Re=3000 curve is steeper

than the others and does not have a tail at the high efficiency end, whereas the other two curves are more s-shaped. The Re=100 and the Re=3000 curves crossover at about an efficiency value of 80%.

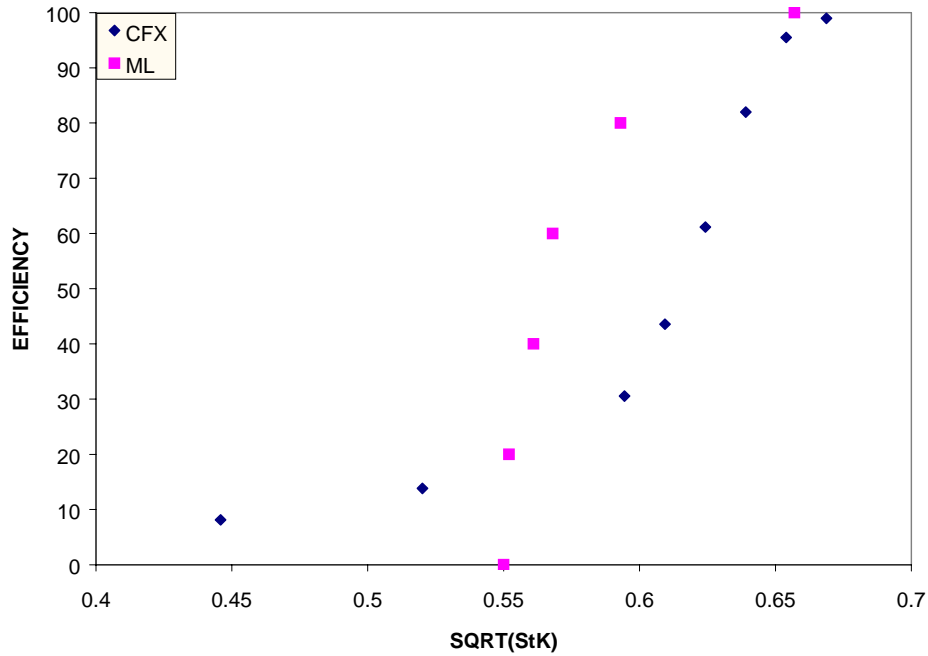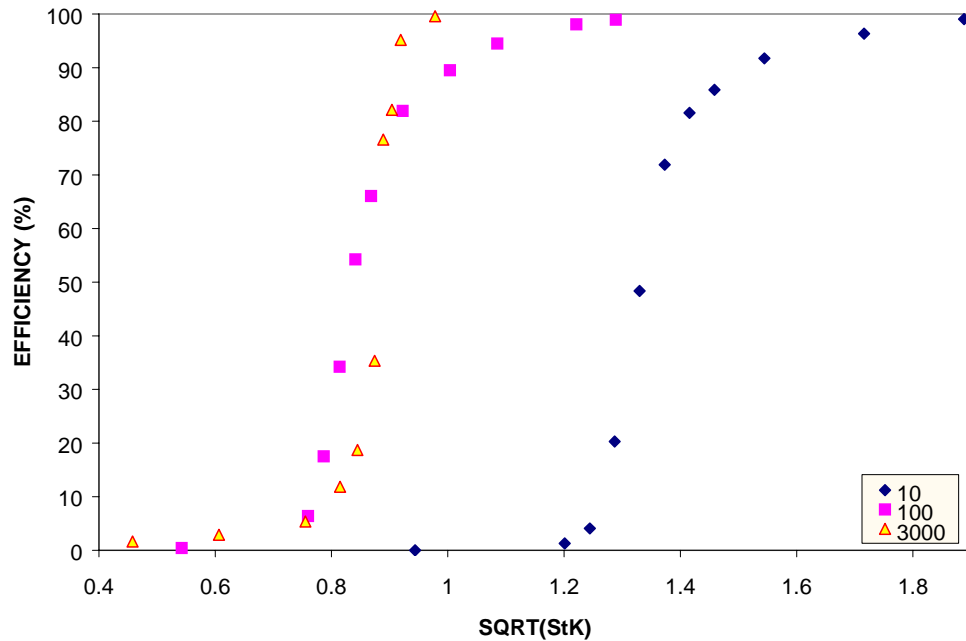Fig. 24. Predicted impactor efficiency curve for S/W=2.0 for the various Reynolds numbers

Figure 25 presents the comparison of the CFX-4.4 prediction of the impactor efficiency curve against the results of Marple and Liu, for the Re=3000 case. As before, it seems that there is substantial difference between the predictions.

(f) Case 6: S/W = 5.0

The impactor efficiency curve for this case is presented in Figure 26. The trend of the results for this case is closer to the previous result. The Re=100 and Re=3000 curves seem to nearly overlap each other, though their shapes are different. Compared to
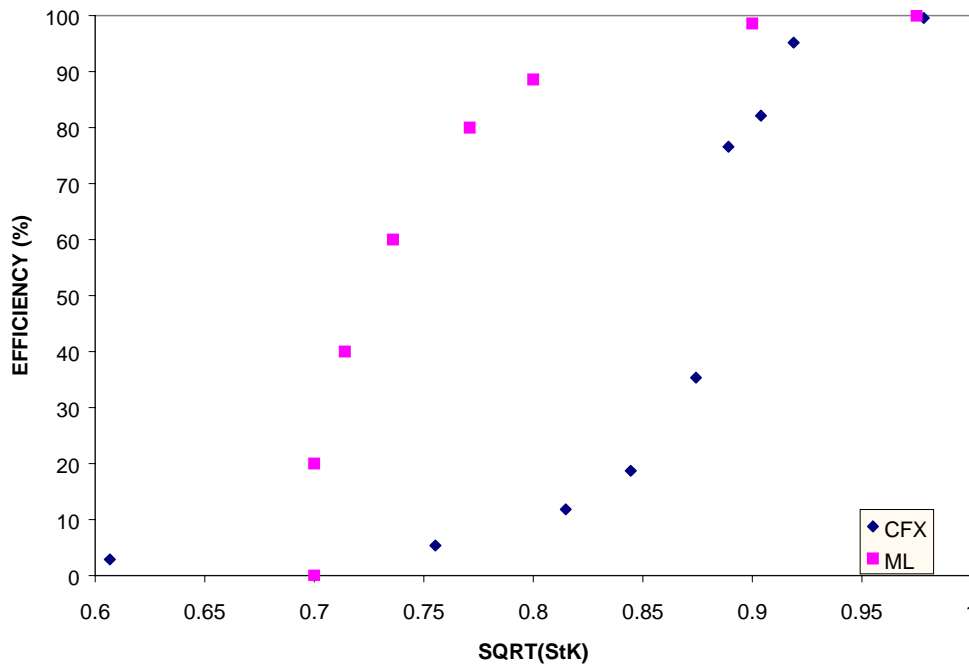
Fig. 25. Comparison of the CFX-4.4 predictions of the impactor efficiency curve against the results of Marple and Liu (Re=3000, S/W=2.0).
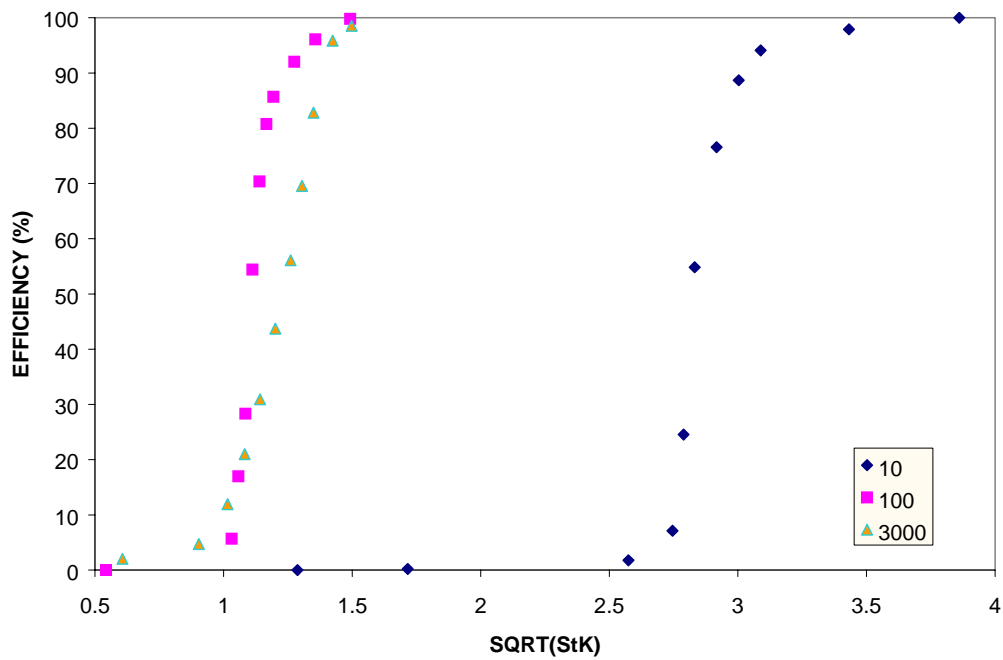
Fig. 26. Predicted impactor efficiency curve for S/W=5.0 for the various Reynolds numbers.

the previous case, the curves crossover at an efficiency value of 15%, which is far lower than the previous case. Also the tail at the high efficiency end for the Re=100 is far less than the previous case. The curve for Re=10 is far removed and is located to the right of these curves.
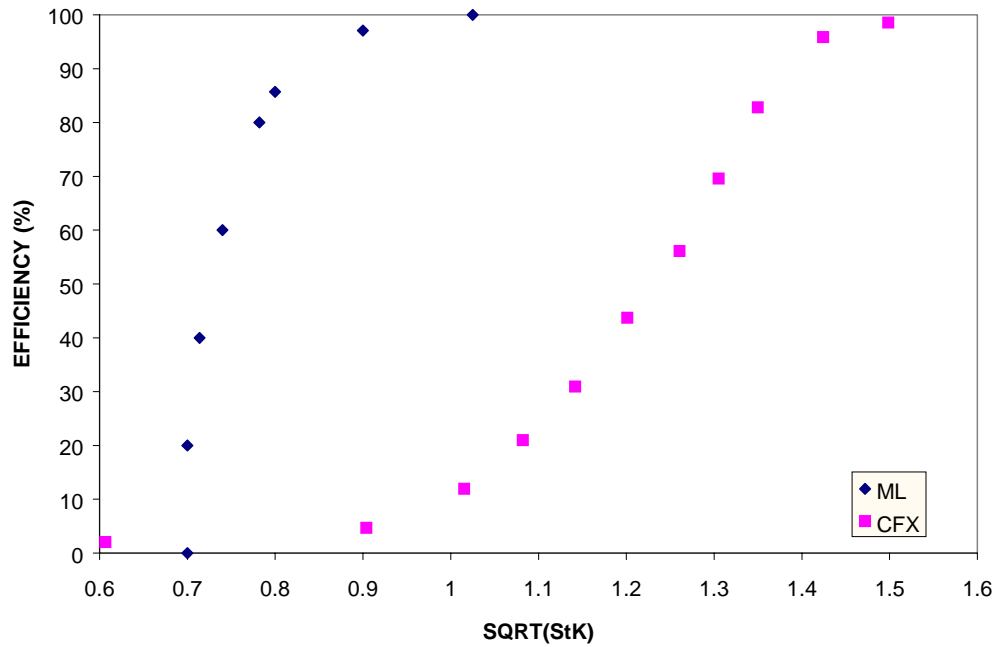
Fig. 27. Comparison of the CFX-4.4 predictions of the impactor efficiency curve against the results of Marple and Liu (Re=3000, S/W=5.0).

Figure 27 compares the impactor efficiency curve obtained from CFX-4.4 against those of Marple and Liu[22] for the Re=3000 case. This result also shows that there is substantial difference between the predictions. A general observation of these results suggests that the discrepancy between our results and those of Marple and Liu[22] increased with the increase in the ratio of S/W.

Table III summarizes the results of the present simulations. The SQRT $(StK)_{50}$ values for various values of S/W (Constant T/W=1) for the three Reynolds numbers 10, 100, and 3000 are presented. These results are also presented in a graphical form in Figure 28.
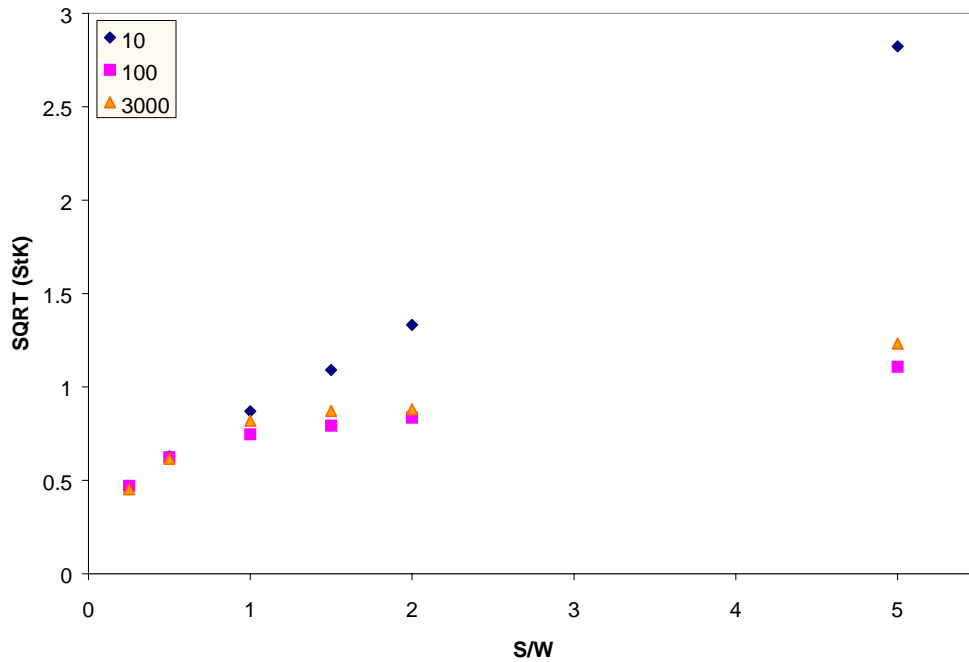
Fig. 28. Plot of the predicted SQRT $(StK)_{50}$ values as a function of S/W.

It can be seen from the figure that a nearly linear relationship exists between the values of SQRT $(StK)_{50}$ and S/W for the Re=10 case. For the case of Re=100, there is a quadratic increase in the value of SQRT $(StK)_{50}$ until S/W=1; subsequently, the rate of increase becomes linear. In the case of Re=3000, it was found that the value of SQRT $(StK)_{50}$ increases rapidly until S/W=1. In the region, $1 < S/W < 2$, the rate of increase is much slower. However, as we go to S/W=5, the value of SQRT $(StK)_{50}$ increases at a linear rate.

TABLE III

Predicted SQRT $(StK)_{50}$ for the Various Configurations

S/W						
Re	0.25	0.5	1	1.5	2	5
10	0.4633	0.6288	0.8695	1.0908	1.3326	2.8226
100	0.4702	0.6238	0.7462	0.7924	0.8347	1.1076
3000	0.4523	0.6153	0.8190	0.8713	0.8807	1.2325

IV. C .4. Conclusions

The performance of the standard inertial impactor described by Marple and Liu[22] was numerically simulated using the CFD program CFX-4.4. Keeping the T/W ratio constant, simulations were performed for three Reynolds numbers 10, 100, and 3000, for S/W ratios ranging from 0.25 to 5.0.

The results predicted by the CFX-4.4 code are compared to the results of Marple and Liu[22] and Rader and Marple[21], wherever applicable. There is a general agreement between the results of the present study and those of Marple and Liu[22] and Rader and Marple[21] for Reynolds numbers 10 and 100. However, as can be seen, there seems to be substantial difference in the results for Re=3000 case.

Marple and Liu[22] had compared their predictions against experimental results for the Re=3000 case and found substantial difference between their predictions and experiment. It can be seen from Table II that for the Re=3000 case, very low under-relaxation factors (URF) had to be used to obtain the necessary level of convergence that

was set in the study. It seems that the throat velocity (and the corresponding Reynolds number) is high enough to cause flow instability in the jet. This is the reason why such low values of URF had to be used to obtain convergence.

Another significant observation that needs to be made is regarding the shape of the efficiency curve. While the efficiency curve obtained from experiments is normally 'S' shaped, results of the studies of Marple and Liu[22] and Rader and Marple[21] predict that there is more or less no tail in the low-efficiency end of the curve. Other investigators[25] have also observed this anomaly when they repeated the studies of Marple and Liu[22] and Rader and Marple[21]. In this regard, it can be seen from the simulation results that the present work is consistently able to capture the shape of the curve for the various geometrical configurations investigated.

Some of the important aspects on which this study differs from the previous study of Marple and Liu[22] and Rader and Marple[21] are presented below:

(a) In the study of Marple and Liu[22] and Rader and Marple[21], the vorticity-stream function formulation was used to solve for the flow field. However, in the case of CFX-4.4, the primitive variable approach is used to solve the Navier-Stokes equations (NSE) and the velocities and pressure are obtained directly.

(b) Whereas Marple and Liu's[22] and Rader and Marple's[21] studies used the Finite-Difference formulation, CFX-4.4 uses the Finite Volume formulation to discretize the Navier-Stokes equations (NSE).

(c) While the study of Marple and Liu[22] used the standard formulation to calculate the drag coefficient, in the study of Rader and Marple[21], based on

the range of the particle Reynolds number, two different formulae were used to calculate the drag coefficient. However, the CFX-4.4 code has only the standard formulation for the whole range of particle Reynolds number.

(d) To investigate the effect of using the ultra-stokesian drag (USD) formulation for estimating the drag coefficient on the efficiency curve prediction, simulations were performed for the Re=3000 case with S/W=1 and 1.5. The predicted efficiency curves were compared against the results of Rader and Marple[21] (obtained using the USD formulation), in Figures 18 and 23. Substantial discrepancy can be noticed between the results.

(e) In addition to the drag force, the virtual mass force was also included in the particle force balance equations, in the present study. This force is automatically included in the CFX-4.4 code (by default). This force was not considered in the calculations of Marple and Liu[22] and Rader and Marple[21].

(f) While the studies of Marple and Liu[22] and Rader and Marple[21] do not include the slip correction term in the calculation of the Stokes number, in the present study slip correction was accounted for, wherever appropriate.

(g) In the present study, a global convergence criteria of <0.1% of the inlet mass flow rate was used for the resolution of the flow field, before starting the particle trajectory calculations. Also, for each case, it was ensured that the predicted efficiency curve was grid independent. Present experience with the simulations suggests that this is a very important step as the predicted efficiency curve was found to be sensitive to the above parameters.

Taking all the above-mentioned factors into consideration, further investigation is required to resolve the observed difference in trends.

IV. D. Conclusions

Simulations were performed with a view to validate the lagrangian particle transport algorithm implemented in the CFD code CFX-4.4, as it is being proposed to be used as a tool for modeling aerosol transport. A couple of cases were chosen as test cases for the validation study. The first case simulated using the code was a rectangular slit real impactor used for aerosol collection, for which experimental data was available. It was found that the results of the simulation were in excellent agreement with experimental data. The code was able to capture the exact shape of the impactor efficiency curve and the SQRT $(StK)_{50}$ value obtained experimentally. The next case simulated was a numerical study performed in the past, on different geometrical configurations of rectangular slit real impactors. It was found that good agreement was obtained with the results of this study, for the case of low Reynolds numbers. However, as the Reynolds numbers started increasing toward higher values (3000), there was substantial discrepancy between the results.

The results of the validation study suggest that the particle transport algorithm implemented in the CFX-4.4 code performed well for low Reynolds number. The code should serve as a good tool to study aerosol transport in the laminar flow range.

CHAPTER V

OPTIMIZATION OF A VIRTUAL IMPACTOR USING CFD TECHNIQUE

Virtual impactors[9] are devices used for the selective classification of particles based on their size. They are being used in a variety of applications as (i) sampling instruments for aerosolized particulate matter from air streams, and (ii) concentration and detection of bio-aerosols. They work on the principle of inertial separation.

Recently, numerous papers have appeared in the literature on the construction and performance evaluation of both the slit and the round-nozzle virtual impactors. However, to the best of our knowledge, there have been only a few papers in which the performance of the virtual impactor has been numerically (theoretically) studied. Hassan et al.,[28] were the first to demonstrate that the numerical technique can be used to analyze the performance of the virtual impactor. They obtained the characteristic efficiency and loss curves for a round nozzle virtual impactor. Shortly afterward, Marple and Chien[29] presented the results of a study in which the various aspects related to the performance of a round nozzle virtual impactor were analyzed in detail. Forney et al.,[30] and Ravenhall et al.,[31] analyzed the performance of a slit nozzle virtual impactor both theoretically and experimentally. However, the geometry of the slit virtual impactor used by them was different.

The studies of Chen and Yeh[32] and Loo and Cork[33] on the design and performance evaluation of round nozzle virtual impactors are considered as a standard in the field or virtual impactor design. Sioutas et al.,[34] presented the results of a study in which a round nozzle virtual impactor was designed and optimized for operation at a

very low cutpoint diameter and pressure drop. Han and Moss[35] have studied the internal flow field in a round nozzle, water model virtual impactor using flow visualization techniques.

Sioutas et al.,[36,37] also present two studies on the design, performance evaluation and optimization of very low cut point slit virtual impactors. In the first study[36], the performance of a specific design was evaluated both at the laboratory and on the field and the results are presented. The second study[37] concerns itself with the optimizing the impactor performance with different geometrical configurations and the laboratory evaluation of their performance.

On the numerical front, Asgharian and Godo[38] conducted CFD studies on the round nozzle virtual impactor geometry of Chen and Yeh[32] and Chein and Lundgren[39]. After solving for the flow field in the device using the FIDAP[4] code, they used their own code to calculate the particle trajectories. They obtained the classical virtual impactor efficiency and loss curves for spherical particles and compared their results against the experimental results of Chen and Yeh[32]. They also generated the impactor efficiency and wall loss curves for particles with different aspect ratios.

In a recent study, Ding et al.,[40] have presented the development and evaluation of a high volume slit nozzle virtual impactor used for concentrating coarse particles. To increase the impactor sampling flow, they tried increasing the nozzle length and using multiple nozzles. The study also presents the results of a variety of other investigations on using different geometrical configurations and the performance evaluation of each configuration investigated.

V. A. Introduction

This chapter demonstrates how the Computational Fluid Dynamics (CFD) technique can be used as a design and development tool at the research stage to troubleshoot and optimize the performance of industrial equipment. In this study, preliminary investigations on the performance of a prototype slit virtual impactor developed at ATL were carried out using CFX-4.4. Based on suggestions from the literature, modifications were incorporated to some of the geometrical parameters of importance, on the prototype design, and its performance was optimized and improved. The optimized and improved design was chosen as the base design and the impactor efficiency and wall loss curves were generated for (i) a variety of major-to-minor flow split ratios (10, 20, and 30%), and (ii) for a range of Reynolds numbers. The effect of modifying the radius of curvature of the receiving section for the base design, on the impactor performance was studied. The impactor efficiency and wall loss curves were generated for different curvatures. Some general observations are made on the CFD modeling of the virtual impactor performance.

V. B. Schematic of a Virtual Impactor

A two-dimensional view (front) of the schematic of a virtual impactor is presented in Figure 29 (assume that the virtual impactor is infinitely long across the paper). The fluid stream loaded with particles enters the device and is accelerated through a V-type converging section. The accelerated flow then passes through a uniform area throat section and a major part of this flow is drawn through the sides (known as the major flow). The rest of the flow is directed into a receiver throat section

(known as the minor flow) that is slightly wider than the acceleration section. As a result of this geometrical configuration, the flow near the walls of the receiving section, after penetrating a little into the receiving section, take a bend, breaking its downward movement and flow to the sides, whereas, the flow in the core region of the jet is directed downward.
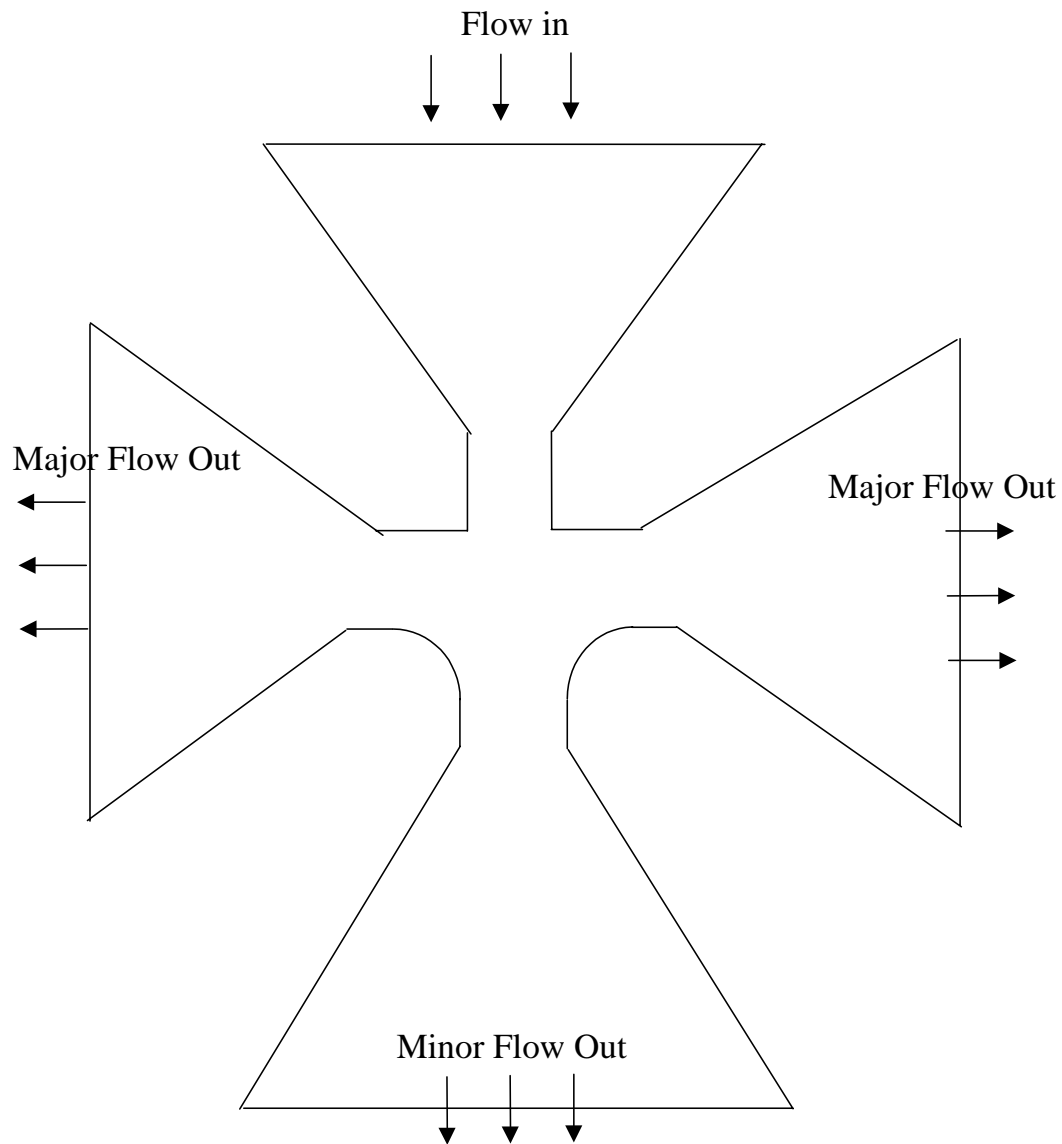
Fig. 29. A two-dimensional schematic of a virtual impactor.
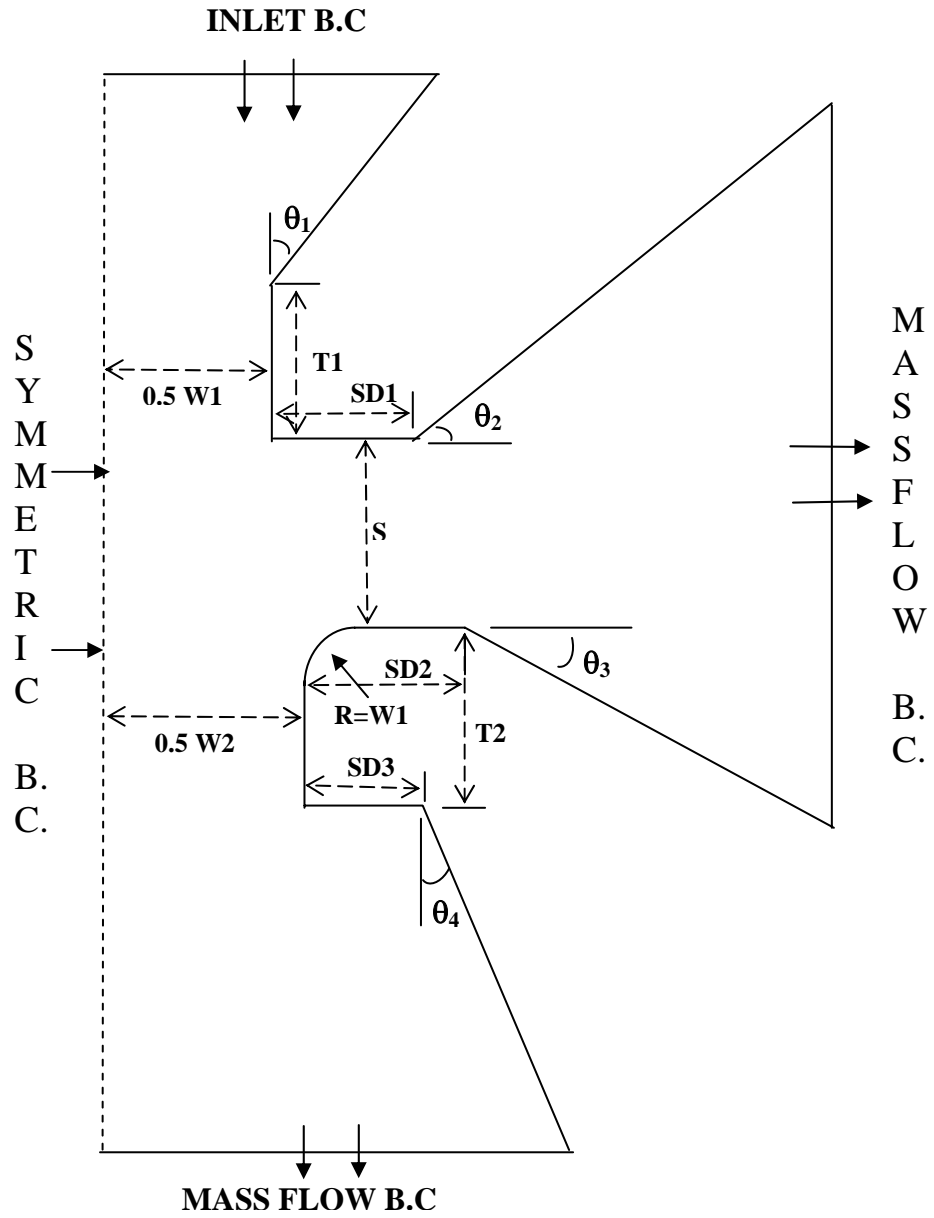
Fig. 30. One-half section of a virtual impactor with dimensions and boundary conditions.

The corner wall of the receiver throat section is given a small curvature to facilitate the streamlines breaking from the main flow to take a smooth bend into the sides. Heavier particles that acquire sufficient inertia during the acceleration process

keep their path and enter into the receiver throat, irrespective of the fluid streamline in which they are carried along. However, lighter particles follow the fluid stream and end up either into the receiver nozzle or the major flow.

Figure 30 presents a one-half section of the slit virtual impactor. The various geometrical parameters that characterize the performance of the slit virtual impactor are

(i) the throat width, W1, and depth, T1, of the acceleration nozzle

(ii) the throat width, W2, and depth, T2, of the receiver nozzle

(iii) the separation distance, S, between the acceleration and receiver nozzles

(iv) the various stand-off distances, SD1, SD2, and SD3 in the acceleration and receiver nozzles, and

(v) the various angles θ_1, θ_2, θ_3, and θ_4 in the acceleration and receiver nozzles.

A one-half section was chosen for the present simulations, as the flow is symmetric about the mid-plane. More information on the boundary conditions and other relevant details will appear in the next section. Table IV presents a summary of the various configurations and the above parameters chosen for each of the virtual impactor configurations whose performance was computationally investigated in this study.

V. C. Grid Information and Boundary Conditions

The exact physical geometry corresponding to each of the configurations was constructed in the CFX-4.4 pre-processor and a block-structured, body-fitted grid system was generated over the domain. The code's mesh generation algorithm generated an optimized mesh over the domain, for each configuration. As the flow field is two dimensional, unit width was prescribed in the third dimension.

TABLE IV

Details of the Various Geometrical Configurations Investigated

CONF	W1	W2	T1	T2	R	S	SD1	SD2	SD3	θ_1	θ_2	θ_3	θ_4
ORG	0.0125"	1.44 W1	0.8 W1	1.6 W1	0.8 W1	1.44 W1	0.8 W1	1.6 W1	1.6 W1	30°	15°	15°	45°
MOD1A-T	0.012"	1.5 W1	W1	1.5 W1	1.0 W1	1.5 W1	1.0 W1	1.5 W1	W1	45°	30°	30°	30°
MOD1A-2T	0.012"	1.5 W1	W1	3.0 W1	1.0 W1	1.5 W1	1.0 W1	1.5 W1	W1	45°	30°	30°	30°
MOD1B	0.012"	1.5 W1	W1	1.5 W1	1.0 W1	1.5 W1	1.0 W1	1.5 W1	NO	45°	30°	30°	30°
MOD2	0.012"	1.5 W1	W1	1.5 W1	0.16 W1	1.5 W1	0.5 W1	0.25 W1	NO	45°	30°	30°	30°
MOD3	0.012"	1.5 W1	W1	1.5 W1	0.315 W1	1.5 W1	0.615 W1	0.4 W1	NO	45°	30°	30°	30°

TABLE V

Details on the Numerical Simulation for the Various Configurations

CONFIGURATION		DIFFERENCING SCHEME		URF		SOLUTION ALGORITHM		# OF CELLS
		v	p	v	p	v	p	
ORG		HDS	CDS	0.3	1.0	BLOCK STONE	ICCG	45732
MOD 1A-T		HDS	CDS	0.3	1.0	BLOCK STONE	ICCG	62880
MOD 1A-2T		HDS	CDS	0.3	1.0	BLOCK STONE	ICCG	69960
MOD 1B-C (COARSE)		HDS	CDS	0.3	1.0	BLOCK STONE	ICCG	31840
MOD 1B-F (FINE)	RE=100	HDS	CDS	0.3	1.0	BLOCK STONE	ICCG	59880
	RE=508	HDS	CDS	0.3	1.0	BLOCK STONE	ICCG	59880
	RE=1016	HDS	CDS	0.1	1.0	BLOCK STONE	ICCG	59880
	RE=2000	HDS	CDS	0.05	1.0	GEN AMG	ICCG	59880
MOD 2		HDS	CDS	0.3	1.0	BLOCK STONE	ICCG	96960
MOD 3		HDS	CDS	0.3	1.0	BLOCK STONE	ICCG	67200

The various boundary condition specifications are detailed in the schematic of the one-half section of the virtual impactor, presented in Figure 30. Uniform, normal velocity condition was prescribed at the inlet plane and a symmetric (mirror) boundary condition was specified at the left boundary, and, on both faces of the third dimension. Mass flow boundary conditions were specified at the major flow and minor flow outlets. The rest of the surfaces were automatically treated as wall boundaries with zero slip velocity conditions.

Discretization schemes for the pressure and velocity equations, the total number of elements, under-relaxation factors adopted to solve the pressure and velocity equations, and the type of solver employed for each configuration are summarized in Table V. Pressure-velocity coupling was implemented using the SIMPLEC algorithm. Convergence was declared when the residual mass source tolerance of less than 0.1% of the inlet mass flow rate was achieved.

Once the converged flow field is achieved, a fixed number of particles were uniformly released at the inlet patch with the velocity equal to the inlet fluid velocity. The position of each particle is determined by integrating the particle force balance equations, for a very small time step. The integration process is continued until the time when the particle exits the domain through either of the outlets or gets deposited on the wall. This procedure is repeated for different particle sizes and a characteristic impactor efficiency and wall loss curve was generated.

As in the case of a real impactor, the virtual impactor performance is also characterized in terms of the Reynolds and the Stokes numbers. However, in this case, in

addition to the classification efficiency curve, there would be another curve that characterizes the particle losses in the internals of the impactor. The impactor efficiency and wall loss curves are expressed against the square root of the Stokes number. While the Stokes number is calculated the same way as was done in the real impactor, the Reynolds number in the case of the virtual impactor, is calculated as shown below:

$$\mathrm{Re} = \frac{\rho V_t W_t}{\mu} \tag{35}$$

In the above expressions, ρ and μ are the fluid density and viscosity, V_t and W_t are the average velocity in the throat section of the acceleration nozzle and the width of the throat section.

In the case of a virtual impactor, since there are two flow streams, major and minor, it is customary in the literature to express the particle classification efficiency in terms of collection in the minor flow, for the different major-to-minor flow split ratios. In our simulation, for each particle size, the minor flow efficiency and the percentage wall loss were calculated as follows:

$$\eta_{\min} = 100 * \frac{n_{\min}}{(n_{\min} + n_{maj} + n_w)} \tag{36}$$

$$WL = 100 * \frac{n_w}{(n_{\min} + n_{maj} + n_w)} \tag{37}$$

where the $\eta_{\min}$ is the classification efficiency based on the collection in the minor flow,

$n_{\min}$ is the number of particles collected in the minor flow, n_{maj} is the number of

particles collected in the minor flow and n_w is the number of particles deposited in the

wall. The quantity in the denominator is the total number of particles introduced at the

inlet
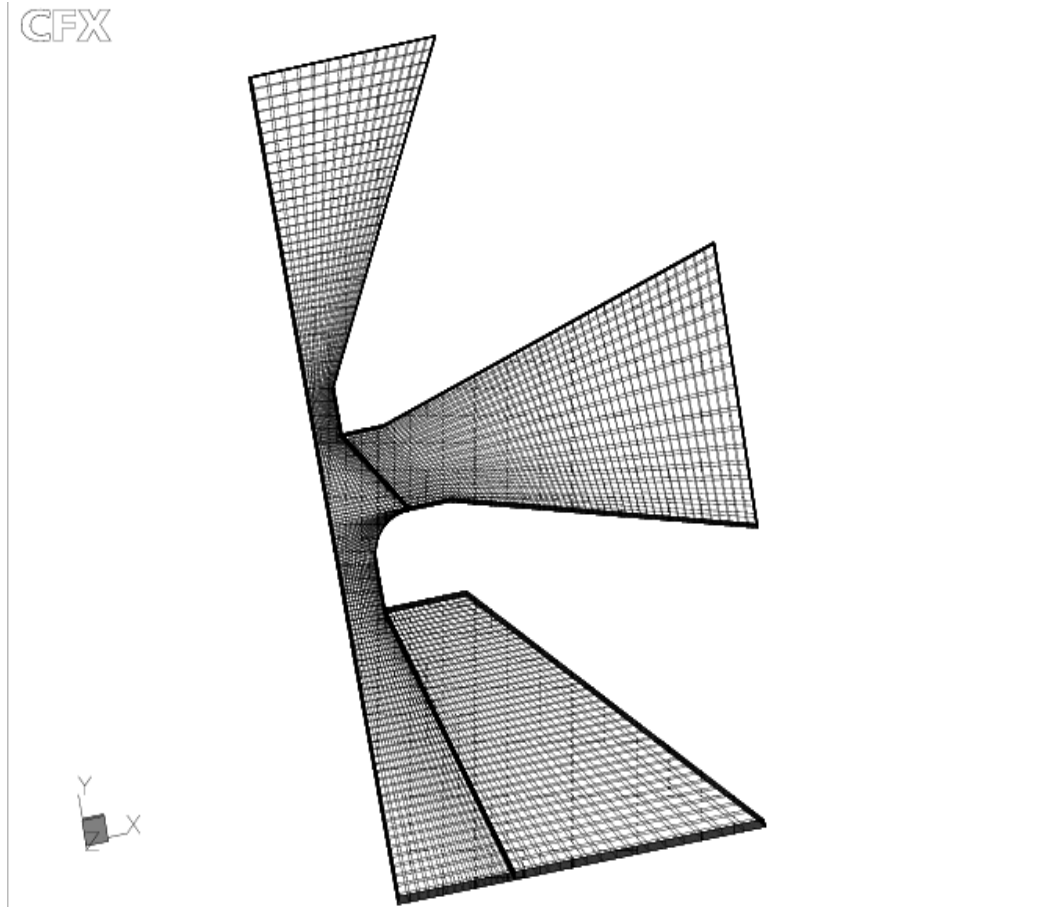
Fig. 31. Computational grid for the original prototype configuration.
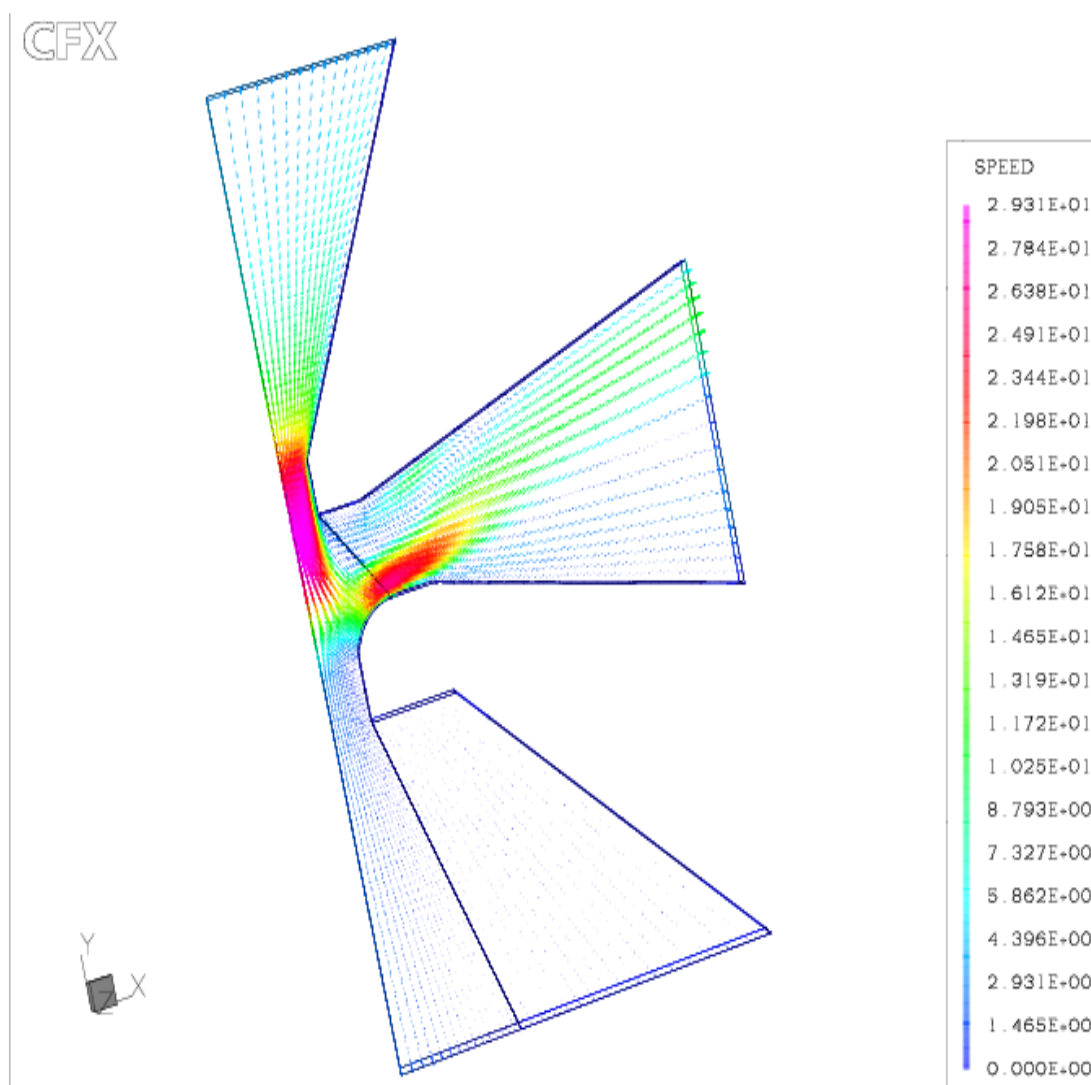
Fig. 32. Velocity vectors for the original prototype configuration.

V. D. Results and Discussion

Results of the simulations are categorized as follows. In Table V, under the head "CONFIGURATION", the nomenclature ORG is the computational model corresponding to the prototype design conceived at ATL. The simulation was carried out for a throat velocity of 25 m/s (corresponding to a Reynolds number of ~530) and for a major-to-minor flow split ratio of 90:10. The computational grid and velocity vectors corresponding to this configuration is presented in Figures 31 and 32.
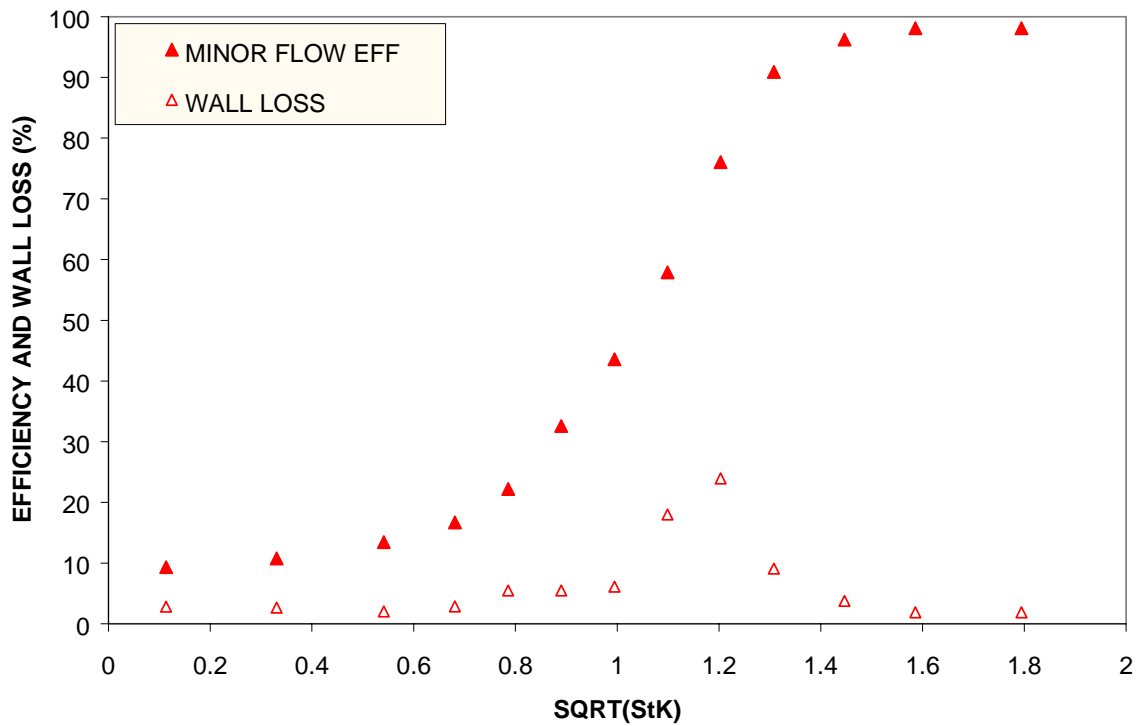
Fig. 33. Impactor efficiency and wall loss curves for the original prototype configuration (10% minor flow, throat velocity = 25 m/s).

The efficiency and wall loss curves for this case are presented in Figure 33. It can be seen from the figure that the SQRT $(StK)_{50}$ value for this case is of the order of 1.05. The wall losses, characteristically, peak near the cut point Stokes number. However, a closer look at the results indicate that the peak wall loss (~24%) occurred near the SQRT $(StK)_{50}$ value of 1.2, that corresponds to a minor flow efficiency of 76%. The next highest wall loss (~18%) occurred at an SQRT $(StK)_{50}$ value of 1.1, that corresponds to a minor flow efficiency of 58%. This uncharacteristic result indicated that there is some other phenomenon that caused the wall loss.
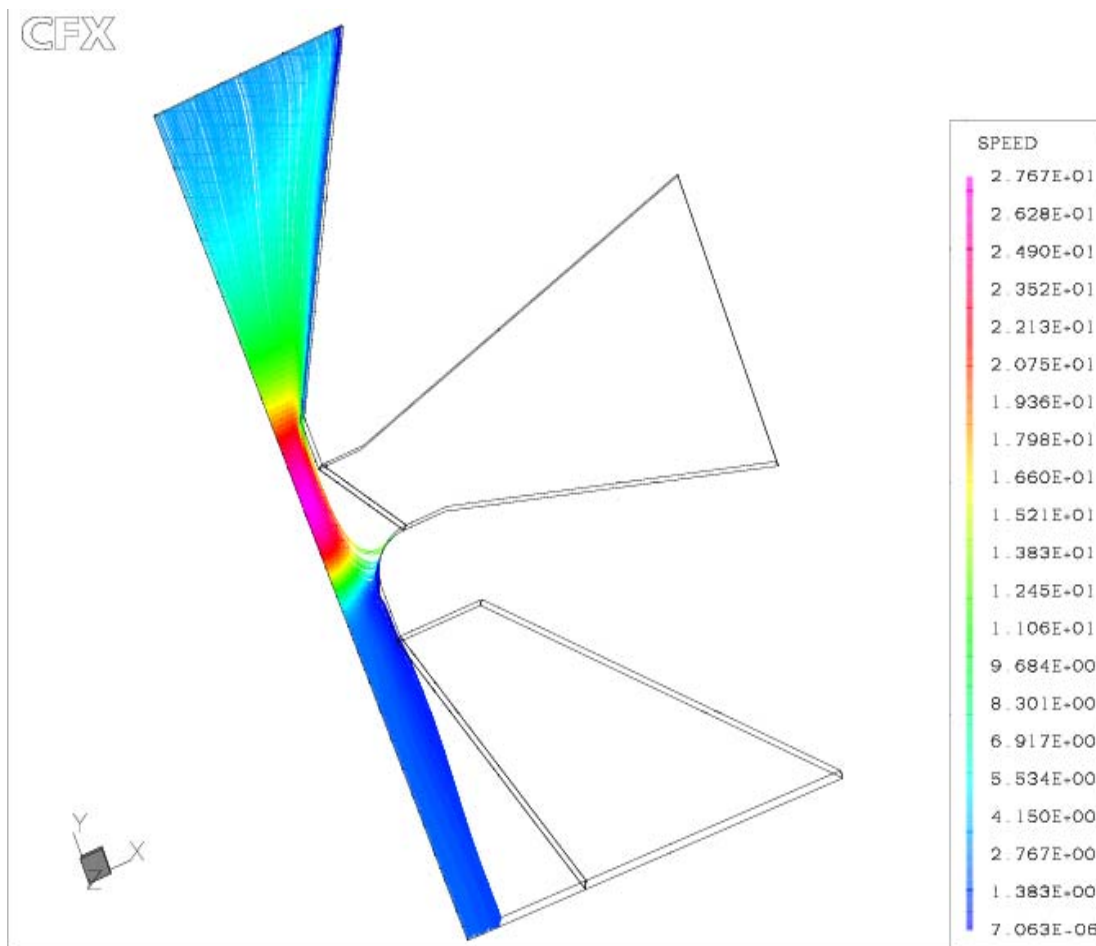
Fig. 34. Particle tracks for the peak wall loss case (1.65 μm AD particles).
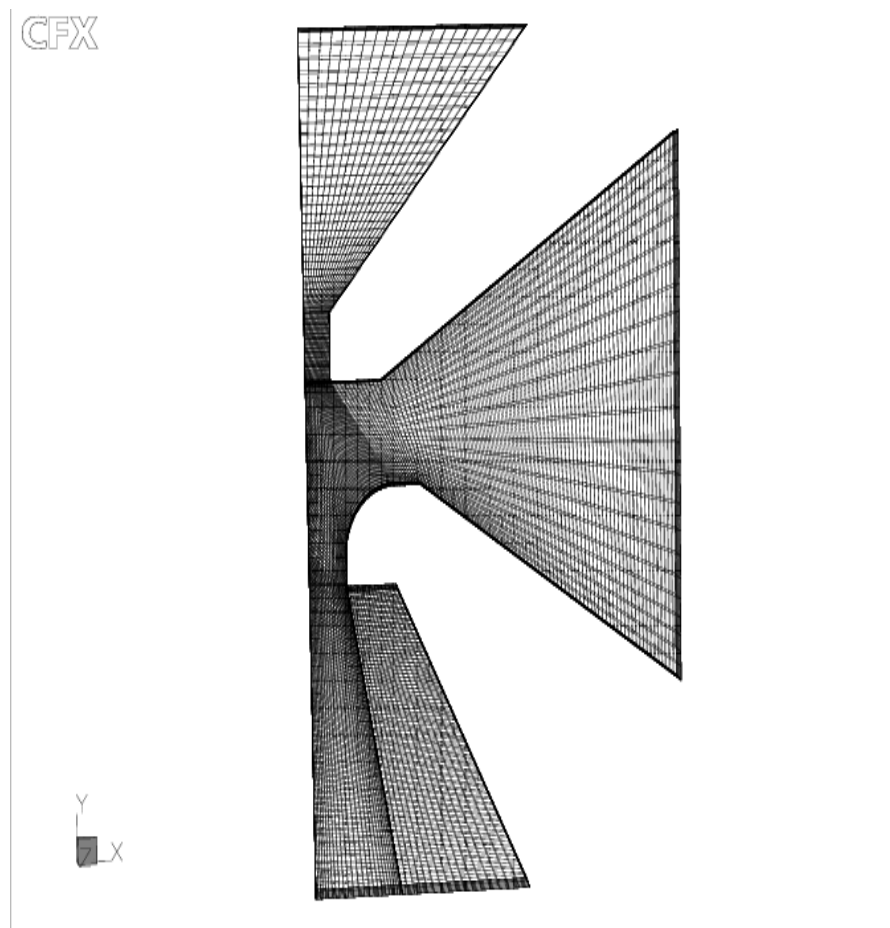
Fig. 35. Computational grid for the configuration MOD1A-T.

When the particle tracks for the particle size corresponding to the peak wall loss, presented in Figure 34, were visualized, it was found that except those particles that make into the minor flow, the rest of the particles impinge on the curvature in the receiving section. For particle sizes above the size corresponding to the peak loss value, almost all the particles made it to the minor flow. Also, for all particle sizes below the peak loss value (except the one immediately below), the wall loss was negligible. This suggested that at least for those two particle sizes, the particles were not able to negotiate the curvature, being not too heavy to acquire enough inertia to get past the breaking

streamlines into the minor flow, nor too light to be carried along the streamline into the major flow. Hence, it was decided that modifications to the prototype design were required to reduce the wall loss.
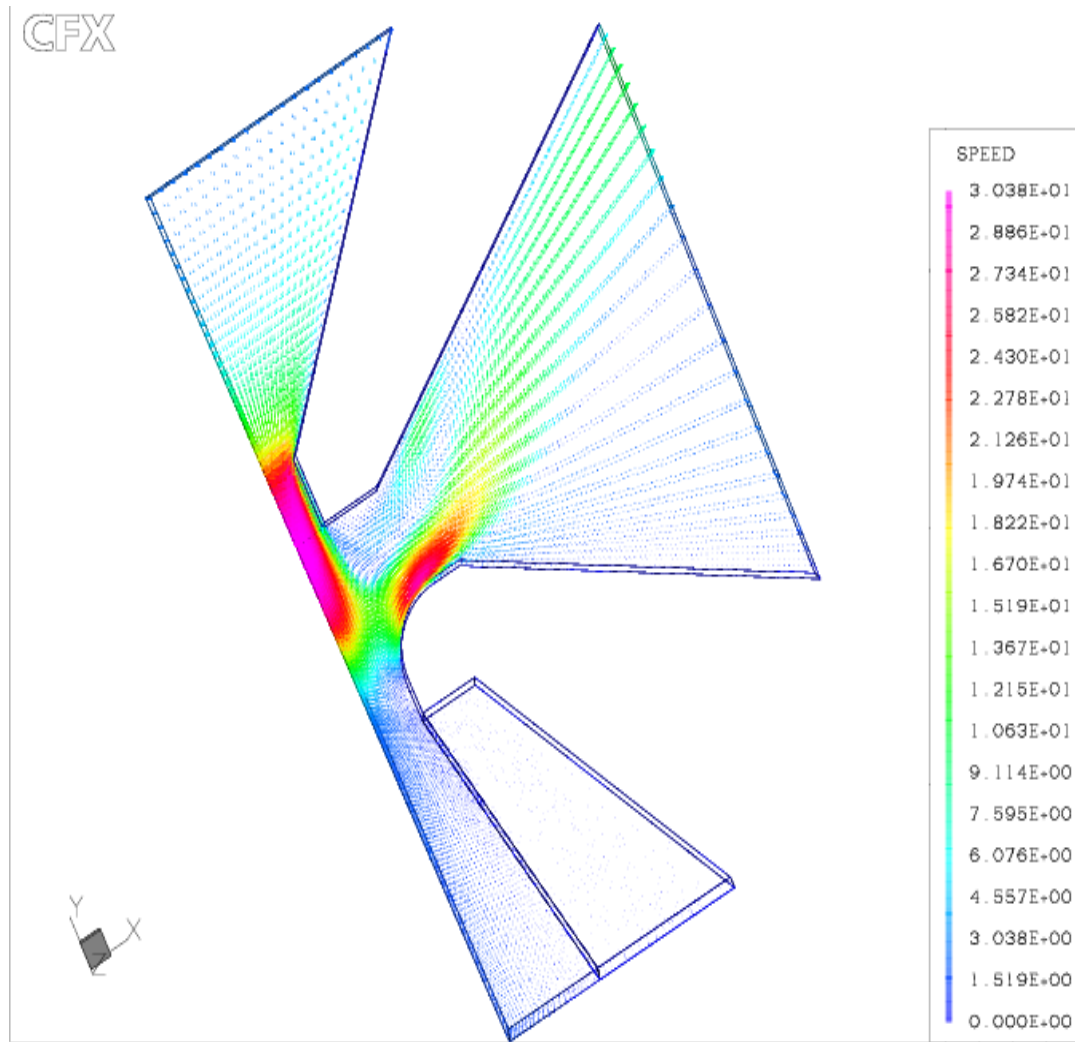
Fig. 36. Velocity vectors for the configuration MOD1A-T.

Taking suggestions from the literature, numerical investigations were performed on the prototype design on which different geometrical modifications were effected. The modifications, summarized in Table IV, are briefly reminded below:

(a) The angle θ_1 was increased to 45 and the other angles θ_2, θ_3, and θ_4 were modified.

(b) The separation distance, S, between the acceleration and receiver nozzles and the standoff distances SD1, SD2, and SD3 were modified.

The modified prototype is referred to in Tables IV and V as MOD1A-T. The simulation was carried out for a throat velocity of 25 m/s (Corresponding to a Reynolds number of ~508) and for a major-to-minor flow split ratio of 90:10. The important numerical aspects for this simulation are presented in Table V. The computational grid and velocity vectors for this case are presented in Figures 35 and 36.
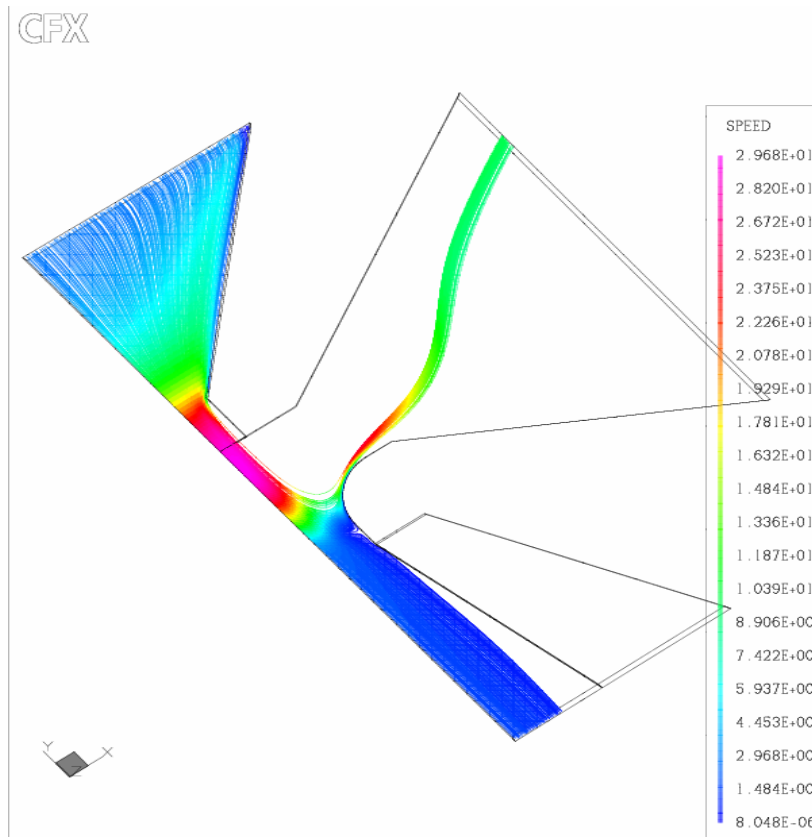
Fig. 37. Particle tracks for the peak wall loss Size (1.3 μm AD) for the configuration MOD1A-T (10% minor flow, throat velocity of 25 m/s).

Figure 37 presents the particle tracks for the particle size corresponding to the peak wall loss. The impactor efficiency and wall loss curves obtained for this case are presented in Figure 38, and, are compared against the results of the prototype design. The cutpoint SQRT $(StK)_{50}$ value is found to be 0.95 for this case, in comparison to 1.05 for the prototype. More importantly, the peak wall loss near the cut point stokes number has decreased considerably ($\sim$ 9%) and is even less for the other particle sizes. Moreover, it can also be seen that the efficiency curve is steeper that that of the prototype design.
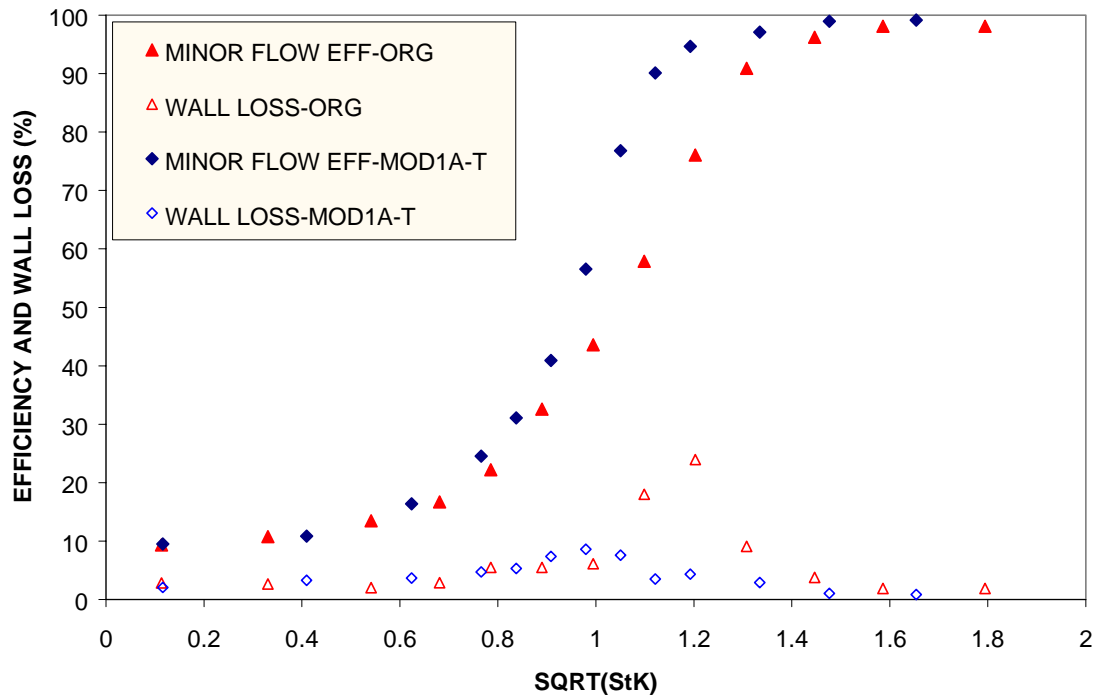
Fig. 38 Comparison of the efficiency and wall loss curves for configuration MOD1A-T against the original configuration (ORG) (10% minor flow, throat velocity = 25 m/s).

It seems that the modifications that were effected to the prototype geometry have been successful in that they have been able to reduce the wall losses. It is felt that among

other things, the effect of increasing the angle of convergence has had a profound effect. This effect, known as the "aerodynamic focussing effect" is well known to the impactor design community[25].
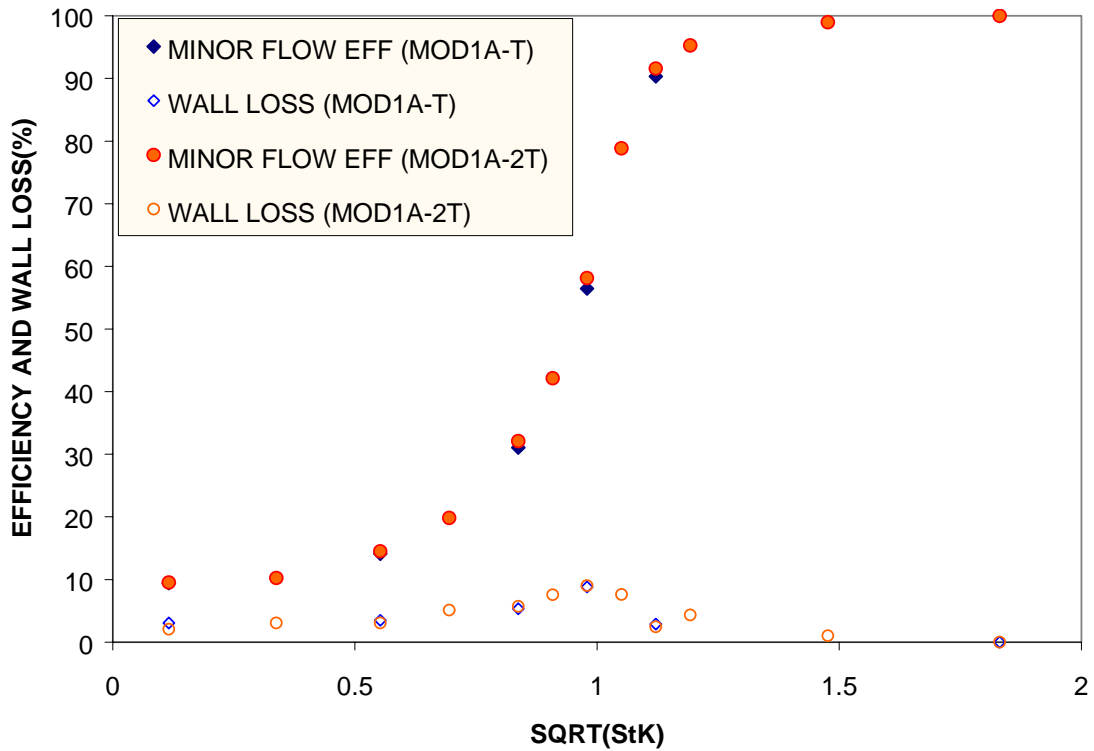
Fig. 39. Comparison of the efficiency and wall loss curves for configuration MOD1A-T against the configuration MOD1A-2T (10% minor flow, throat velocity = 25 m/s).

As can be seen from the particle tracks for the cases, the increased angle of convergence at the acceleration section results in keeping the particle trajectories away from the walls, focussing them more toward the axis of the throat section. This effect becomes more pronounced at higher stokes numbers (and higher efficiencies); facilitates

the heavier particle to get collected in the minor flow, by keeping them away from the bending fluid streamlines found in the vicinity of the wall.

The efficiency curve for this case (MOD1A-T) shifts to the left of original curve (ORG), and, is sharper than the original curve. Marple and Chien[29] observed this shift in the efficiency curve, in their computational study. Chen and Yeh[32], as they summarized their results and the experimental results of Loo and Cork[33], mentioned about this shift.

In the next study, the throat length of the receiver section was increased to twice its original value, keeping the other parameters constant. Simulations were repeated for the same conditions as the previous case. Important numerical aspects of this simulation are presented in Table V. Impactor efficiency and wall loss curves obtained for this case is compared against the previous results, in Figure 39. It can be seen from the figure that the results overlap, suggesting that increase in the throat length of the receiver section has negligible effect on the impactor performance.

Also, the particle tracks for the particle sizes corresponding to the lowest and the highest particle sizes in the impactor efficiency curves are presented in Figures 40 and 41. The "aerodynamic focussing effect" can be clearly discerned from the particle tracks for the heavier particle, Figure 41. The particle tracks are well focussed as a thin sheet toward the axis of the impactor, and, are far removed from the impactor walls.

In the next study, the presence/absence of the section SD3 was investigated, keeping the rest of the geometry the same. The geometrical details of this configuration are presented in Table IV and the numerical details are presented in Table V. The simulation was carried out for a throat velocity of 25 m/s (Corresponding to a Reynolds

number of ~508) and for a major-to-minor flow split ratio of 90:10. The study was first performed on a coarse mesh (MOD1B-C) and was repeated on a fine mesh (MOD1B-F), which had twice the number of cells as the coarse mesh.
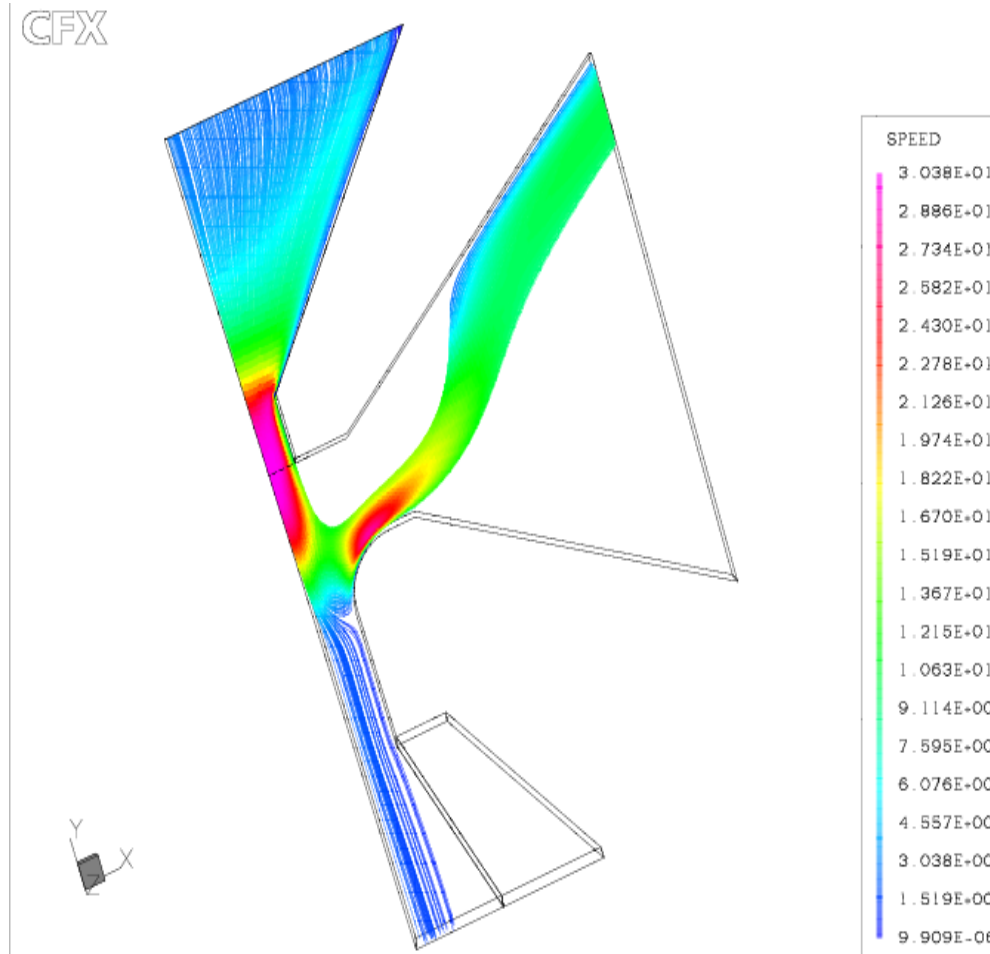
Fig. 40. Particle tracks for the lowest particle size (0.1 μm AD) for the configuration MOD1A-2T (10% minor flow).

Figure 42 presents the impactor efficiency and wall loss curves for the coarse and fine meshes. It can be seen from the figure that though the efficiency curves for the coarse and fine meshes are not very different, the peak wall loss (near the cut point) for the coarse mesh is higher (~19%) compared to the fine mesh (~9%). It seems that as the

mesh gets finer, the flow field gets resolved better and the particle is tracked more closely, and, in a smaller control volume. As a result, the wall loss decreases and the efficiency curve gets a little sharper. It seems that this is the main reason why computational results reported in the literature, predict a very high wall loss value. For our case, it is our opinion that ~60000 cells are required to get proper wall lass predictions.
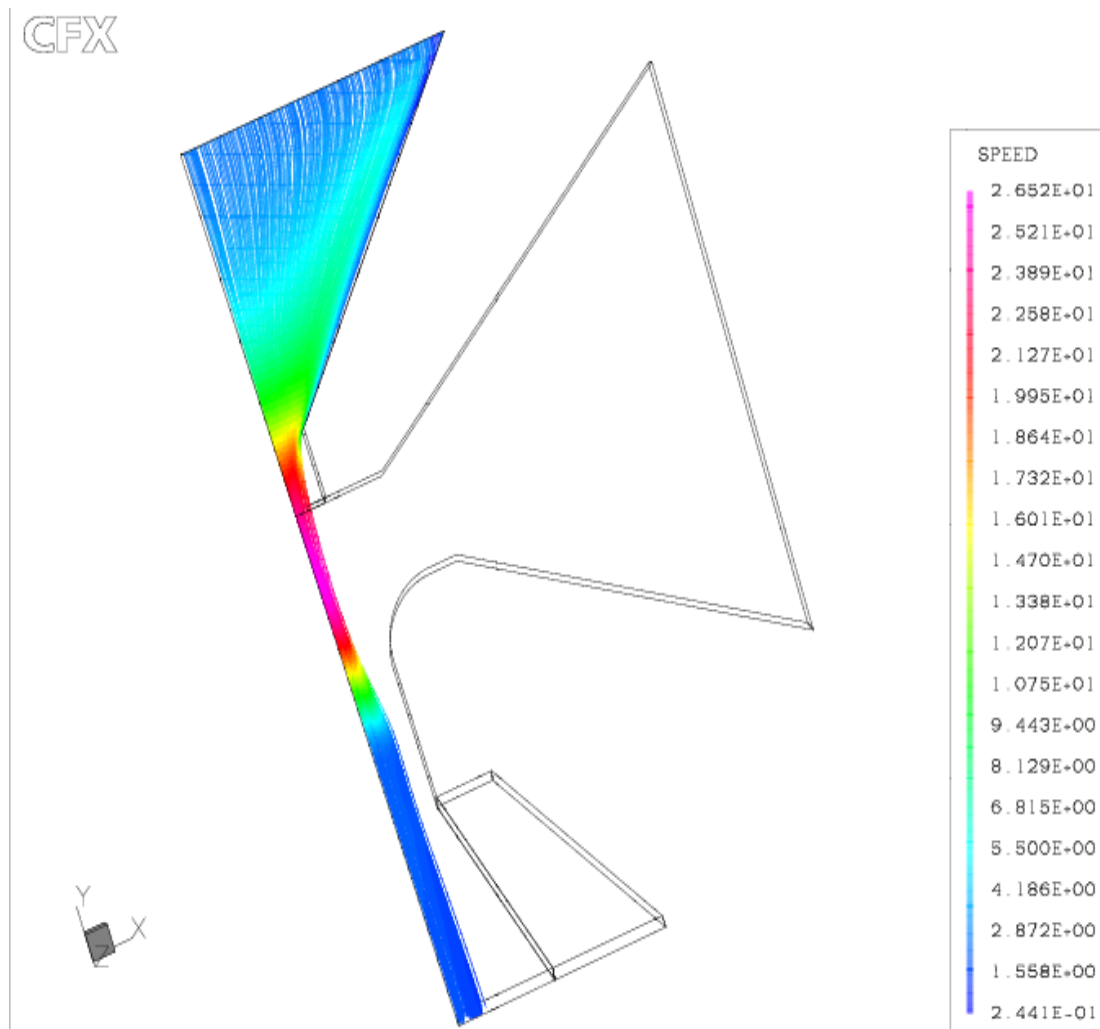
Fig. 41. Particle tracks for the highest particle size (2.5 µm AD) for the configuration MOD1A-2T (10% minor flow).
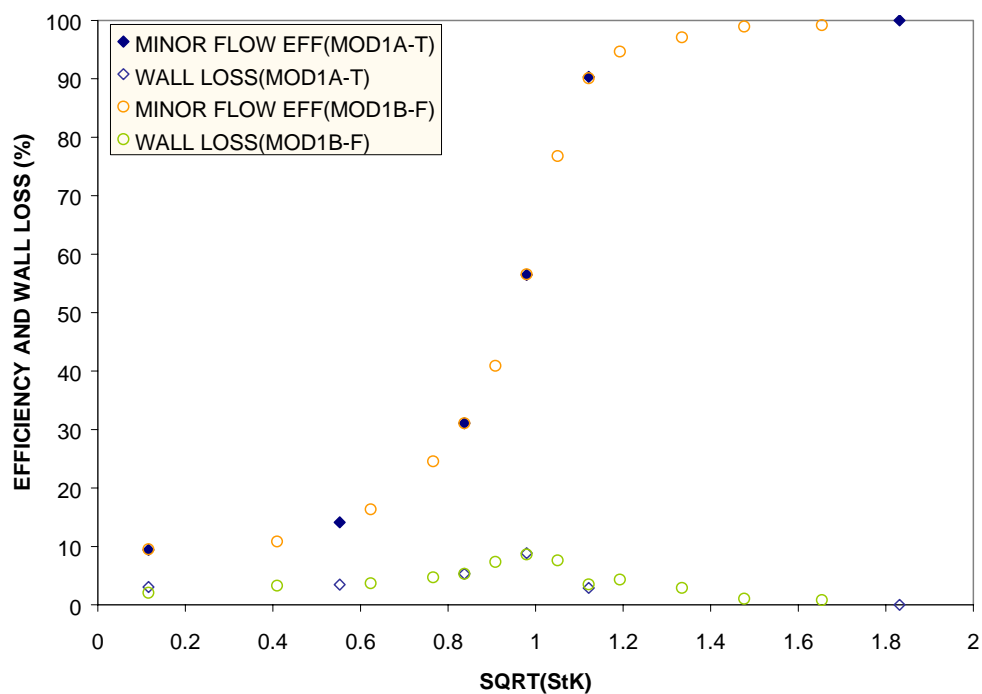
Fig. 42. Comparison of the efficiency and wall loss curves for configuration MOD1B-C against the configuration MOD1B-F (10% minor flow, throat velocity = 25 m/s).
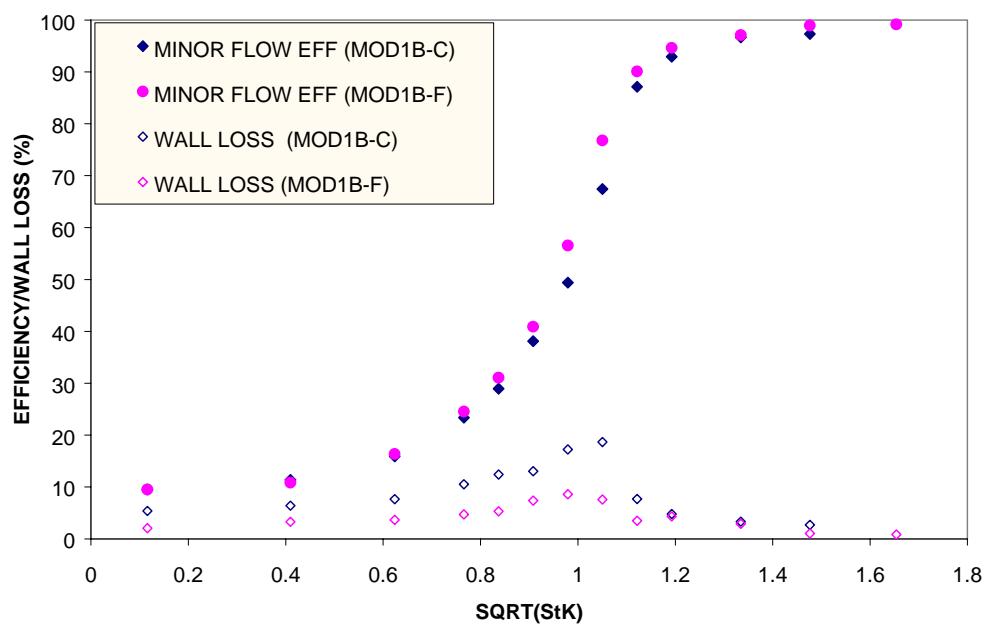
Fig. 43. Comparison of the efficiency and wall loss curves for configuration MOD1B-F against the configuration MOD1A-T (10% minor flow, throat velocity = 25 m/s).

Figure 43 compares the results of the fine mesh (MOD1B-F) against the previous result, where section SD3 was present. It can be seen form the figure that the results overlap each other suggesting that the presence/absence of the section is not important from the viewpoint of impactor performance. It seems that this particular region lies outside the domain where the separation phenomenon takes place; hence, it has no influence on the performance characteristics. This geometrical configuration was taken as the base configuration, as, from the computational viewpoint, the number of cells required is less. Further studies on the influence of major-to-minor flow split ratio and operation at different throat velocities (Reynolds numbers) were carried out on this configuration. The results of these studies are presented below.
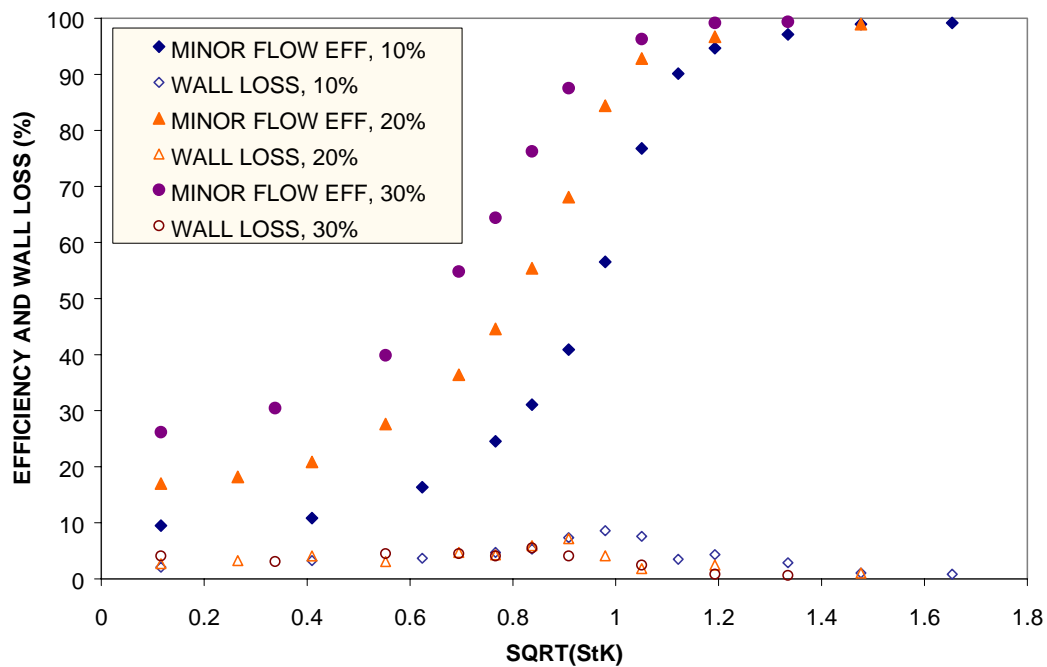
Fig. 44. Comparison of the impactor efficiency and wall loss curves for configuration MOD1B-F for different major-to-minor flow split ratio (throat velocity = 25 m/s).

Figure 44 compares the efficiency and wall loss curves for three different major-to-minor flow split ratios, for the base case, at a Reynolds number of 508. It can be seen from the figure that the curves start moving to the left as the major-to-minor flow split ratio decreases. Also, there is a gradual reduction in the SQRT $(StK)_{50}$ cut point value as well as the peak wall loss corresponding to the cut off SQRT $(StK)_{50}$. These observations are consistent with the experimental and numerical results presented elsewhere in the literature. The values of SQRT $(StK)_{50}$ and peak wall loss with the change in the major-to-minor flow split ratio are summarized in Table VI.

TABLE VI

Summary of the Predicted Cutpoint Stokes Number and Peak Wall Loss for Different Major-to-Minor Flow Split Ratios for the Base Configuration at Re=508

MAJOR-TO-MINOR FLOW SPLIT RATIO	CUT POINT STOKES NUMBER	PEAK WALL LOSS (%)
90-10	0.94	8.6
80-20	0.8	7.2
70-30	0.64	5.5

Figure 45 presents the effect of the throat velocity on the impactor performance for a 90:10 major-to-minor flow split ratio. As can be seen from the figure, the efficiency curve gets sharper with increasing throat velocity. The 50% cut point diameter value decreases rapidly from 2.6 μm AD (at a V_t~5m/s) to about 1.25 μm AD (at V_t~25m/s). As throat velocity is further increased to values of 50m/s and 100m/s, the corresponding cut point value decreased to 0.85 μm AD and 0.65 μm AD, respectively.
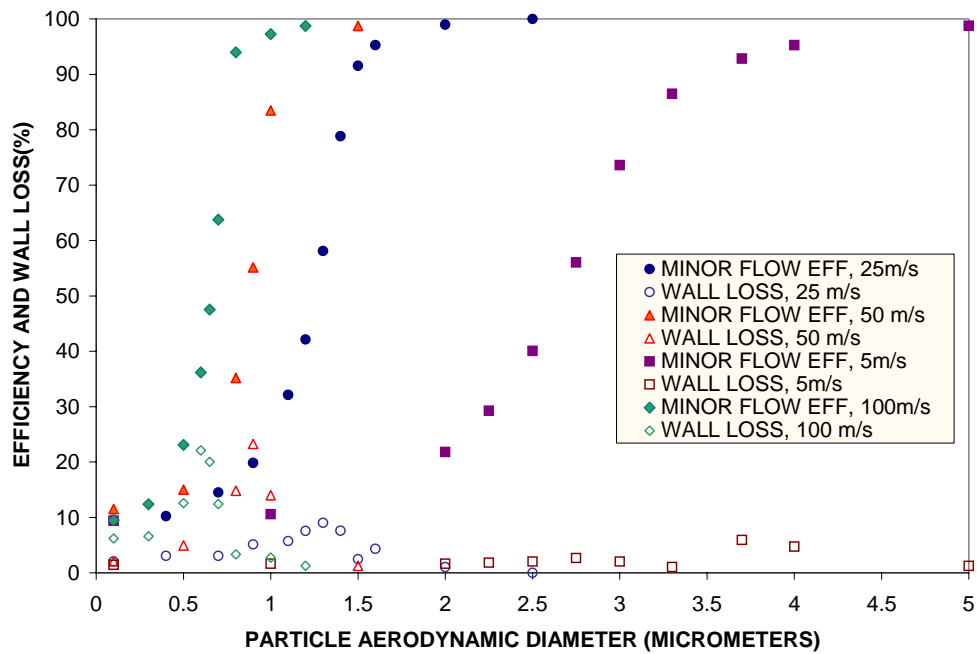
Fig. 45. Comparison of the impactor efficiency and wall loss curves for configuration MOD1B-F for operation at different throat velocities (in terms of particle size).
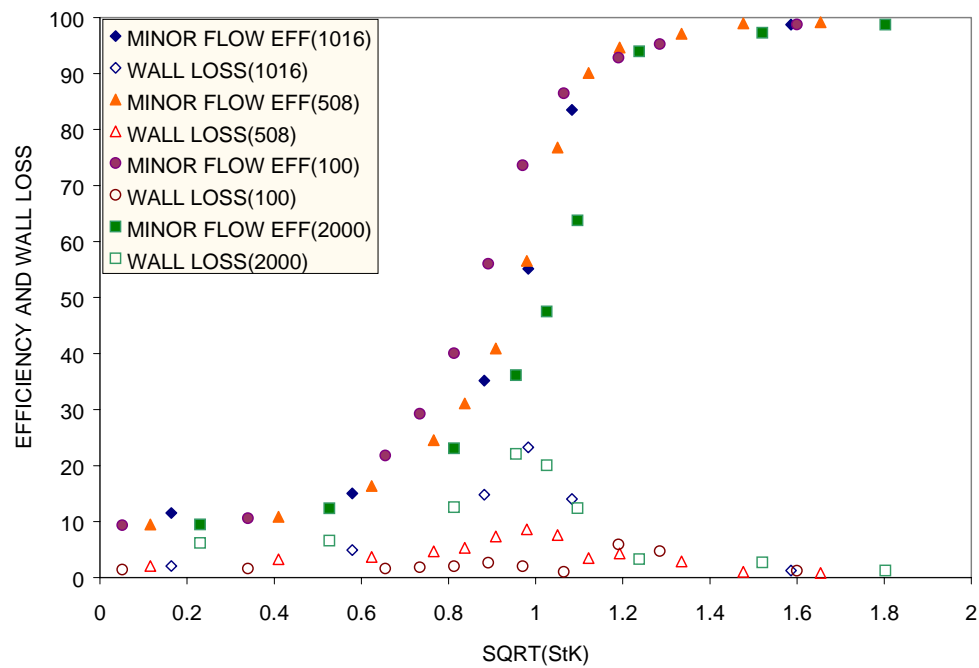
Fig. 46. Comparison of the impactor efficiency and wall loss curves for configuration MOD1B-F for operation at different Reynolds numbers (in terms of Stokes number).

Figure 46 presents the same curve, now expressed in terms of the non-dimensionalized SQRT (StK), instead of the actual particle size. It can be seen that the minor efficiency curves for all the four Reynolds numbers overlap in the head and tail region. However, in the mid-efficiency range (15%-90%), the curve for Re=100 lies slightly to the left, the curves for Re=500 and Re=1000 overlap, and, the curve for Re=2000 lies slightly to the right of the overlapping curves.

In the case of real impactor, it is well known that the efficiency curves are a function of the Reynolds number (throat velocity). The present observation indicates a behavior that is contrary to the real impactor case. In this respect, unlike the real impactors, it seems that the virtual impactor efficiency curve is unique for a particular combination of geometrical parameters and independent of Reynolds number, when expressed in the non-dimensionalized form. Also, the difference between the curves that is observed in the mid-efficiency range is a reflection of the fact that in the mid-efficiency range the wall loss for the different Reynolds numbers is different.

From the viewpoint of wall losses, it is seen that the peak wall loss was ~23% for Re=1000, ~22% for Re=2000, and, ~9% for Re=500. However, in the case of Re=100, after attaining a peak in wall loss of ~3%, near the cut-off diameter value, the wall loss curve exhibits a secondary peak (~6%) in the particle size range of 4 μm AD. The particle tracks for this case are presented in Figure 47. When the particle tracks were visualized for this case, it was found that few of the particles were not able to surmount the curvature and get deposited on the curvature region. Again, for the next higher particle size (5 μm AD), wall loss decreased as the particles made into the minor flow.
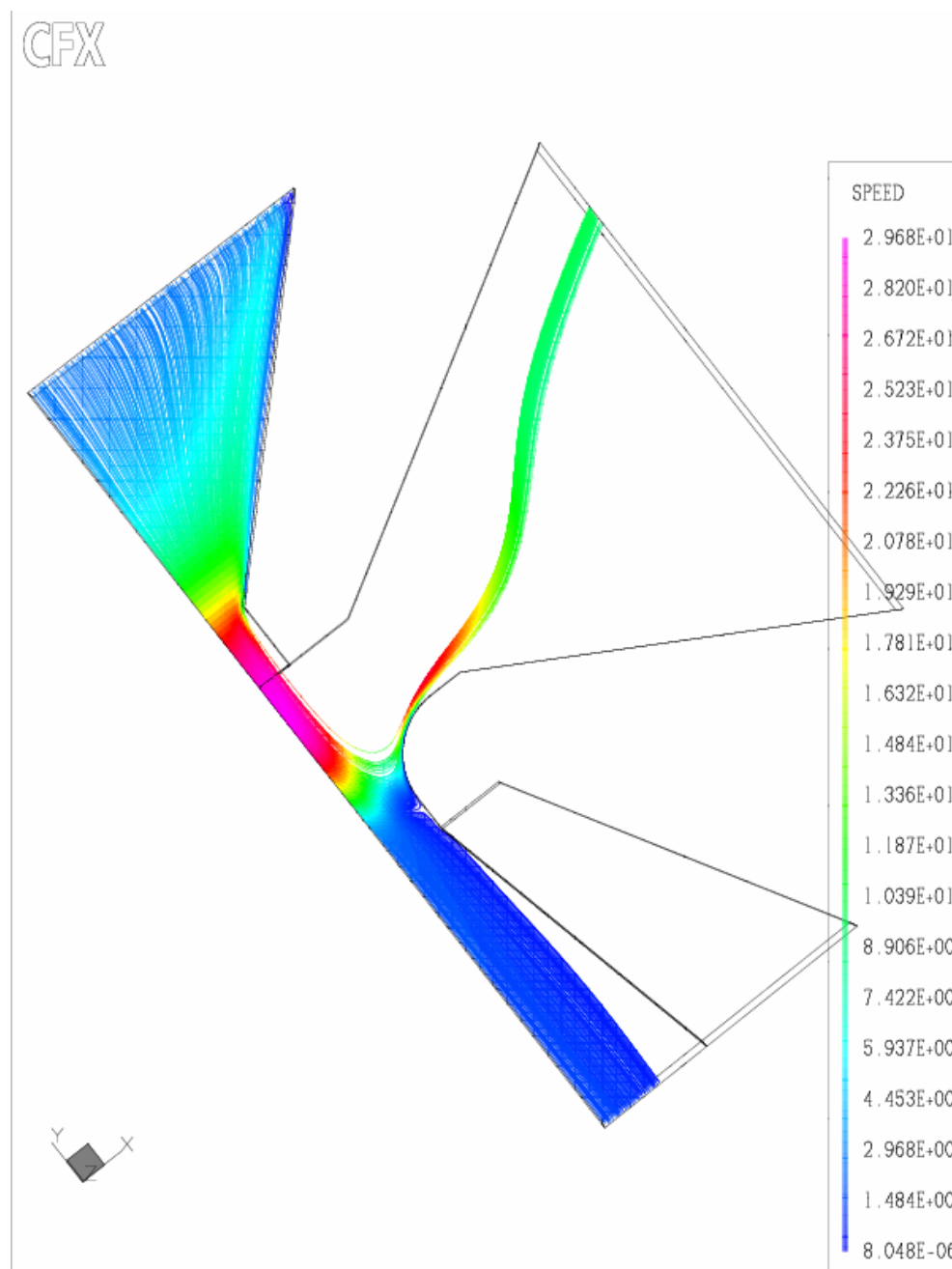
Fig. 47. Particle tracks for the secondary peak wall loss size (3.7 μm AD) for the configuration MOD1B-F (Re = 100, 10% minor flow).
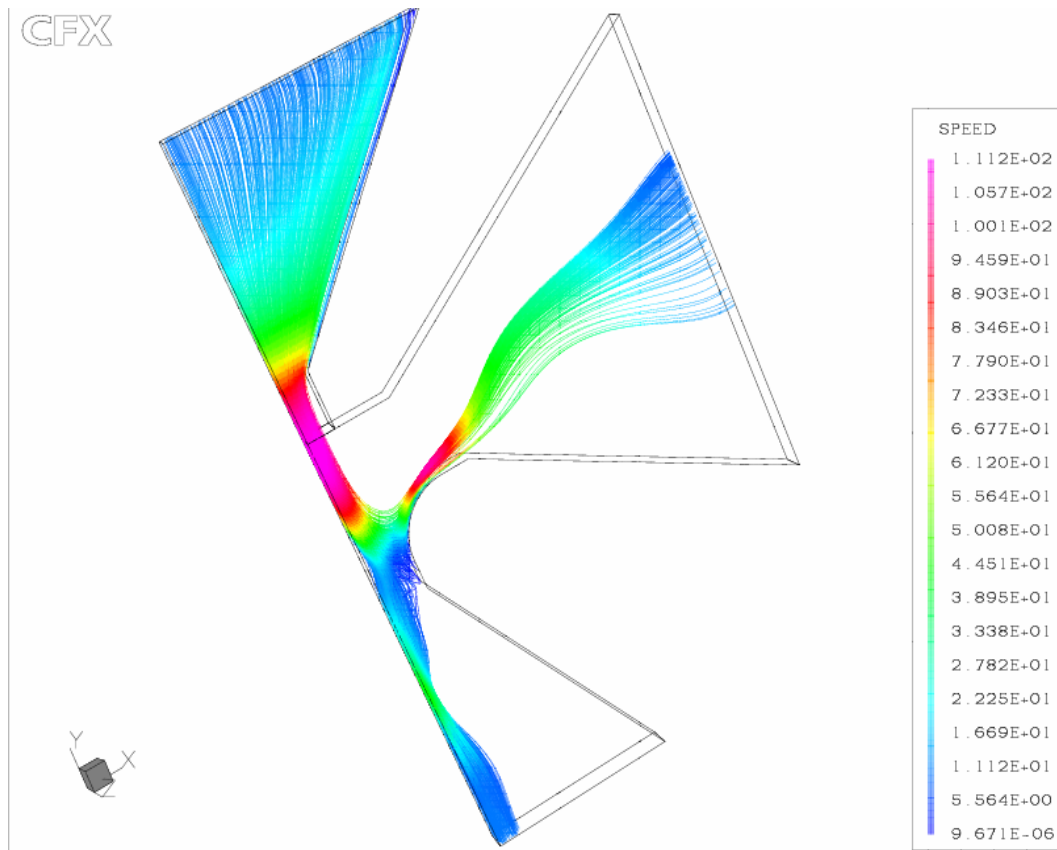
Fig. 48. Particle tracks for the peak wall loss size (0.6 μm AD) for the configuration MOD1B-F (Re = 2000, 10% minor flow).

For the Re=2000 case, it was interesting to note that the peak wall loss occurs even before the SQRT $(StK)_{50}$ value was reached, at a minor flow efficiency of ~40%. This abnormal behavior prompted a closer look at the flow and particle behavior for this case. Figures 48 and 49 present the particle tracks and the streamline plots for this case. It can be seen that strong recirculation zones are setup in the major and minor flow nozzles, as the throat velocity is very high for this case. This seems to be the main reason for the anomalous trend noticed for this case. Table VII summarizes the results of the study.
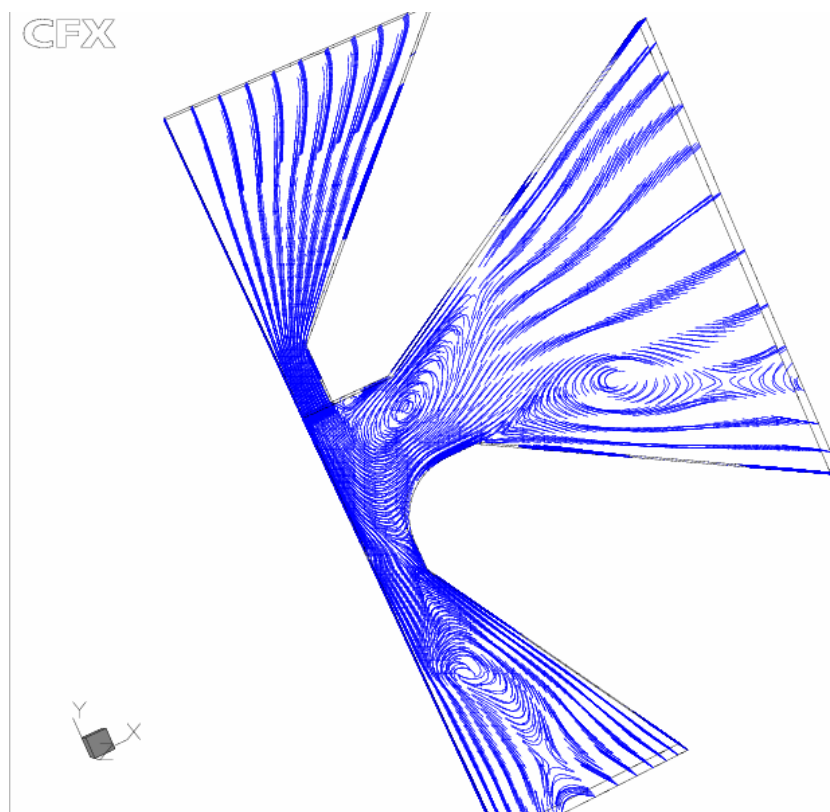
Fig. 49. Flow streamlines for the configuration MOD1B-F
(Re =2000, 10% minor flow).

TABLE VII

Summary of the Predicted Cutpoint Stokes Number and Peak Wall Loss for Different
Reynolds Numbers for the Base Configuration

REYNOLDS NUMBER	CUT POINT STOKES NUMBER	CUT POINT PARTICLE SIZE(μm)	PEAK WALL LOSS (%)
100	0.85	2.65	6.0
500	0.95	1.25	8.6
1000	0.95	0.85	23.25
2000	1.03	0.65	22.1

In the final part of the study, the effect of different radii of curvature of the receiver nozzle, on the impactor performance was investigated. Two different radii of curvature values were chosen (and the corresponding stand-off distances SD1 and SD2 were also modified) for the investigation. The configurations are referred to as MOD2 and MOD3. The investigation was conducted for a throat velocity of 25 m/s (Re=508) and a major-to-minor flow split ratio of 90:10. The details of the geometrical configuration are presented in Table IV and the numerical information is presented in Table V.
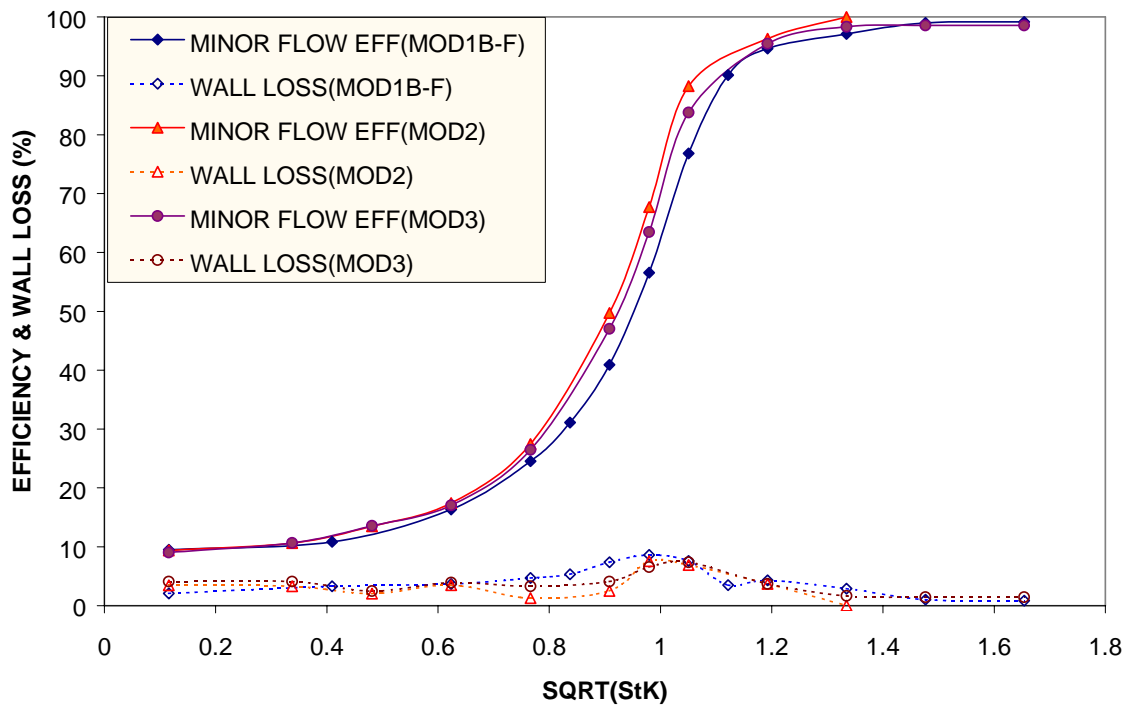
Fig. 50. Comparison of the impactor efficiency and wall loss curves for different radii of curvature
(Configurations MOD1B-F, MOD2 and MOD3, 10% minor flow, Re=508).

The impactor efficiency and wall loss curves generated from the simulations are compared against the results of the base configuration, MOD1B-F(R=W), in Figure 50. It can be seen that as the radius of curvature decreases, the efficiency curve starts getting sharper and the SQRT $(StK)_{50}$ decreases. As the radius of curvature decreases from R=W to R=0.315W, there is a perceptible change in the SQRT $(StK)_{50}$ value; however, in going from R=0.315W to R=0.16W, the change is minimal. Interestingly, the tail in the high efficiency end of the efficiency curve disappears, as the radius decreases from R=0.315W to R=0.16W. In other words, it seems that decrease in the radius facilitates collection of the heavier particles in the minor flow.

This prediction is consistent with the experimental observation of Chen and Yeh[6] and the recommendations of Loo and Cork[7]. Also, the peak wall loss corresponding to the cut-off SQRT $(StK)_{50}$ value is ~9% for the base case and ~7.5% for the reduced curvature cases and the wall loss at other particle sizes are lesser. It seems that a smaller radius of curvature (that is limited by machining considerations) would be desired to minimize wall losses. The results of this study are summarized in Table VIII

TABLE VIII

Summary of the Predicted Cutpoint Stokes Number and Peak Wall Loss for Different Curvature Ratios (Re=508)

CURVATURE RATIO	CUT POINT STOKES NUMBER	CUT POINT PARTICLE SIZE(μm)	PEAK WALL LOSS (%)
R=W	0.95	2.65	8.6
R=0.315W	0.92	1.24	7.4
R=0.16W	0.91	1.225	7.6

V. E. Conclusions

The performance of a prototype virtual impactor design, conceived at the Aerosol Technology Laboratory (ATL), was analyzed using CFD methods. Based on design suggestions from the literature, effect of various geometrical modifications was investigated on the prototype design and its performance was optimized. The optimized design was taken as the base design and its performance characteristics for different major-to-minor flow split ratios, and, for operation at a range of Reynolds numbers were generated. Also, the effect of the radius of curvature of the receiving section on the impactor performance was investigated. Performance characteristics of the impactor were determined for three different radii of curvature values.

CHAPTER VI

SIMULATIONS ON THE LINEAR SLOT VIRTUAL IMPACTOR

In this chapter, details of the numerical simulations conducted on a linear slot virtual impactor (LSVI), fabricated based on the results of the optimization study are presented. The performance of the virtual impactor was experimentally evaluated at the Aerosol Technology Laboratory (ATL). Detailed information pertaining to the fabrication and experimentation on the LSVI are available elsewhere[41].

Simulations were first performed on a preliminary model constructed with the important geometrical dimensions. Later, additional geometrical information was incorporated and the model was refined. Simulations were performed on the refined model and the impactor efficiency and wall loss curves were generated. Sensitivity studies were performed on the refined model to investigate the effect of the depth of the inlet section on the prediction of the efficiency curve and the results are presented. Finally, the simulation predictions of the efficiency/wall-loss curves are compared against experimental data and the results are presented.

VI. A. Schematic of the Linear Slot Virtual Impactor

Detailed information on the measurement of critical geometrical dimensions of importance, from the viewpoint of impactor performance, is available in reference 41. The schematic of the LSVI simulated remained similar to the one shown is Figures 27/28. However, measurements indicated that there were offsets, both in the horizontal and vertical planes, compared to the symmetric, one-half section schematic presented in Figure 28. In addition, there was a small radius of curvature on the throat section of the

accelerating nozzle. These details were taken into consideration when the new geometry

was constructed for the simulations.

TABLE IX

Summary of the Geometrical Parameters of the LSVI
(In thousandths of an inch)

Parameter	Nominal Value (Ideal)	Average Value	Worst Case Value
W1	12.76	12.76	**12.76**
W2	19.14	18.90	**18.80**
S	19.14	19.14	**19.14**
T1	12.76	8.01	**7.51**
T2	19.14	23.62	**24.44**
SD1	12.76	5.73	**4.66**
SD2	19.14	17.22	**17.22**
SD3	0	22.33	**22.0**
R1	0	1.14	**1.55**
R2	0	9.50	**9.80**
T1'	12.76	9.73	**9.62**
T2'	19.14	21.96	**21.13**
SD1'	12.76	6.05	**6.49**
SD2'	19.14	15.83	**14.86**
SD3'	0	22.45	**22.71**
R1'	0	1.44	**1.53**
R2'	0	8.16	**9.19**
$\delta1, \delta2$	0	0.26	**0.36**
θ_1, θ_1'	45	45	**45**
θ_2, θ_2'	30	30	**30**
θ_3, θ_3'	30	30	**30**
θ_4, θ_4'	30	30	**30**

Table IX summarizes the important geometric details supplied for performing the

simulations. To be consistent with Figure 28, the geometrical details pertaining to the

other half of the impactor were denoted by primed quantities in Table IX. For each

parameter, the nominal (ideal), average, and the worst case value of the measurement is

presented. The various parameters for construction of the geometry were so chosen that

the chosen combination would represent the worst case scenario, from the viewpoint of performance. By worst case scenario, it is meant that constructed geometry included all possible combinations of asymmetry on both the planes. The chosen value of each parameter for constructed geometry is highlighted in the table.

For sake of clarity, it is reminded here again that

(a) the accelerator nozzle had a small curvature, and

(b) the impactor geometry was mis-aligned on both the horizontal and vertical axes.

It can be seen from Figure 28 that these two features were absent and were not considered in the optimization study. So, to account for these features, four new parameters R1, R2, δ1 and δ2 are introduced in this chapter. While the parameter R2 (previously R) refers to the radius of curvature of the receiving section of the nozzle, the parameter R1 represents the radius of curvature of the accelerator nozzle. Counterparts of the above parameters on the other half of the impactor are represented by primes, as explained earlier. Parameters δ1 and δ2 refer to the misalignment in the horizontal and vertical axis respectively. It can be seen from Table IX that most of the geometric parameters of importance have been taken care, at the time of fabrication, to be precise enough to follow the suggestion presented in references 32 and 33, and, to the conclusions that were arrived at in the optimization study. However, due to practical limitations, some of the parameters are found to be not conforming to the recommendations.

113

INLET B.C.

56.13

45° **45°**

1.53 **9.62** **12.76** **7.51** **1.55**

30° **6.49** **4.66** **30°**

0.36

19.14 **19.14**

P
R
E
S
S
U
R
E

B
C

38.33

P
R
E
S
S
U
R
E

B
C

43.09

30° **14.86** **17.72** **30°**

9.19 **21.13** **0.36** **9.8**

22.71 **18.8** **24.44** **22.00**

30° **30°**

78.34

MASS FLOW B.C.

NOTE:
Values presented are thousandth's of an inch
Figure not to scale

Fig.51. Two-dimensional schematic of the LSVI preliminary model.

Figure 51 presents a two dimensional schematic of the impactor geometry with the critical geometrical dimensions. The width at the throat section of the impactor was 3.24104E-04 m and the length of the impactor (normal to the page) was 0.0889 m. The nominal operational flow rate of the impactor was 80 SCFH. Based on the above values, the following calculations can be done:

(a) The average fluid velocity at the throat section of the impactor is 21.84 m/s.

(b) The ratio L/W is approximately 275.

VI. B. Grid Information and Boundary Conditions

The exact physical geometry corresponding to each of the configurations was constructed in the CFX 4.4 pre-processor and a block-structured (comprising 11 blocks), body-fitted grid system was generated over the domain. The code's mesh generation algorithm generated an optimized mesh over the domain, for each configuration. The boundary conditions are explained with reference to the schematic in Figure 51.

Uniform normal velocity condition was prescribed at the inlet plane. As the L/W ratio is high, the flow field can be assumed to be two-dimensional. Unit width was prescribed in the third dimension (normal to the page) and symmetric (mirror) boundary conditions were assigned. Mass flow boundary condition was assigned to the minor flow outlet as the major-to-minor flow split ratio determines the percent of the inlet flow that ends up as the minor flow. Pressure boundary conditions with zero reference pressure were specified at the major flow outlets. The rest of the surfaces were automatically treated as wall boundaries with zero slip velocity conditions.

TABLE X

Details of the Numerical Simulation for the LSVI

CONFIGURATION		DIFFERENCING SCHEME		URF		SOLUTION ALGORITHM		# OF CELLS
		v	p	v	p	v	p	
PRELIMINARY (COARSE)		HDS	CDS	0.65	1.0	STONE3D	ICCG	17860
PRELIMINARY (FINE)		HDS	CDS	0.65	1.0	STONE3D	ICCG	25775
REFINED (RITW9.1)		HDS	CDS	0.65	1.0	BLOCK STONE	ICCG	26610
RITW15.25	COARSE	HDS	CDS	0.65	1.0	STONE3D	ICCG	11652
	MEDIUM	HDS	CDS	0.65	1.0	STONE3D	ICCG	19012
	FINE	HDS	CDS	0.65	1.0	STONE3D	ICCG	37960
RITW19.27		HDS	CDS	0.65	1.0	STONE3D	ICCG	37632
RITW25.56	MB1	HDS	CDS	0.65	1.0	STONE3D	ICCG	59184
	MB2	HDS	CDS	0.65	1.0	STONE3D	ICCG	48864
	SB	HDS	CDS	0.65	1.0	STONE3D	ICCG	38784

V1. C. Results and Discussion

Details regarding the characterization of the virtual impactor performance and the generation of the performance curve for the impactor were already explained in the previous chapter and are not repeated here. As explained already, the first study was performed on a preliminary model. More geometrical information was included in the next simulation and this model is referred to as the refined model Subsequent studies were performed on the refined model. More information on the exact geometry used in each simulation would be provided when the results of the simulation are presented. The important numerical details regarding these simulations are summarized in Table X.

VI. C. 1. Preliminary and Refined Models: A Comparison

In the preliminary model, the ratio of the width of the inlet section to the throat was approximately 4.5 and the ratio of the width of the minor flow outlet to the throat was approximately 6.25. These details can be inferred from Figure 51. Studies were performed, first with a coarse mesh and then with a fine mesh, in the throat region. The impactor efficiency and wall loss curves obtained for both the coarse and fine mesh cases are presented in Figure 52.

It can be seen from the figure that the two curves overlap, suggesting that the results are mesh independent. The predicted cutpoint SQRT (StK)$_{50}$ value is of the order of 0.87 and the peak wall loss is of the order of 3.25% for both the mesh configurations. Moreover, the wall loss spectrum displays a peculiarly low value for the whole range of stokes numbers (particle sizes) simulated in this study. This suggested that further investigations needed to be undertaken with an improved model that included more

geometrical information, to verify these results. To this effect, a refined model was constructed. Details on the construction of the refined model and the studies performed on the refined model are presented in the next paragraph.
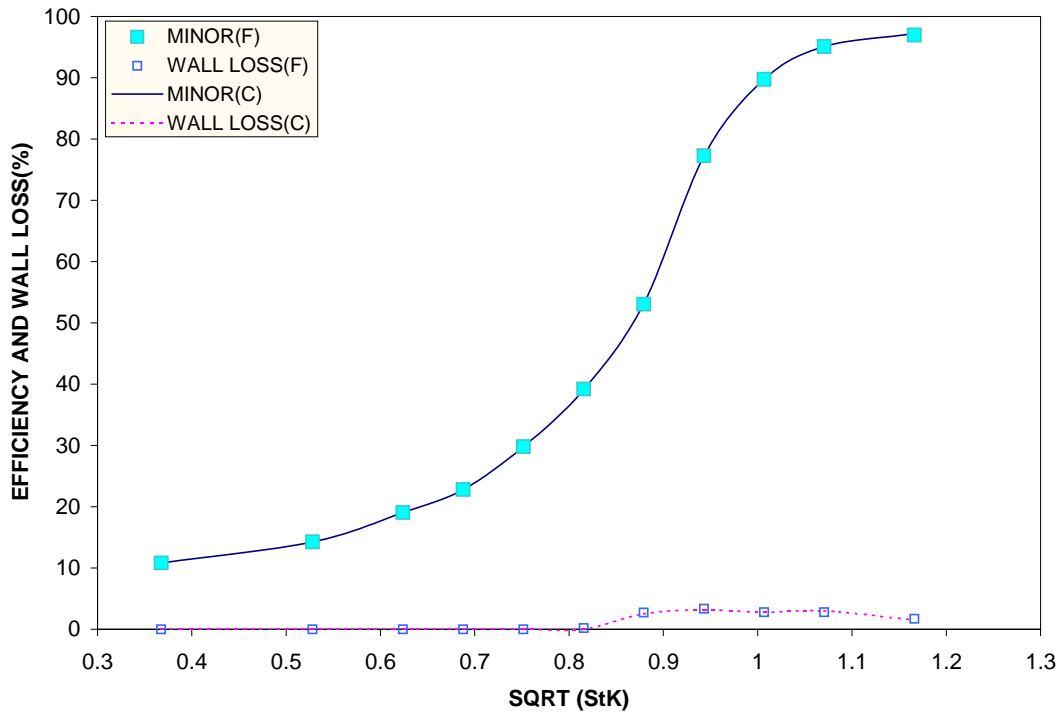
Fig.52. Comparison of the impactor efficiency and wall loss curves for the preliminary LSVI model for the coarse and fine mesh.

A schematic of the refined model is presented in Figure 53. It can be seen on comparing the present schematic with Figure 49 that the depths of all the sections have been increased. In particular, the ratio of the widths of the inlet section and the minor flow outlet section to the throat are now approximately 9. Also, the major flow outlets have been increased by 40% compared to the previous model. Simulations were performed on this geometrical model, keeping all the other conditions same as before. Important numerical details of the simulation are presented in Table X.

Fig. 53. Two-dimensional schematic of the refined LSVI model.
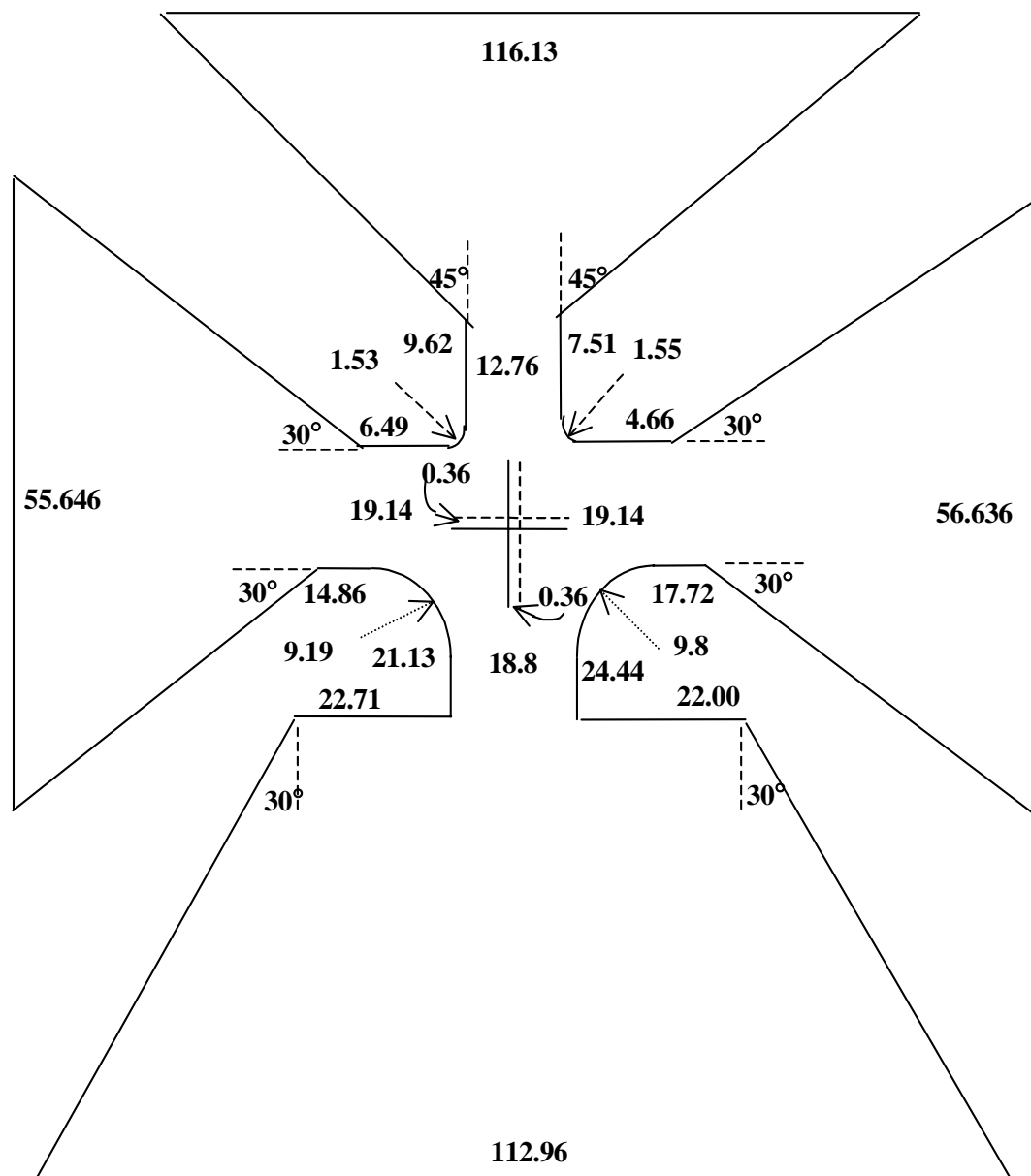
NOTE:
(a) Dimensions are in thousandth's of an inch
(b) Dimensions not to scale

The impactor efficiency and wall loss curves obtained from the results of the simulation are presented in Figure 54. The results of the previous model are presented alongside for comparison. The alphabet within the parentheses of the legend indicates that R is the refined model and P is the preliminary model.
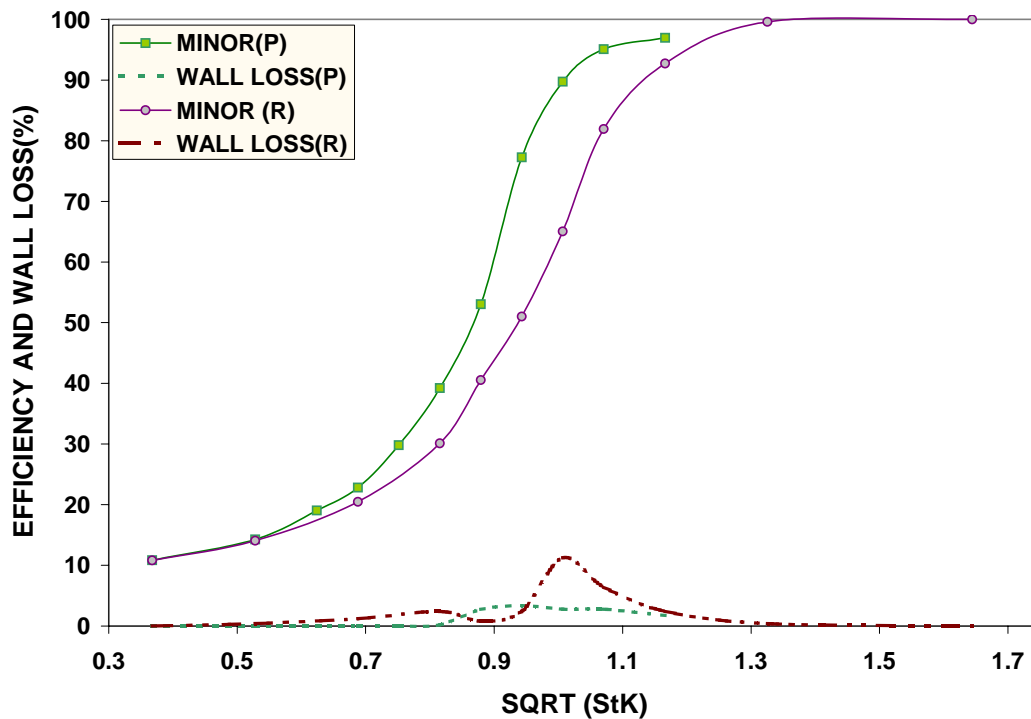
Fig.54. Comparison of the impactor efficiency and wall loss curves obtained for the preliminary LSVI model against the refined model.

It can be seen from the figure that there is a profound difference between the results of the previous prediction and the present prediction. The predicted cutpoint SQRT $(StK)_{50}$ value is 0.92, nearly 6% more than the previous prediction. Also, the shape of the curve is more spread out. The wall loss spectrum also is very different, with the predicted peak wall loss now being 11%, nearly a three-fold increase over the previous predictions.

The difference between the two results demanded further investigation. So, further studies were performed to investigate the effect of the depth of the inlet converging section (keeping the rest of the geometry unchanged), on the impactor performance. Three models with different depths of the inlet section were built. In these models, the ratio of the inlet width to the throat width was kept to be approximately 15,20, and 25, respectively, compared to the ratio of 10 in the refined model. These models are called by the general name RITW (meaning Ratio of the Inlet to the Throat Width) and the number accompanying the name is the value of the actual ratio. Table X presents the summary of the numerical information pertinent to the simulations.

VI. C. 2. Studies on the RITW15.25 Model

Three different meshes were constructed on this model; a coarse mesh [C], a medium fine mesh [M] that was approximately twice finer than the coarse mesh, and, a fine mesh [F] that was approximately thrice finer than the coarse mesh (exact details are available in Table X). This study was performed to assess the sensitivity of the predicted results to mesh density (or) the number of cells used in the simulation. Results of this study would ensure that the predictions are mesh independent. The impactor and wall loss curves obtained for the cases are presented in Fig.55.

It can be seen from the figure that the impactor efficiency and wall loss curves for the medium-fine mesh [M] and the fine mesh [F] are nearly in agreement, whereas, the coarse mesh [C] curves are different. From this it can be concluded that the simulation predictions can be assumed to become nearly mesh independent if the mesh density is at least of the order of the medium-fine mesh [M].
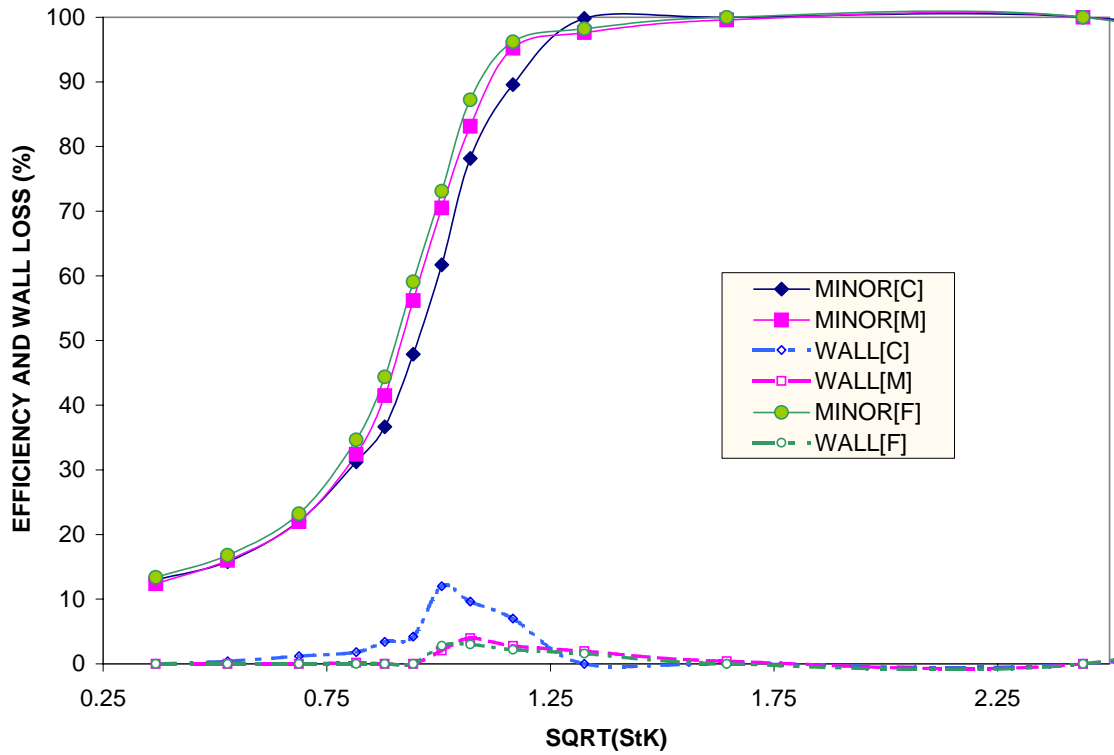
Fig. 55. Comparison of the impactor efficiency and wall loss curves obtained for the RITW15.25 case with different mesh densities.

Further analysis of the figure shows that the C and M efficiency curves overlap in the low efficiency range (up to 30%). However, the M curve starts deviating away from the C curve shortly, and stays close to F curve afterward, for the remaining range of the Stokes numbers. This is due to the different wall loss curve for the C case, compared to the F and M cases. It is seen that while the wall loss spectrum for the M and F meshes are nearly the same, the coarse mesh spectrum is different. This difference manifests itself in the respective efficiency curves.

Further comparison of the efficiency curves suggests that the tail of the M and F curves at the high efficiency end is spread out, whereas, in the case of the C curve, it is abrupt. This is also due to the difference in the wall loss spectrums for the cases. The

wall loss spectrum for the C case abruptly drops to zero corresponding to a value of 1.3 in the abscissa, whereas, for the M and F cases, there is a gradual decrease. This is the reason for the above behavior.

The different wall loss spectrum observed for the cases is a clear indication of the fact that the mesh density in coarse mesh case is insufficient to capture the important details on the flow and particle behavior.

Fig. 56. Comparison of the impactor efficiency and wall loss curves obtained for the RITW15.25 [F] model against the refined model.

In Figure 56, the impactor efficiency and wall loss curves obtained for the fine model of the RITW15.25 case is against the results of the refined model (RITW9.1). There is a slight difference between the results, indicating that the results are not still independent of the depth of the inlet section used for the simulations.

At this point, as the experimental group at the Aerosol Technology Laboratory (ATL) wanted to investigate the performance characteristics of the impactor for higher stokes numbers (particle sizes). The present study was extended to include high particle sizes. Simulations were performed with particle sizes up to 10 μm. Figure 55 presents the results of the simulation.
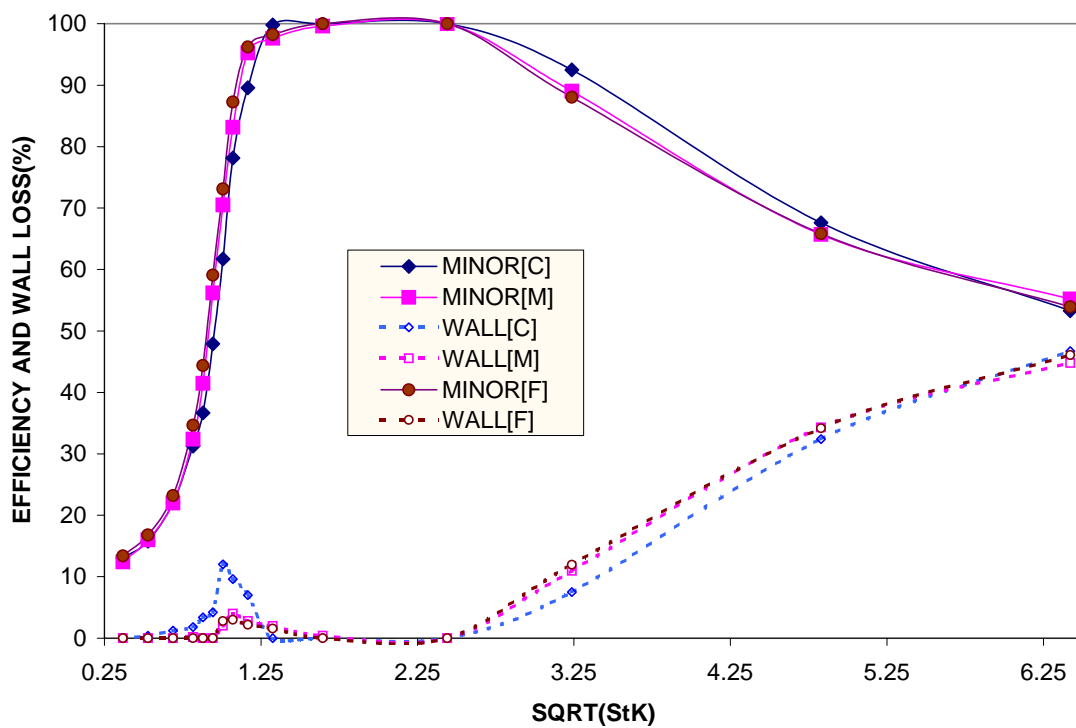
Fig. 57. Comparison of the impactor efficiency and wall loss curves obtained for the RITW15.25 case for the complete range of Stokes numbers.

It can be seen from Figure 57 that as the value of the SQRT $(StK)_{50}$ starts increasing beyond 2.5 approximately, the efficiency starts decreasing rapidly as the wall losses start increasing dramatically. At the highest stokes number simulated (corresponding to a particle size of 10 μm), the predicted efficiency is approximately 55% and the wall loss is 45%.

As observed previously, there is a difference in the predictions for the different mesh sizes. Though this difference is not very important, it is again indicative of the fact that a mesh independence study needs to be performed to ensure the accuracy of the predictions.

In the process of the above study, as simulations were being performed with higher sized particles, it was found that a significant number (~10 to 20%) of particles of sizes above 5 μm were impinging on the walls of the converging section close to the inlet patch. These particles needed to be discounted from the total number of particles (500) used for the simulation, while generating the efficiency and wall loss curves. To prevent the results from being biased, it was decided that the depth of the inlet convergence section would be further increased.

VI. C. 3. Studies on the RITW19.27 Model

As suggested in the name of the model, in this study, the ratio of the inlet to the throat width was approximately 20. The important numerical details on the simulation are available in Table X. Figure 58 presents the results of the simulation. The impactor efficiency and wall loss curves predicted for this case are compared against the previous case (RITW15.25).

It can be seen from Figure 56 that there is not much difference the efficiency and wall loss curves for the different cases. There is a very slight difference in the predictions at the high efficiency tail region (>80%). Again, this is due to the reason that the wall loss spectrum for the RITW15.25 case is slightly shifted to the right of the RITW19.27 case (toward higher Stokes numbers), and more spread out.
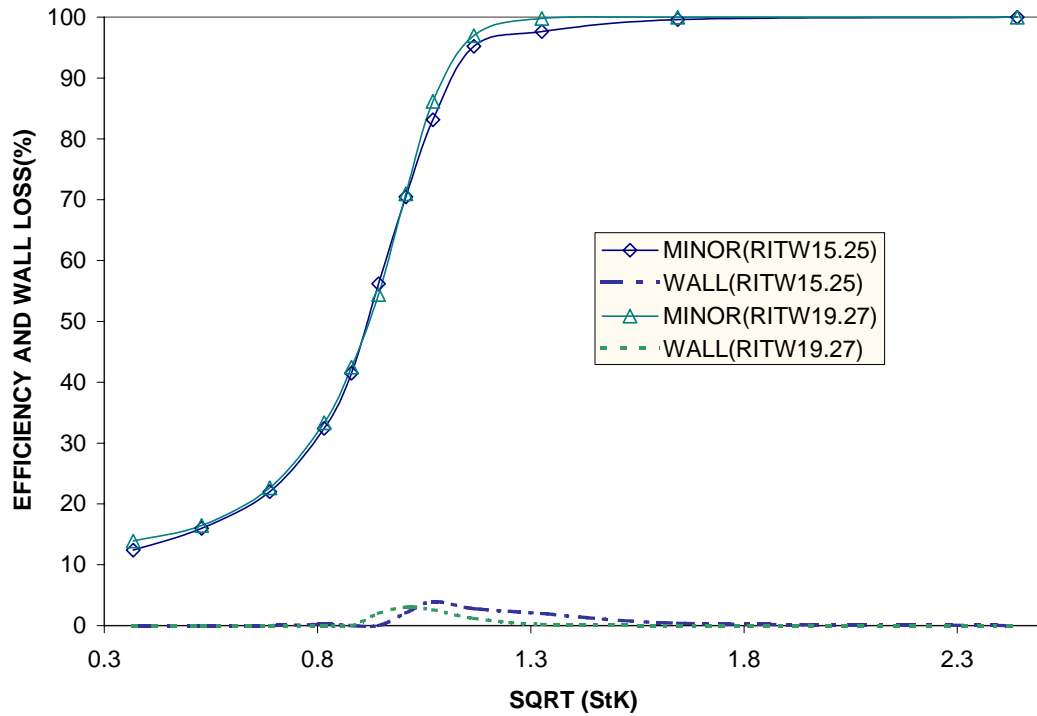
Fig. 58. Comparison of the impactor efficiency and wall loss curves obtained for the RITW15.25 case against RITW19.27 case.

Figure 59 presents an extended version of the curves with higher Stokes number (higher particle sizes) included. It can be seen that there is a small improvement (~10%) in the prediction of the efficiency and wall loss curves at higher Stokes numbers. The efficiency at the maximum Stokes number increases to about 60% and the wall loss drops to about 40%.

From the results of the simulation it was seen that the percentage of the higher size particles that were impinging on the walls of the inlet convergence section was reduced to about 10% of the total number, by increasing the ratio of the inlet to the throat width. This resulted in a decrease in the bias on the results. This was the objective to be achieved in the present study.
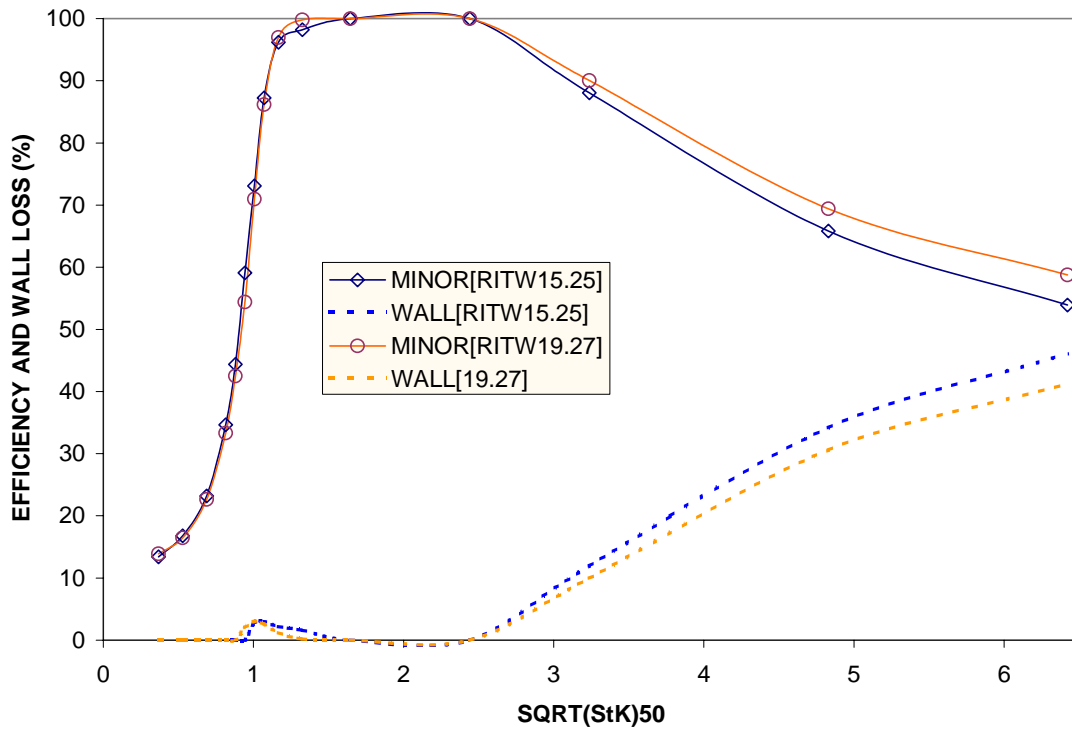
Fig. 59. Comparison of the impactor Efficiency and wall loss curves obtained for the RITW15.25 case against RITW19.27 case for the complete range of Stokes numbers.

VI. C. 4. Studies on the RITW25.56 Model

It is to be noted from the results of the previous section that the increase in the depth of the inlet convergent section had not affected the impactor efficiency curve prediction in the lower range of Stokes number. However, there had been a selective improvement in the predictions at higher Stokes numbers. So, it was decided that simulations would be performed on a model in which the ratio of the inlet to the throat width was approximately 25. The geometry on which the simulations were performed is presented in Figure 60. This has been done with a view to explain certain important numerical concepts that have been adopted in this section of the study.
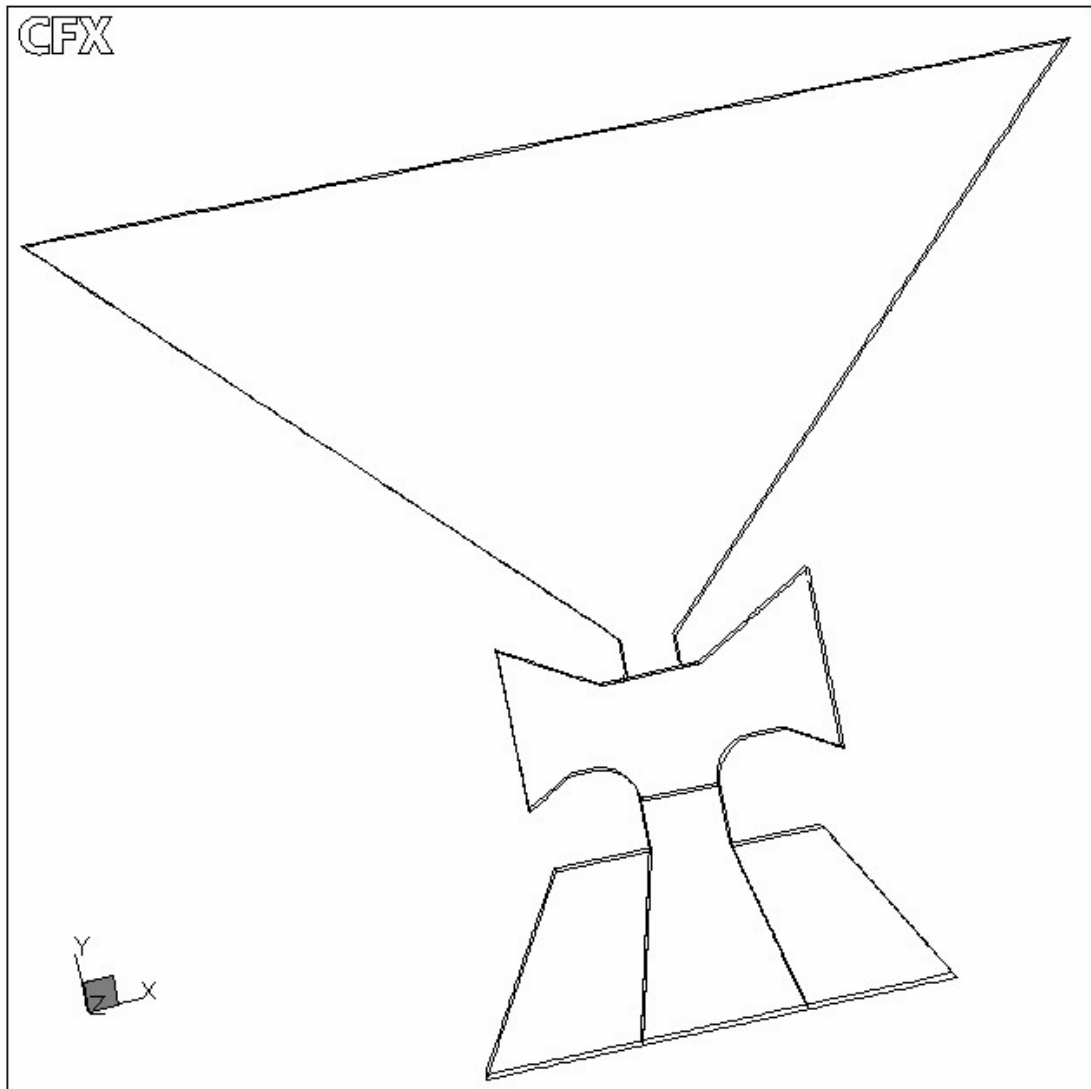
Fig. 60. Outline of the RITW25.56 model.

Figure 61 presents the results of the present study. The impactor efficiency and wall loss curves obtained for this case are compared against the previous results (RITW19.27 and RITW15.25). It can be seen from Figure 61 that there is no difference between the efficiency and the wall loss curves for the cases and the curves overlap in the lower Stokes number region. In this respect, it seems that the curves have attained independence from the depth of the inlet convergence section used for the simulations.
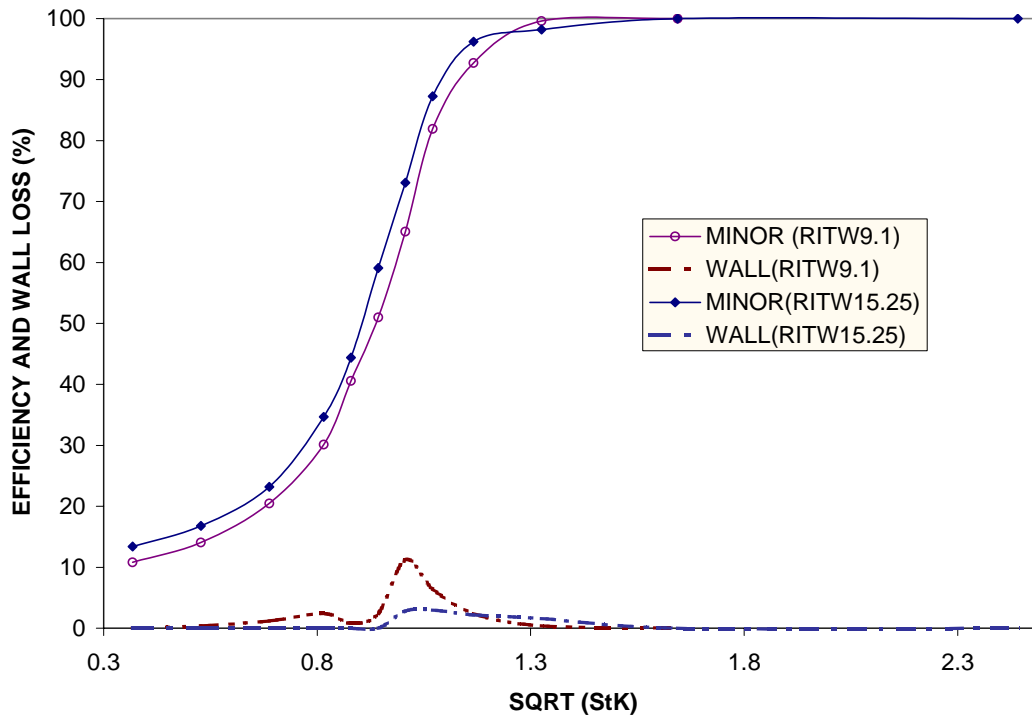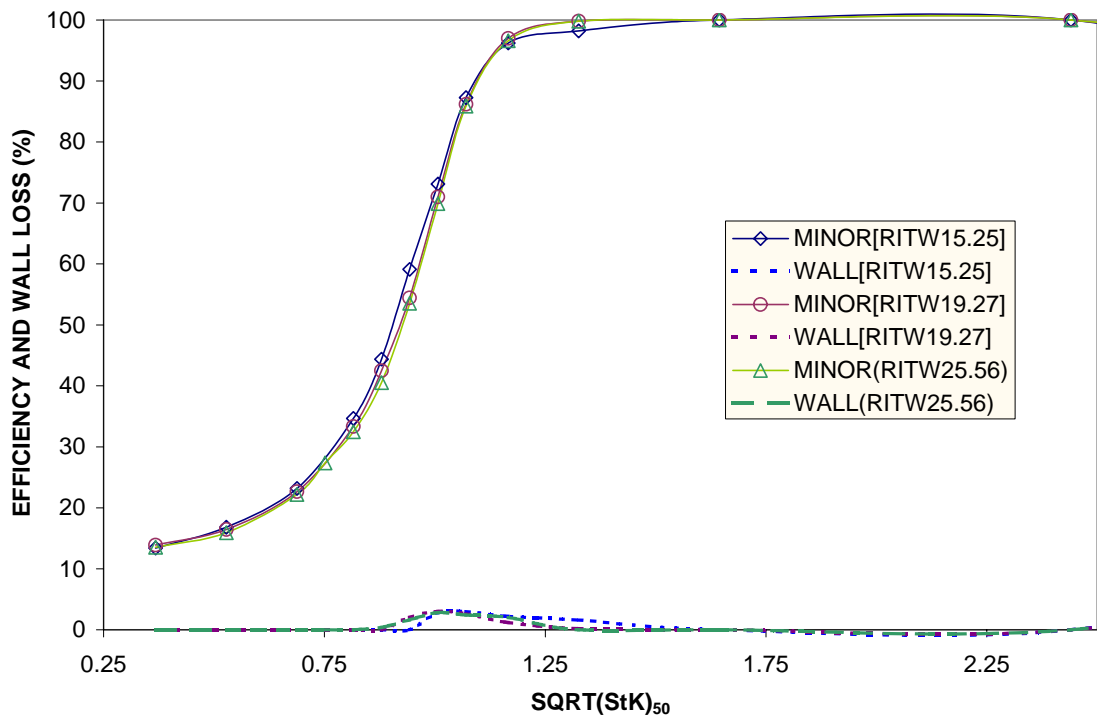
Fig. 61. Comparison of the impactor efficiency and wall loss curves obtained for the RITW25.56 case against the previous cases.

Figure 62 presents a comparison of the curves over the whole range of Stokes numbers. It can be seen from the figure that there is a further improvement in the efficiency/wall loss prediction for the highest stokes number. While the efficiency prediction increased to a value of 65% from a value of 59% (for the RITW19.27 case), the wall losses decreased to a value of 34% from the previous prediction of 41%.

From the results of the simulation it was seen that the percentage of the highest size particle that was impinging on the walls of the inlet convergence section was reduced to about 7% of the total number, by increasing the ratio of the inlet to the throat width. For the next two smaller particle sizes, the number was even less; 4% and 1% respectively. This resulted in a further decrease in the bias on the results, for those two

sizes. As can be seen from the figure, the previous and the present prediction are nearly the same for these sizes now.
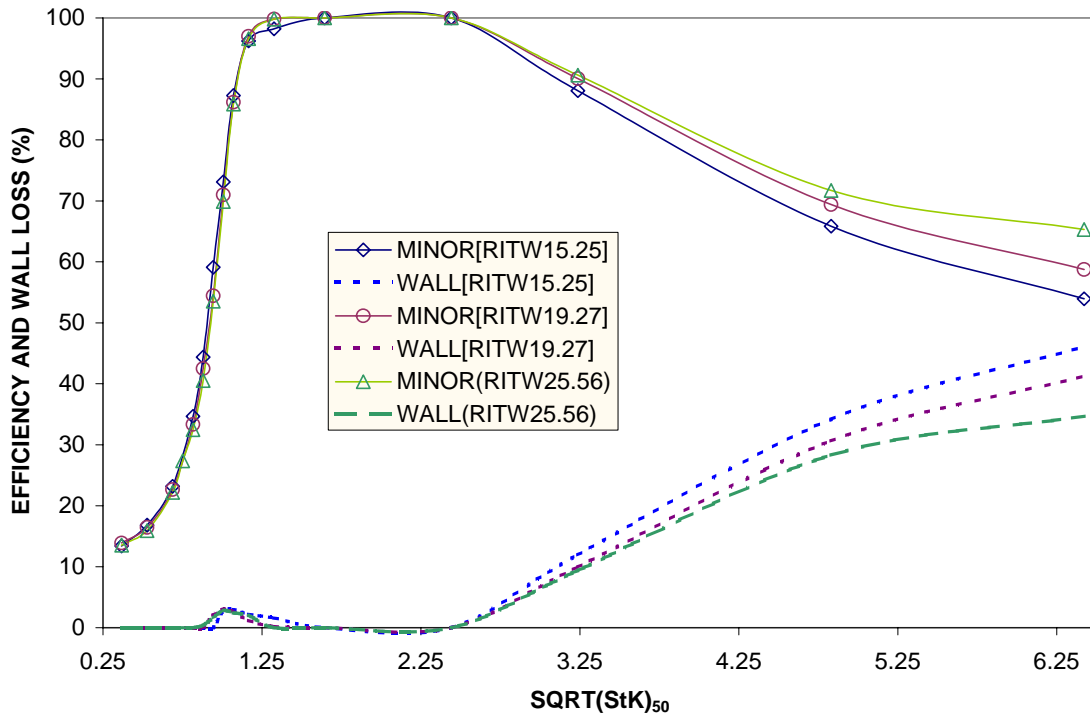
Fig. 62. Comparison of the impactor efficiency and wall loss curves over the complete range of Stokes numbers.

As already discussed in Chapter III, a body-fitted, block-structured methodology is adopted in CFX4.4. In the process of creating the exact geometry on the pre-processor, the geometric domain is broken down to smaller sub-domains, also known as blocks. The different blocks are glued together, to construct the geometry. A study was performed on the present geometry, but, on a model with a different block-structuring methodology adopted in the inlet convergence section. The reason for performing this study will be made known shortly.
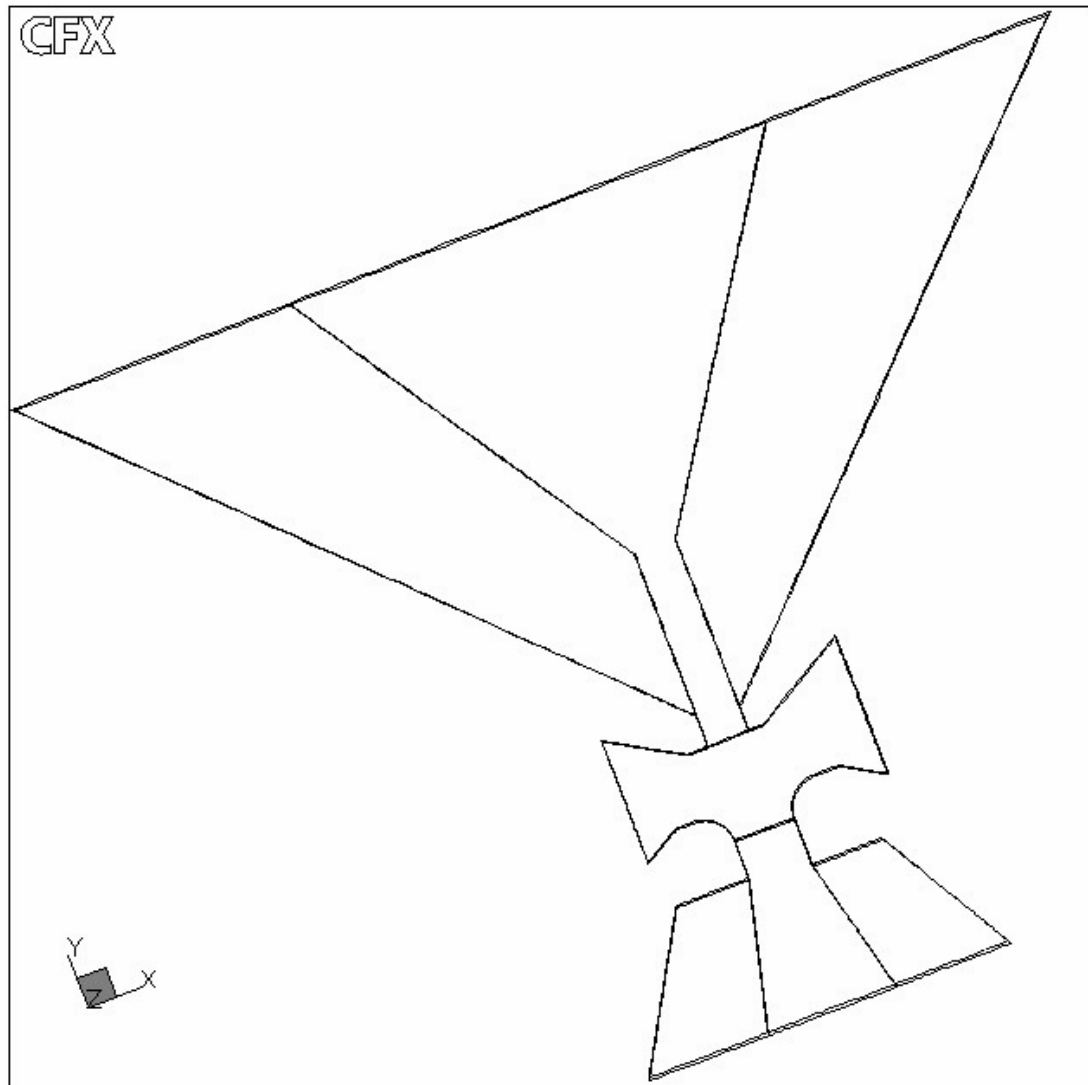
Fig. 63. Outline of the multi-block RITW25.56 model.

To illustrate the difference in the approach between the present and the previous models, an outline of the multi block RITW25.56 model is presented in Figure 63. A comparison of Figures 60 and 63 shows that they basically differ in the way in which the inlet convergence section was blocked. In the RITW25.56 model (Figure 60), the convergence section remained as a single block. However, in the multi block RITW25.56 model (Figure 63), the section was broken down into four blocks.

The reason for doing this was to avoid the errors that would arise from the propagation of the mesh from the throat section into the inlet section. In the single block inlet section RITW25.56 model, the mesh structure across the width of the throat would propagate all the way to the inlet patch. Though the mesh is extremely fine in the throat section, as the mesh propagates into the inlet section, those cells at the center of the domain start getting coarser. As a rough estimate, the width of the mesh at the center of domain at the inlet patch would be 25 times the width at the throat section.

However, by breaking down the domain into four blocks (as has been done in the multi-block RITW25.56 model), it can be seen that the propagation of the mesh from the throat is limited to approximately the middle one-third width of the inlet patch. By splitting the block, adverse effects arising from mesh propagation was reduced, and a better control of the mesh in the inlet convergence section was achieved. However, this also resulted in an increase of the total number of cells, as can be seen from Table X.

The results of the simulation are presented in Figure 64. The impactor efficiency and wall loss curves obtained for this case (labeled MB) is compared against the previous result (single block, labeled SB), for comparison. It can be seen from Figure 64 that the efficiency and wall loss curves are slightly different. The present efficiency curve is spread out with a longer tail at the high efficiency end, whereas, the old curve was steep. When the wall loss spectrum for the present model is compared against the previous model, it is seen that the present spectrum is spread out over a wider range of Stokes numbers, compared to the previous case. The deviation that is observed in the efficiency curves is a direct reflection of the difference in the wall loss spectrum.
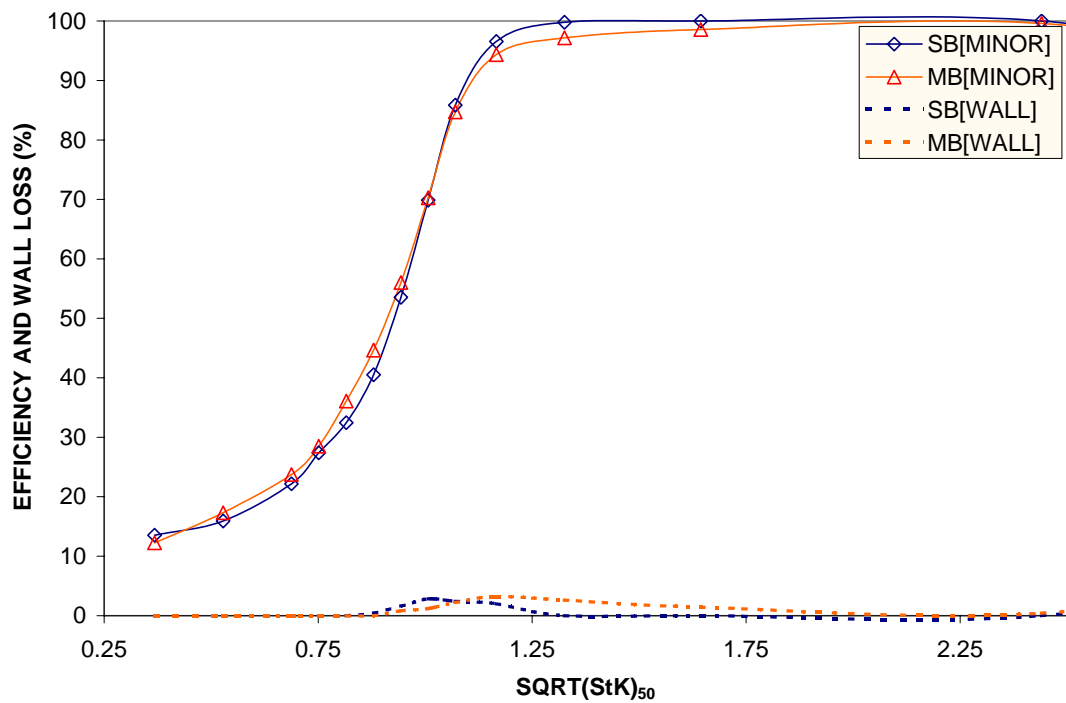
Fig. 64. Comparison of the impactor efficiency and wall loss curves for the cases.

Figure 65 presents the efficiency and wall loss curves for the present case with both the single block and the multi-block models (in the convergence section) over an extended range of Stokes numbers. As in the previous figure, the present result is compared against the old result. In addition to the previously observed difference in the low stokes number range, it can now be seen from the figure that the present prediction of the wall loss for the last two higher stokes number values is 3 to 4 percent less than the previous prediction. Consequently, the present efficiency prediction is increased by an equal value. When the present (multi-block) results are compared to the RITW19.27 case, the corresponding efficiency/wall loss values are different by 5% and 11% respectively, for the last two higher stokes number values, which is significant.
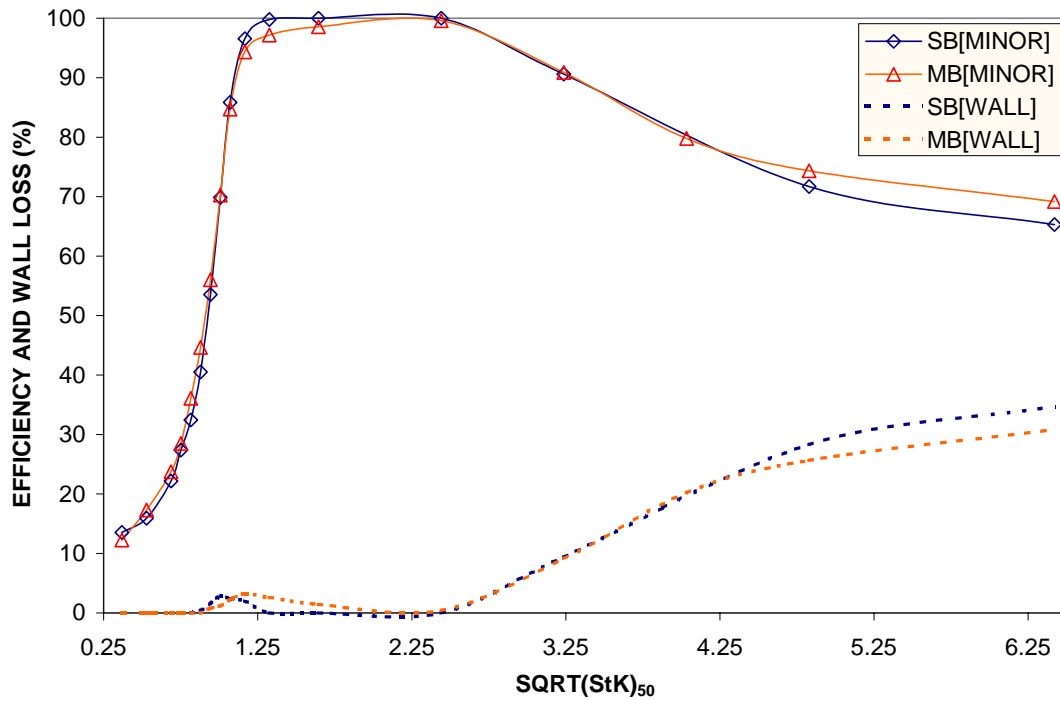
Fig. 65. Comparison of the impactor efficiency and wall loss curves for the models over the complete range of Stokes numbers.

When the results of the simulation were analyzed to determine the bias in the predictions for the two highest Stokes number particle sizes, between the single and the multi-block models, it was seen that the percentage bias for the models was nearly the same. The observed difference in the predicted results, then, is to be attributed entirely to the multi-block strategy adopted in the inlet convergence section.

In Figure 66, the predicted velocity profiles from the single block model (labeled SB) and the multi-block model (labeled MB) for the inlet convergence section, are compared. The comparison is made at the end of the throat section of the impactor, and, the exact location corresponds to a line that is drawn across the impactor, connecting points on the opposite sides of the impactor wall, just before the curvature region.
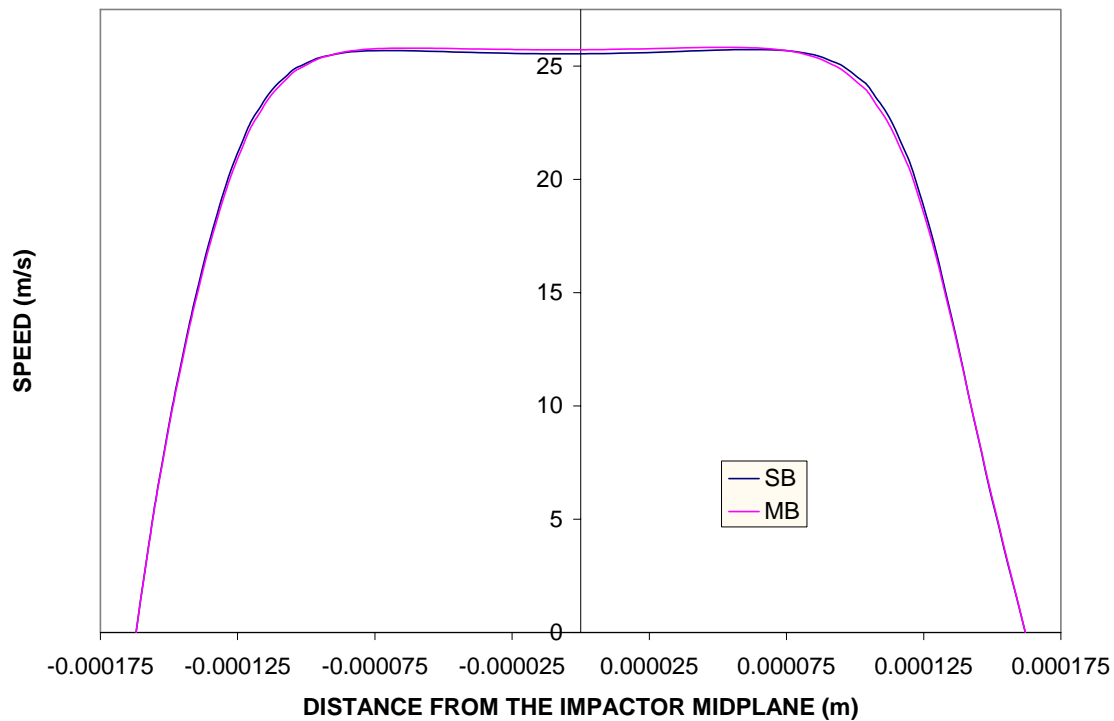
Fig. 66. Comparison of the velocity profile predictions for the single block and the multi block models at the throat region of the impactor.

It can be seen from the figure that though the velocity profiles match at the edges (near wall region), as we go to the core region, there is a difference and the profiles don't match exactly. To illustrate the difference in the predictions, the velocity profile in middle 80% of the impactor throat region is presented in Figure 67. It can clearly be seen from the figure that the centerline value is higher for the multi-block case. However, as we go away from the centerline, the profiles cross over at about 55% distance from the centerline. Subsequently, the single block values are higher all the way as we go to the impactor wall. Though the magnitude of the difference is seemingly small, there is a difference in the velocity profiles obtained from the two models.
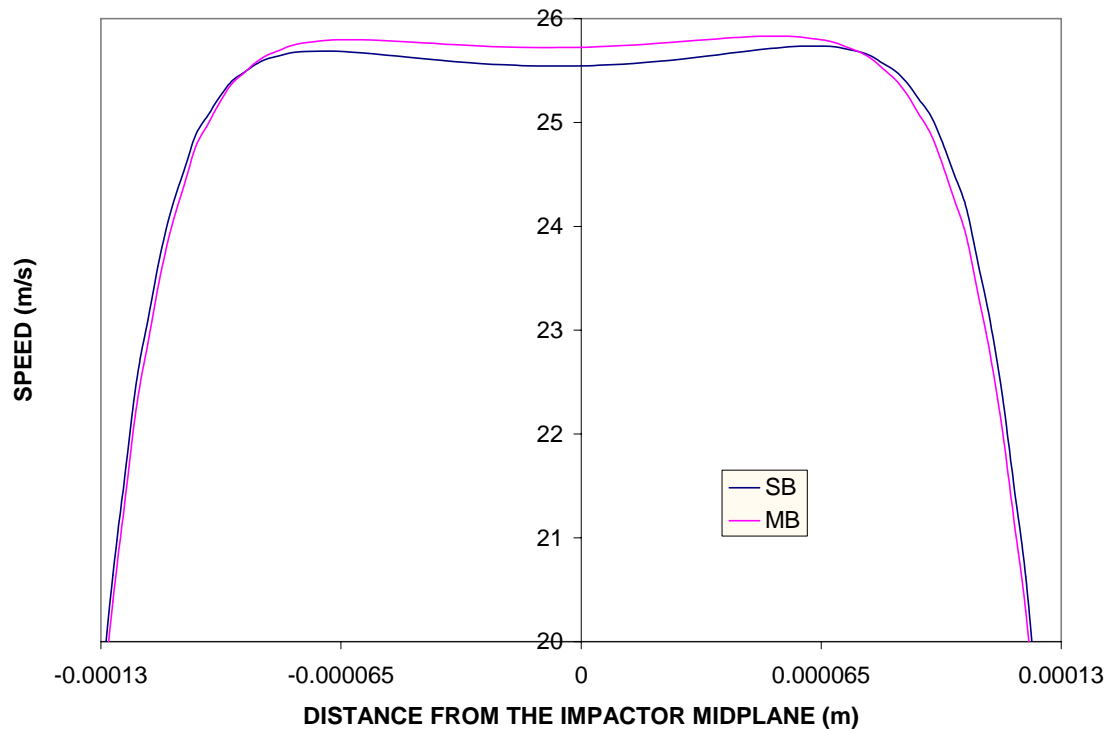
Fig. 67. Comparison of the velocity profile predictions in the middle 80% of the throat region of the impactor.

It seems that the adopted multi-block strategy and the associated effect of a finer meshing in the inlet convergence section resulted in a better resolution of the velocity field in the region. It is to be remembered that the multi-block mesh is 20% finer than the single block mesh. Since the mesh in the other regions remained the same, the increase in the total number of cells for this case in solely due to the increase of the number of cells in the inlet convergence section.

The better-resolved velocity field in the inlet convergence section, in turn, produced a more accurate interpolated velocity for the particle, when the particle transport calculations were performed. The observed difference in the impactor

efficiency and wall loss curves is due to the above reason. The above study shows that multi-blocking of the inlet convergence section certainly resulted in an improvement of the prediction, in particular, for higher Stokes number particles.

VI. C. 5. Behavior of the Various Sized Particle Inside the LSVI

As already stated, one of the advantages associated with a CFD study performed with commercial CFD codes is the availability of excellent post-processing capabilities. The post-processor is equipped with tools that aid in the visualization of the physical phenomena occurring in the internals of the simulated domain. In this section, this concept is illustrated by presenting the particle tracks inside the impactor.

Particle tracks are presented for the following particle aerodynamic diameters (in μm AD): 0.5,1.4,1.5,2.0,2.5,3.75,5.0,7.5 and 10.0, in Figures 68 through 76, respectively. Particle sizes have been chosen carefully so that tracks of the above particle sizes differ in a small way from each other. This was done with the intention to illustrate some of the important characteristics of the inertial impaction process and the effect of the critical geometrical dimensions on the particle behavior.

The visuals start with the smallest particle size (0.5 μm). These particles behave more as a fluid particle. The next one is for a particle size that is close to the 50% cutpoint (1.4 μm). The rest of the chosen particle sizes are significantly bigger than the cutpoint. The presented visuals illustrate lucidly the behavior of the different sized particles inside the critical region of the impactor. They provide a good opportunity to enhance our understanding of the particle physics. The obtained understanding would, in turn, contribute toward better design of the impactor.
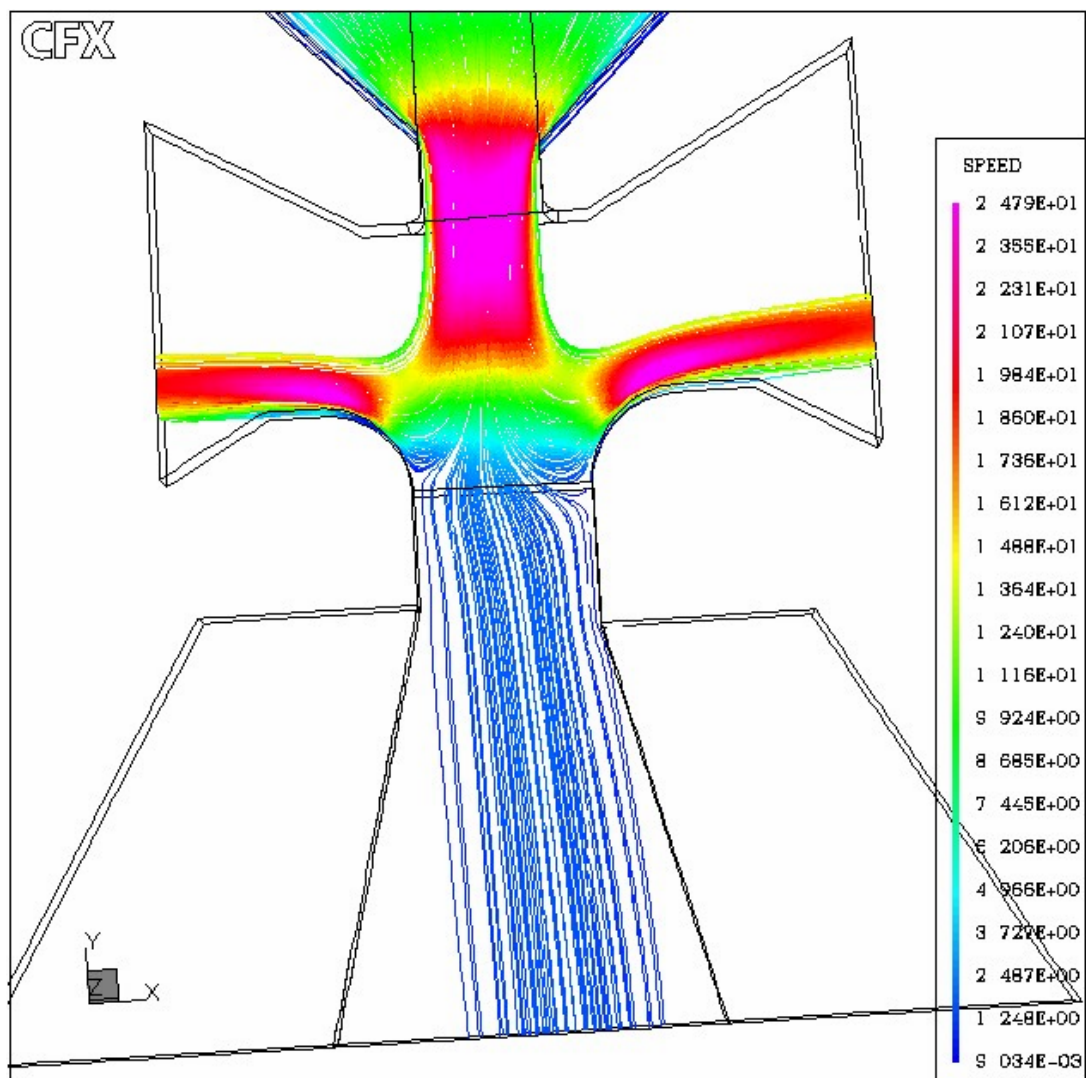
Fig. 68. Particle tracks for 0.5 µm AD particles.
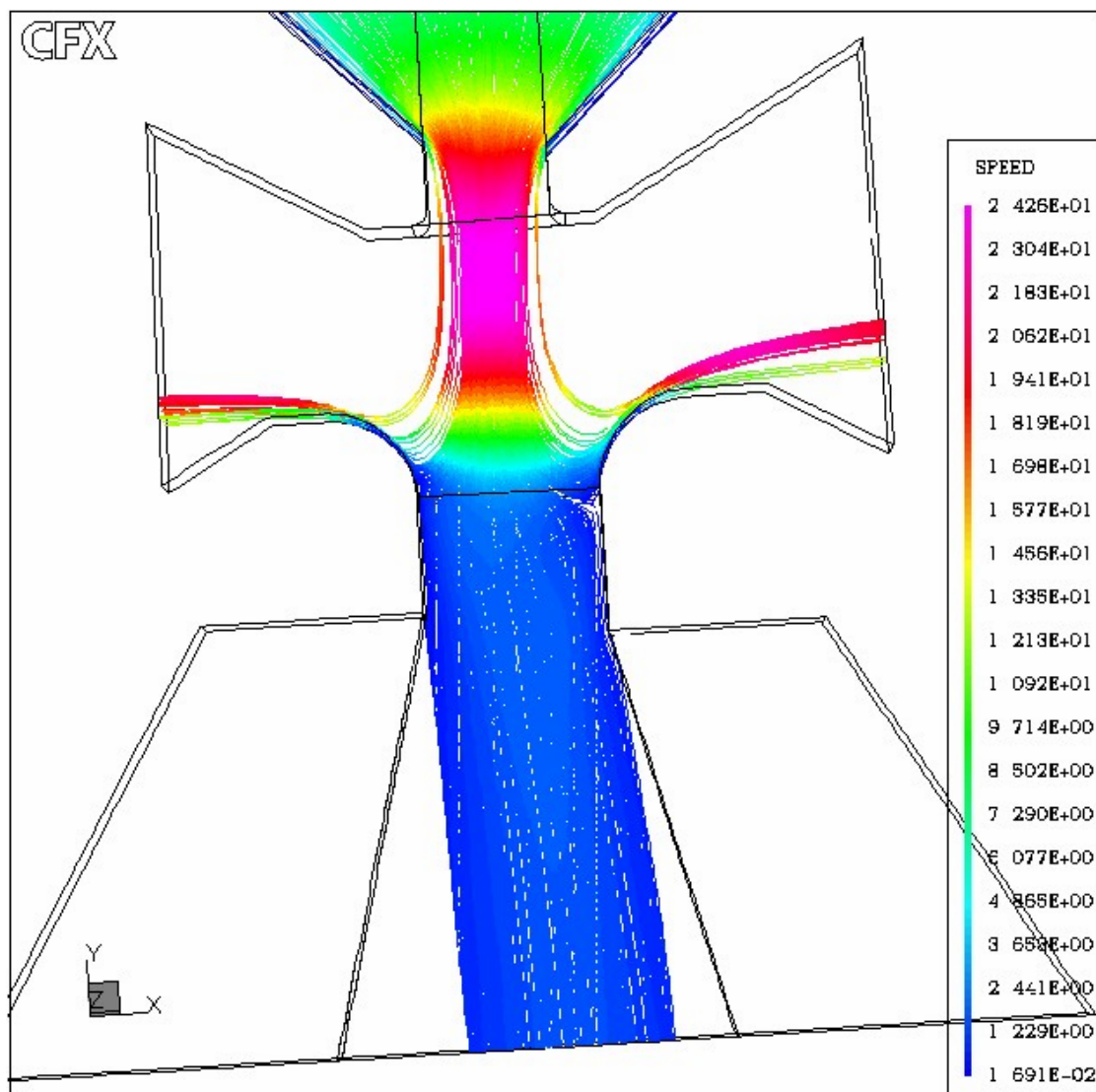
Fig. 69. Particle tracks for 1.4 µm AD particles.
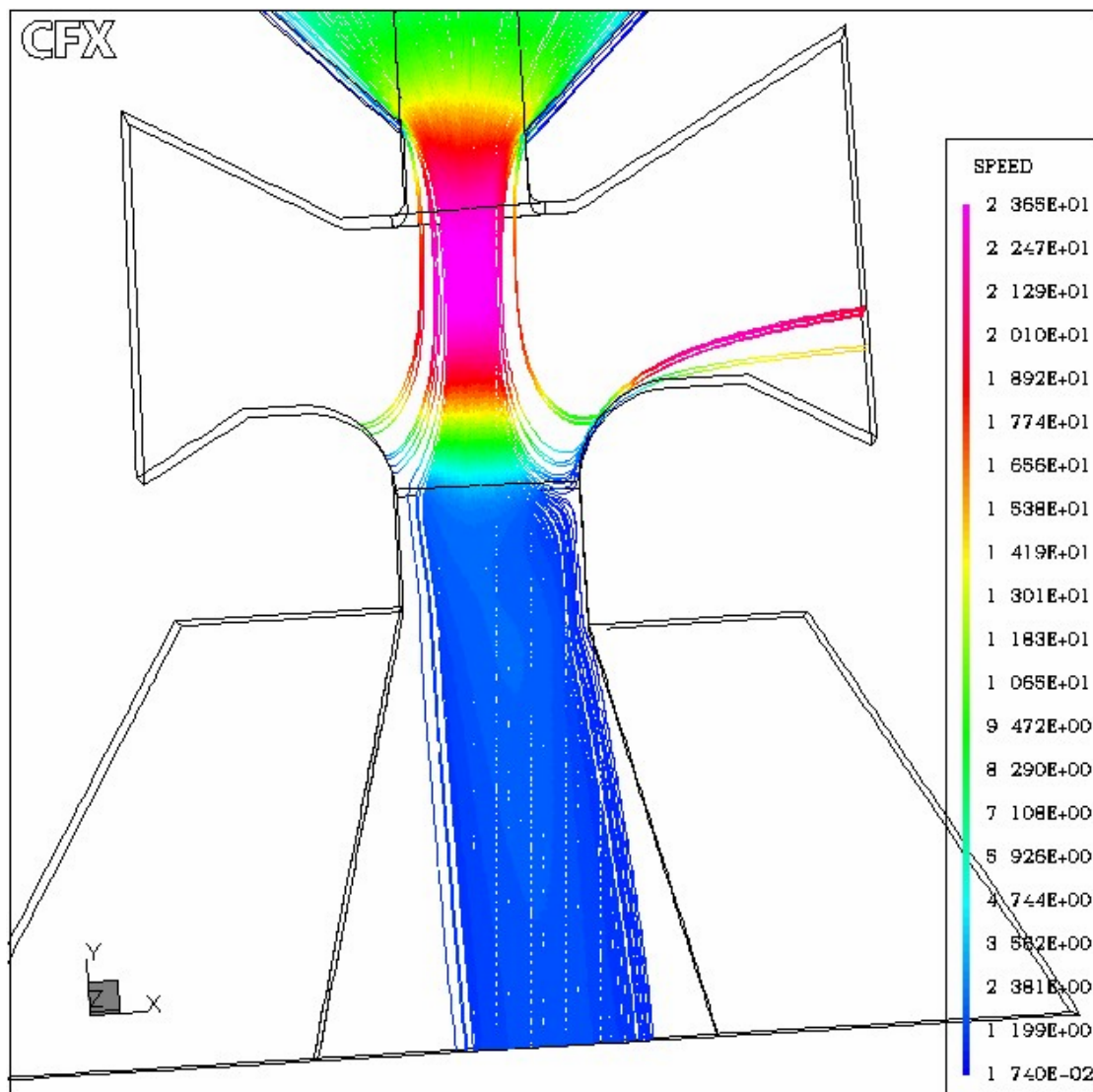
Fig. 70. Particle tracks for 1.5 µm AD particles.
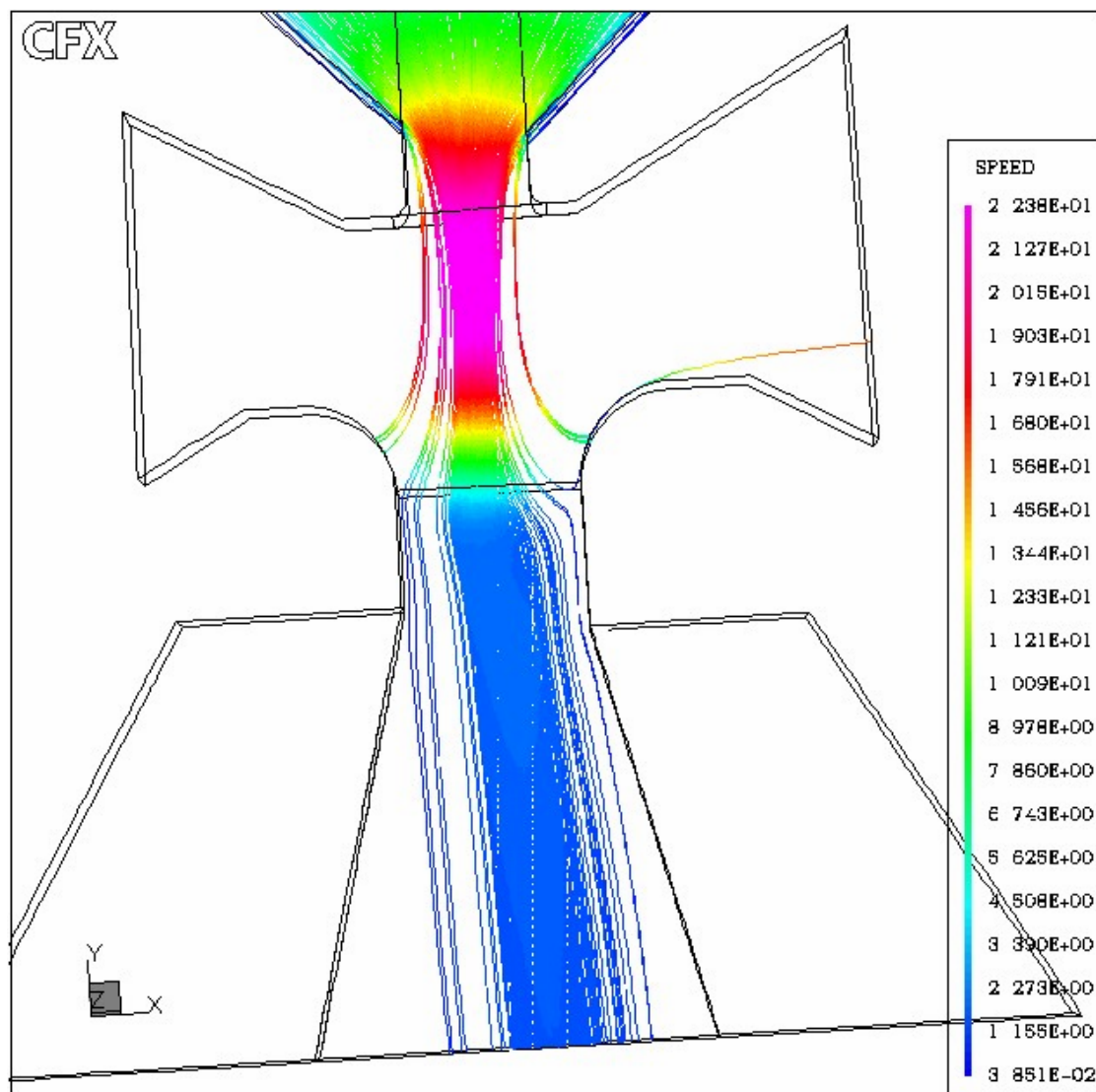
Fig. 71. Particle tracks for 1.75 μm AD particles.
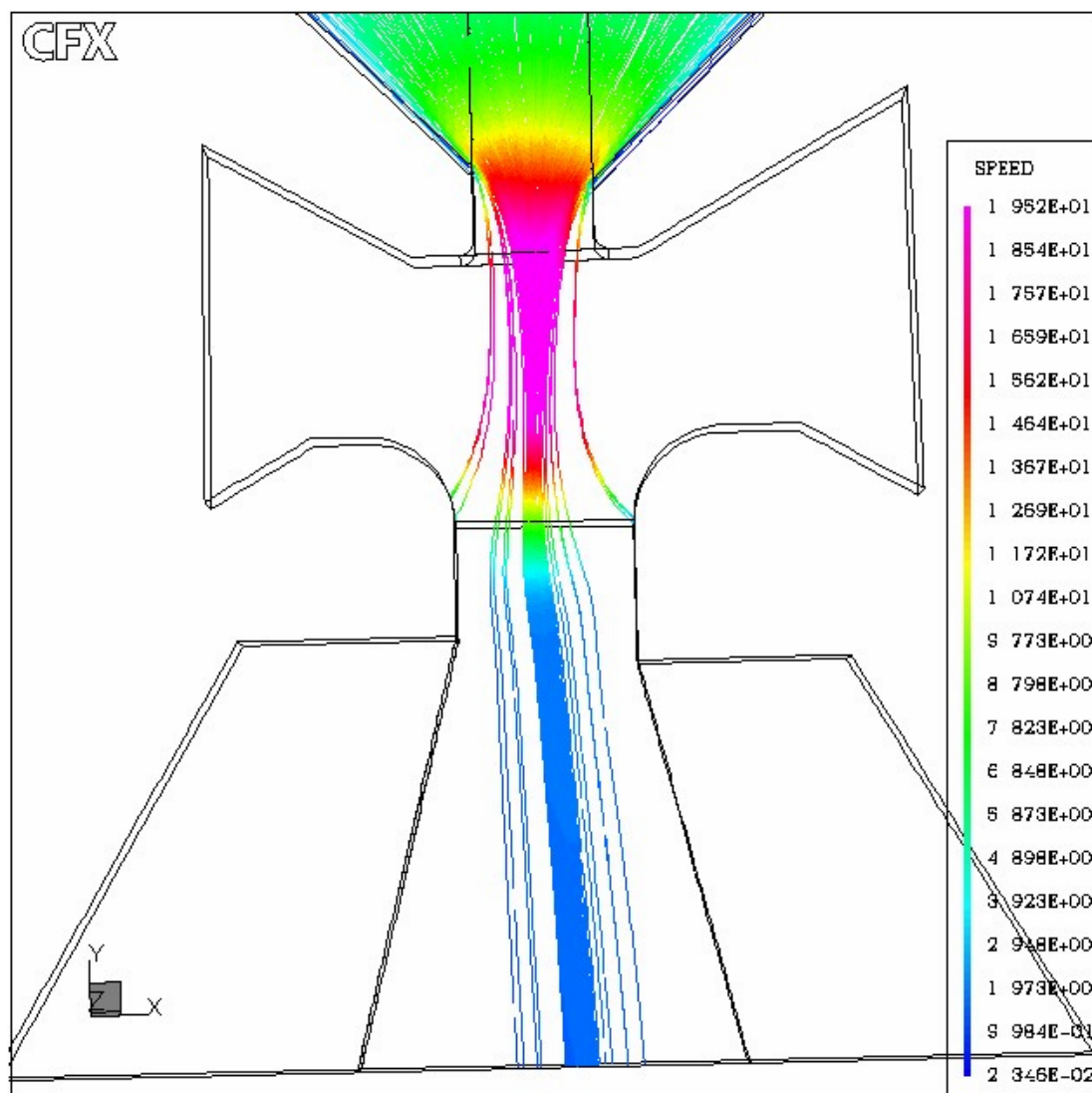
Fig. 72. Particle tracks for 2.5 μm AD particles.
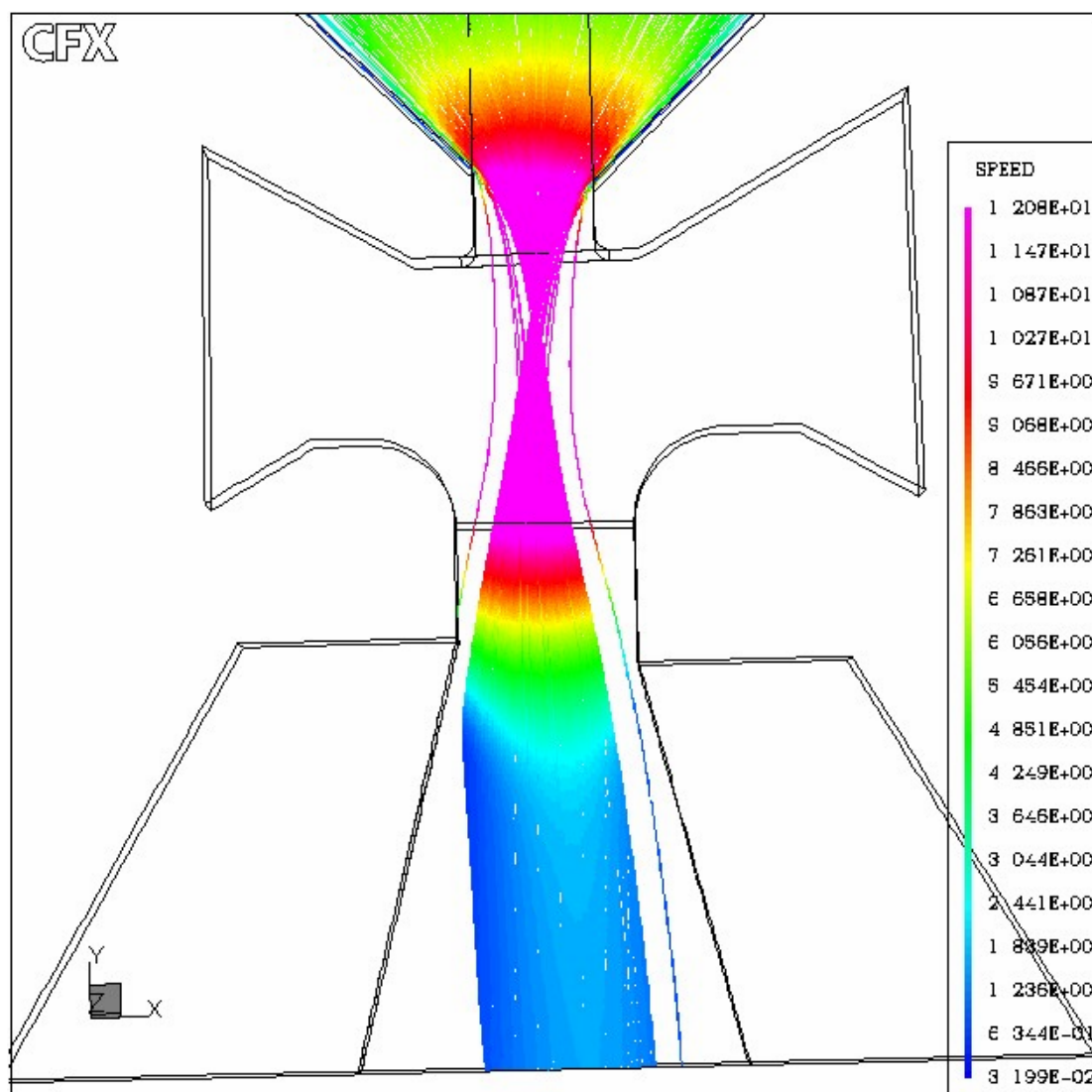
Fig. 73. Particle track for 3.75 µm AD particles.
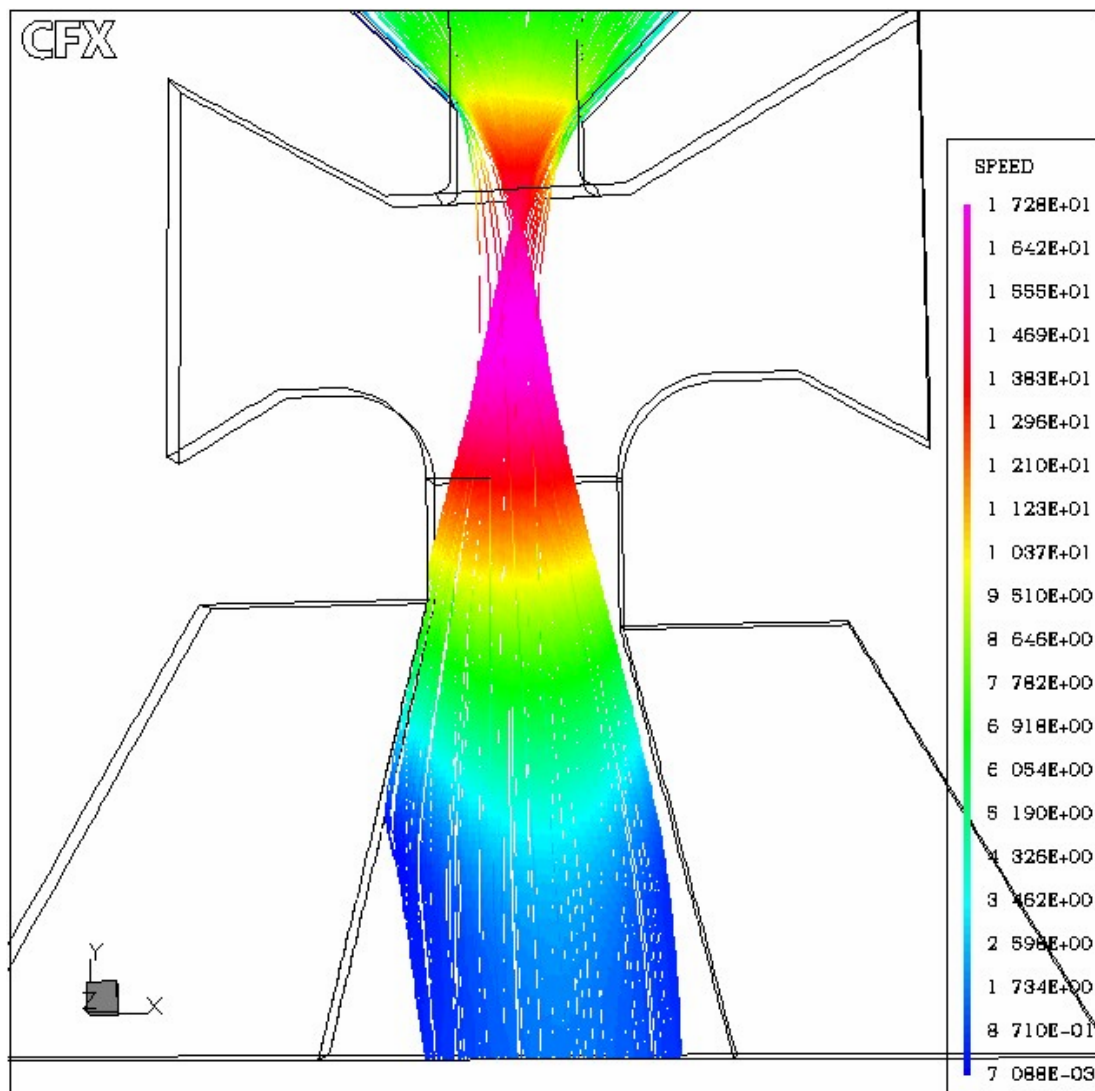
Fig. 74. Particle tracks for 5.00 μm AD particles.
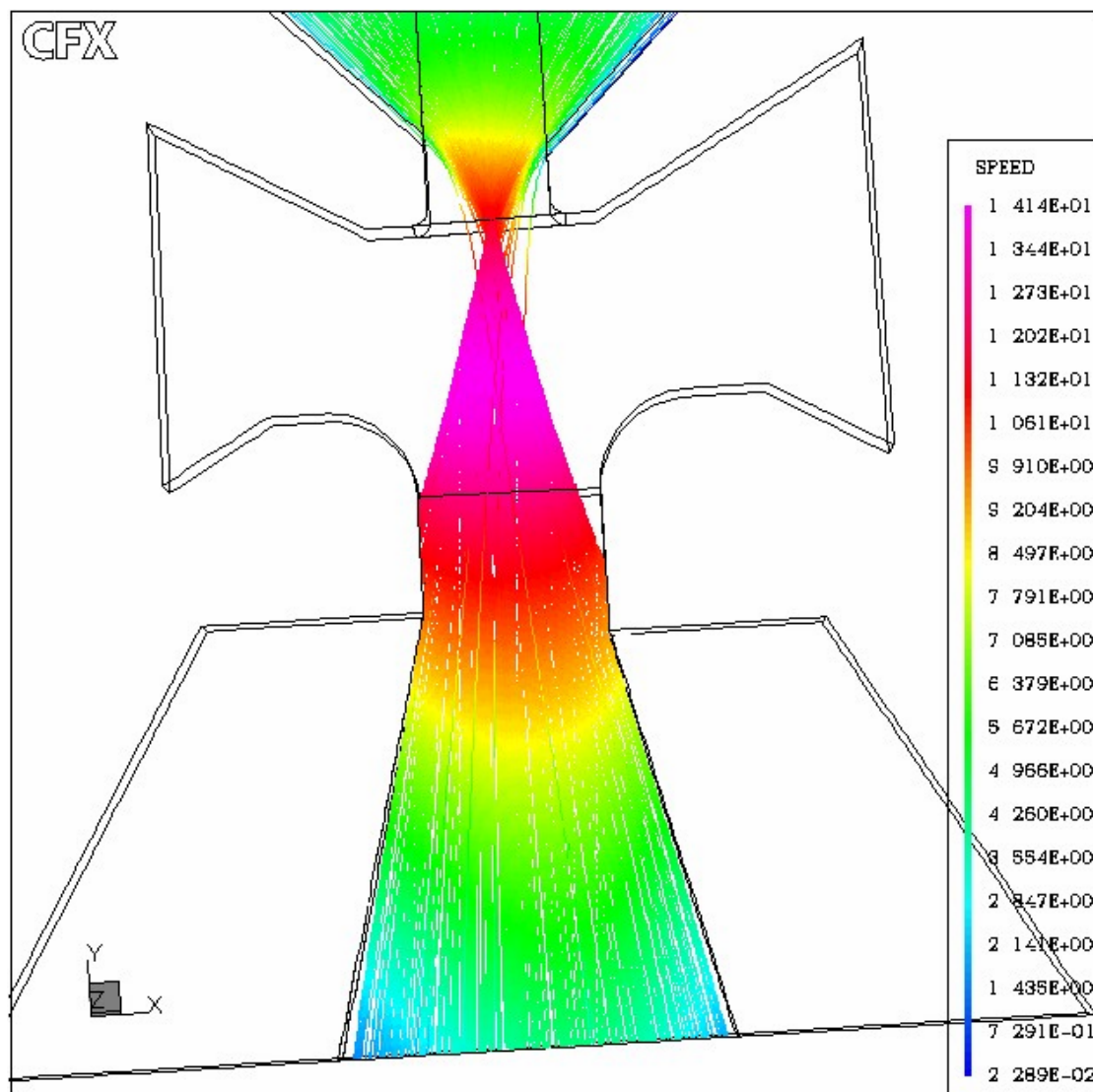
Fig. 75. Particle track for 7.50 µm AD particles.
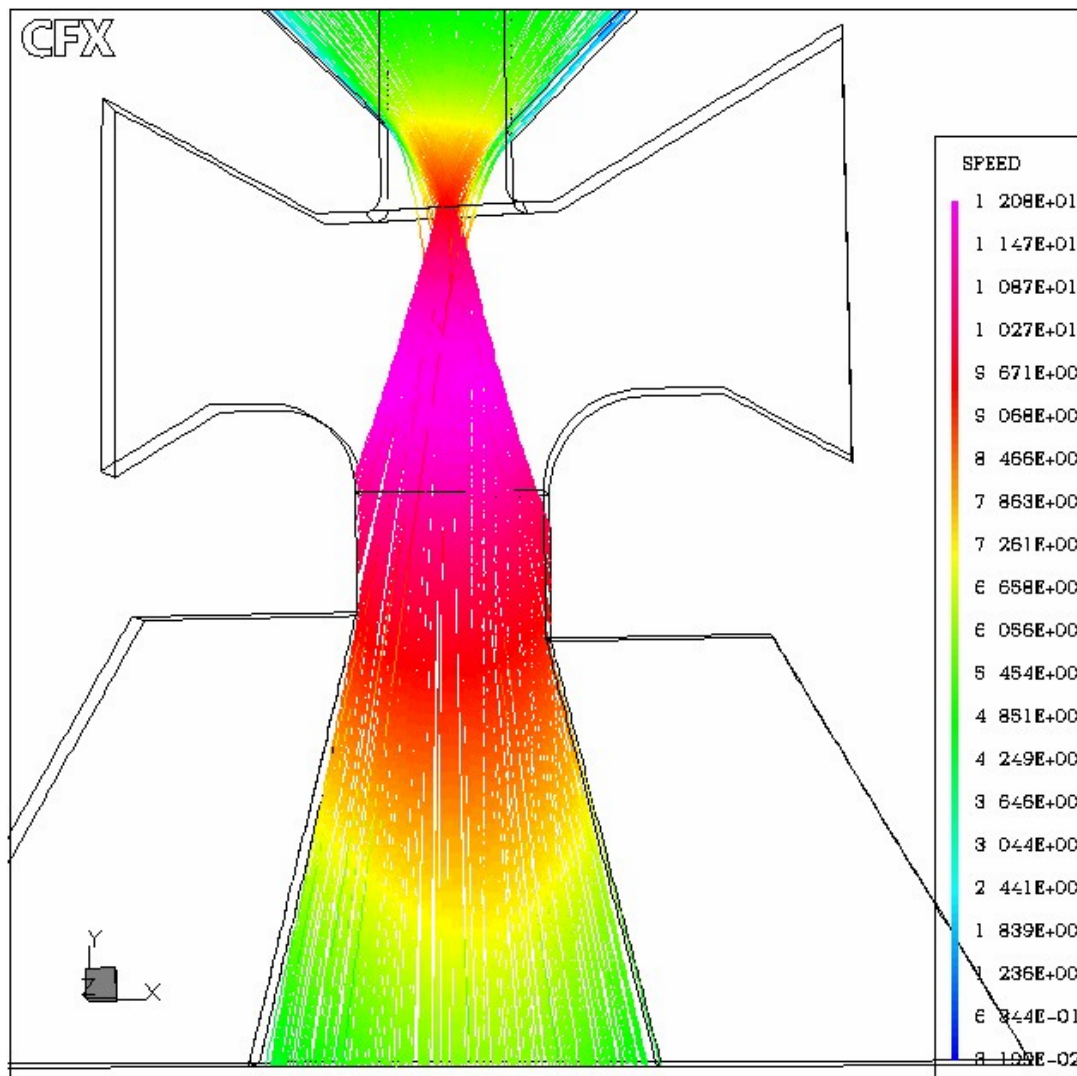
Fig. 76. Particle tracks for 10.00 μm AD particles.

Some of the general observations that can be made after a visual inspection of the particle tracks of the different sized particles are summarized below:

(a) The particle tracks are seen to be preferentially oriented to the right side of the receiver section for particle sizes up to 3.75 μm AD, instead of being symmetric about the midplane. This is due to the asymmetry in the impactor geometry. The asymmetry in the impactor geometry results in a flow asymmetry in the impactor and this affects the particle behavior.

(b) For a given impactor operating at a particular flow rate, there is a range of particle sizes in which the impactor would retain its separation characteristics. If higher particle sizes beyond the optimum size are used, there may be a significant wall loss.

(c) For the lowest particle size (0.5 μm AD), the particle tracks are seen to form a small band as they evolve from the throat and into the receiver section. As the particle size starts increasing, the width of the band starts decreasing. This band reaches a minimum width for a particle size of 2.5 μm AD.

(d) For particle sizes of 3.75 μm AD and above, the particle trajectories are seen to cross over. However, the band of 3.75 μm AD particles that evolves from the throat region is focussed enough that no wall losses occur.

(e) For particle sizes of 5.00 μm AD and above, the crossing trajectory effect dominates and the particle invariably end up on the walls of the receiver section, resulting in significant wall losses.

V1. D. Comparison against Experimental Results and Discussion

As explained in the beginning of the chapter, the performance of the LSVI was experimentally determined at the ATL. The details on the experimental procedure and the determination of the impactor efficiency and wall loss curves are presented in reference 41. In this section, the experimental results are compared against the numerical predictions on the LSVI worst-case (RITW-25.56) models.
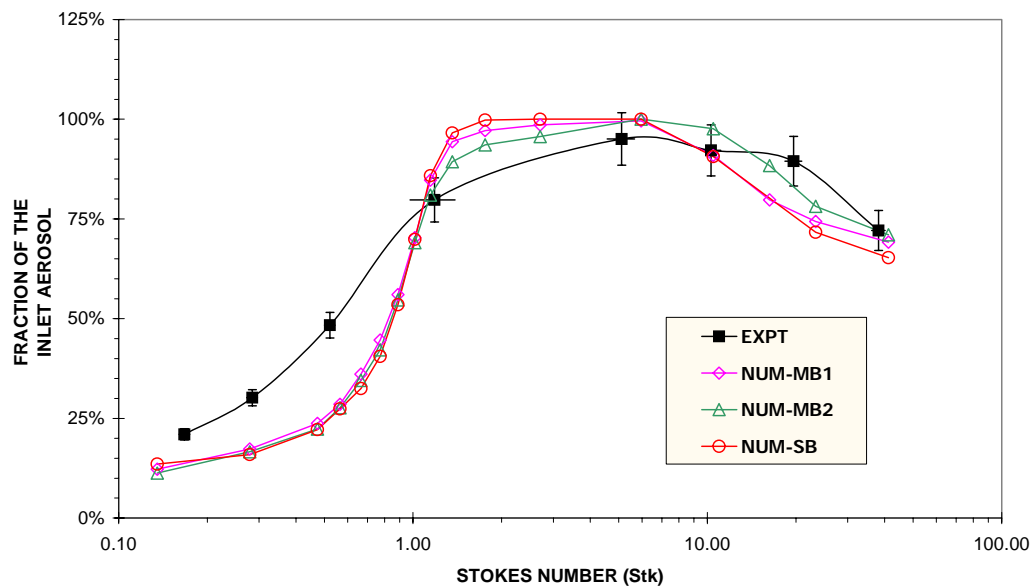
Fig. 77. Comparison of the experimentally obtained impactor efficiency curve against numerical predictions obtained for the LSVI worst-case (RITW25.56) models.

Figure 77 presents the impactor efficiency curve obtained experimentally against the numerical results. Three numerical curves presented in the figure. The curve NUM-SB corresponds to the curve obtained with the model in which the inlet convergence section was a single block. The curve NUM-MB1 (previously MB) corresponds to the curve obtained with the model where a multi-block configuration was adopted in the inlet convergence section. These results were presented in the previous section.

The third curve labeled NUM-MB2 was the curve obtained when the same multi-block model was meshed in a different manner compared to the way it was done in NUM-MB1. This was done to satisfy the continuity of mesh dimensions across different blocks. In the process of satisfying the continuity of mesh dimensions across adjacent blocks in a multi-block structure, there is a possibility that the continuity across some other set of adjacent blocks may be jeopardized. The appropriate meshing to be adopted is then left to the modeler's choice. A judicious decision would have to be made based on experience and physical intuition. The efficiency curve is, however, presented here to illustrate this phenomenon and for the reason that this is the curve against which the experimental results have been compared in reference 41.

It can be seen that there is a fair agreement between the experimental and numerical results. The numerical curves display a sharper separation characteristic, compared to the experimental curve. Moreover, the curves crossover at about efficiency value of 75%.

Considering the fact that

(a) the simulations were performed on a fictitious LSVI geometry incorporating the worst possible combination of critical geometrical parameters (as indicated in Table X), and,

(b) experimental results were obtained for the equal flow split conditions among the major flow outlets, whereas, equal pressure boundary conditions were imposed in the simulations,

the agreement needs to be deemed as being good.

The corresponding wall loss curves are presented in Figure 78. It can be seen from the figure that there are discrepancies. It can be reviewed from the cited references (experimental and numerical) on the impactor performance that the characteristic wall loss curve exhibits a sharp and narrow peak near the 50% cutpoint and tapers off on either sides of the cutpoint. Whereas the numerical predictions are consistent with this observation, the experimental wall loss curve displays a behavior that is not consistent with the numerical results, and, the results presented in the literature. This is possibly due to the reason that the number of experimental points is insufficient to capture the wall loss curve. Other important observations on the efficiency and wall loss curves would be discussed later in the section.
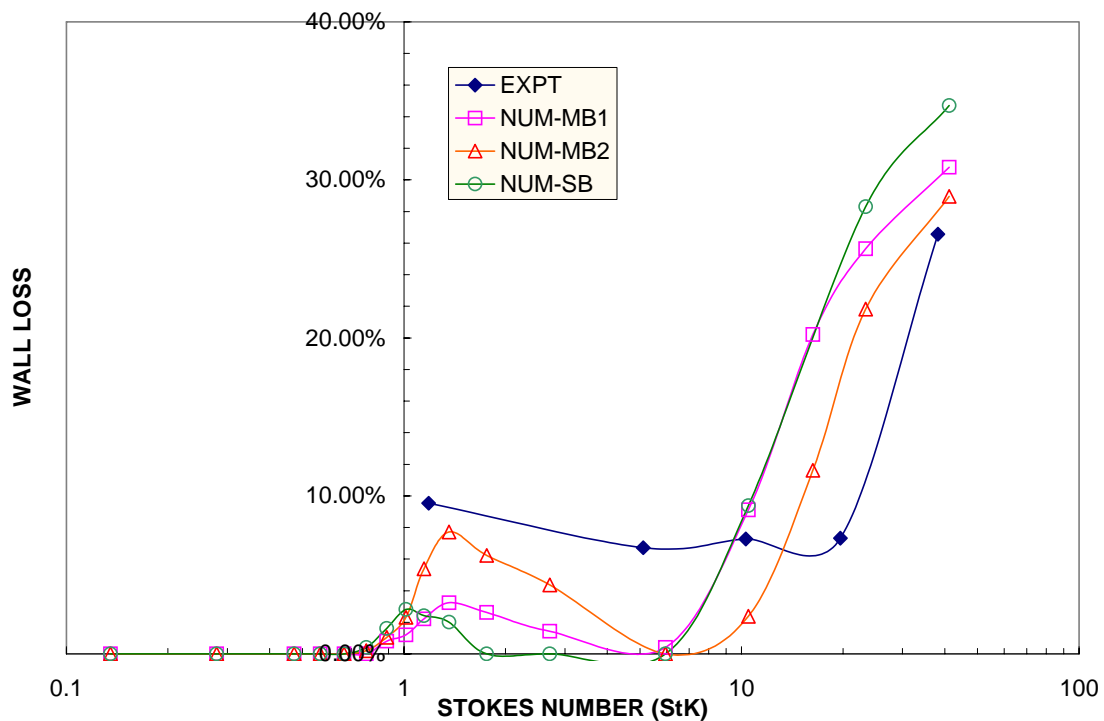
Fig. 78. Comparison of the experimental wall loss curve against numerical predictions.

It is to be noted from Figure 77 that all the three numerically predicted efficiency curves overlap until an efficiency value of 75%. This also corresponds to the point at which the experimental and numerical curves crossover. The subsequent mismatch between the numerical efficiency curves occurs due to the difference in the wall loss spectrums presented in Figure 78. It seems that the different blocking and meshing operations performed on the inlet convergence section has an influence on the resolution of the flow field in this section of the impactor geometry. The low Stokes number particles are less affected by the happenings in this section, as they are more susceptible to the flow behavior that is predominant in the throat section of the geometry. However, the higher stokes number particles carry the information that they imbibe in this section of the geometry, due to their inertia. This is the reason for the observed difference in the curves for higher efficiency values above 75%.

VI. E. Conclusions

Simulations have been performed on the LSVI whose performance was experimentally determined at the Aerosol Technology Laboratory. Simulations were performed on a fictitious model that was constructed based on a worst possible combination of critical geometric parameters (with asymmetries on both the vertical and horizontal plane), that would give a conservative estimate of the LSVI performance. Initial simulations were performed on a preliminary model that was built with a basic outline of the LSVI geometry. However, refinements were carried out to the preliminary model by including more geometric information and subsequent studies were performed on the refined model.

The effect of the depth of the inlet convergence section adopted in the simulated model on the predictions of the impactor performance was studied. Moreover, the effect of multi-blocking of the inlet convergence section of the impactor on the simulation predictions was investigated. When the simulation results were compared against experimental data[41], it was found that a fair agreement was obtained, considering the fact the simulated model was a worst case representation of the LSVI, and, the boundary conditions imposed on the simulated model were different from the experiment.

It is customary in the literature to present only that part of the efficiency curve in which the value of the Stokes number in the abscissa corresponds to 100% efficiency in the value of the ordinate. The rest of the region that includes the higher Stokes number particles is not normally presented. However, in this study, for the first time, simulations were performed for particle sizes beyond the 100% efficiency value and it was shown clearly that the minor flow efficiency starts dropping after a particular Stokes number value is reached. This important observation was also corroborated from the present experimental results[41] and from the results of one of the recent studies presented in the literature[40].

Some of the other important observation from the results of the present study and the study in the previous chapter are summarized below:

(a) It was shown in the previous chapter that though the virtual impactor is operated at different throat Reynolds number, when the efficiency curves are Stokes scaled, the curves would overlap to a unique curve, with only a small difference near the 50% cutpoint Stokes number value. The observed

difference arises due to the different wall loss curves for the cases. This is consistent with the present experimental results[41] and the experimental results presented in reference 32. As stated already, it seems that in this respect, the virtual impactor efficiency curves differ from the real impactor efficiency curves, which are a function of the Reynolds number.

(b) For the first time, simulations were performed on an impactor that was asymmetric and offset on both the horizontal and vertical planes. Effect of this asymmetry and the other critical geometric parameters on the flow split to the major flow outlets, and, the behavior of different sized particles, were illustrated with particle tracks for the different particle sizes.

(c) It was seen that the flow split to the two major flow outlets were not equal for the same imposed boundary conditions on the patches. There was a 3% difference between the flows on the outlets i.e., on one of the outlets, the flow was 46.5% of the total flow, 3% more than the flow on the other outlet.

(d) The difference in the flow-split ratio between the minor flow outlets also affects the distribution of the low Stokes number particles arriving at the outlets. While the smallest particles (0.50 μm AD) are less sensitive to the difference in the flow split and distribute nearly equally between the outlets, as the particle size increases, the inequality in the distribution of particles increases. For a particular particle size, all the particles were collected in only one of the minor flow outlets. This phenomenon was confirmed during experimental evaluation of the impactor performance.

(e) It was shown clearly that the particle behavior is very sensitive to geometrical parameters and, wall losses for higher Stokes number particle would be accentuated by the asymmetry in the impactor geometry. This is due to the reason that the heavier particles acquire enough inertia in the process of getting accelerated in the convergence section and don't respond to the behavior of the flow field. Instead, they are found to just shoot through the throat region and impinge on the curvature in the receiver section or on the walls of the throat in the receiver section

(f) A study was conducted to determine the minimum depth of the inlet convergence section that needs to be adopted in the simulation model, to get consistent efficiency curve predictions. It was found that the ratio of the width of the inlet patch to the throat should at least be 15, to get consistent prediction of the curve, for the lower Stokes number particles. However, higher Stokes number particles that were released from the edges of the inlet patch were found to impinge on the wall regions near the corners of the inlet patch and had to be discounted from the total number of particles used in the simulation to determine the impactor efficiency curve. This was causing a bias in the predicted efficiency values in the curve for the higher Stokes number particles. This was overcome by increasing the depth of the section to that value where the ratio of the width of the inlet patch to the throat was order of 25. This decreased the percentage of the highest Stokes number

particle (10.00 µm AD) that are lost to a value of approximately 7% of the total and 4% for next lower Stokes number particle (7.50 µm AD).

(g) Another study was conducted to minimize the above problem and also the problem that arises from mesh propagation errors. A multi-block configuration for the inlet convergence section was adopted by breaking the section (that was a single block previously) into four different blocks. Two different mesh options had to be investigated to maintain continuity of the mesh density across adjacent blocks. In one case it was found that bias remained the same, as in the single block. However, in the other case it was found that the percentage of the highest Stokes number particle (10.00 µm AD) that are lost to a value of approximately 9% of the total and 5.8% for next lower Stokes number particle. The predicted impactor curves for the three cases were found to be consistent till an efficiency value of 75%. However, for the rest of the Stokes numbers, there were differences between the curves, owing to their different wall loss spectrums. This is possibly due to the difference in the resolution of the velocities that arise from the different blocking and meshing operation performed for the cases.

CHAPTER VII

MODELING TURBULENT FLOWS WITH AEROSOLS

In the previous chapters, simulations were performed on different types of inertial impactors. In the case of the real impactor, the geometry was simple and the block structuring of the domain was straightforward. Cartesian system with rectangular blocks was adopted in the construction of the domain and no curvature effects were present. In the case of the virtual impactor, the geometry was more complicated and curvature effects were introduced in the domain. As a result of the above, block structuring of the domain was difficult. However, the flow conditions were laminar in both the real and virtual impactor case.

In the present chapter, studies were performed to assess the suitability of the code for the prediction of aerosol transport, in turbulent flow. As a beginning, a simple turbulent pipe flow with aerosols was simulated[42]. The simulated experiment is considered as a standard in the field of aerosol transport under turbulent flow conditions. The predictions of the code are compared against experimental data. A detailed analysis of the physical and technical aspects related to the turbulence dispersion model available in the code is presented.

VII. A. Brief Description of the Turbulent Flow Experiment

In this experiment, the behavior of different sized aerosols under turbulent flow condition, in a circular pipe, was determined. An excellent description of the experimental setup, conduct and the results are presented in reference 42. A brief description of the above information is presented in the following paragraphs.

In essence, the primary flow was considered to be a fully developed, turbulent flow of air, in a vertical glass pipe having an internal diameter of 0.0127m and a length of 1.02m. The measured rate of deposition of monodisperse uranine-tagged olive oil droplets (density of 910 kg/m^3) of sizes ranging from 1.4 to 21.0 μm, for two different flow conditions corresponding to Reynolds numbers of 10000 and 50000, were reported. The flow orientation was facing downward (aided by gravity) and the pipe was divided into 8 equal sections of 0.127m each. An average deposition result that was measured over a series of experimental runs was reported for 0.508m of the test section, comprising sections 3 to 7.

VII. B. Simulation Details

To simulate the present pipe flow experiment, two approaches can be utilized. In the first approach, advantage can be taken of the flow symmetry in the pipe and a one-half, or, a one-quarter model of the geometry can be constructed in rectangular geometry, by utilizing the two-dimensional axy-symmetric option available in the code. The other option would be to construct the pipe geometry, as it is, and perform the simulations. Even though turbulent flows are random, chaotic and three dimensional, the former approach can be justified from the technical viewpoint of RANS computations and the two-equation modeling approach to resolve turbulence. However, a physical understanding of the results based on visualization is not possible. So, in the present study, the second approach was preferred.

A model of the pipe geometry with a pipe diameter of 0.0127m and an L/D (length-to-diameter) ratio of 65 was constructed. This was done with a view to ensure

that fully developed flow conditions would exist beyond an L/D ratio of approximately 25, as a normal inlet velocity profile is specified at the inlet. The simulation was performed for a Reynolds number of 10000. The k-ε turbulence model was chosen to represent turbulence for two reasons, namely, (i) there are no curvatures in the flow, and (ii) to ensure consistency with the particle dispersion model that would be used later to account for the effects of fluid turbulence on particles.
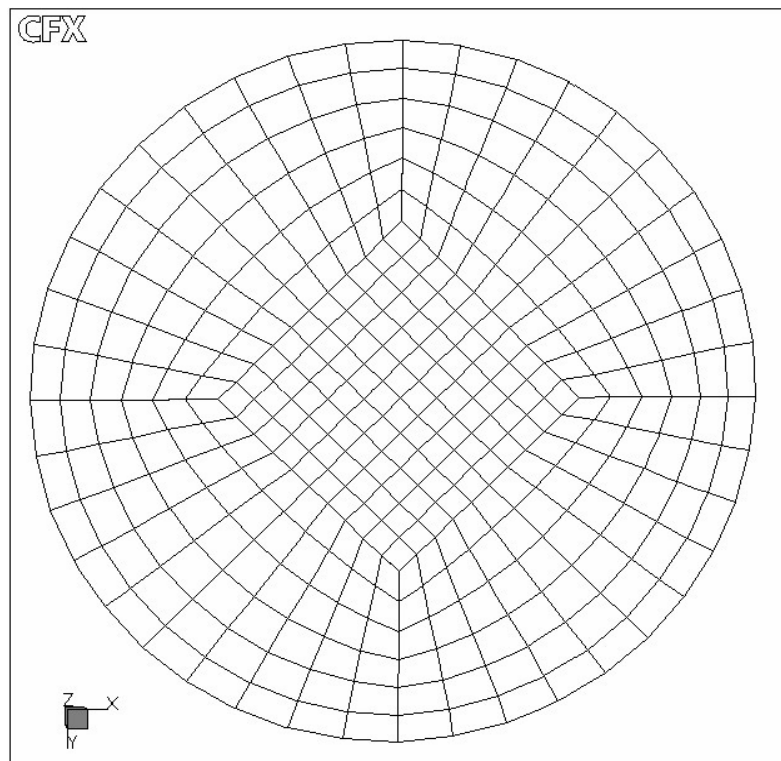
Fig. 79. Block-structuring at the inlet patch of the pipe geometry

The concept of multi-block grid was discussed in the previous chapter. CFX-4 solver manual discusses the adverse effects that would arise as a result of the absence of this grid structure. The pipe geometry was constructed according to the directions provided in the manual. A five- block structure is required as a minimum precondition

for ensuring a proper, structured grid for the pipe geometry. Figure 79 illustrates the block structuring adopted in the inlet patch of the pipe.

Normal inlet velocity conditions were specified at the inlet patch. Free boundary conditions are automatically assigned to the outlet patch by the code, based on mass conservation, and, all the surfaces not described by the other conditions are automatically treated as walls with no-slip conditions. Initial conditions for turbulence parameters can be specified in terms of k and ε values or in terms of the turbulence intensity and a dissipation length scale. As an estimate of the turbulence intensity value was not provided in the original study, a value of 5% was assigned. After consultation with one of the present faculty involved in the turbulence research[43], the Taylor microscale[11] was computed for the flow conditions and assigned as the initial condition for the dissipation length scale.

As the standard k-ε turbulence model has been chosen to represent turbulence, it is necessary that the first grid point in the normal direction to the wall needed to be beyond a non dimensional distance, computed in terms of the well known y^+ value[11], of 11. A trial and error procedure was resorted to determine the mesh density that would satisfy the above condition, by assigning different grid densities, on the line in the normal direction to the flow. After a series of repetitions, it was found that a grid structure corresponding to 42500 cells satisfied the criterion required.

A convergence criterion of less that 0.1% of the inlet mass flowrate was adopted and the simulation was continued beyond the iteration number that satisfied the above conditions, until such time the residuals were found to be invariant with the number of

iterations. At the completion of the run, particles of different sizes were introduced as a point source from the center of the pipe, at an axial location corresponding to an L/D ratio of 25, with an initial velocity set equal to the average fluid velocity in the pipe. The particle penetration, defined as the fraction of the particles that reach the outlet of the pipe, compared to the total number of particles seeded at the inlet, was monitored.

Initially, particles of different sizes ranging from 1 to 20 μm AD were introduced and the percentage penetration was determined, without the inclusion of the optional forces. This was to ensure if, in the absence of any turbulence and other forces, all the particles are able to reach the outlet. The turbulent dispersion force and the pressure gradient force options were activated later and subsequent studies were performed with the inclusion of the forces. It is to be remembered that the virtual mass force is included by default by the code, when particle transport calculations are performed.

As the turbulence dispersion (TD) force adopted in the code is not a conventional body force but a force of stochastic nature, a study was performed to determine the total number of particles to be used to obtain the necessary statistical details. In the case of laminar flow, it was determined that the code predictions of the efficiency curve would be independent of the number of particles used in the simulations, for a total particle number in the order of 500. This was taken as an initial number and the total number of released particles was increased slowly till 5000, and the penetration curve predictions were examined for variations. This study was performed for a particle size of 1 μm AD. The total number of particles to be used in subsequent simulations was inferred from the results of this study.

VII. C. Results and Discussion

The important details on the simulations are summarized in Table XI. The results

of the above study are presented in this section and discussed

TABLE XI

Important Geometrical and Numerical Parameters of Interest

GEOMETRICAL DETAILS			
PIPE DIAMETER = 0.0127 m PIPE LENGTH = 1.02 m L/D = 80		FLUID:AIR AT STP FLOW RATE = 1510 m^3/s AVERAGE VELOCITY = 11.686 m/s Re = DV$_0$ / v = 9894	
NUMERICAL DETAILS			
TOTAL # OF COMPUTATIONAL CELLS =42500 MASS SOURCE RESIDUALS = 4800 (CORRESPONDING TO 0.1% INLET MASS FLOW RATE)			
EQN	DIFFERENCING SCHEME	SOLUTION ALGORITHM	UNDER RELAXATION FACTOR
U,V,W	HYBRID	STONE3D	0.65
P	CENTRAL	ICCG	1.00
k , ε	CENTRAL	LINE SOLVER	0.7

Figure 80 presents the mean velocity profiles obtained at different distances from

the pipe inlet, represented in terms of the L/D ratio, along with the profiles at the inlet

and the outlet patches. The profile is extracted on a straight line that runs at the center of

the pipe on the vertical direction, from wall to wall. Compared to the imposed normal

inlet velocity profile, it can be seen that the velocity profile for the different L/D ratios is

developed well enough. It can be seen that the profile can be split into two distinct

regions, one near the wall and the other toward the pipe center. The point where the

transition takes place is the point where the first grid point is situated.
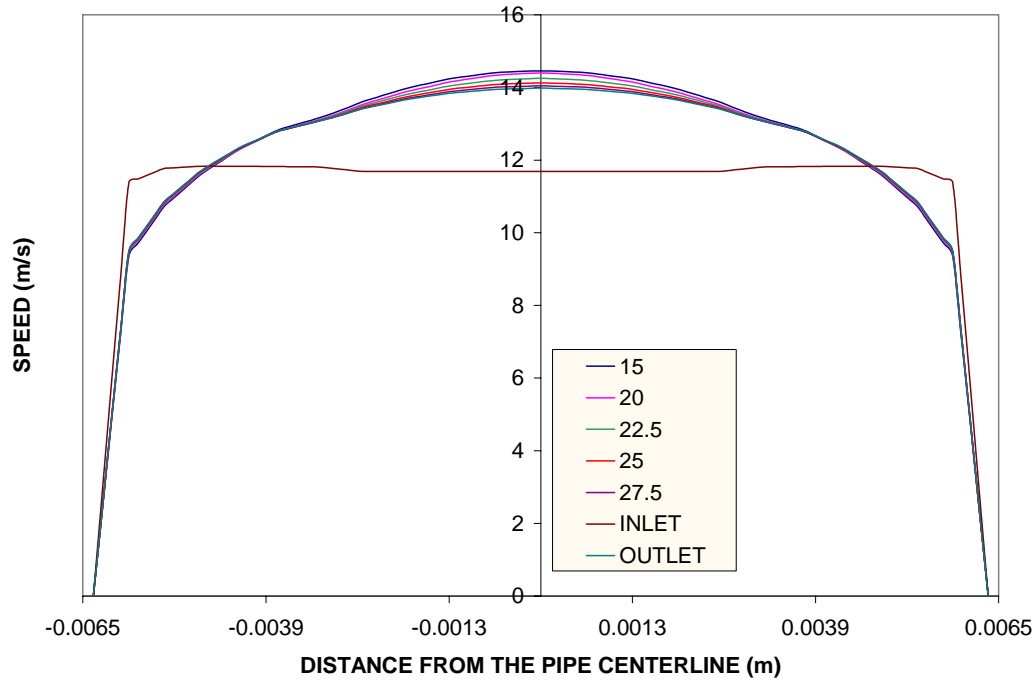
Fig. 80. Comparison of the predicted mean velocity profile at different L/D ratios.

The linear profile in the near-wall wall region is obtained from the universal law of the wall[11]. The conservation equations for the turbulence quantities, k and, ε are solved for, in the rest of the pipe and the values are matched at the interface point. Except for minor variation in the middle 50% of the pipe, it can be seen that the profiles are matching. If the region in the middle 50% of the pipe is focussed, it can be seen that the centerline velocity decreases very slowly, as the L/D ratio increases. There is very little variation between the centerline velocity at the outlet patch and that at L/D ratios in excess of 25. This indicates that the flow is fully developed beyond an L/D ratio of 25.

A theoretical consideration[44] shows that the ratio of the average velocity to the centerline velocity should be in the range of 0.79 to 0.87, if it is assumed that the flow profile follows the one-sixth or the one-tenth-power law profile representative of a fully

developed turbulent flow. Figure 81 presents the variation of this ratio as a function of the L/D ratio. It can be seen from Figure 81 that after a steep rise in the initial stages, the ratio attains a nearly constant value of approximately 0.835, for the rest of the pipe region.
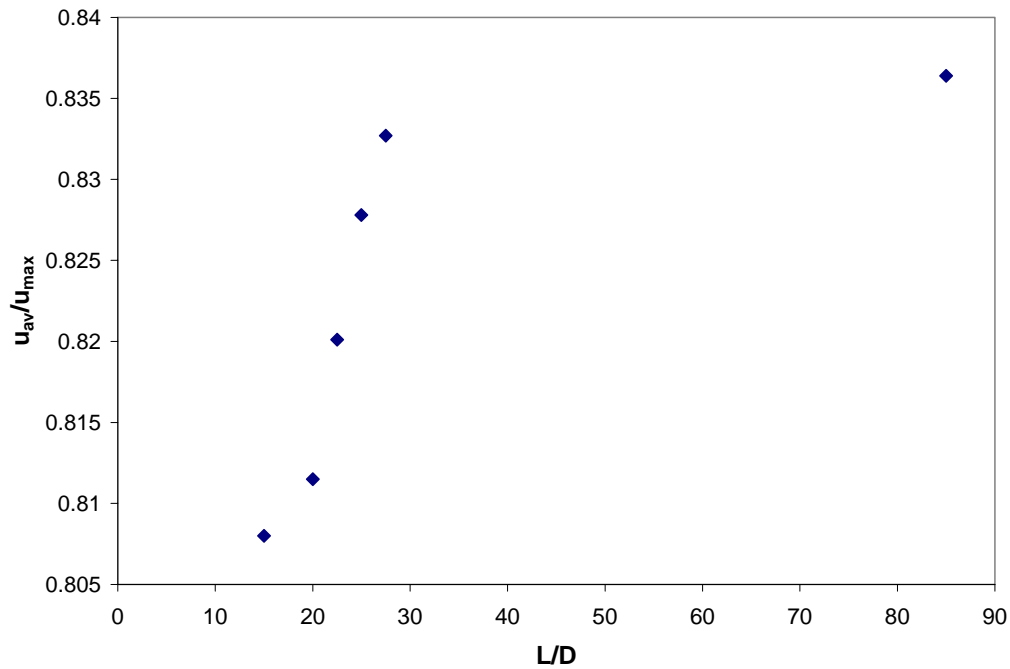
Fig. 81. Variation of the ratio of the average to the maximum velocity as a function of the L/D Ratio.

If calculations are performed based on an assumption of the famous one-seventh power law profile, this ratio is found to be 0.82 approximately. In this respect, it seems that the value of 0.835 obtained for the present case is a very slight overprediction, considering the fact that Reynolds number is only 10,000. However, the estimate should only be taken as an indication and except for this minor aberration, on an overall basis, the fact that the obtained flow profile is fully developed cannot be neglected.

Figures 82 and 83 present the profiles of the turbulent kinetic energy, k, and, dissipation, ε, at the axial location where the particles were seeded. As stated before, it is to be remembered that the profiles are obtained on a vertical straight line that runs from wall to wall, across the pipe diameter.
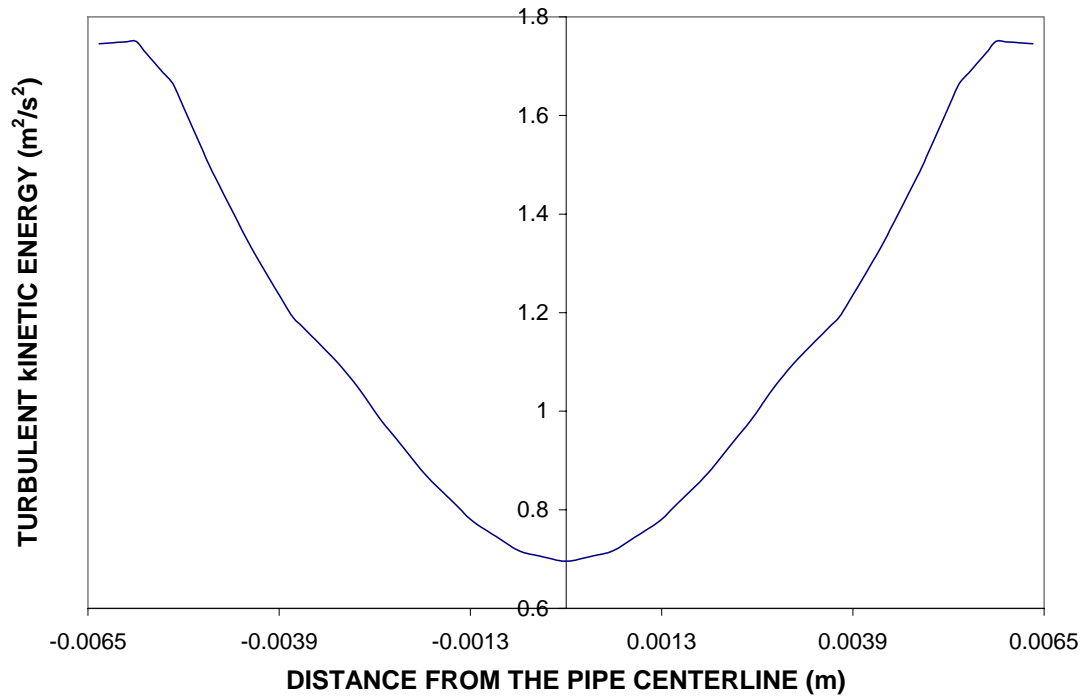
Fig. 82. Radial profile of the turbulent kinetic energy, k (L/D =25).

As before, the straight line at the edge of the profile represents the k value obtained from the Universal Law of the Wall. The resolved profile in the rest of the pipe shows a parabolic trend with a minimum value at the center of the pipe, that is less than half of the maximum value. The dissipation, ε however, shows a trend that is slightly different from k, with sharp change near the walls and a flatter central region. The minimum value is attained in the central region and its magnitude is orders less compared to the maximum value.
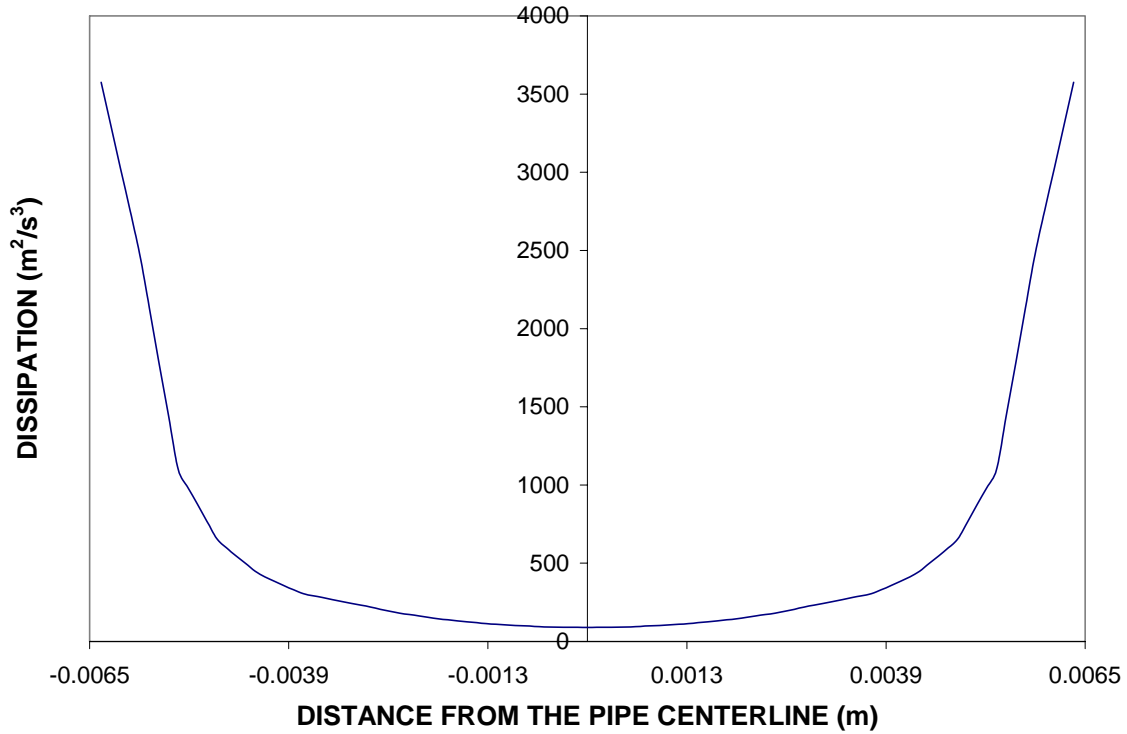
Fig. 83. Radial profile of the dissipation, ε (L/D =25).

In the next couple of figures, particle tracks of 5 nos. of 1 μm AD particles introduced into the flow are presented. Figure 84 indicates the tracks without the effect of turbulence dispersion and Figure 85 indicates the tracks if the turbulence dispersion force is included, when the particle transport calculations are performed. It can be clearly seen from the figures that in the absence of the TD force, the particles follow a straight path (flow streamlines) and exit the pipe. However, with the inclusion of the TD force, each particle is randomly dispersed and follows different zigzag paths, ending up either at the wall or at the exit. These figures give a clear indication that the TD force option available in the code is functioning properly, in the sense that the particles are dispersed differently, though they all start from the same point.
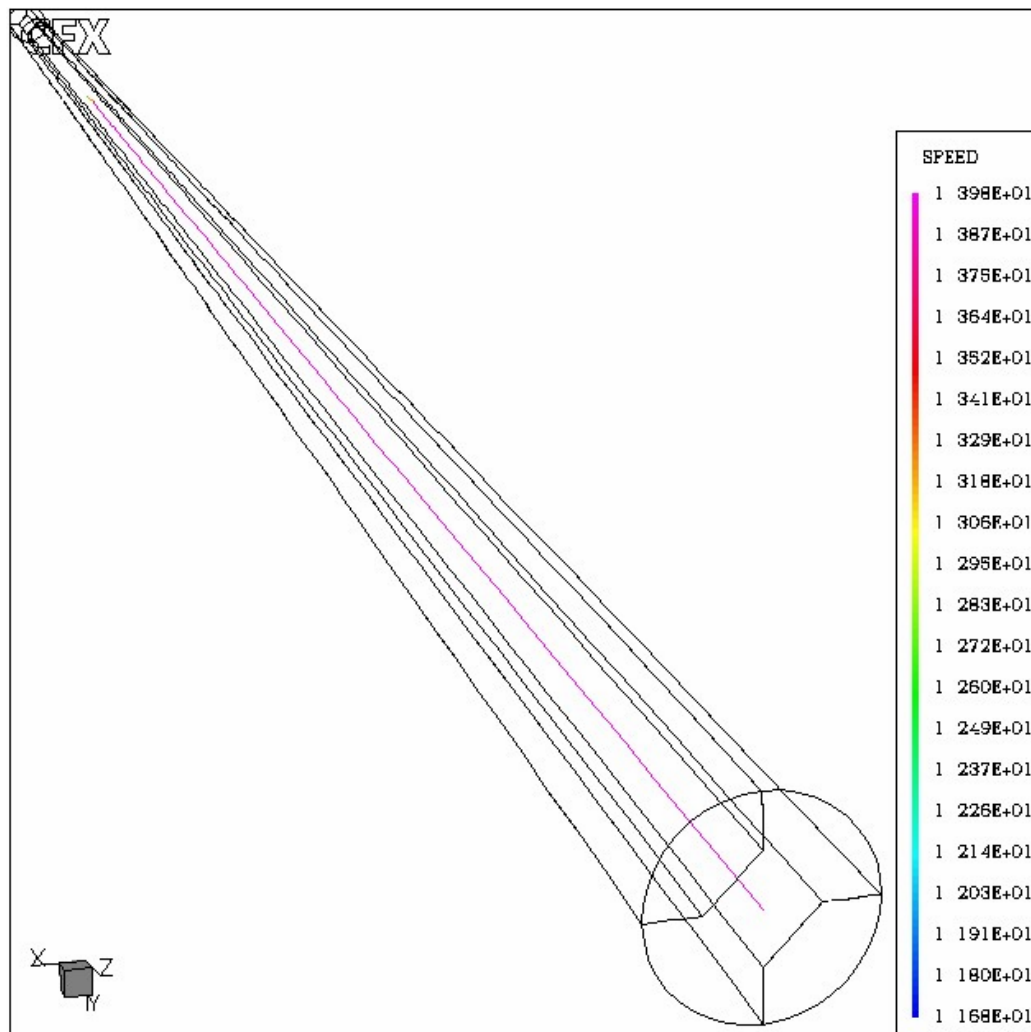
Fig. 84. Particle tracks for 5 Nos. of 1 μm AD particle without the turbulent dispersion force.

A closer look at the tracks shown in Figure 84 also indicates the fact that though the particles are introduced into the flow with a velocity set equal to the average flow velocity, they attain equilibrium with the local fluid velocity conditions. The velocity equilibrium condition was achieved as soon as they are introduced into the flow. For the rest of the journey through the pipe, the particles follow a straight line with the same velocity.
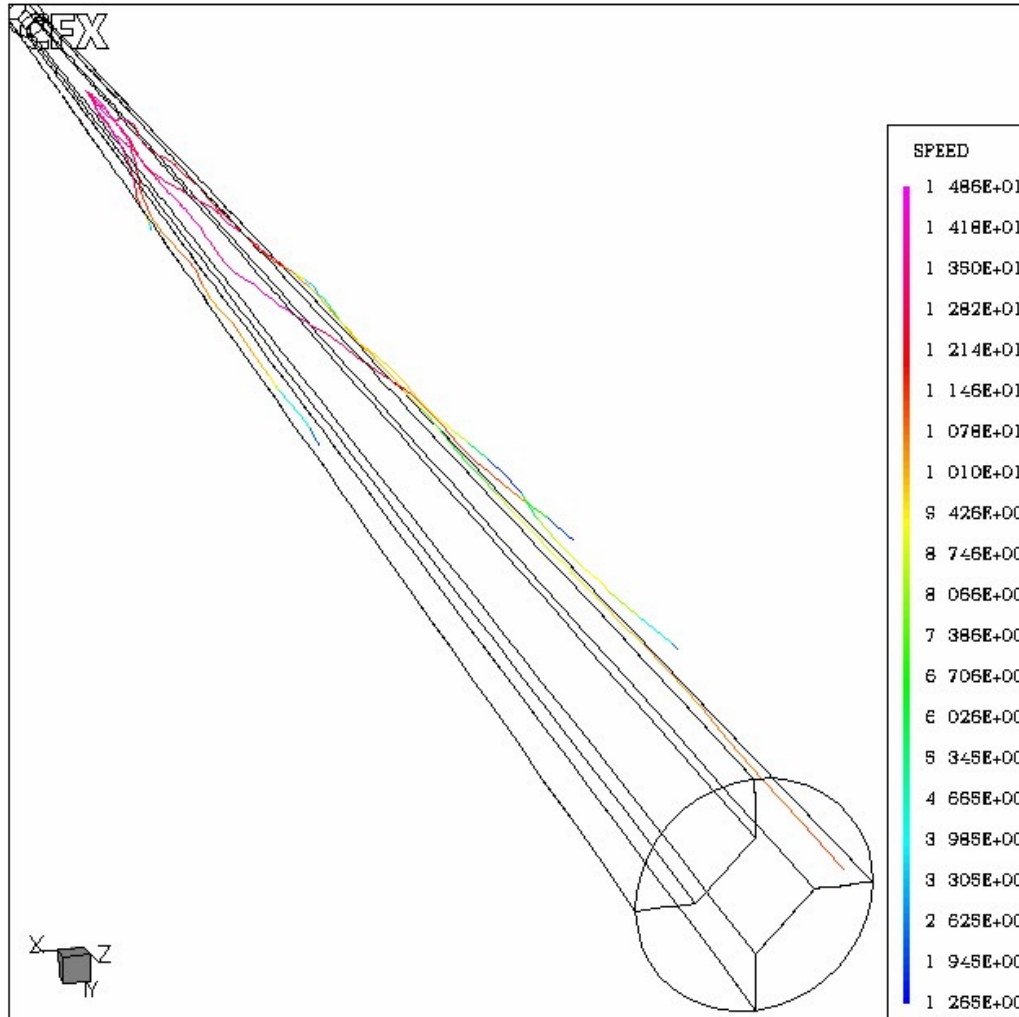
Fig. 85. Particle tracks for 5 Nos. of 1 μm AD particle with the turbulent dispersion force.

In the present case, with the turbulent dispersion force activated, the particles start dispersing randomly in different directions. Four of the five particles end up at different locations on the pipe wall, whereas, one of them exits the pipe. In this case also, equilibrium with local fluid velocity conditions is attained as soon as they are introduced into the flow. However, as the particles get dispersed into different regions inside the pipe, their velocities are found to be different from each other.

Figure 86 presents the results of the study performed to determine the total number of particles that are required to be used in the simulation, to obtain particle independence of the predicted results. It can be seen that the penetration value is constant around a value of 32%, as the number of particles used in the simulation is increased from 500 all the way until 5000.
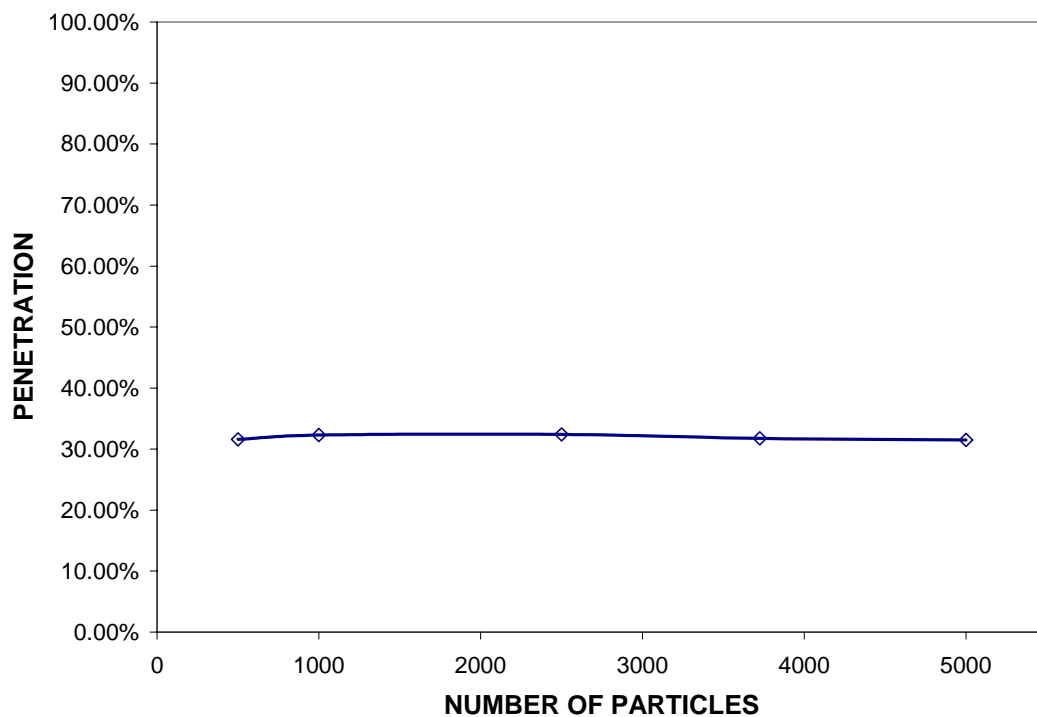
Fig. 86. Penetration predictions as a function of the total number of particles used in the simulations (for a 1 μm AD particle)

The code manual recommends that the total number of particles to be used in turbulent flow simulations with particles should atleast be an order of magnitude higher than the value used for the laminar flow conditions. If this rule of thumb is adopted along with our previous laminar flow results and the present results, it seems that the total number of particles needs to be in the order of 5000, to obtain predictions that are

independent of the particle number. This was the number that was adopted in the studies performed subsequent to the present one.
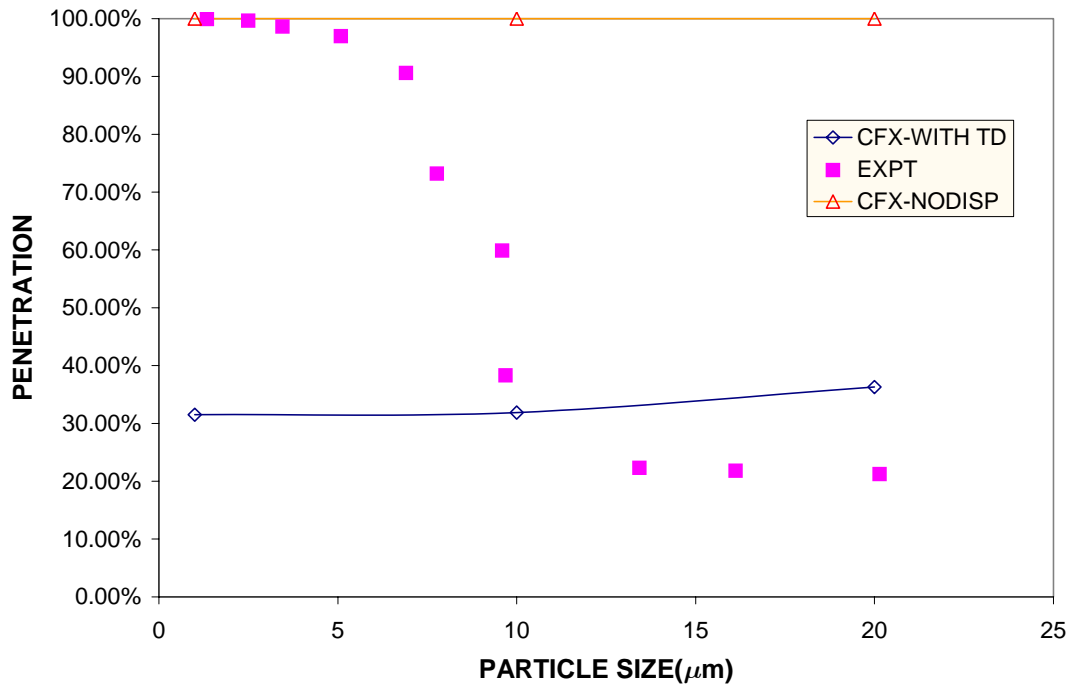
Fig. 87. Comparison of the penetration predictions of the code with and without the turbulent dispersion model against experimental data.

In Figure 87, a comparison of the code predictions for the penetration of different particle sizes, against the experimental results obtained by Liu and Agarwal[42] are presented. The code predictions obtained without the activation of the turbulent dispersion model is labeled as CFX-NODISP and that with the TD model activated as CFX-WITH TD. It can be seen that in the absence of the TD model, the penetration is 100%. This is the condition when only the drag force is dominant and the other forces are absent. It can be seen that the particles follow the streamlines and the predicted penetration value is 100%, as it should be, for all particle sizes.

However, when the dispersion model is activated, it is seen that there is no correspondence, whatsoever, between the code predictions of the penetration and the experimental results. The experimental penetration value is around 100% for smaller particles and starts decreasing rapidly for particles above 5 μm AD. For a particle size of 13 μm AD the penetration had decreased to nearly 20%. The penetration curve is seen to flatten out for the rest of the particle sizes, all the way till 20 μm AD.

The computationally predicted penetration curve is seen to be nearly flat in the particle size range of 1-10 μm AD with a value of around 31%, even for a 1μm AD. However, as the particle size increases to 20 μm AD, the penetration increases to around 36%. This behavior is completely in contrast to the experimental observation and is physically unrealistic.

A detailed literature survey was undertaken to investigate if there are studies reporting the use of the particle transport algorithm in the code, under turbulent flow conditions. It was found that there was at least one study in which CFX-TASCflow[3] had been used to study the deposition of aerosol particles in the mouth-throat region, assuming turbulent flow conditions[45]. This is a code in the CFX series of CFD codes that specialize in turbomachinery applications; the dispersion model is the same in both the codes. In fact, the purpose of the above study was to investigate if the k-ε based turbulent modeling approach present in the code was suitable for estimating aerosol deposition. The numerical predictions were compared against experimental results.

As in the present case, the authors found a good agreement between the code prediction and experimental results for particle transport under laminar flow conditions.

However, the code predictions of the particle deposition under turbulent flow conditions were found to be thrice the experimental value. The reported result was for a 4.8 MMD (mass mean diameter) particle. They concluded that the discrepancy is due to a combination of different factors that arise from

(a) using the two-equation turbulence modeling approach that has insufficient physics in it to resolve the fluid behavior, in a complex geometry as the human throat, and,

(b) Complication added to this by the dispersion model that uses the parameters obtained from the turbulence model to generate the characteristic parameters that is reflected on the particle behavior.

VII. C. 1. Discussion

Computational modeling of turbulent flows with aerosols is a very interesting and challenging problem. There are important two aspects involved in the computational prediction of the aerosol behavior under turbulent flow conditions. The first aspect is regarding the resolution of the details of flow and the second aspect is related to the effect of the resolved flow field on the particles.

In the case of laminar flows, resolution of the flow field is simple and straightforward, as the streamlines are straight. Once, the flow field is resolved, the drag force is the only force of major significance to be accounted for, for the present case, during the particle transport calculations. Inaccuracies in the solution can only arise from an improper grid on the domain and the order of the differencing scheme used in the discretization phase of the governing equations. The details of the flow field can be

resolved to a good accuracy, by employing a fine grid on the domain. If need be, more accurate differencing schemes can be employed in the discretization.

However, in the case of turbulence flows, the picture is completely different. The turbulent flow field is random, unsteady, chaotic and three-dimensional[11]. The limitations from a computational viewpoint to resolve the finer details of turbulence and the need for a time-averaged modeling approach were already introduced in Chapter II. At this juncture, it is to be remembered that the two-equation modeling approach, is the most popular form of approximation that is prevalent in the CFD community, due to its simplicity and computational ease, to extract details of the turbulence in the flow field.

It is known that the k-ε model can handle evolving turbulent flows. The evolution referred here is with respect to the mean flow alone, the turbulent scales assumed to be intricately coupled with the mean velocity field. Specifically, the model assumes production and dissipation to be close to each other, while developing an expression for the eddy viscosity. In the process, it neglects the anisotropy in velocity fluctuations. Also, the details of the turbulence obtained from a two-equation model are time-averaged and not instantaneous. It will be seen later that, this fact has important implications on the particle transport calculations.

Having obtained some details of the turbulence from the two-equation model, the effect of the fluid turbulence is conveyed to the particles by the Eddy Dispersion Model (EIM), as was seen in the second chapter. In the EIM, a stochastic force known as the "turbulent dispersion force" is introduced on the particles, in addition to the drag force, to account for the dispersion of the particles, due to the fluid turbulence. The

characteristic parameters of the above force are computed from the details of the turbulence obtained from the two-equation model, based on some simplified assumptions. The predicted aerosol particle behavior in turbulent flow conditions is a combined effect of all of the above features.

In the previous section, it was shown that the details of the mean flow are in fair agreement with the theory. In one of our earlier studies on turbulent flow in pipes, it was shown that the mean flow is resolved fairly accurately, by the available turbulence models in the code[46]. It is to be believed that the turbulence details are resolved satisfactorily, within the framework of the model assumptions, as the flow is simple and does not involve mean streamline curvature and other complications. However, there is an important aspect of the near-wall resolution of the turbulence details that will be discussed later.

(a) Analysis of EIM

As a confirmation of the details of the mean flow field was obtained, attention was focussed on the turbulent dispersion model. The original work of Gosman and Ioannides[18] was reviewed to understand the functioning of the turbulent dispersion model (EIM). It was found that the model was developed to account for the effect of fluid turbulence on the dispersion of the droplets that evolve from the spray nozzle of liquid fuelled combustors.

In modeling the effect of fluid turbulence on the particles using the EIM, there are two most important issues. The first one is the requirement of the instantaneous velocity of the particle at every time step, at the particle location. The instantaneous

velocity is the sum of the mean and fluctuating components. This value is required in the process of integrating the particle force-balance equations. While the mean flow velocity is obtained from the solution of the RANS equations, there is no possibility of obtaining the value of the corresponding fluctuating velocities, unless the turbulent field is resolved using the LES or the DNS based approach.

However, in cases where the turbulence details are obtained using the two-equation modeling approach, the fluctuating part of the instantaneous velocity is generated artificially from the value of the turbulent kinetic energy (k), corresponding to the node in which the particle is present. This is the approach used in the EIM to generate the fluctuating velocities.

The second aspect of importance is the way in which the fluid turbulence interacts with particles. It is assumed that the turbulence flow field is comprised of a series of eddies whose time and length scales are determinable from the local k and ε values obtained from the turbulence field. The way in which the particle-eddy interaction occurs was explained in detail in the second chapter.

Having seen the basic details on the EIM, in the next few paragraphs, a detailed discussion on the possible sources of error that would cause the observed discrepancy in the results would be presented. As a beginning in this regard, some of the basic assumptions in the EIM are presented below:

(a) The turbulence fluctuations are isotropic throughout the domain

(b) After generating the fluctuations from the turbulent kinetic energy, the value is multiplied with a random number whose mean is zero and the standard

deviation is one, to normalize the generated fluctuation velocities to follow a Gaussian distribution

(c) The length and time scale of the turbulent eddies are determinable from the local k and ε values, and

(d) The generated turbulent fluctuations are not correlated in time.

Some of the important observations on this approach are summarized below:

(a) The are no wall boundaries present in the domain that would affect the flow

(b) The source from where the droplets evolve is a point source and is at a fixed location in space

(c) The droplets will be undergoing combustion and will be disappearing from the flow; the possibility of the particles remaining in the flow is small, and

(d) As a consequence of the above, the time-frame over which the dispersion of the droplets occurs due to fluid turbulence is short.

It can easily be inferred that the nature of the problem for which the EIM was developed is completely different from the problem for which the model is being applied. While the EIM was developed to estimate the dispersion of particles due to the turbulent fluctuations in the fluid phase, the use of the model is being extended to estimate the deposition of particles. Clearly, 'dispersion' and 'deposition' are two distinctly separate physical phenomena. It is clear that the suitability of the above model for the present purposes is questionable. Neglecting this important fact, most of the commercial CFD codes (CFX, FLUENT, STAR-CD) have included this model, without distinguishing between the two phenomena.

From a practical viewpoint, assumptions of the EIM that would be violated in applying the model to predict the aerosol behavior in a pipe are

(a) The aerosol is uniformly mixed in the fluid stream and need not evolve from a point source.

(b) Unlike the diesel droplet, the aerosol stays in the flow till it exits the domain or sticks to the wall.

(c) As a consequence, the time frame over which the dispersion effect is present is large.

At this juncture, as a minor deviation from the above discussion, it needs to be pointed out that the particles were released as a point source from the center of the pipe, in the present simulations. It can now be seen why this was done; the intention was to ensure compliance with the assumptions based on which the model was developed. By doing this, errors associated with different mode of evolution of the dispersed phase were eliminated.

In the original case for which the model was developed, the near-wall happenings are of very little importance, as the objective was to estimate the dispersion of the particles. So, efforts were not made to address this issue. In fact, the model was validated (a fair agreement was obtained) against

(a) analytical results for the dispersion of inertialess particles from a point source in homogeneous, isotropic turbulent flow, and,

(b) experimentally measured averaged dispersion rate of individual particles introduced into a turbulent flow downstream of a grid.

There were a couple of other cases for which the model predictions were found to be not so good. However, the authors attributed this discrepancy to the non-availability of definite details about the initial conditions. They also indicated that the model's prediction of the dispersion agreed well for heavier particles but not so well for the lighter particles. In particular, it can be seen that the model developers did not even anticipate that the model would be used for estimating the aerosol deposition in confined wall-bounded flows!

When the model is used to estimate deposition of aerosol particles, the near-wall happenings are of utmost importance, as particle deposition is governed by near-wall mechanics of the fluid-particle interaction. The development of a unified analytical model to represent turbulent deposition of aerosol particles had eluded researchers for decades. Kallio and Reeks[47] have listed a few papers that were solely dedicated to analyzing experimental data and developing a model for deposition. This is an excellent indication of the complexity involved in understanding the deposition process, and provides a hint on the technical difficulties that would be encountered in model development.

Some of the important numerical aspects in the near-wall resolution of the flow field, within the realm of the present modeling approach, are discussed. It was mentioned in the previous section that the first grid point in the normal direction to the wall was placed in the vicinity of the non-dimensional distance equal to 11, to satisfy the requirements of the turbulence model. It was also indicated that for the near-wall region, the universal law of the wall is assumed to hold good[11].

However, the universal law of the wall is strictly valid for flows with Reynolds number in excess of 50000. The model constants of the k-ε turbulence model are obtained from high Reynolds number turbulent flow data. In the process of using the standard k-ε model to capture turbulence details, we are indirectly forced to use the law of the wall. This would be inappropriate for the present case as the Reynolds number is around 10000, and introduces an uncertainty in the obtained near-wall turbulence profiles. This, in turn, introduces an error in the fluctuating velocities generated in the near-wall region, based on the 'k' values obtained from universal law of the wall.

This error can be overcome if the low Reynolds number k-ε turbulence model, in place of the standard k-ε turbulence model. Under such a condition, the natural law of the wall formulation can be dispensed with. However, as the equations will be solved to the wall now, an extremely fine grid resolution is required in the near-wall region to capture the steep gradients. Further information on this aspect will be discussed later.

From a physical viewpoint, it is to be understood that the boundary layer thickness starts decreasing with increasing Reynolds number, and the mean velocity profile starts getting flatter. For the present case, the thickness of the boundary layer should be greater, as the Reynolds number is around 10000. The mean velocity profile should be close to a 'one-sixth' power law profile, instead of the standard 'one-seventh' profile[44], that is representative of high Reynolds number turbulent flows.

In addition to the above, the fact that the flow is not a free-shear flow as in a round jet, but, a boundary layer flow, introduces further complications. The presence of wall not only introduces variation in the mean velocity profile at any cross section in the

domain, but also on the fluctuating velocities. The components of the fluctuating velocity transport the particles away from the mean flow and responsible for the particle deposition. Presently, this information is not available in the EIM. This is an additional limitation in using the EIM to wall bounded flows.

The next aspect of importance in the understanding of the EIM is the determination of the eddy length and time scales. As described in the second chapter, the eddy length and time scales are determined based on the turbulence details obtained from the k-ε model. Again, the near-wall determination of the length and time scales would be in error, due to the same reasons that were described earlier, namely, use of the universal law of the wall. However, these two aspects related to the generation of the artificial fluctuating velocity and the estimation of the length and time scales, in the near-wall region essentially determine the deposition process. More details on this front would also be presented later.

(b) <u>Literature Survey</u>

Having thoroughly analyzed the EIM and the details of the present simulations, a literature search was performed to know if this model had been used to predict aerosol dispersion and deposition. This was done with a view to gain further understanding about the technical details of the various parts of the model, if it is used for the prediction of aerosol deposition. Some studies found reported in the literature are reproduced here for the sake of completing the present investigation and embarking on the future course of action.

The first and the most incisive of the studies on the EIM and several other stochastic models available in the literature for their predictions of particle dispersion was performed by MacInnes and Bracco[48]. In their study, the characteristics of various stochastic models were examined for predictions on particles that have very small inertia, both for homogeneous and non-homogeneous flows. They clearly showed that the models based on the present approach, as the EIM, give satisfactory dispersion prediction for homogeneous flow. However, for the inhomogeneous flow case, the predictions are completely wrong.

The inhomogeneous cases considered were a self-similar turbulent mixing layer and an axi-symmetric jet. It was shown that in the case of the case of the mixing layer, though uniformly mixed at the inlet, the EIM tends to disperse the particles to such an extent that the core region is depleted of particles. Due to model artifacts, there is an incorrect pumping effect on the particles from the core and subsequent accumulation near the low-velocity edge of the mixing layer.

It was found that number density, relative to the correct value, increased by up to 550% at the edges and depleted to less than 50% at the core. After a thorough analysis, they showed the imposed fluctuation velocity was not divergence free. In other words, the mean of the artificially generated fluctuation velocity imposed in the transverse direction is non-zero. This resulted in a mean leakage of particles in the transverse direction, across the mean streamlines. It is to be recalled here that this is the velocity generated artificially from the local 'k' value.

This is exactly what was observed in the present study where the EIM was used to predict the aerosol particle behavior. Irrespective of the particle size, nearly 70% of the particles are deposited at the low-velocity wall region (For the 20 μm AD particle, however, this number is less by 5%, owing to particle inertia). It is clear now that the problem is inherent to the EIM and there is no remedy.

The other problem associated with the EIM was that the fluctuation velocity sampled for the eddy remained constant throughout the lifetime of the eddy. They showed that this caused the particles to be ejected by turbulent motion from the shear layer, but could not be assisted back into the layer. This resulted in particle accumulation in the free-stream region adjacent to the edge of the layer. They also suggested normalizing the generated fluctuation velocities by multiplying the obtained value with the local turbulence intensity, to overcome this problem and showed that the modified predictions would be improved.

The second study was a more recent one in which simulation was performed on the same case that is being investigated in the present study[49]. They clearly state at the beginning of the study that a proper representation of the primary flow is crucial for the adequate prediction of the particle deposition rate. They state that problems were faced when the conventional k-ε modeling approach was chosen for the prediction of the primary flow, and that the rate of deposition of the small particles was overpredicted. This is exactly what we observed in the present case.

So, instead of solving for the fluid field, they defined the primary field. The axial mean field was obtained from the law of the wall equation and the turbulence quantities

are curve fitted from the DNS results. A number of modifications were carried out to the EIM, some based on suggestions from the literature and the rest based on obtaining agreement with experimental results. After doing all the above modifications, the whole study is then narrowed down to tracking particles in the defined flow field and numerically studying the particle behavior.

Finally, it is shown that good agreement with experimental results is achievable. Further investigations are performed to study the effect of releasing particles in two different ways, first, as a point source at the pipe centerline, and, next, as a uniform release at the pipe inlet. The importance of the time step used in the integration of particle equations on the penetration predictions is also demonstrated.

Most of the above suggestions are practically impossible to be implemented into the CFX-4.4 code as it is a commercial code and this would amount to rewriting the code. However, this study serves as an eye-opener on the complications involved in simulating aerosol behavior under turbulent flow conditions. In addition, it is an excellent reference material for those involved in working on the numerical aspects of aerosol transport, as the important technical aspects related to the modeling are explained in detail.

In the third study, Graham[50] proposed improvements to the EIM, based an analytical considerations and experimental observations, for the dispersion of particles under conditions of Homogeneous, Isotropic and Stationary Turbulence (HIST). This is an excellent study that rigorously analyzes the EIM performance, by dissecting the model into separate parts. The limitations of each of the parts are delineated with proper

illustrations of its performance, and remedies are suggested. There are a couple of observations on this study that are summarized below:

(a) This study basically concentrates on the dispersion aspects and not on the deposition, per se. However, it is to be remembered that proper prediction of the dispersion phenomena is required before devising methods to apply it to deposition. In this respect, this study is important as efforts are made to improve the EIM predictions of particle dispersion consistent with physics.

(b) Because of the above reason, the results of this study would serve as a good guide in the code development stage, where most of the suggestions/conclusions that are arrived at, can be implemented.

The final study of Wang and James[51] exactly addressed the present problem with applying the EIM based dispersion models for the prediction of aerosol deposition in wall bounded flows. Important aspects of this study would be dealt with in detail, in the next couple of paragraphs, as it proposes a solution to the present problem.

It was seen that when using the EIM, the fluctuating components of the instantaneous fluid velocity are isotropically reconstructed from the local $'k'$ value. In the case of wall-bounded flows, this assumption may be valid in the core region, far away from the walls. However, it is known, from both experimental[52] and numerical results[53] that assumption of isotropy does not hold, in the shear-layer near the wall.

The result of the above studies suggested that in the shear dominated near-wall region (approximately till a value of $y^+ = 30$), the fluctuating velocities are strongly anisotropic and the above assumption in inaccurate. It was found that the fluctuation

component in the normal direction, obtained by the isotropic assumption, was grossly overestimated. Moreover, the fluctuation component in the streamwise direction was greater, and, that in the lateral direction was smaller, than the value obtained by the isotropic direction. The normal component was found to be far smaller than the above two components, due to the damping effect of the wall.

It is to be remembered the near-wall region is the most important region from the viewpoint of the deposition of particles. They argued that the above assumption was one of the main factors that lead to the large discrepancy observed in the particle deposition results. To overcome the problem, they suggested the concept of 'damping functions', in which the fluctuating velocities generated by the EIM will be damped, for y^+ values less than 80, to be consistent with experimental observations.

In the 'damping function' approach, three functions f_u, f_v, f_w are introduced corresponding to the three directions, where x is the streamwise direction; y is the normal direction, and z, the spanwise direction. The damping functions f_u and f_v are defined as the ratio of the streamwise and normal velocity components to their values determined by the EIM, i.e.

$$f_u = \left(\overline{u'_x u'_x}\right)^{1/2} \Big/ \left(2k/3\right)^{1/2}, \ f_v = \left(\overline{u'_y u'_y}\right)^{1/2} \Big/ \left(2k/3\right)^{1/2}, \text{ and,}$$

f_w is found from

$$f_w = \sqrt{\left(3 - f_u^2 - f_v^2\right)}.$$

They curve fitted the DNS data[53] to the above framework and expressed the damping functions in terms of the non-dimensional y^+ value as

$$f_u = 1 + 0.285\left(y^+ + 6\right)\exp\left[-0.455\left(y^+ + 6\right)^{0.53}\right],$$

$$f_v = 1 - \exp\left(-0.02\,y^+\right)$$

(38)

They also introduced another modification that is related to the determination of the time scale. It was found in the second chapter that the particle-eddy interaction time is chosen to be the minimum of the eddy lifetime and the time taken by a particle to cross an eddy. However, to facilitate comparison with previous literature[47], they assumed the interaction time to be equal to the eddy lifetime, which is evaluated as $t_e = 0.53 \dfrac{k}{\varepsilon}$.

At this moment, it is worthwhile to quote references 17, 48 and 50 among others, to mention their observations on the fact that different authors had adopted different coefficients in the determination of the length and time scales. The choice of constants seems to have has been guided by reasons that are beyond technical considerations, mostly to fit the experimental results. In this respect, reference 17 also makes another interesting observation about the ratio of the constants being 1.5, while, the constants themselves may be varying independently by a factor of 2.8 times!

(c) Implementation of the Damping Function Approach into the EIM

Efforts to implement the 'damping function' approach into the code were explored. In the process, the following difficulties were encountered. It was mentioned in the third chapter that the code performs an internal coordinate transformation from the physical space to the computational space and calculations are performed in the

computational space. The code manual mentions that the particle transport calculations are performed in the computational space, using the already available flow field results.

At the beginning of the chapter, it was mentioned that five-block geometry was constructed for the present simulations. Since, the fluctuation velocities are generated in the computational space; it is necessary to know the flow orientation in the computational space. Moreover, the correspondence among the blocks is rearranged in the computational space. A proper knowledge of all the above details is needed before the implementation of the 'damping function' approach in the code is performed, so that the fluctuation velocities can be appropriately damped.

Efforts were initiated with the code developers to get the above details. Unfortunately, not much progress could be made in this front. The code developers provided the necessary subroutines but were neither ready to participate in the implementation nor to verify the implementations. Efforts to convince them to run a trial case with the code to make them know that the code results are completely unphysical were not successful.

However, implementation of the 'damping function' approach into the code was performed under certain assumptions. Complete details regarding the implementation are presented in reference 46, and a brief description is provided here. In essence, the 'damping functions' described previously, were implemented into the subroutine TDISP that performed the turbulence dispersion calculations. The logic implemented into the subroutine was to compute the non-dimensional distance from the wall, y^+, corresponding to the particle location at each time step.

If the value was less than 80, then,

(a) the damping functions were computed from the expressions given previously, using the y^+ value, and,

(b) Multiplying the obtained value with the appropriate damping function damped the fluctuation components of the velocity generated in the subroutine.

$$u'(new) = f_u \times u'(computed),$$
$$v'(new) = f_v \times v'(computed), \qquad (39)$$
$$w'(new) = f_w \times w'(computed)$$

The previous simulations were repeated after the implementation of the damping function approach into the code. The orientation of the transformed geometry in the computational plane was assumed to be such that u' represents the fluctuation velocity along the flow direction, v' represents the fluctuation velocity in the normal direction and w' represents the fluctuation along the lateral direction. The results are presented in Figure 88. The original results and the experimental results are included along with the present results, for comparison.

It can be seen from the figure that there is really no difference in the penetration results with (labeled CFX-DAMP+TD) and without (labeled CFX-WITH TD) the damping function approach. This result was very surprising, and it may possibly be an indication that the assumption on the geometrical orientation on the computational plane was wrong. At this point, queries were made to the code developers seeking certain technical clarifications to proceed further with this study. However, satisfactory response was not forthcoming and the study had to be aborted at this stage.
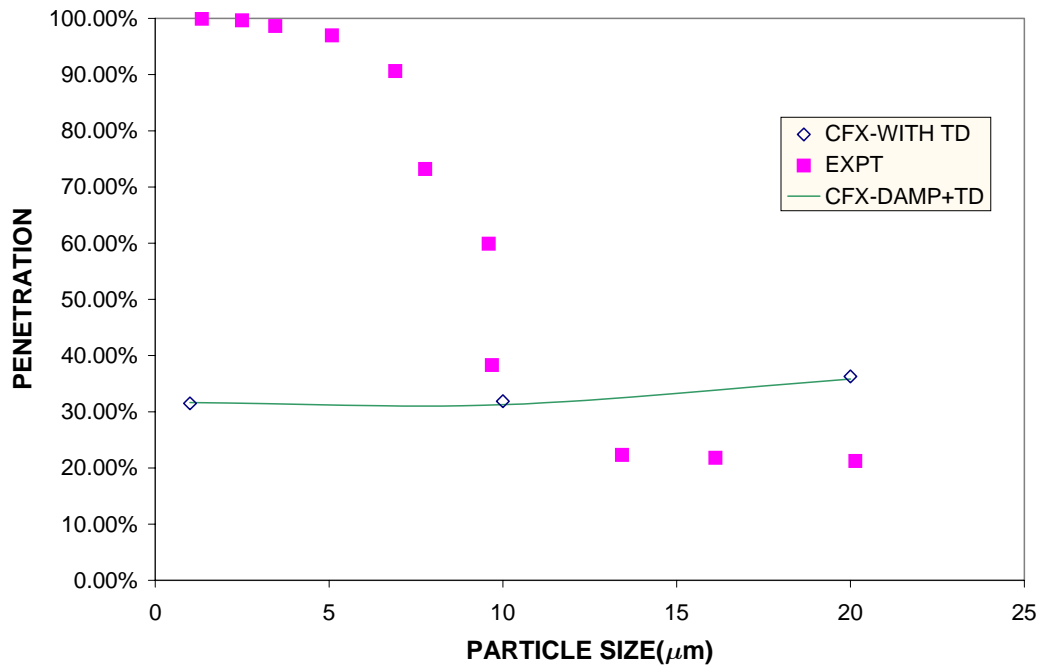
Fig. 88. Comparison of the penetration predictions of the code with and without the damping function against experimental data

It is necessary to recall now that in the previous study reported in reference 46, it was shown that a fair agreement was obtained for the present case, under the same set of assumptions regarding the geometrical orientation in the computational plane. However, there were a couple of observations about the previous study that need to be stated here, so that the present results may be viewed in the proper perspective:

(a) In the previous study the k-ω model was used and not the k-ε model. The k-ω model is a low-Reynolds number model and does not use the universal law of the wall formulation to capture the near-wall behavior. Instead, k and ω equation are solved up to the wall.

(b) A mock simulation on a fictitious geometry was conducted where the flow Reynolds number was nearly the same as the present study. The constants in the determination of the eddy length and time scales were tuned until the penetration results obtained on the mock geometry were consistent with the experimental observations presented in reference 42 and the standard results presented in references 42 and 49, before repeating the present simulations.

(c) Being a low-Reynolds number model, a very-fine mesh structure had to be adopted to satisfy the code requirements on the near-wall mesh density, for using the turbulence model. It could be seen in reference 49 that the number of computational cells in the mock case and the original case were of the order of 372,000 and 720,000. In spite of the mesh being so fine (compare 44200 for the present simulations), it was found that the code requirements on the mesh-density could not be satisfied. The simulations, however, were performed under the same conditions.

(d) The results obtained were not reproducible i.e., when the tuned algorithm was tested for different set of flow conditions, it was not possible to obtain predictions consistent with standard results presented in references 42 and 49.

It could have been possible that the near-wall happenings were captured better in that study, as the mesh density in the near-wall region was many times more than that of the present study. However, the agreement shown in that study needs to be taken more as fortuitous and coincidental, rather than a rigorous and conclusive proof of the 'damping function' approach, due to the above reasons.

Moreover, from a computational viewpoint, it can be seen that the number of cells when the k-ω (low Reynolds number) model was used, was nearly 10 times more that used for the standard turbulence model. This was the case even without being able to satisfy the code and model requirements regarding the near-wall mesh density. So, from a practical viewpoint, it seems that the use of a low Reynolds number model would be computationally expensive, even for a simple case as the present one.

There is another common and important observation to be made on the works presented in reference 47, 49 and 51. In the above three works where the wall deposition was studied numerically, the primary flow field was not obtained by solving the NSE. Instead, the details of the average and fluctuating quantities were defined in the simulation, either from previously available experimental data or from numerical data obtained from DNS, before performing the particle tracking computations.

There are some others studies in the literature that report using higher order turbulence models as the Reynolds Stress model (RSM), to resolve the turbulent flow field[54, 55]. In those studies, the length and time scales of the were eddy calculated on a directional basis to account for the anisotropy, based on the Reynolds Stress values and other advanced features that were introduced into the dispersion model. They tested the implementations for the prediction of particle dispersion for a variety of experimental data available in the literature on unbounded flows as axi-symmetric jets, grid turbulence, quarl burners etc., but not for the wall deposition in the case of bounded flows. Moreover, in both the studies, a two-way coupling between the phases was invoked and coupled calculations were performed for two to three iterations.

There would be no problem to invoke the Reynolds Stress model to obtain the turbulent details. However, implementation of the above recommendations into the code would again be a very involved process as new probability density functions, and, new definitions based on advanced statistics and complex algebra would have to be defined. In other words, this would amount to writing a completely new model for the turbulence dispersion phenomenon. With the present knowledge of the code and the level of technical interaction with the code developers, it is unclear whether the above features can be implemented into the code and made operational.

However, a main consideration in applying this model to wall bounded flows is that even when the Reynolds Stress model in the code is invoked to obtain details about the turbulence, the near-wall details would still be obtained using the universal law of the wall. The physics of the deposition process is governed by the near-wall details. However, the universal law of the wall cannot capture the near-wall anisotropy in the fluctuation velocities. For this reason, it should be expected that not much improvement in the code predictions would be obtainable, assuming that the above suggestions could be implemented in the code.

Again, if the RSM is used with the EIM that is presently available in the code, there are other disadvantages in addition to the one discussed in the previous paragraph. Advanced details on the turbulence obtained using the RSM, would be taken to a gross form i.e., would be converted to k, to generate the fluctuation velocities and the length and time scales in the EIM. So, the effort expended on obtaining these finer details would be wasted in the conversion process and the benefits would not be realized.

However, as there were hints on the coupled approach being used in the simulations, studies were performed with a two-way coupling. The results obtained with the coupled approach are presented in Figure 89. CFX-COUP2 refers to the results with the number of iterations being 2 and CFX-COUP3 is that corresponding to the number of iterations being 3. The previous result with one-way coupling (CFX-NOCOUP) and the experimental results (EXPT) are presented alongside for comparison.
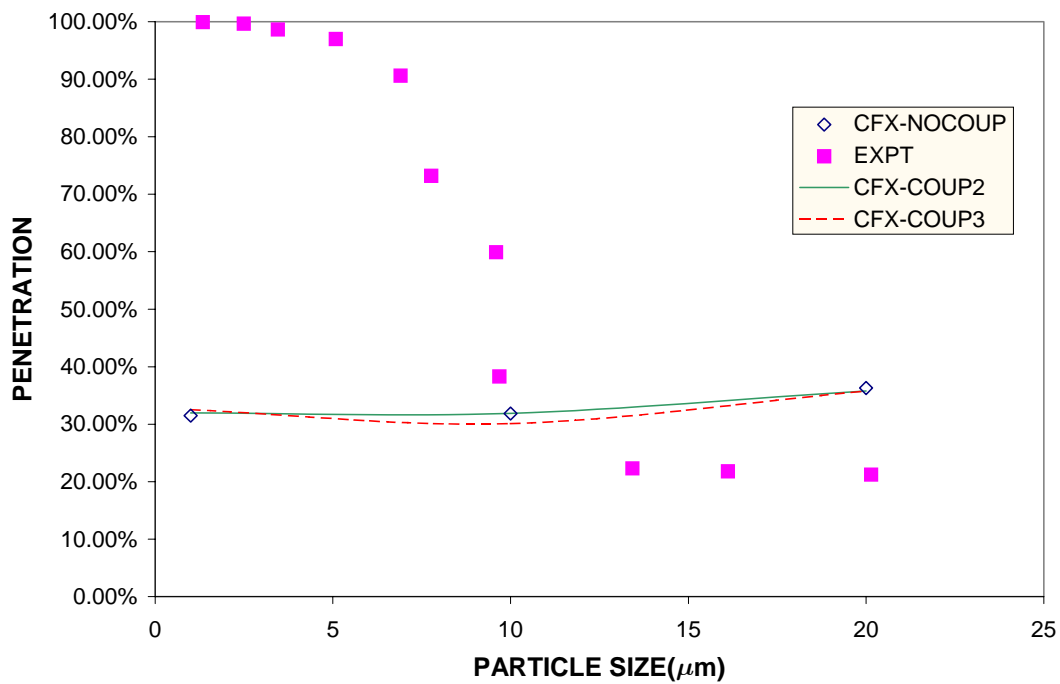
Fig. 89. Comparison of the penetration predictions of the code with and without coupling against experimental data.

It can be seen that though there is a slight difference between the predictions for the uncoupled and the coupled cases, when compared to the experimental data, the difference is trivial and the predictions are completely wrong, as before. This indicates

that the absence of coupling mechanism in the previous simulations was not responsible for the erroneous predictions obtained from the code.

Having investigated most of the possible options, a final study was performed in which efforts were undertaken to investigate how changes in the prediction of the primary flow field would affect the deposition predictions. In this study, the constant $C_{\varepsilon 2}$ in the k-ε model was slowly decreased from its original value of 1.92 to a value that is close enough to the constant $C_{\varepsilon 1}$ i.e., 1.44, based on personal advice and suggestions available in the literature[56].

From a modeling viewpoint, it amounts to modifying the ratio of the unresolved to the total kinetic energy in flow. As the value of the constant $C_{\varepsilon 2}$ is decreased toward the value of the constant $C_{\varepsilon 1}$, the ratio of production to dissipation under equilibrium conditions is unity. This means that the production and dissipation mechanisms are balanced. From a computational viewpoint, as the value of $C_{\varepsilon 2}$ decreases toward $C_{\varepsilon 1}$, it is as though performing a DNS simulation. More details on this novel approach are elaborated in the reference.

This approach was tried out for the present case, however, with a slight difference in the initial conditions; the turbulence intensity was specified to be 1%. A series of studies were performed decreasing the $C_{\varepsilon 2}$ value all the way until 1.44. The results obtained for the case $C_{\varepsilon 2} = 1.55$ is presented in Figure 90 as an illustration, along with the original predictions and the experimental results. It can be seen that the present

results display the same trend and are shifted to lower penetration values, with less than 10% of the particles introduced at the inlet making it to the outlet.

At the end of the above study, it was concluded that the effect of the EIM is completely dominating the predictions of particle deposition. Due to the above reason, any changes that are made to the primary flow are simply superceded. Having performed enough investigations, it was now clear that there is no possibility of improving the model predictions.
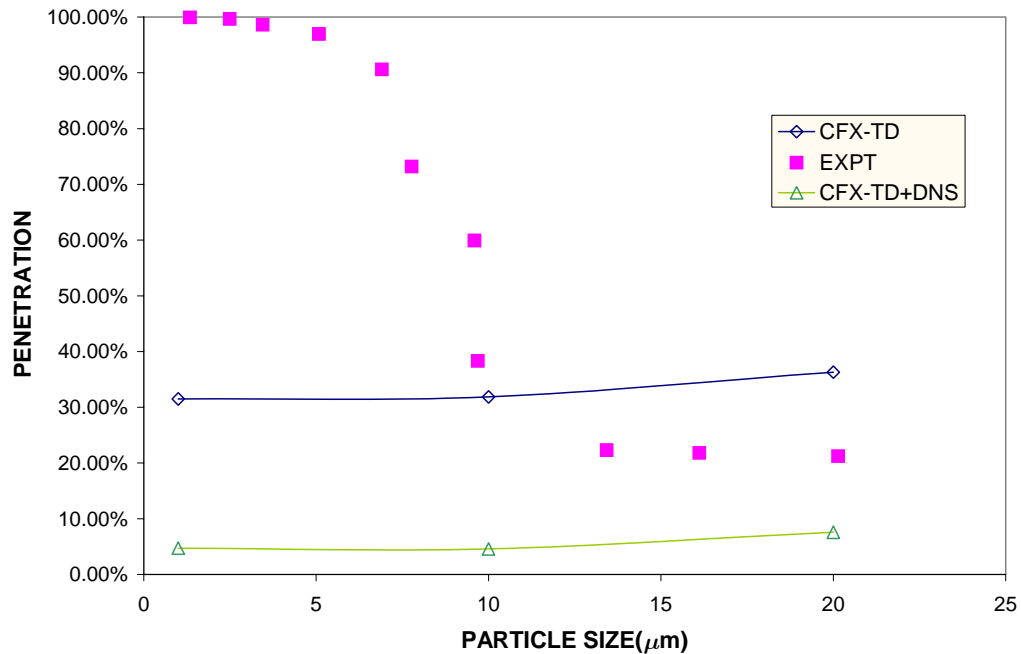
Fig. 90. Comparison of the penetration predictions of the code with the novel approach and EIM against experimental data.

At this point, attention was turned to a couple of studies that had used a slightly different approach compared the EIM to account for the effect of the fluid turbulence on the particles[57,58]. In the first study, the performance of a shrouded probe sampling under

turbulent flow conditions was numerically simulated. The simulation results were shown to be in good agreement with experimental data. In the second study, deposition of aerosol particles on the walls of a turbulent channel flow was simulated.

In both the above studies, the fluctuating components of the turbulent velocity field were generated using a time-correlated approach, unlike the EIM, where they were uncorrelated. As in the EIM, turbulence was assumed to be homogeneous and isotropic. However, the interaction part of EIM, where the particles interact with a series of eddies as they traverse through the domain, was not present. Moreover, the near-wall effects on the fluctuation velocities was accounted for in the later study, whereas, it was neglected in the former study.

As a next step, efforts were made to implement the time-correlated approach into the code. While the velocity fluctuations would be the same as generated by the EIM, for time steps after the initial time (t=0), the fluctuation velocities would be obtained as

$$u_i'\left(t_j\right) = \sqrt{\alpha}Y_i'\left(t_j\right) + \sqrt{1-\alpha}Y_i'\left(t_{j-1}\right), \tag{40}$$

Where the value of $\alpha = 0.2$ was used in the studies presented in references 57 and 58, and $Y_i'\left(t_j\right)$ is the fluctuation velocities generated presently by the EIM. This would amount to obtaining the velocity fluctuation of the present time step as a combination of values of the present and previous time steps. From a physical basis, this is equivalent to saying that the fluctuations of successive time steps are auto-correlated. This is true as long as the time interval is short.

While the above implementation was performed in the TDISP subroutine, the interaction part of the EIM was left intact. This was done to avoid any adverse effects

that may arise from de-activating this part of the subroutine on the computations, as it was calling and was being called by other subroutines in the code. Simulations were then performed with the modified subroutine on the same problem being investigated; keeping all the other conditions same as before.

As a first step, when simulations were performed with the modified routine, it was found that nearly all the released particles (97%) were getting deposited at the wall, even for a 1 μm AD particle. Compared to the previous case, it can be seen that the deposition increased in the present case. While the mean velocity field remained the same between the present and the previous cases, the only difference lies in the way in which turbulent fluctuations were generated. The observed result (increased particle deposition) indicates that the magnitude of the fluctuation velocities increased for the present case, as compared to the previous case.

It was decided that a study would be performed to investigate on the possible ways to decrease the magnitude of the fluctuations that would decrease the percentage deposition. As the fluctuation velocities are generated based on the local $'k'$ values, it was decided that the profile of $'k'$ would be shifted down. After a trial and error process was carried out, it was determined that the $'k'$ profile would be scaled down to be 25% of its original value. Previous simulations were then repeated with this modification and the results are presented in Figure 91.

It can be seen from Figure 91 that the modified time-correlated EIM (CFX-TCTD) gives predictions that are slightly better than the standard EIM (CFX-TD). Though the predictions are still very different compared to the experimental results, for the first time, a decrease in penetration with increasing particle size is observed. The magnitude of decrease is far from that in the experiment.
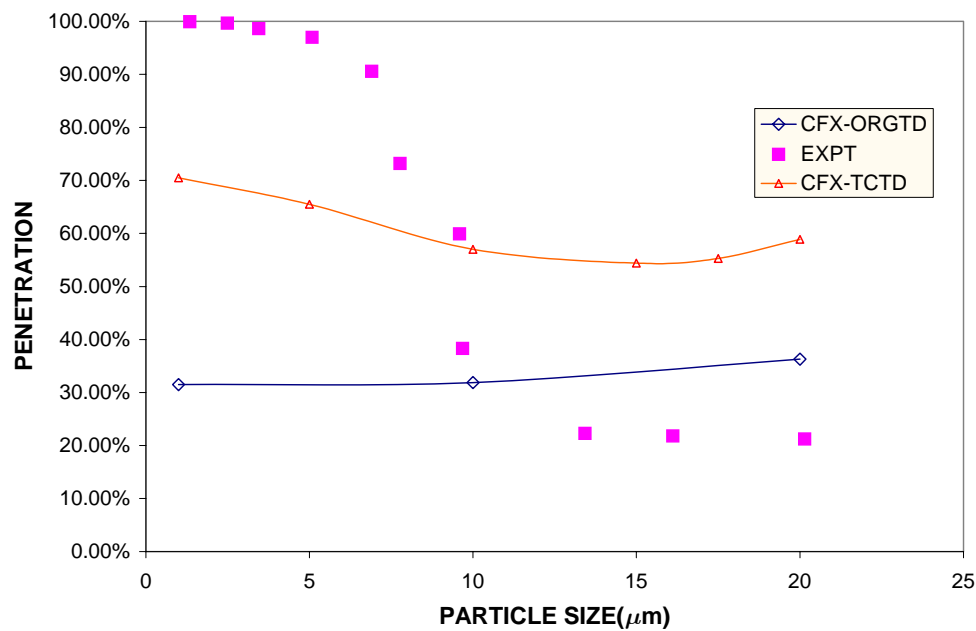
Fig. 91. Comparison of the penetration predictions of the Code with the modified time-correlated EIM and standard EIM against experimental data.

There is another observation that needs to be pointed out. After the penetration decreases to a value of ~55% for a 15 μm AD particle, it again shows a slightly increasing trend. While this has been observed experimentally at higher Reynolds numbers for the corresponding particle size[42], for the present case it is not correct.

Further investigations were performed with the modified time-correlated EIM to see if the predictions can be improved. The value of the correlation coefficient, α, used in the generation of the fluctuation velocities was increased gradually from 0.1, to determine the point at which the predicted penetration would reach a value of 100% for a 1 μm AD, for the present flow conditions. The results of the study are presented in Figure 90. It can be seen from Figure 92 that the penetration starts increasing from a value of ~50% for $\alpha = 0.1$, all the way up to ~100%, for $\alpha = 0.7$.
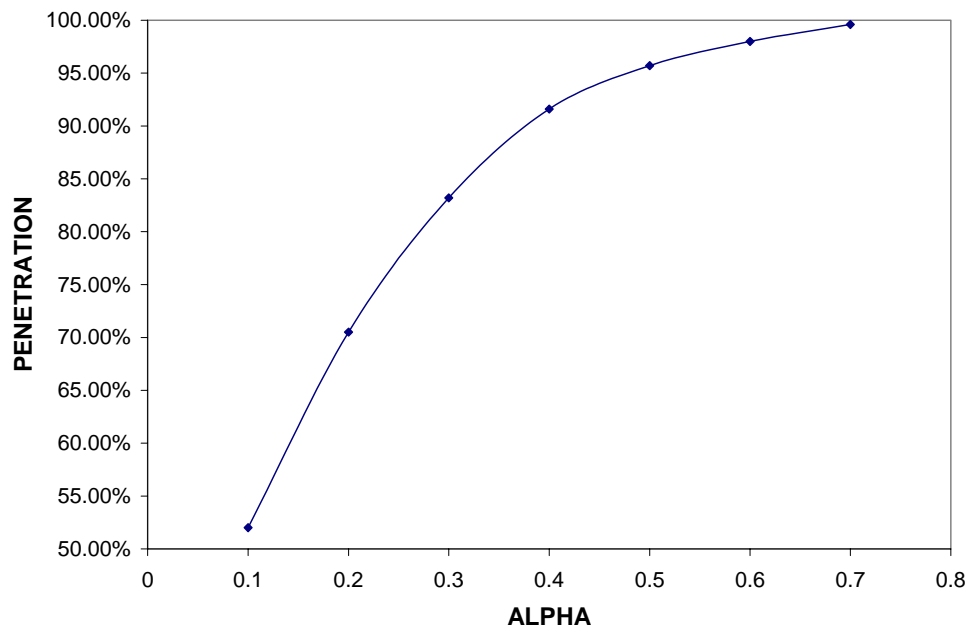
Fig. 92. Penetration predictions of the code for the modified time-correlated EIM as a function of the Correlation Coefficient α (for 1 μm AD particle).

Having determined the value of α that gives 100% penetration for a 1 μm AD particle, the penetration predictions for the whole range of the particle sizes was

obtained using the modified time-correlated EIM, with the value of $\alpha = 0.7$. The results of this study are presented in Figure 93.

In Figure 93, the present predictions ($\alpha = 0.7$) are denoted by CFX-TCTDA. The predictions obtained previously with the modified time-correlated EIM with $\alpha = 0.2$ (CFX-TCTD), Standard EIM (CFX-TD) and the experimental results (EXPT) are presented alongside for comparison. It can be seen that in the process of trying to improve the predictions, the present modification on the α value has resulted in a complete deterioration of the previous predictions.
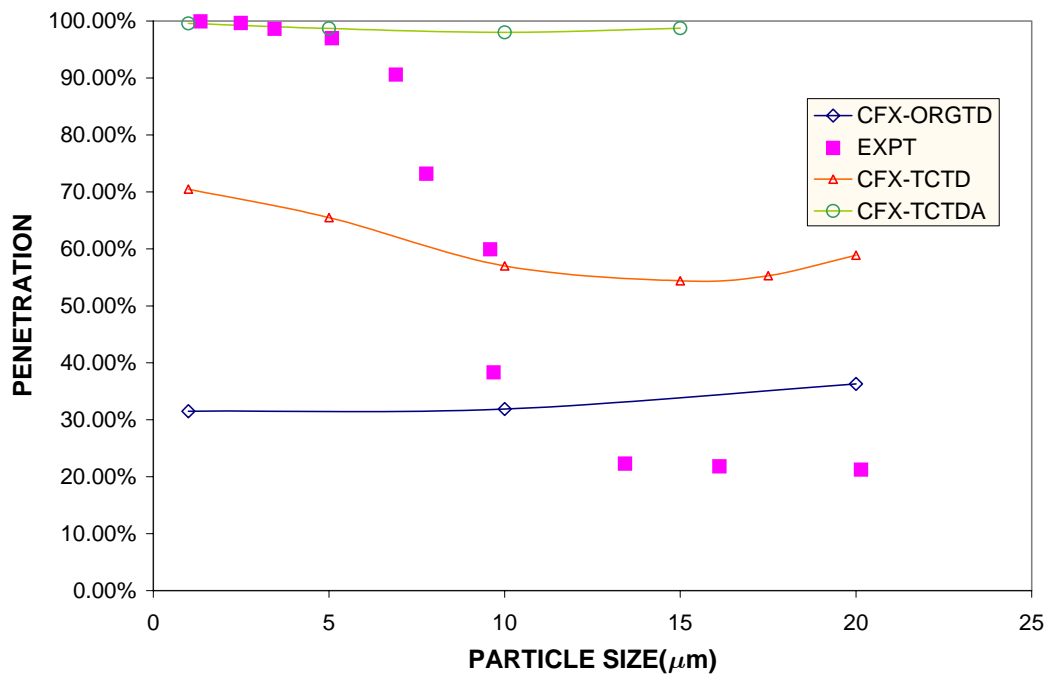
Fig. 93. Comparison of the penetration predictions of the code for the modified time-correlated EIM with different α values against standard EIM and experimental results.

Further studies were performed by modifying the coefficients in the determination of the length and time scales that appear in the eddy interaction part of the

modified time-correlated EIM (with $\alpha = 0.2$). It was found that the predicted penetration curve got shifted in magnitude, either above or below the predictions presented in Figure 93, keeping the same trend. Hence, no improvement in the results was obtained.

At this point, mention has to be made about an important observation on the time step used in the integration of the particle transport equations. Most of the references presented in this chapter have indicated the importance of choosing a proper value for the time step, as the penetration predictions are very sensitive to the chosen value. However, there is no option available in the code for the user to choose the time step. Instead, there is some internal mechanism in the code that chooses the time step value for the particle transport calculations. Information on the criterion adopted to determine the time step is unavailable in the solver manual.

However, as some of the subroutines were made available in the course of the present work, the time step chosen by the code was altered indirectly by making some changes to one of the subroutines. It was shown in the previous study (reference 46) that the value determined by the code was optimum from the viewpoint of the penetration predictions made by the code as any decrease in the value of timestep below that value did not change the penetration predictions. It is unclear, however, on whether the choice of the timestep chosen by the code is consistent with the suggestions available in the literature.

Another important aspect that has not been discussed until now is the size range of the particle that was investigated in the present study. It is to be mentioned that the size of the particles used in most of the experimental studies reported in the literature,

for which the performance of the various turbulent dispersion models as the EIM have been evaluated, were comparatively higher (references 54,55). It was only in reference 48 that the evaluation of the EIM was performed on particle sizes that are comparable to those in the present study. Moreover, it is also to be noted that there were no instances where the EIM was used to estimate the deposition phenomena in wall-bounded flows. In most of the studies, the EIM was only used to estimate the particle dispersion by fluid turbulence.

In spite of the various efforts undertaken until this point, it has not been possible to obtain any trend in the code predictions that is indicative of the experimental behavior. A lot of time and effort was expended in trying to improve the predictions of the code, based on various suggestions from the literature. However, the behavior of the EIM, either in its original form or in the modified form, was not tractable, under a scientific or a logical framework. Hence, the present study was terminated at this point.

VII. D. Conclusions

In the present chapter, efforts were commenced to investigate the capabilities of the CFX-4.4 code for the simulation of aerosol transport under turbulent flow conditions. Simulation of a simple experiment in which aerosol transport was studied under fully developed turbulent flow conditions in a circular pipe was performed. The results of this experiment are treated as a standard in the field of aerosol deposition under turbulent flow conditions[42].

The standard $k\text{-}\varepsilon$ turbulence model was chosen to resolve the details of the turbulent flow field. The turbulent dispersion force option in the code was invoked to

account for the dispersion and deposition of the aerosol particles due to fluid turbulence. It was found that the penetration curve generated from the results of the simulation, as a function of particle size was completely erroneous. In fact, the code predictions of the penetration as a function of particle size showed a trend that is physically incorrect.

The results of the study prompted a detailed literature search. It was found that the same behavior was observed in one of the previous studies in which the turbulent dispersion model was used. A detailed study of the original material on the development of the turbulent dispersion model adopted in the code was undertaken. It was found that the present model was developed to account for the effect of fluid turbulence on the dispersion of droplets evolving from a point source (jet spray) in liquid fuelled combustors. Oblivious of the above fact, most of the commercial CFD software as CFX-4.4 adopted this dispersion model and claim that their code can simulate particle transport under turbulent flow conditions.

In the present case, the model that was developed to account for particle dispersion in self-similar flow conditions was being used to obtain estimates on the deposition of aerosol particles in the case of wall-bounded flows. The unsuitability of the above approach for the present case was recognized as 'dispersion' and 'deposition' are two distinctly different physical processes. Though the dispersion of particles by the turbulence in the fluid field is necessary before deposition can occur at the walls, the physical mechanism that governs the deposition process in the near-wall region is not related to the particle dispersion in the free stream.

Further literature search revealed some of the important details pertaining to the EIM. In one of the studies, the exact technical deficiency of the model was vividly presented. Even though the EIM was developed for self-similar flows, the assumptions inherent in its formulation preclude its uses in conditions where the assumption would be violated. This was demonstrated in the study by conducting simulations of experimentally available particle dispersion data on inhomogeneous, self-similar flows. It was shown that a large discrepancy existed when the EIM predictions of particle behavior were compared against experimental data.

It was also shown that the artificially generated fluctuation velocity field does not satisfy continuity, and, as a result, there was leakage in the transverse direction, across the mean flow. This was resulting in an incorrect pumping effect on the particles from the core toward the edges. This deficiency is inherent to the model and is not rectifiable.

Observations presented in another study where suggestions were made to account for the near-wall anisotropy of the fluctuation velocities, when using the EIM for wall-bounded flows, were implemented into the code with some assumptions. However, the obtained results were no different from the previous results.

As a final effort, a time-correlated scheme for the generation of fluctuation velocities was implemented in the code, as suggested in another study. After some modifications, it was seen that a trend that is indicative of experimental observations was observed. However, efforts to improve this trend to obtain correspondence with experimental data were unsuccessful and no further improvements were forthcoming.

At this point, investigations were concluded, as the obtained predictions until now do not show any correspondence to experimental data, in spite of the time and effort expended on model improvement. Moreover, the performance of the EIM has not been tractable either under a technical or a logical framework.

Some of the observations of the present investigations are summarized below for the benefit of posterity:

(a) Care should be exercised when using the standard k-ε turbulence model for resolving the turbulence details for conditions such as the present case where the flow Reynolds number is 10000. This is due to the reason that the near-wall turbulence profile would be obtained using the universal law of the wall that was formulated based on high Reynolds number (Re>30000) experimental data. The obtained near-wall turbulence detail would be erroneous and this would affect the subsequent particle transport calculations.

(b) One way to avoid this is to use the low Reynolds number k-ε turbulence model (or) k-ω model, which is a low Reynolds number model. However, application of the model would necessitate using a very fine mesh in the near-wall region that would result in a substantial increase in the total number of computational cells. Previous experience suggested that even a 20 fold increase over the number of cells required for the standard k-ε turbulence model was not sufficient to satisfy the criterion required by the code to use the model.

(c) In view of all the above problems encountered with the resolution of the turbulence details using the two-equation modeling approach, it is felt that efforts should be undertaken to explore using Large Eddy Simulation (LES) to resolve the turbulence.

CHAPTER VIII

CONCLUSIONS AND FUTURE WORK

In this study, the Computational Fluid Dynamics (CFD) technique has been used as a tool to study aerosol transport. Performance of a variety of aerosol sampling devices was numerically simulated using the commercially available CFD code CFX-4.4. The study was performed as a supplement to the experimental work that is presently in progress at the Aerosol Technology Laboratory (ATL), to design, develop, and optimize the performance of aerosol sampling equipment.

Aerosol transport through the sampling devices was treated as a dilute and dispersed two-phase flow with aerosol as the dispersed phase and the fluid as the continuous phase. Simulations were performed under an Eulerian-Lagrangian framework with a one-way coupling between the phases.

As a first step, the lagrangian particle tracking algorithm available in the CFX-4.4 code was validated against experimental data available at ATL, and, data from the results of previous numerical simulations. Both these data were obtained for a rectangular slit real impactor operating under laminar flow conditions. It was found that, in the former case, code predictions of the impactor efficiency curve was in excellent agreement to the experimentally obtained curve. In the latter case, while the code predicted impactor efficiency curve was in fair agreement with the numerical predictions for the low Reynolds number cases, there were differences when the flow Reynolds number increased to 3000. However, it is believed that the results of the present computations are more accurate than the previous results, not only because they were

performed two decades earlier, but also due to the observed trend of the impactor efficiency curve being more in tune with the experimental results.

Having validated the particle transport algorithm in the code, the performance of a slit virtual impactor was optimized using the code. Starting with a preliminary design of a prototype slit virtual impactor, the effect of modifying the important geometrical parameters of the impactor, using suggestions available in literature, were numerically explored. Based on a series of studies, an optimized design of the impactor was arrived at. Performance details (efficiency and wall loss curves) of the optimized design for different operating conditions (operation at different major-to-minor flow split ratio, throat velocities etc.) were estimated. The effect of modifying the radius of curvature in the receiver section on the impactor performance was explored and the performance curves for three different radii of curvature were obtained.

Unlike the real impactor, it was shown that the impactor efficiency curve in the case of a virtual impactor, for a given geometry, was unique, for operation at different Reynolds numbers (throat velocities), and, is not a function of the flow Reynolds number. Small differences in the middle region of the efficiency curve arise due to difference in the internal wall losses, when operated at different throat velocities.

In the next study, the performance of a Linear Slot Virtual Impactor (LSVI), fabricated based on the recommendations of the previous study, was investigated. Simulations were performed on a model that was a highly conservative representation of the original LSVI, in the sense that combination of the geometrical parameters used for

building the model incorporated all sorts of asymmetry and the worst-case values of the measured dimensions.

As before, simulations were first performed on a preliminary model. However, more geometrical information was incorporated to the preliminary model. Using the above as the base model, the impactor efficiency and wall loss curves were obtained. The effect of the depth of the inlet convergence section of the impactor on the predicted performance was investigated.

It was shown that even small amounts of offset (asymmetry) in the geometry would result in unequal flow split between the major flow outlets, under conditions of imposed equal pressure. This unequal flow split would also result in an unequal split of the particles between the outlets. This effect would be pronounced for particle sizes around and above the Stokes cut point value.

For the first time, simulations were extended to cover particle sizes far beyond the size corresponding to the normal range of collection efficiency values (0-100%). A lot of new information important in the case of virtual impactor operation was inferred from the results of the study. This information was either not known conclusively, or, had been overlooked in the literature in the past and had not been found reported in the literature.

It was found that the efficiency of collection in the minor flow would start decreasing and the internal wall loss would start increasing, as the particle size starts increasing beyond the size corresponding to the normal range of collection efficiency values. The offset in the geometry would accentuate the wall loss.

From the viewpoint of the numerics, it was shown that sufficient depth of the inlet convergence section is necessary to get unbiased results for the prediction of heavier particles. Also, a multi-block strategy was adopted in the inlet convergence section. It was shown that small difference in the results for higher particle sizes are possible for different blocking configurations.

Numerical predictions of the impactor efficiency and wall loss curves were shown to be in fair agreement to the experimental results. Considering the fact that the numerical results were obtained on a worst-case model of the LSVI with imposed equal pressure on the minor flow outlets (compared to the equal flow split in the experiment), this agreement is good.

In the final study, the performance of the code for the prediction of aerosol transport under turbulent flow conditions was explored. A fully developed turbulent pipe flow experiment (Re=10000) involving aerosol transport was simulated. It was found that the predicted results of the aerosol deposition were completely erroneous compared to the experimental result. This problem was traced to the turbulent dispersion model in the code that conveyed the effect of fluid turbulence on the particle behavior. The unsuitability of the present model for the study of aerosol deposition in turbulent flows was explained. Also, the inapplicability of the standard turbulence model in the code for obtaining the turbulence details for the present conditions was discussed.

Evidence was adduced from the literature to prove the fact that there are inherent technical deficiencies in the turbulent dispersion model that cannot be remedied. Primary deficiency arises from the fact that artificially generated fluctuation velocity field in the

model does not satisfy the continuity equation. As a result of the above, there is leakage in the transverse direction and an incorrect pumping effect whereby the particles cross the mean streamlines and start getting accumulated at the edges, resulting in a depletion of the particles at the core region.

A variety of remedial measures were initiated based on suggestions from the literature to improve the code predictions. After spending much time and effort on this front, the study was terminated as there was no indication whatsoever that the code predictions would be able to replicate the experimental trend.

At this point, based on the results obtained in the present study, it seems that the code can be used with confidence to obtain aerosol transport prediction for laminar flow conditions. However, for prediction of aerosol transport under turbulent flow conditions, it seems that the present model in the code is incapable of, and, unsuitable for predicting details pertaining to the deposition of aerosols under turbulent flow conditions.

Future work in the case of LSVI should concentrate on the construction of a new LSVI model. The new model should be built with the optimum set of geometrical parameters given in Table X. As there are practical difficulties involved in the accurate measurement of some critical geometric parameters, and, the number of parameters involved is large, it is difficult to individually characterize the uncertainties. However, an effort needs to be undertaken to arrive at the best combination of the critical geometric parameters that could be considered as the optimum combination.

Simulations would then have to be repeated on that model with the same set of flow conditions, but with mass flow boundary conditions assigned to the minor flow

outlets (instead of pressure boundary conditions that were assigned in the present study), to be consistent with the experiment. Those simulations would have to be performed with equal flow split among the minor flow outlets. The results of the simulation should be compared against the experimental results presented in reference 41 to obtain a realistic picture of the situation.

At the same time, experiments need to be performed at intermediate particle sizes to investigate if the present efficiency and wall loss curves are unique (or) would be altered with the new data obtained for the other particle sizes. This needs to be done as a means of verification/confirmation that the obtained trend is consistent, as the present wall loss curve seems to be different from those reported in the literature.

In the case of simulations involving aerosol transport under turbulent flow conditions, the feasibility of using a LES (Large Eddy Simulation) based lagrangian particle tracking approach should be explored. While in the past, this approach was used to study particle dispersion and deposition in simple geometries such as pipes and ducts[59,60], there is recent evidence that this approach has been used successfully to predict particle behavior in complex machinery as a cyclone separator[61].

There are a lot of advantages in using a LES based lagrangian particle tracking approach for the present case. The primary and the most important advantage with this approach is the fact that the 3D, time-dependent, instantaneous turbulent velocity field, that is required for the particle transport calculations, is directly obtainable from the results of the LES simulation. This approach would therefore obviate the use of the RANS based two-equation modeling approach used for obtaining the details of the

turbulent flow field and the turbulent dispersion model that needs to be used in conjunction with the two-equation model. Thus, this approach would help to overcome the limitations and shortcomings involved with the EIM model used in the present study.

REFERENCES

1. C. H. FLETCHER, *Computational Techniques for Fluid Dynamics*, Vols. 1 & 2, Springer-Verlag, New York (1991).

2. P. J. ROACHE, *Fundamentals of Computational Fluid Dynamics*, Hermosa Publishers, New Mexico (1998).

3. CFX-4.3, CFX-4.4 & CFX-5.6, ANSYS Canada Ltd., Waterloo, Ontario, Canada (2003).

4. FLUENT 6, Fluent USA Inc., Lebanon, New Hampshire (2002).

5. STAR-CD V3.150, CD adapco Group, New York (2003).

6. J. H. GOO and J. W. LEE, " Stochastic Simulation of Particle Charging and Collection Characteristics for a Wire-Plate Electrostatic Precipitator of Short Length, *J. Aerosol Sci.*, **28,** 875 (1997).

7. Z. ZHANG, C. KLEINSTREUER, and C. S. KIM, "Flow Structure and Particle Transport in a Triple Bifurcation Airway Model," *Trans. ASME*, **123**, 320 (2001).

8. A. KEATING, "Numerical Prediction of Erosion-Corrosion in Bends," *Corrosion*, **57**, 621 (2001).

9. W. C. HINDS, *Aerosol Technology: Properties, Behavior, and Measurement of Airborne Particles*, John Wiley Publishers, New York (1998).

10. C. T. CROWE, M. SOMMERFIELD, and Y. TSUJI, *Multiphase Flows with Droplets and Particles*, CRC Press, Boca Raton, Florida (1998).

11. J. W. POPE, *Turbulent Flows*, Cambridge University Press, Cambridge, UK (2000).

12. F., M. WHITE, *Viscous Fluid Flow*, McGraw Hill Inc, New York (1991).

13. D. C. WILCOX, *Turbulence Modeling for CFD*, DCW Industries Inc., La Canada, California (1993).

14. J. O. HINZE, *Turbulence*, McGraw Hill Inc, New York (1987).

15. S. PATANKAR, *Numerical Heat Transfer and Fluid Flow*, Taylor and Francis Publishers, Philadelphia, Pennsylvania (1980).

16. J. H. FERZIGER and M. PERIC, *Computational Methods for Fluid Dynamics,* Springer-Verlag Berlin Heidelberg, Germany (1996).

17. J. S. SHIROLKAR, C. F. M. COIMBRA, and M. Q. MCQUAY, "Fundamental Aspects of Modeling Turbulent Particle Dispersion in Dilute Flows," *Prog. Energy Combust. Sci.*, **22**, 363 (1996).

18. A. D. GOSMAN and E. IOANNIDES, "Aspects of Computer Simulation of Liquid-Fuelled Combustors," ***AIAA-81-0323***, AIAA 19th Aerospace Sciences Mtg., St. Louis, Missouri (1981).

19. J. S. SHUEN, L. D. CHEN, and G. M. FAETH, "Evaluation of a Stochastic Model of Particle Dispersion in a Turbulent Round Jet,", *AIChE J.,* **29**,167 (1983)

20. S. LEE, A Slit Impactor Utilizing a Transpirated Impaction Surface for the Collection of Bioaerosols, M.S. Thesis, Texas A&M University, College Station (2002).

21. V. A. MARPLE and B. Y. H. LIU, "Characteristics of Laminar Jet Impactors," *Environ. Sci. Technol.,* **8**, 648 (1974).

22. D. J. RADER and V. A. MARPLE, "Effect of Ultra-Stokesian Drag and Particle Interception on Impaction Characteristics," *Aerosol. Sci. Technol.,* **4**, 141 (1985).

23. N. A. FUCHS, *Mechanics of Aerosols*, Macmillan Publishers, New York (1964).

24. *"Aerosol Measurement: Principles, Techniques, and Applications,"* P. A. BARON, K. WILLEKE, Eds., Wiley-Interscience Publishers, New York (2001).

25. B. JURCIK and HWA-CHI WANG, "On the Shape of Impactor Efficiency Curves," *J. Aerosol. Sci.,* **26(7),** 1139 (1995).

26. H. COLLAZO, W. A. CROW, L. GARDNER, B. L. PHILIPS, V. A. MARPLE, and B. OLSON, "Inertial Impactors to Measure Aerodynamic Diameters of Man-Made Organic Fibres," *Aerosol. Sci. Technol.,* **36**, 166 (2002).

27. C. HUANG and C. TSAI, "Influence of Impaction Plate Diameter and Particle Density on the Collection Efficiency of Round-Nozzle Inertial Impactors," *Aerosol. Sci. Technol.,* **36**, 714 (2002).

28. Y. A. HASSAN, B. G. JONES, and T. J.YULE, "An Analytical Study of Virtual Impactor Aerosol Separators," *Trans. Am. Nuclear Soc.*, **33**, 182 (1979).

29. V. A. MARPLE and C. M.CHIEN, "Virtual Impactors: A Theoretical Study," *Environ. Sci. Technol.,* **14**, 976 (1980).

30. L. J. FORNEY, D. G. RAVENHALL, and S. S. LEE, "Experimental and Theoretical Study of a Two-Dimensional Virtual Impactor," *Environ. Sci. Technol.,* **16**, 492 (1982).

31. D. G. RAVENHALL, L. J. FORNEY, and A. L. HUBBARD, "Theory and Observation of a Two-Dimensional Virtual Impactor," *J. Colloid Interface Sci.,* **85**, 508 (1982).

32. B. T. CHEN and H. C. YEH, "An Improved Virtual Impactor: Design and Performance," *J. Aerosol Sci.,* **18**, 203 (1987).

33. B. W. LOO and C. P. CORK, "Development of High Efficiency Virtual Impactors," *Aerosol Sci. Technol*., **9**, 167 (1988).

34. C. SIOUTAS, P. KOUTRAKIS, and B. A. OLSON, ""Development and Evaluation of a Low Cutpoint Virtual Impactor," *Aerosol Sci. Technol*., **21**, 223 (1994).

35. R. HAN and O. R. MOSS, "Flow Visualization Inside a Water Model Virtual Impactor," *J. Aerosol Sci.,* **28**, 1005 (1997).

36. C. SIOUTAS, P. KOUTRAKIS, and R. M. BURTON, "Development of a Low Cutpoint Slit Virtual Impactor for Sampling Ambient Fine Particles," *J. Aerosol Sci.,* **25**, 1321 (1994).

37. C. SIOUTAS, P. KOUTRAKIS, and R. M. BURTON, "A High-Volume Small Cutpoint Virtual Impactor for Separation of Atmospheric Particulate from Gaseous Pollutants," *Part. Sci. Technol.,* **12**, 207 (1994).

38. B. ASGHARIAN and M. N. GODO, " Transport and Deposition of Spherical Particles and Fibers in an Improved Virtual Impactor," *Aerosol Sci. Technol*., **27**, 499 (1997).

39. H. CHEIN and D. A. LUNDGREN, "A Virtual Impactor with Clean Air Core for the Generation of Aerosols with Narrow Size Distributions, " *Aerosol Sci. Technol*., **18**, 376 (1993).

40. Y. DING, S. T. FERGUSON, J. M. WOLFSON, and P. KOUTRAKIS, "Development of a High Volume Slit Nozzle Virtual Impactor to Concentrate Coarse Particles," *Aerosol Sci. Technol*., **34**, 274 (2001).

41. H. JOHN, A Slit Impactor Utilizing a Transpirated Impaction Surface for the Collection of Bioaerosols, Ph.D. Dissertation, Texas A&M University, College Station (2003).

42. B. Y. H. LIU and J. K. AGARWAL, "Experimental Observation of Aerosol Deposition in Turbulent Flow," *J. Aerosol Sci*., **5***, 145 (1974).

43. S. K. GIRIMAJI, Department of Aerospace Engineering, Texas A&M University, College Station, Personal Communication (2003).

44. R. W. FOX and A. T. McDONALD, *Introduction to Fluid Mechanics*, John Wiley Publishers, New York (1992).

45. K. W. STAPLETON, E. GUENTSCH, M. K. HOSKINSON, and W. H. FINLAY, "On the Suitability of k-ε Turbulence Modeling for Aerosol Deposition in the Mouth and Throat: A Comparison with Experiment," *J. Aerosol Sci.,* **31**, 739 (2000).

46. A. R. McFARLAND, Y. A. HASSAN, D. PHARES, G. YESILYURT, G. SHARMA, and S. HARI, "Study to Evaluate and Assess the Global Collection Efficiency of IMS Air Sampling Systems: Computational Results of Flow and

Aerosol Particle Deposition," Report Submitted to the Lovelace Respiratory Research Institute, Albuquerque, New Mexico (2002).

47. G. A. KALLIO and M. W. REEKS, "A Numerical Simulation of Particle Deposition in Turbulent Boundary Layers, "*Int. J. Multiphase Flow*, **15**, 433 (1989).

48. J. M. MACINNES and F. V. BROCCO, "Stochastic Particle Dispersion Modeling and the Tracer Particle Limit," *Phys. Fluids A* **4 (12)**, 2809 (1992).

49. E. A. MATIDA, K. NISHINO, and K. TORII, "Statistical Simulation of Particle Deposition on the Wall from Turbulent Dispersed Pipe Flow, " *Int. J. Heat & Fluid Flow,* **21**, 389 (2000).

50. D. I. GRAHAM, "An Improved Eddy Interaction Model for Numerical Simulation of Turbulent Particle Dispersion," *J. Fluids Eng*., **118**, 819 (1996).

51. Y. WANG and P. W. JAMES, " On the Effect of Anisotropy on the Turbulent Dispersion and Deposition of Small Particles," *Int. J. Multiphase Flow*, **25**, 551 (1999).

52. B. E. LAUNDER, G. J. REECE, and W. RODI, "Progress in the Development of a Reynolds-Stress Turbulence Closure," *J. Fluid Mech*., **68**, 537 (1975).

53. J. KIM, P. MOIN, and R. MOSER, "Turbulence Statistics in Fully Developed Channel Flow at Low Reynolds Number," *J. Fluid. Mech.*, **177***, 133 (1987).

54. A. BERLEMONT, P. DESJONQUERES, and G. GOUESBET, "Particle Lagrangian Simulation in Turbulent Flows," *Int. J. Multiphase Flow*, **16**, 19 (1990).

55. D. BURRY and G. BERGELES, "Dispersion of Particles in Anisotropic Turbulent Flows," *Int. J. Multiphase Flow*, **19**, 651 (1993).

56. S. S. GIRIMAJI, "Unsteady RANS Method for Turbulence: Fundamentals and Model Development," under consideration for publication in *J. Fluid Mech.*, (2002).

57. H.GONG, N. K. ANAND, and A. R. McFARLAND, "Numerical Prediction of the Perrformance of a Shrouded Probe Sampling in Turbulent Flow," *Aerosol Sci. Technol.,* **19**, 294 (1993).

58. S.ABUZEID, A. A. BUSNAINA, and G. AHMADI, "Wall Deposition of Aerosol Particles in a Turbulent Channel Flow," *J. Aerosol. Sci.,* **22***,* 43 (1991).

59. W. S. J. UIJTTEWAAL and R. V. A. OLIEMANS, "Particle Dispersion and Deposition in Direct Numerical and Large Eddy Simulations of Vertical Flows," *Phys. Fluids* **8 (10)**, 2590 (1996).

60. Q. WANG and K. D. SQUIRES, "Large Eddy Simulation of Particle Deposition in a Vertical Turbulent Channel Flow," *Int. J. Multiphase Flow*, **22**, 667 (1996).

61. J. J. DERKSEN, "Separation Performance Predictions of a Stairmand High-Efficiency Cyclone," *AIChE J*., **49**, 1359 (2003).

APPENDIX

In Chapter IV, it was mentioned that Collazo et al.,[26] reported that the effect of gravity needed to be included to obtain proper agreement with experimental results. It was also mentioned that they defined a parameter known as the 'gravity vector' in their study that was defined as

$$\hat{G} = \frac{gW}{V_0^2} \tag{1}$$

where g is the acceleration due to gravity, W is the nozzle diameter, and, V_o is the throat velocity. It was also mentioned that this parameter is the inverse of the square of the Froude number, a non-dimensional number that is important in free-surface flows[44], defined as follows:

$$Fr = \frac{u^2}{gd} \tag{2}$$

where u is the flow velocity, g is the acceleration due to gravity and d is a characteristic dimension in the flow geometry.

As can be seen from the definition, Froude number is the ratio of the Inertial to the gravitational force. In the case of our real impactor, the flow velocity for the determination of Froude number can be taken as the average velocity in the throat region and the characteristic dimension, twice the throat width ($2W$), to be consistent with the definition used for calculating the Reynolds number. The actual values are $W = 2.54E-04$ m, $g = 9.8$ m/s^2 and $u = 32.262$ m/s. If the Froude number is calculated from the above, the final value is $Fr = 2.09E+05$.

For the circular impactor of Collazo et al.,[26], the characteristic dimension to be considered is the diameter of the nozzle (d). In their case, the actual values are $d =$ 3.81E-03m, $g = 9.8$ m/s^2 and $u = 1.575$ m/s. The value of Froude number determined from the above parameters is $Fr = 66.42$.

As can be seen from the above calculations, the inertial force is many orders of magnitude higher than the gravitational force in our case, whereas, in the case of Collazo et al.,[26], it is not so. This is the reason why inclusion of gravity in their simulations was needed, to get results consistent with the experiment, whereas, in our case, there is no difference in the predictions with and without gravity.

VITA

Sridhar Hari, son of Hari Krishna Rao and Lakshmi Hari, was born on July 3, 1970 in Srirangam, India. He earned his bachelor's degree in chemical engineering from Annamalai University, India in June 1991. He then joined a one year orientation course in nuclear science and engineering at the Bhabha Atomic Research Center, India and, on completion of the above course in July 1992, started working as an engineer with the Rare Materials Project, Bhabha Atomic Research Center, India. He was involved in projects associated with the recovery of uranium from alkaline solutions and scrubbing of noxious fluoride gases.

His interest in the nuclear field led him to pursue graduate studies at Texas A&M University. He joined the Department of Nuclear Engineering in Fall 1997 and completed his master's degree in nuclear engineering in Fall 1998. His research was on the thermal-hydraulic safety analysis of research reactors using the RELAP5/MOD3.2 computer code.

On completion of his master's degree, he continued with his doctoral studies at Texas A&M University working on computational fluid dynamics (CFD). His research work was related to the modeling of dispersed two-phase fluid-particle flows in aerosol sampling equipment using the commercially-available CFD code CFX-4.4.

Dr. Hari's permanent address is 40-A, North Chitra Street, Srirangam, Tiruchirappalli-620006, Tamilnadu State, India.